Department of Engineering Science
University of Oxford

Protein-loaded Microbubbles to Investigate Ultrasound-Mediated Microbubble-Cell Membrane Interactions



Veerle Antoinette Brans
Oxford-Nottingham Biomedical Imaging CDT
New College, University of Oxford

22nd of April, 2022

A thesis submitted for the degree of
Doctor of Philosophy

Institute of Biomedical Engineering
Supervisors: Prof Eleanor Stride and Dr Erdinc Sezgin



‘Jong geleerd, oud gedaan.’

Carla Schoo Fotografie
April 1997, Amsterdam

Abstract

The immune response is regulated by the dynamic spatiotemporal regulation of signalling proteins at the interface between immune cells and their targets. The broadened knowledge of immunology and antitumour immune responses has led to the development of a novel cancer therapy avenue: immunotherapy. Unfortunately, the immune system's response to growing cancers is often weakened, and cancer cells have the distinct ability to evade the immune response. From this, two avenues to tackle this problem could readily be identified: (i) increasing the potency of immune cells or (ii) making diseased target cells, such as cancer cells, more visible to the immune system.

This work applies a novel strategy employing protein-loaded microbubbles to 'tag' cell membranes of interest with a relevant protein and investigates cavitation-induced microbubble-cell membrane interactions. To this end, microbubbles functionalised with a model protein were successfully produced and characterised, using a metallochelating complex through an NTA(Ni) and histidine residues interaction as an efficient loading strategy.

Proof-of-principle confocal microscopy experiments showed protein/dye-lipid material transfer, or 'membrane tagging' to a model cellular membrane using ultrasound in adherent A549 cells. This material transfer was subsequently investigated quantitatively in suspension using flow cytometry. It was observed for two cell types - A549 cells and Jurkat T cells - that cells undergo a morphological change upon ultrasound exposure, increasingly so with increasing pressures and duty cycles. Interestingly, a similar dependence of the 'membrane tagging' bioeffect on ultrasound was not observed in the suspension cell models. Potential evidence of a recovery mechanism was observed for both cell types after ultrasound exposure, indicating sonoporation and subsequent resealing of the cell membrane.

Lastly, these protein-functionalised microbubbles were modified to selectively bind microbubbles to cells of interest to improve the specificity of the proposed 'membrane tagging' and limit potential off-target interaction. Microbubbles were functionalised with His-transferrin, as A549 cells overexpress transferrin receptors on their outer membranes. The results show a significant increase in microbubble-cell attachment of His-transferrin functionalised microbubbles compared to control His-human serum albumin microbubbles. There was also limited binding of His-transferrin functionalised microbubbles to A549 cells with transferrin

receptors blocked by excess free transferrin, confirming targeting specificity. Again, ultrasound did not significantly affect the fraction of cells showing 'membrane tagging'.

In conclusion, this *Thesis* shows the successful fabrication and characterisation of NTA(Ni) microbubbles to which His-tagged proteins can be conjugated. Subsequently, the use of the microbubbles to 'tag' cellular membranes with these proteins was assessed both qualitatively with adherent A549 cells and quantitatively with A549 and Jurkat T cells in suspension. Lastly, this effect was greatly enhanced by functionalising microbubbles with the targeting protein His-transferrin to specifically target A549 cells expressing the equivalent receptor. This *Thesis* lays the groundwork for the use of custom-made protein-functionalised microbubbles in immunomodulation and, if successfully developed, may provide an inexpensive, low-risk alternative to CAR T cell therapy.

Statement of Originality

22nd of April 2022

I hereby declare that this submission is my own work, and to the best of my knowledge, it contains no materials previously published or written by another person or substantial proportions of material that have been accepted for the award of any other degree or diploma at the University of Oxford or any other educational institution, except where due acknowledgement is made in the thesis.

Any contribution made to the research by others with whom I have worked at the University of Oxford or elsewhere is explicitly acknowledged in the thesis. I also declare that the intellectual content of this thesis is the product of my own work, except to the extent that assistance from others in the project's design and conception or style, presentation and linguistic expression is acknowledged.



Veerle Antoinette Brans

Acknowledgements

The work presented in this *Thesis* would not have been possible without the valuable contributions and support of numerous people.

First, I would like to thank my supervisors, Professor Eleanor Stride and Associate Professor Erdinc Sezgin, for their constructive feedback, valuable advice, unwavering support and unlimited optimism over the past three and a half years. Thank you for allowing me to 'do something different' and, therefore, for facilitating the birth of this project. Thank you for helping me see the good amidst the bad.

Secondly, I would like to express my gratitude to Associate Professor Rebecca Burton and Dr Rebecca Capel for taking a chance on me - allowing me to work with them at the Department of Pharmacology, University of Oxford - and opening my eyes to a career in research. Without you, I would have never started a DPhil at the University of Oxford when I did.

I would like to equally express my gratitude to the Clarendon Fund and New College for my full scholarship, as well as the VSBFonds, Studiefonds KETEL 1 and the Oxford-Nottingham Biomedical Imaging CDT (EPSRC/MRC) for their belief in my academic and personal path and financial contribution towards it.

I would like to thank past and present members of the BUBBL group. Your guidance and support have been invaluable. Especially to Dr Michael Gray, thank you for answering my endless ultrasound questions and for never making me feel stupid asking them, to Dr Luca Bau, for his honest advice, guidance and help at every hour of the day, to Dr Oliver Vince, for holding up a mirror to me and helping me see the bigger picture, especially in the early stages of this *Project*, to James Fisk, for accepting my paper sketches and turning ideas into set-ups, and, lastly, to Dr Alexander Martin, for finding joy in the hours-long experiments at awful hours, for picking me up off the floor, quite literally, and for your outside-of-the-box advice.

Since my arrival at New College and the University of Oxford, I have felt right at home thanks to the wonderful people I have been fortunate to meet and call my friends. Thank you to Eimi Satoh, Rory McKinnon, Mark Henstridge, Oscar Lyons, Alice Caddock, Matthew Rogers and Sayyam Khurana for always being there for me, no matter how far away, and supporting me in this endeavour called life. At times,

I could not have done it without you. Thank you to the Windmill Road crew - Nicola Dinsdale, Katie Banecki, Charles Hill and Charles Millard - for giving me a home away from home and taking care of me when I struggled to do so myself.

Ik wil ook graag mijn vrienden uit Nederland bedanken: de 'Hé Kapitein' groep en Sarith Jonker voor hun vriendschap en vertrouwen in mij. Ik hoop altijd 'mamabeer' te mogen blijven.

Verder wil ik graag mijn ouders en zusje bedanken voor hun begrip, steun, vertrouwen, interesse en de moeite die zij genomen hebben de afgelopen jaren om enigszins te begrijpen waar deze thesis over gaat. Jullie hebben soms meer in mij geloofd dan ikzelf.

Mama, bedankt voor je vele kaarten die me een hart onder de riem staken wanneer ik het nodig had, het denken aan alles wat ik door de drukte nogal eens vergat, je oneindige interesse in mijn leven hier en het zuchtend toleren van mijn 'het is wat het is'. Papa, bedankt voor je rustige luisteren naar mijn perikelen, je nuchterheid en het bellen met mij, ook al heb je een hekel aan telefoneren. Ik hoop dat ik jullie trots gemaakt heb. Sophie, bedankt voor je heerlijk directe mening waar ik nooit om hoef te vragen en je onvoorwaardelijke steun. Je blijft altijd mijn kleine zusje waar ik zo trots op ben.

Ook wil ik graag opa Jacques van der Graaf bedanken, die helaas dit proefschrift nooit heeft kunnen zien, maar zo trots was op zijn kleindochter. Bedankt voor de pannenkoeken, de 'goed genoeg' en de vele krantenartikelen die u voor mij heeft uitgeknipt over de jaren.

Lastly, I would like to thank Alexander Martin. You manage to make me laugh, even when I really do not want to. Thank you for letting me be me - the good, the bad and the ugly. Thank you for the late-night Tesco trips, the runs and walks, and the endless conversations about things that matter and things that do not. I hope I will be giving you my excellent directions - left, left, left - for a long time.

Dissemination

Peer-reviewed Journal Articles

1. *Gray, M., *Vasilyeva, A. V., ***Brans, V.**, & Stride, E. (2021). Studying Cavitation Enhanced Therapy. *JoVE (Journal of Visualized Experiments)*, (170), e61989.

2. Browning, R. J., Aron, M., Booth, A., Rademeyer, P., Wing, S., **Brans, V.**, ... & Stride, E. (2019). Spectral imaging for microbubble characterization. *Langmuir*, *36*(2), 609-617.

*These authors contributed equally

Conference Presentations and Posters

1. 182nd Meeting, Acoustical Society of America, Denver, Colorado, USA - Lecture Presentation & Poster (First Prize - Biomedical Acoustics Best Student Paper Award)

   Brans, V., Gray, M., Sezgin, E., & Stride, E. (2022). *Exploration of ultrasound-mediated microbubble-cell membrane interactions using novel protein-loaded microbubbles and their role in immunomodulation*.

2. 2020 European Symposium on Ultrasound Contrast Imaging, Rotterdam, The Netherlands - Poster

   Brans, V., Gray, M., Sezgin, E., & Stride, E. (2020). *Investigating cell membrane modulation by microbubbles and ultrasound using confocal fluorescence microscopy.*

3. Leeds Microbubble Symposium 2019, Leeds, United Kingdom - Poster (Runner Up Poster Prize)

   Brans, V., Vince, O., Aron, M., Gray, M., Sezgin, E., & Stride, E. (2019).*Ultrasound-Mediated Modulation of Cell Membranes by Lysophosphatidylcholine-Incorporated Microbubbles*.

4. 'Imaging the Biomechanics of Life', TOPIM 2019, Chamonix, France - Lecture Presentation and Poster

   Shrivastava, S., **Brans, V.**, Cleveland, R. (2019). *On measuring shock wave induced dynamic state changes in lipid membranes using solvatochromic fluorescent probe Laurdan*.

Attributions

Chapter 1 and 3

For Chapter 1 and Chapter 3, the JoVE paper, as found in the *Dissemination*, by Dr M. Gray, A. Vasilyeva, **V. Brans** and Prof. E. Stride was paraphrased. Elements of the paper's *Introduction*, written by V. Brans, are used in these Chapters, and inspiration for the *Methods* section in Chapter 3 was taken from the paper's *Protocol* section, for which acknowledgement is specifically due to Dr M. Gray. Acknowledgement is also due to Dr M. Gray for the design and characterisation, and to J. Fisk for the realisation of the SATs.

Chapter 2 - The Design and Fabrication of Protein-Loaded Microbubbles

1. *Section 2.3.4 - Diffusion: Fluorescence Correlation Spectroscopy*

   Experiments were performed together with Dr E. Sezgin, analysis using FoCuS-point software was performed by Dr E. Sezgin.

Chapter 4 - Quantitive Assessment of His-Functionalised Microbubble-Cell Membrane Interactions

1. *Section 4.3.2.1 - Pilot study: His-AF488 functionalised microbubbles versus control microbubbles*

   Experiments were performed with Dr C. Smith and Dr A. Martin, to allow for exposure of samples to ultrasound, and immediate analysis using confocal microscopy and flow cytometry. Specifically, Dr C. Smith assisted with the ultrasound exposure, Dr A. Martin assisted with running the flow cytometer.

2. *Section 4.3.3 - Quantitative observation of functionalised lipid transfer and/or microbubble fusion in Jurkat cells*

   Experiments were performed together with Dr A. Martin, to allow for exposure of samples to ultrasound

and immediate flow cytometry analysis, to accommodate the quantity of samples to be analysed. Specifically, Dr A. Martin assisted with running the flow cytometer.

3. *Section 4.3.4 - Comparison of His-AF488 and SonoVue microbubble behaviour under ultrasound exposure*

   Experiments were performed together with Dr A. Martin to allow for the rapid subsequent ultrasound exposure of 97 samples.

Content

Abbreviations **16**

Chapter 1 - Introduction **18**

1.1 Motivation 19

1.2 Biological membranes: structure & function 21

1.3 Ultrasound 25

1.3.1 Biological effects of ultrasound due to cavitation phenomena 25

1.3.2 Microbubbles 29

1.3.3 Ultrasound in drug delivery 31

1.3.3.1 Sonoprinting 33

1.4 Cancer and immunotherapy 35

1.4.1 Overview of cancer immunotherapy 37

1.5 Application of ultrasound for enhanced immunotherapy 42

1.5.1 Ultrasound tumour ablation and immunity 42

1.5.2 Sonoporation-assisted immunotherapy 44

1.5.3 Immunotherapy assisted by microbubbles and ultrasound 45

1.5.4 Liposomes and bubble-liposomes 47

1.6 Thesis overview and research objectives 48

1.6.1 Research objectives 50

Chapter 2 - The Design, Fabrication and Characterisation of Protein-Loaded Microbubbles **53**

2.1 Introduction 54

2.2 Methods 57

2.2.1 Microbubble fabrication 57

2.2.1.1 Saturated (16:0) and unsaturated (18:1) DGS-NTA(Ni) 60

2.2.1.2 His-GFP and His-AF488 60

2.2.2 Microbubble characterisation 61

2.2.2.1 Brightfield microscopy 61

2.2.2.2 Multisizer 61

2.2.2.3 Confocal microscopy 61

2.2.2.4 Fluorescence Correlation Spectroscopy (FCS) 62

2.2.2.5 Serum and temperature incubation 66

2.2.2.6 Binding of a variety of His-tagged entities 66

2.2.2.7 Statistical analysis 67

2.3 Results 67

2.3.1 Microbubble population characterisation: concentration and size 67

2.3.2 Microbubble population stability 69

2.3.3 Specificity 70

2.3.4 Diffusion: Fluorescence Correlation Spectroscopy (FCS) 71

2.3.5 Domains 71

2.3.6 Loading capacity of His-AF488-functionalised DGS-NTA(Ni) microbubbles 73

2.3.7 Effect of physiological conditions on His-AF488-functionalised DGS-NTA(Ni) microbubbles 75

2.3.8 Applicability of 2%-18:1 DGS-NTA(Ni) microbubbles to bind a variety of His-tagged entities 76

2.4 Discussion 79

2.4.1 Microbubble population characterisation: concentration and size 79

2.4.2 Microbubble population stability 79

2.4.3 Diffusion: Fluorescence Correlation Spectroscopy (FCS) 80

2.4.4 Domains 81

2.4.5 Loading capacity of His-AF488-functionalised DGS-NTA(Ni) microbubbles 81

2.4.6 Effect of physiological conditions on His-AF488-functionalised DGS-NTA(Ni) microbubbles 82

2.4.7 Improvements and future *in vivo* work 82

2.5 Conclusion 84

Chapter 3 - Proof-of-Concept: Qualitative Assessment of His-Functionalised Microbubble-Cell Membrane Interactions 86

3.1 Introduction 87

3.2 Methods 89

3.2.1 Microbubble fabrication 89

3.2.2 Cell culture 90

3.2.3 Ultrasound set-up 91

3.2.3.1 SAT2 91

3.2.3.2 Mini-SAT 93

3.2.3.3 SAT3 94

3.2.3.4 Ultrasound Experimental Protocol 95

3.2.3.5 Data Collection 96

3.2.4 Confocal microscopy 97

3.2.5 Microbubble behaviour - ultrasound exposure parameter study 98

3.3 Results and Discussion 99

3.3.1 The qualitative observation of functionalised microbubble material transfer in the SAT2 99
3.3.2 The qualitative observation of functionalised microbubble material transfer in the Mini-SAT 102
3.3.3 The qualitative observation of functionalised microbubble material transfer in the SAT3 104
3.3.4 Comparison of His-AF488 and SonoVue microbubble behaviour under ultrasound exposure 108
3.4 Limitations and Future work 110
3.5 Conclusion 112
Chapter 4 - Quantitative Assessment of His-Functionalised Microbubble-Cell Membrane Interactions 113
4.1 Introduction 114
4.2 Methods 114
4.2.1 Microbubbles 114
4.2.2 Cell culture 115
4.2.3 Ultrasound set-up 115
4.2.3.1 SAT3 115
4.2.3.2 Pilot Experiment Set-Up 116
4.2.4 Confocal microscopy 116
4.2.5 Flow cytometry 117
4.3 Results and Discussion 118
4.3.1 Overview 118
4.3.2 Quantitative observation of functionalised lipid transfer and/or microbubble fusion in A549 cells 120
4.3.2.1 Pilot study: His-AF488 functionalised microbubbles versus control microbubbles 120
4.3.2.2 Varying pressures: 0, 100, 150 and 200 kPa PNP, and two microbubble concentrations 125
4.3.2.3 Varying duty cycles: 0, 10, 20, 40, 80 and 100% 131
4.3.3 Quantitative observation of functionalised lipid transfer and/or microbubble fusion in Jurkat cells 136
4.3.3.1 Varying pressures: 0, 140 and 200 kPa PNP, and three microbubble concentrations 136
4.3.3.2 Varying pressures: 0, 50, 100, 150 and 200 kPa PNP, and two microbubble concentrations 141
4.3.3.3 Varying duty cycles: 1, 5, 10, 20, 40, 80 and 100% 148
4.4 Conclusion 153
Chapter 5 - Targeting of His-Functionalised Microbubbles to Cell Membranes 156
5.1 Introduction 157
5.2 Methods 160
5.2.1 Microbubbles 160
5.2.2 Cell culture 161

5.2.3 Ultrasound set-up 162
5.2.4 Targeting protocol 162
5.2.5 Targeting assessment - confocal microscopy 163
5.2.6 Targeting assessment - flow cytometry 164
5.3 Results and Discussion 165
5.3.1 Qualitative observation of His-Tf microbubbles targeting to A549s using confocal microscopy 166
5.3.1.1 His-Tf targeted microbubbles versus control microbubbles 166
5.3.1.2 His-Tf versus His-HSA microbubbles with regular and Tf-receptor blocked A549s 168
5.3.2 Quantitative observation of His-Tf microbubbles targeting to A549s using flow cytometry 172
5.3.2.1 His-Tf versus His-HSA microbubbles without ultrasound 172
5.3.2.2 His-Tf versus His-HSA microbubbles at 0, 100 and 150 kPa PNP 174
5.3.2.3 His-Tf versus His-HSA microbubbles with regular and Tf-receptor blocked A549s 177
5.4 Conclusion 181
Chapter 6 - Targeting of His-Functionalised Microbubbles to Cell Membranes 183
6.1 Objectives and Conclusions 184
6.1.1 Contributions 184
6.1.1.1 Chapter 2: The Design, Fabrication and Characterisation of Protein-Loaded Microbubbles 184
6.1.1.2 Chapter 3: Qualitative Assessment of His-Functionalised Microbubble-Cell Membrane Interactions 185
6.1.1.3 Chapter 4: Quantitative Assessment of His-Functionalised Microbubble-Cell Membrane Interactions 185
6.1.1.4 Chapter 5: Specific Targeting of His-Functionalised Microbubbles to Cell Membranes 187
6.2 Limitations 188
6.3 Future work 189
6.3.1 In Vitro 190
6.3.1.1 Improving microbubble stability in in vivo conditions 190
6.3.1.2 Exploration of the ultrasound regime for suspension cells 190
6.3.1.3 High-speed camera experiment to visualise microbubble behaviour 191
6.3.1.4 ImageStream: Combining Confocal Microscopy and Flow Cytometry 192
6.3.1.5 Co-Culture Targeting Experiment 192
6.3.1.6 His-tagged protein localisation on or within the cellular membrane 193
6.3.2 In Vivo 193
6.3.2.1 T cell 'Membrane Tagging' 194
6.3.2.2 Solid Tumour Challenge Study 195
6.3.2.3 The Effect of Ultrasound-Mediated Targeted Microbubbles on Established Tumours 196

Appendix **198**

A.1 The effect of the microbubble fabrication method on microbubble material transfer 199

A.1.1 Microbubble fabrication 199

A.1.2 Microbubble behaviour - ultrasound exposure parameter study 200

A.1.3 Results and Discussion 200

A.2 'Membrane tagging' versus 'internalisation', using lyso-microbubbles 206

A.2.1 Microbubble fabrication 206

A.2.2 Results and Discussion 207

A.3 Chapter 4 - supplementary figures 211

A.4 Chapter 5 - supplementary figures 215

A.5 ImageStream: combining confocal microscopy and flow cytometry 219

References **221**

Abbreviations

A549 cells	adenocarcinomic human alveolar basal epithelial cells
AF488/680	Alexa Fluor 488/680
AFP	alpha-fetoprotein
AHNP	anti-HER2/Neu Peptide
AntpHD	antennapedia Homo Domain
APC	antigen-presenting cell
APC-700	allophycocyanin-700
BBB	blood-brain barrier
BCMA	B-cell maturation antigen
CAR	chimeric antigen receptor
CD	cluster of differentiation
DAMP	damage-associated molecular pattern
DAPI	4′,6-diamidino-2-phenylindole
DBCO	dibenzocyclooctyne
DBPC	1,2-dibehenoyl-sn-glycero-3-phosphocholine (22:0 PC)
DC	dendritic cell
DGS (18:1) / DOGS	1,2-dioleoyl-sn-glycero-3-succinate
DMEM	Dulbecco's Modified Eagle Medium (DMEM)
DNA	deoxyribonucleic acid
DPBS	Dulbecco's phosphate-buffered saline
DPPC	1,2-dipalmitoyl-sn-glycero-3-phosphocholine (16:0 PC)
DSPC	1,2-distearoyl-sn-glycero-3-phosphocholine (18:0 PC)
DSPE	1,2-Distearoyl-sn-glycero-3-phosphoethanolamine
ECD	Electron Coupled Dye
EDTA	ethylenediaminetetraacetic acid
ELISA	enzyme-linked immunosorbent assay
EPR	enhanced permeability and retention
FBS	fetal bovine serum
FCS	fluorescence correlation spectroscopy
FDA	United States Food and Drug Administration
FITC	fluorescein isothiocyanate
FSC	forward scatter
FUS	focussed ultrasound
GFP	green fluorescent protein
GM-CSF	granulocyte macrophage colony-stimulating factor
GUV	giant unilamellar vesicle
HeLa	immortal cervical cancer cell line, taken from Henrietta Lacks
HER2	human epidermal growth factor receptor 2
HIFU	high-intensity focused ultrasound
His	histidine
HPLC	high-performance liquid chromatography
HSA	human serum albumin
ICAM	intercellular adhesion molecule
IDA	iminodiacetic acid
IFN	interferon
IL	interleukin
LC	liquid condensed
LE	liquid expanded
LSM	laser scanning microscopy
MAGE	melanoma antigen gene
MB	microbubble

MHC	major histocompatibility complex
mRNA	messenger ribonucleic acid (RNA)
MS	mass spectrometry
NA	numerical aperture
NBD	nitrobenzoxadiazole
Ni	nickel
NK	natural killer
NTA	nitrilotriacetic acid
OVA	ovalbumin
PAM	passive acoustic mapping
PB450	Pacific Blue 450
PC	phosphatidylcholines
PCD	passive cavitation detection/detector
PD	programmed death
PDMS	polydimethylsiloxane
pDNA	plasmid deoxyribonucleic acid
PE	polyethylene
PEG	polyethylene glycol
PEG40S	polyoxyethylene (40) stearate
PI	propidium iodide
PMT	photomultiplier tube
PNP	peak-negative pressure
POPC	1-palmitoyl-2-oleoyl-glycero-3-phosphocholine (16:0-18:1 PC)
ROS	reactive oxygen species
RPMI	Roswell Park Memorial Institute Medium
SAT	system for acoustic transfection
SF_6	sulfur hexafluoride
SIM	structured illumination microscopy
siRNA	small interfering RNA)
SMLM	single-molecule localisation microscopy
SSC	side scatter
STED	stimulated emission depletion
TA	tumour antigen
TCR	T-cell receptor
Tf	transferrin
TfR	transferrin receptor
TIL	tumour-infiltrating leukocyte
TNF	tumour necrosis factor
UK	United Kingdom
US	ultrasound
USA	United States of America
VCAM	vascular cell adhesion protein
VEGF	vascular endothelial growth factor

Chapter 1 - Introduction

1.1 Motivation

The work demonstrated in this *Thesis* was born out of a combination of two main research avenues: (i) the quest to fundamentally understand ultrasound-mediated interactions between microbubbles (MBs), widely used in diagnostic and therapeutic applications in the clinic, and target cell membranes, and (ii) the optimisation of cancer immunotherapy, the efficiency of which leaves room for improvement due to various reasons, such as the lack of knowledge regarding the underlying molecular processes, as well as cancer's ability to escape the immune response.

Microbubbles were initially developed as contrast agents for ultrasound (US) imaging due to their excellent acoustic scattering properties. Gramiak and Shah serendipitously discovered this in 1968, when upon injection of a saline solution containing a low concentration of small gas bubbles, the ultrasound contrast improved substantially (Gramiak & Shah, 1968; Lajoinie *et al*., 2016; Roovers *et al*., 2019c). Since then, these gas bubbles have developed into clinically approved ultrasound contrast agents (Wheatley, Schrope & Shen, 1990; Linder, 2004), as well as pre-clinical ultrasound-mediated therapeutic agents for drug delivery and gene therapy (Dijkmans *et al*., 2004; Ferrara, Pollard & Borden, 2007; O'Reilly & Hynynen, 2018).

The interaction between microbubbles and living cells in an ultrasound field has been shown to cause permeabilisation of the cell membrane, or, in other words, the formation of temporary pores, a process which is often termed sonoporation, as well as an enhancement of endocytosis (Meijering *et al*., 2009; De Cock *et al*., 2015). This mechanical disruption of the cell membrane in the presence of microbubbles as a result of ultrasound exposure is hypothesised to be caused by various physical phenomena, including acoustic radiation forces (Dayton *et al*., 1999; Hill, Bamber & ter Haar, 2004; Postema *et al*., 2004), fluid shear stress due to a phenomenon referred to as microstreaming (Wu, Ross & Chiu, 2002; Marmottant, Biben & Hilgenfeldt, 2008; Collis *et al*., 2010), generation of shock waves and fluid jets as a result of the collapse of microbubbles (Prentice et al., 2005; Garbin *et al*., 2007; Zhou et al., 2012; Hu, Wan & Alfred, 2013), and direct deformation of the cell membrane due to volumetrically oscillating microbubbles, as demonstrated by Van Wamel *et al*. (Van Wamel *et al*., 2004; Van Wamel *et al*., 2006).

In addition, alternative mechanisms have been postulated as candidate mechanisms for enhancing ultrasound-mediated drug delivery, including the direct transfer of therapeutics from the microbubble shell to

cell membranes via microbubble-cell fusion, microbubble destruction, and/or lipid shedding (Carugo *et al*., 2017). This hypothesised microbubble fusion opens up the path to direct mixing of the microbubble cargo with the lipids present in the cell membrane, thereby bypassing the endocytic pathway for uptake and, subsequently, avoiding endosomal degradation (De Cock *et al*., 2015). Despite very promising preliminary data (Lajoinie *et al*., 2016; Carugo *et al*., 2017; Mulvana *et al*., 2017), the underlying biological and biophysical principles and mechanisms of the interactions between microbubbles and target cell membranes are currently poorly understood.

In recent years, the broadened knowledge of immunology and antitumour immune responses has led to the development of a novel cancer therapy avenue: immunotherapy. This therapy focuses on counteracting the immunosuppressive effects of the tumour and enabling the patient's immune system to fight the disease, in comparison to conventional treatment strategies, such as chemo- and radiotherapy, and surgery, which are often invasive and cause severe systemic side effects due to a lack of specificity. Unfortunately, the response of the immune system to growing cancers is often weakened, as, even though products of the various genetic and epigenetic mutations cancer cells undergo would potentially be recognisable by the immune system as foreign antigens, they are, ironically, seen as 'self' (Schreiber, Old & Smyth, 2011 in Topalian *et al*., 2012, Topalian, Weiner & Pardoll, 2011). Secondly, cancer cells have the distinct ability to evade the immune response, noted as one of the four additional hallmarks of cancer identified by Hanahan and Weinberg in 2011 (Hanahan & Weinberg, 2011). Two avenues to tackle this problem could readily be identified: either increasing the potency of immune cells or making diseased cells, such as cancer cells, more visible to the immune system.

One exciting immunotherapy that has emerged in recent years is CAR T cell therapy (Miliotou & Papadopoulou, 2018), which involves removing T cells from a cancer patient or donor and genetically altering them so that they display chimeric antigen receptors (CARs) on the membrane - proteins capable of recognising cancer cells as well as activating the T cell itself. These cells are then reinfused into the patient to combat the cancer cells. In February 2022, a long-term study was published that followed two of the first patients with chronic lymphocytic leukaemia treated with CD19-redirected CAR T cell therapy (Melenhorst *et al*., 2022). These patients achieved complete remission in 2010 and remain in remission to date, with CAR T cells still detectable 12 years later. The $CD4^+$ CAR T cells emerged as the dominant population over time, showing cytotoxic activity

and ongoing proliferation. Though inspiring news, caution should be exercised as the study only reports the results in two patients. Nonetheless, to date, seven CAR T cell therapies have been approved by the United States Food and Drug Administration (FDA) to treat a host of diseases, including leukaemia, lymphomas and myelomas.

However, CAR T cell therapies are expensive, risky and technically demanding and remain a last resort, only to be used when other treatments have failed. This is partly because delivering proteins to the cell membrane in a controlled fashion has proven highly challenging in the development of cancer immunotherapies, requiring complex *ex vivo* procedures. Previous work, both in the BUBBL group and the wider community, has focussed on optimising microbubbles for intracellular drug delivery (Aron *et al*., 2019; Horsley *et al*., 2019; Stride, 2019) and blood-brain barrier opening (McDannold *et al*., 2012; Song, Harvey & Borden, 2018, Meng *et al*., 2021). However, recent studies have unveiled important functions of plasma membrane lipid and cell surface signalling molecule dynamics in regulating T cell signalling, and, hence, modulation of these membrane lipids can be exploited to harness T cell activity (Zhu, Yao & Chen, 2011; Wu *et al*., 2016). With this in mind, there is a need for a microbubble formulation that does not deliver lipids or other cargo intracellularly but 'tags' the cell membrane with relevant proteins to increase the visibility of target cells to the immune system or the potency of immune cells to eliminate diseased cells.

Therefore, this *Thesis* aims to investigate the feasibility of designing a microbubble agent functionalised with a protein to tag target cell membranes and promote immunotherapy. The remaining *Sections* of this *Chapter* summarise the underlying principles and review the state-of-the-art research areas underpinning the work in this *Thesis*, including biological membranes, ultrasound, ultrasound-mediated microbubble-cell interactions, immunotherapy and direct applications of ultrasound for enhanced immunotherapy. Finally, the specific *Research Objectives* are discussed.

1.2 Biological membranes: structure & function

As this *Thesis* is concerned with the interactions between microbubbles and the cell membrane, both with and without ultrasound, this *Section* first focusses on biological membranes, and specifically the plasma membrane. The cell membrane, which functions as a selectively permeable barrier between the extracellular

and intracellular environments, is a self-assembled heterogeneous macromolecular bilayer composed of lipids, including phospholipids, glycolipids and sterols, and proteins (Alberts *et al*., 2014).

The membrane structure consists of a two-ply lipid sheet about 5 nm thick, in which proteins are embedded. To facilitate the transport of nutrients and waste products across the membrane, the membrane is penetrated by highly selective channels and transporters that allow small molecules and ions to be imported and exported (Alberts *et al*., 2014). The mechanical properties of the plasma membrane are fascinating, as when a cell grows or changes shape, so does the plasma membrane. It can enlarge without losing its continuity, can deform without tearing and typically reseals upon being pierced - a property used in sonoporation-based drug delivery methods (Zhou *et al*., 2008; Hu, Wan & Alfred, 2013).

The lipids in cell membranes combine a hydrophilic head with a hydrophobic tail, making them amphipathic molecules. This plays a crucial role in their assembly into bilayers in an aqueous environment. The energetically most favourable configuration consists of the hydrophobic tails facing each other and the hydrophilic heads facing outwards (Alberts *et al*., 2014). While this configuration generally stops lipids from leaving the lipid bilayer, the lipid molecules are free to move within the membrane plane, causing the membrane to behave as a two-dimensional fluid, which is of key importance in maintaining membrane function and integrity. Interestingly, the crossover of lipids from one to the other monolayer is rare without proteins to facilitate that process. In contrast, due to random thermal motions, lipids continuously diffuse within the same monolayer (Alberts *et al*., 2014).

The ease with which this lateral diffusion takes place, or, in other words, the membrane fluidity, is dependent on the nature of the hydrocarbon tails of the phospholipids in the bilayer (Alberts *et al*., 2014). Membrane fluidity is essential in maintaining cellular function. It allows for the diffusion of proteins, which is crucial in, for example, cell signalling and equal distribution of components over daughter cells upon division and cell-cell fusion (Alberts *et al*., 2014). The closer and more regular the packing of the tails, the more viscous and less fluid the bilayer will be, causing the membrane to be in a ‘gel-like’ state.

The organisation of the hydrocarbon tails is affected by both the length of the tails and the saturation, i.e. the number of carbon-carbon double bonds, of the tails. The shorter the chain length, the larger the fluidity of the bilayer due to reduced interaction of the tails with each other (Morrow, Whitehead & Lu, 1992). Secondly, double bonds create small kinks in the tails, causing more steric hindrance in their tight packing in

the lipid layer, and, hence, the presence of unsaturated lipids causes the lipid layer to be more fluid (Kates, Pugh & Ferrante, 1984; Alberts *et al*., 2014). This membrane fluidity is modulated by the inclusion of the sterol cholesterol, which constitutes roughly 20% of the lipids in the membrane by mass. Cholesterol is a short and rigid lipid molecule that fills the gaps left by unsaturated neighbouring lipid tails, causing the lipid layer to become more 'ordered' and less permeable (Xu & London, 2000; Ayee & Levitan, 2016).

While the lipid bilayer provides the permeability barrier to the hydrophilic molecules both intra- and extracellularly, most membrane functions are taken up by membrane proteins, which constitute roughly 50% of the plasma membrane by mass. They serve many functions, such as transporting nutrients, metabolites, and ions across the lipid bilayer and anchoring intracellular structures to extracellular matrix proteins. Others act as receptors to detect chemical signals in the extracellular environment, which are relayed intracellularly or as enzymes that catalyse specific reactions (Alberts *et al*., 2014).

A critical aspect of the function of an enzyme is the thermal fluctuations in its environment (Shrivastava *et al*., 2018). Moreover, these thermal fluctuations are known to affect membrane permeability. Non-thermal fluctuations in, e.g., pH and the interactions of lipids with ions, proteins and other polymers may induce lipid phase transitions, e.g., a shift from a 'gel' or 'ordered' state into a 'fluid' or 'disordered' state and vice versa (Chapman, 1975). The lipid phase state of the plasma membrane is known to affect its physical properties, including the elasticity, compressibility, and diffusion characteristics of membrane proteins. Moreover, this phase state affects vital functions, including enzyme activity, nerve excitation, regulation of cell-cell contacts and vesicular fusion. Shrivastava *et al*. (2018) have investigated the role of an acoustic impulse (~1 MPa peak negative pressure, 10 μs) on the phase state of the lipid membrane using the fluorescence probe Laurdan. Laurdan, a fluorescent probe whose emission spectrum changes as a function of the hydration level within the cell membrane, serves as an indication of lipid order. The results show changes in the dye's emission spectrum, which are correlated with the compression and rarefaction zones of the incident sound wave (Shrivastava *et al*., 2018).

The phase transition behaviour from a 'gel' to a 'fluid' phase of phospholipid membranes has been studied in great depth. For example, Morrow *et al*. (1992) showed that the membrane fluidity was increasingly dependent on the temperature around the phase transition. This effect was more pronounced for shorter lipid chain lengths. Kheyfets *et al*. (2018) hypothesised a microscopic model of the lipid membrane

and the first order 'liquid'-'gel' phase transition, with the latter dependent on three factors: inter-lipid Van der Waal attraction, steric repulsion and hydrophobic tension. They showed that by a decrease in temperature, the system transitions from 'liquid' to 'gel' phase, as the inter-lipid steric repulsion decreases. In contrast, the other two factors are only weakly temperature-dependent.

Interestingly, this membrane fluidity is not a homogenous state, and it was Singer and Nicolson (1972) that proposed the fluid mosaic model for biomembranes. A year later, Yu, Fischman and Steck first observed the separation of red blood cell membranes into detergent-labile and detergent-resistant fractions and hypothesised that biological membranes consist of functionally important membrane subcompartments, or lipid rafts (Yu, Fischman & Steck, 1973). This hypothesis was corroborated by various studies showing lateral heterogeneity on the submicron scale, with lipids and membrane proteins compartmentalised into lipid rafts - a process known as liquid-liquid phase separation. A detailed account of the composition, regulation and roles of these lipid rafts can be found in Sezgin *et al*.'s (2017) review article.

This lateral heterogeneity is also observed in microbubbles. For example, Borden *et al*. (2006) observed phase heterogeneity at various concentrations of the lipopolymer DSPE-PEG2000, which increased with increasing lipopolymer concentration. They showed a composition and temperature dependence of the lipid monolayer, which indicates that phase separation is a thermodynamically driven process. This high degree of heterogeneity in the monolayer illustrates the nonequilibrium state of the shell. The lipid distribution is important as it dictates properties important in drug delivery, or in this case, microbubble-cell membrane transfer/fusion, such as the location and local concentration of the ligand/drug and PEG brush coverage, which may affect the accessibility of the ligand/drug and physiological clearing from *in vivo* systems (Borden *et al*., 2006).

Moreover, Owen *et al*. (2019) showed that domain formation was mainly observed in larger microbubbles and that those larger microbubbles happened to contain a larger concentration of PEG40S. Langeveld *et al*. (2020) investigated the effect of lipid handling via a direct (immediate lipid resuspension in an aqueous solution) and an indirect method (as used in this *Thesis*, by drying off the organic solvent to obtain a lipid film, which subsequently is resuspended in an aqueous solution), and lipid phase transitions on the microbubble coverage, showing that various lipids, such as DPPC and DSPC, and emulsifiers, such as

PEG40S, are present in different phases: a liquid expanded (LE) and a liquid condensed (LC) phase, further elaborated upon in *Chapter 2*.

1.3 Ultrasound

Ultrasound has been used widely as a diagnostic imaging technique because of its safe and non-invasive nature, easy implementation at a patient's bedside, and low cost (Chen & Whitlow, 2011). It is defined as sound with frequencies over 20 kHz, undetectable by the human ear. Even though ultrasound had been used for decades in a diagnostic context, its great potential in enhancing drug delivery was properly recognised in the late 1980s (Fechheimer *et al*., 1987) and is an active area of research regarding the treatment of, for example, cancer, diabetes, thrombosis, skin wounds and bone fractures. Ultrasound propagates through a medium, creating alternating high- and low-pressure zones, known as compression and rarefaction, respectively. The amplitude and frequency of these pressure fluctuations are determined by the ultrasound source, called a transducer.

1.3.1 Biological effects of ultrasound due to cavitation phenomena

An ultrasound wave propagating through a medium can dissipate energy through absorption and/or scattering. Attenuation of the wave causes a loss of acoustic energy during propagation. In tissue, this is due to converting acoustic energy into heat or scattering.

Thermal effects of ultrasound are due to the absorption of the energy from the ultrasound wave, which increases with the frequency and amplitude of the ultrasound wave. Viscous absorption in the liquid immediately surrounding the oscillating bubble can produce a substantial heating effect (Hilgenfeldt *et al*., 2000). The extent of heating due to this absorption depends on the tissue's characteristics (Unga & Hashida, 2014). Temperature increases can be beneficial therapeutically, with mild increases up to 38 - 40 ˚C corresponding to a positive effect on immunogenic responses, tissue healing and transport of oxygen, nutrients and therapeutics. Temperature increases of up to 43 ˚C have even been shown to increase tumour perfusion, making tumour tissue more susceptible to conventional cancer treatment (Marmor & Hahn, 1980).

Moreover, large temperature increases lead to tissue ablation, another technique applied in cancer therapy (Kennedy, 2005; Merckel *et al*., 2016). In contrast, scattering does not involve converting acoustic energy into heat; instead, the wave's amplitude is attenuated along the direction of propagation of the wave as a result of interactions between the propagating wave and the structures of contrasting acoustic properties.

The second significant biological effect of ultrasound waves concerns the nucleation, growth and oscillation of gaseous cavities, known as cavitation (Mitragotri, 2005). Cavitation, initially studied extensively for safety concerns regarding diagnostic ultrasound imaging, has been recognised for its potential in therapeutic applications, such as lithotripsy and drug delivery. These natural gaseous cavities and artificial microbubbles, as elaborated upon later, undergo rapid and dramatic changes in volume in response to changes in pressure and temperature. Subsequently, these volume changes lead to mechanical, thermal and chemical effects.

The expansion of the bubbles occurs against both the inertia and viscosity of the surrounding fluid and the surface tension of the bubble. At low frequencies, the surface tension is the dominating factor, and the pressure required for nucleation is the Blake pressure (Blake, 1949 in Stride & Coussios, 2019). This Blake pressure is higher for smaller cavitation nuclei, which is why nanoparticles and liquid droplets (~0.2 μm) are activated at pressures in the order of MPa rather than kPa as for microbubbles (~1-2 μm) at a 1 MHz driving centre frequency (Stride & Coussios, 2019).

Depending on the intensity and frequency of the incident ultrasound wave and the characteristics of the environment, one way of classifying microbubble behaviour is in terms of non-inertial and inertial cavitation (Flynn, 1975), referring to the sustained low-amplitude oscillatory motion of bubbles, and rapid growth and collapse of bubbles, respectively. Both non-inertial and inertial cavitation, caused by the highly nonlinear nature of bubble oscillations, can generate microstreaming in the surrounding liquid that can enhance drug convection and exerts shear forces on the tissue in the vicinity of the bubbles (Wu *et al*., 2002; Krasovitski & Kimmel, 2004; Collis *et al*., 2010; Doinikov & Bouakaz, 2010; Wang *et al*., 2014). This is particularly prevalent when bubbles are in the vicinity of a boundary, causing bubbles to oscillate non-spherically, and may potentially promote drug uptake through shear-induced permeabilisation (Rifai *et al*., 2010; Kooiman *et al*., 2014; Pereno *et al*., 2020).

Inertial cavitation involves larger amplitude oscillations and rapid collapse of the bubbles, imparting direct mechanical stress and frequently generating shock waves and, hence, large pressure gradients that can disrupt and permeabilise tissues. Shock waves result from supersonic bubble wall velocities, which cause a discontinuity in the pressure in the surrounding liquid (Stride & Coussios, 2019). The permeabilisation of biological membranes at both the tissue and cellular levels is variously referred to as sonophoresis, used primarily in the context of ultrasound-induced enhancement in skin permeability (Mitragotri, 2017; Park *et al*., 2019), and sonoporation, used mainly to describe the reversible permeabilisation of the cell membrane due to the formation of membrane pores (Lentacker *et al*., 2014; Wawryka, Kiełbik & Iwanek, 2019).

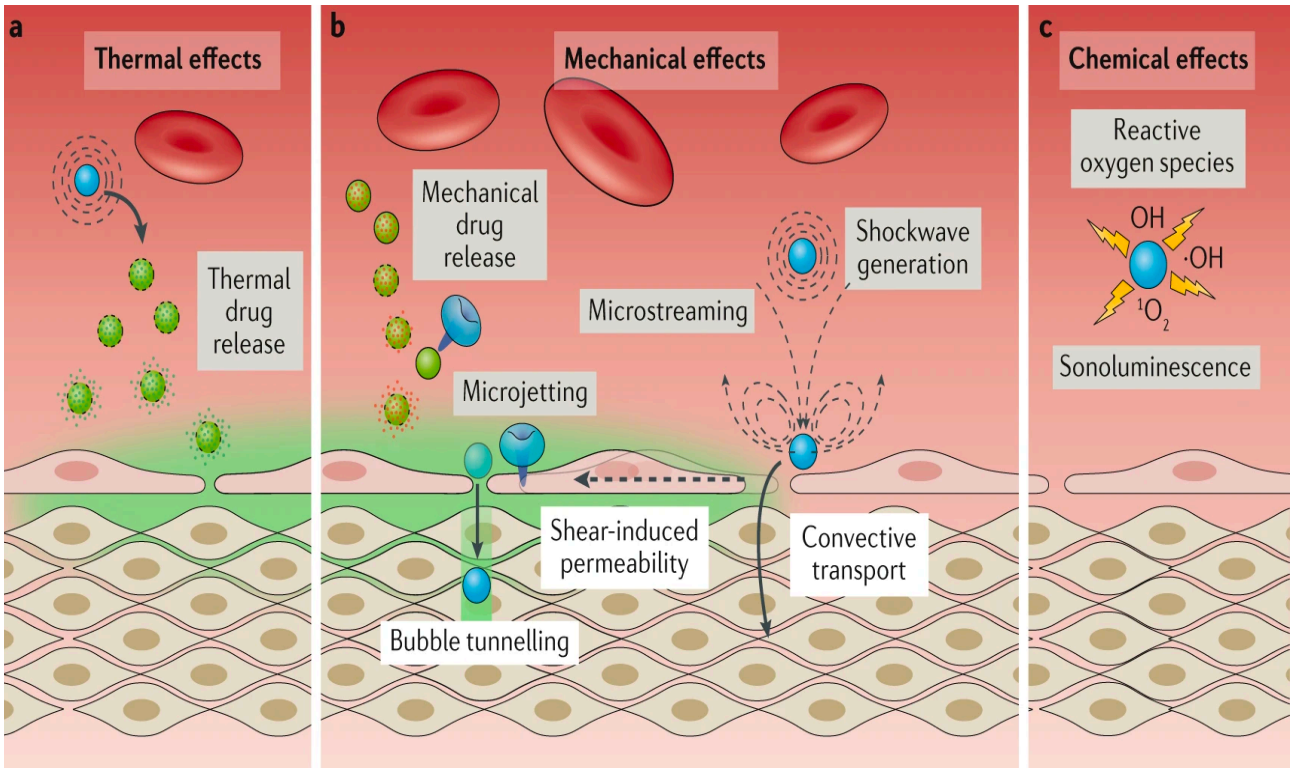


Figure 1.1. Schematic of several effects of cavitation due to ultrasound exposure. *This includes acoustic microstreaming, generation of shear forces, generation of highly reactive species, referred to as sonochemistry, generation of shock waves and subsequent pressure gradients, and liquid microjets due to violent bubble collapse near a surface, such as a cell membrane. Figure adapted from Stride & Coussious, 2019.*

The collapse of bubbles near a surface can also result in high-velocity liquid microjets due to an asymmetric acceleration of the fluid around the collapsing bubble (Li *et al*., 2013). These microjets can penetrate tissue,

potentially creating pores or inducing secondary stress waves (Suslick, 1988; Mitragotri, 2005). Microjets are observed at low frequencies (<500 kHz) and/or high pressures (> 1 MPa at 1 MHz) (Stride & Coussios, 2019). Moreover, the reradiated ultrasound field generated by the microbubble oscillations causes a further pressure gradient in the surrounding medium and a secondary radiation force on the bubbles (Rychak, Klibanov & Hossack, 2005; Acconcia *et al*., 2019). Dependent on the tissue boundary's elastic properties and the microbubbles' frequency and size, this radiation force causes movement either away or towards the boundary. The various effects are summarised in *Figure 1.1*.

Moreover, the highly non-linear oscillations produce acoustic radiation at frequencies higher than the driving ultrasound field. This leads to increased absorption in the surrounding tissue and further heating (Holt & Roy, 2001). Bubble collapse may also be accompanied by chemical effects due to the transient high temperatures (~1000s of K) and pressures in the bubble core. The extremely high temperature and pressure in the core are only sustained for a small amount of time (< 1 μs). Still, they can cause the generation of highly reactive species, particularly reactive oxygen species (ROS), and electromagnetic radiation, known as sonoluminescence (Mitragotri, 2005). These effects have been investigated to assess potential damage and/or activation of relevant cellular pathways for drug delivery (Tan *et al*., 2020) and have been exploited in the local activation of light-sensitive drugs in an approach known as sonodynamic therapy (Costley *et al*., 2015; You *et al*., 2016; Canavese *et al*., 2018; Beguin *et al*., 2019).

The extent of these effects on tissues is dependent on several factors, but the frequency and amplitude of the incident ultrasound wave are the main contributors (Mitragotri, 2005). Many ultrasound-mediated bioeffects may be initiated solely through control of the ultrasound field parameters (pressure amplitude, frequency, pulse length and repetition frequency, and duration of exposure), but reliably generating cavitation in biological tissue often requires high input energies and, hence, carries an elevated risk of damage. The introduction of exogenous or artificial cavitation nuclei may substantially reduce the input energy required to produce the broad range of effects discussed above. Cavitation nuclei include gas bubbles (Stride *et al*., 2020; Lentacker *et al*., 2009), which are elaborated upon in *Section 1.3.2*, liquid droplets (Rapoport *et al*., 2007; Cao *et al*., 2018; Zhang *et al*., 2019) and solid particles (Delogu *et al*., 2012; Paris *et al*., 2018; Mannaris *et al*., 2018), with nanoscale cavitation nuclei being an emergent area of investigation for their

benefits in terms of prolonged circulation time, improved extravasation and prolonged cavitation activity (Paris *et al*., 2018; Kwan *et al*., 2015a; Kwan *et al*., 2015b; Mannaris *et al*., 2019).

The various effects of ultrasound, either with or without the use of cavitation nuclei, have been studied extensively over the last couple of decades, as well as their potential to be employed in experimental and clinical strategies to combat disease, one of which is enhanced site-specific drug delivery, which is discussed further in *Section 1.3.3*.

1.3.2 Microbubbles

Microbubbles are micrometre-sized (1 to 10 μm, typically 1 to 2 μm, in diameter) particles that consist of a gaseous core, usually of a gas with high molecular weight and low aqueous solubility in the surrounding medium, such as perfluorocarbons, surrounded by a protective shell, consisting of a range of materials, including proteins, lipids and polymers, with phospholipids being the most common, as they provide a reduction in surface tension and high flexibility while maintaining sufficient resistance to gas diffusion (Roovers *et al*., 2019c). Common commercially available phospholipid-coated microbubble formulations include Definity (Lantheus, USA) and Sonovue (Bracco, Italy) (Roovers *et al*., 2019c).

They were initially developed for diagnostic imaging as, when exposed to an ultrasound field, the compressibility of the microbubbles causes them to undergo volumetric oscillations, consequently producing strong acoustic scattering, known as echogenicity (Wheatley & Singhal, 1995). Now, microbubbles have been widely explored for drug delivery and gene therapy purposes (Liang, Tang & Halliwell, 2010; Lawrie *et al*., 2000; Suzuki *et al*., 2010). Where diagnostic imaging requires higher ultrasound frequencies of 4 to 20 MHz, the ultrasound frequency range typically spans 0.5 to 2.0 MHz for therapeutic ultrasound applications. The ultrasound peak negative pressure required to obtain therapeutically relevant microbubble oscillation effects is usually less than 1 MPa, with therapeutic peak negative pressures typically ranging from 0.5 to 5 MPa (Stride & Coussios, 2019).

The microbubble coating process also offers a mechanism for encapsulating drugs within the microbubble structure and attaching drugs and/or targeting species to the microbubble surface. This technique facilitates the triggered release of drugs to reduce systemic toxicity (Lentacker *et al*., 2010). It has

also recently been shown that material from the microbubble surface may be transferred to biological structures, enhancing drug delivery through so-called 'sonoprinting', as elaborated upon in *Section 1.3.3.1* (De Cock *et al.,* 2016; Roovers *et al*., 2019b; Carugo *et al*., 2017).

In general, the destruction of bubbles is proportional to the power of the incoming ultrasound wave and inversely proportional to the ultrasound frequency (Wei *et al*., 1997). Unfortunately, due to their size, stability and extravasation of microbubbles from the bloodstream are limited, and most microbubbles have half-life times in the order of a few minutes *in vivo* (Schneider, 1999).

Nevertheless, the microbubble- and ultrasound-assisted enhancement in membrane permeability has been employed both *in vitro* and *in vivo*, coupled with targeting agents, e.g., anti-vascular cell adhesion molecule (VCAM) (Geers *et al*., 2013; Crake *et al*., 2015; O'Reilly & Hynynen, 2018), drug carriers (Lentacker *et al*., 2010; Ferrara, Pollard & Borden, 2007; Dimcevski *et al*., 2016; O'Reilly & Hynynen, 2018) and multimodal imaging agents (Wu e*t al*., 2011; Cai, Yang & Gu, 2012). The conjugation of drugs to the encapsulating lipid shell has been shown to reduce systemic toxicity in mouse models (Chen *et al*., 2018; Nesbitt *et al*., 2018) and to increase cellular uptake (Geers *et al*., 2012). Moreover, the microbubble coating material can be modified to increase the permeability of cells, such as by using a lysophosphatidylcholine lipid (lysolipid) (Aron *et al*., 2019).

As mentioned previously, cavitation, whether facilitated by natural or exogenous cavitation nuclei, can heat the surrounding tissue. The acoustic emissions from microbubbles include integer multiples of the driving frequency, called harmonics, and fractional components, called sub- and ultraharmonics. These higher frequency components are increasingly absorbed in biological tissue, contributing to increases in temperature due to cavitation. This effect is exploited in, for example, the design of heat-triggered release drug carriers, such as ThermoDox (Lyon *et al*., 2017).

The full extent to which the aforementioned chemical effects, including the generation of reactive oxygen species (ROS) and sonoluminescence, can directly be exploited in tissue remains to be investigated. ROS are hypothesised to induce inter- and intracellular transport and are known to activate a particular class of drugs in so-called sonodynamic therapy - a treatment in which off-target toxicity is kept to a minimum (Tachibana, Feril & Ikeda-Dantsuji, 2008; Costley *et al*., 2015).

1.3.3 Ultrasound in drug delivery

Successful treatment regimes depend on optimal drug delivery at the target site while minimising systemic effects in healthy tissue. Common systemic delivery encounters a variety of delivery barriers, including a limited systemic concentration of the drug due to its toxicity, a limited circulation time due to either degradation or clearance, and the need to extravasate from the bloodstream into the target tissue and potentially target cellular compartment, which is particularly difficult for molecules with a greater molecular weight or a higher net negative or positive charge.

Combining ultrasound and encapsulation of the drugs in carriers, such as microbubbles, nanoparticles or liposomes, delivers a strategy for ultrasound-triggered release of the drugs at the target location. As discussed, ultrasound-driven microbubbles can trigger a wide range of downstream effects. Sonoporation, which is the reversible generation of membrane pores, can open inter-endothelial junctions, such as the blood-brain barrier (Mesiwala *et al*., 2002; McDannold *et al*., 2005; McDannold *et al*., 2006; Meng *et al*., 2021), increase capillary permeability, resulting in extravasation of particles into the interstitial space and stimulate endocytosis (Price *et al*., 1998; Skyba *et al*., 1998). In this way, they provide a means to temporarily and reversibly deliver macromolecules, such as therapeutics, across biological membranes and endothelial barriers using drug carriers (Unga & Hashida, 2014). Furthermore, as ultrasound can be focused, it is possible to deliver drugs in a highly localised manner.

In 1954, the first successful attempt at sonophoresis, also known as phonophoresis, was performed (Fellinger & Schmidt, 1954 in Mitragotri, 2005). This technique involves reversible permeabilisation of the skin using ultrasound. Acoustic cavitation and the associated shock waves were used to disrupt the topmost layer of the skin to allow transdermal drug administration. The technique was used to deliver drugs, including hydrocortisone, salicylic acid and lidocaine, to treat conditions such as polyarthritis. The use of this technique in vaccine delivery has also been explored, as it allows for the transdermal delivery of the vaccine in close contact with the skin's immune cells (Ita, 2016). Further localisation can be achieved by using stimuli-responsive drug carriers, such as temperature-sensitive liposomes (Grüll & Langereis, 2012; Gray *et al*., 2019), which have been shown to release their therapeutic load upon exposure to ultrasound with microbubbles (Ferrara, Pollard & Borden, 2007; Hernot & Klibanov, 2008).

Furthermore, acoustic cavitation has been shown to be a major contributor to the uptake of both smaller and larger molecules in cells and tissues, for example, the uptake and activation of radionuclides in pancreatic tumour cells (van Wamel *et al*., 2004), chemotherapeutic drugs in leukaemia cells (Tachibana *et al*., 2000) and drugs in the brain by both permeabilising the cell membrane as well as opening tight junctions present in capillary endothelial cells in preclinical models (Mesiwala *et al*., 2002; Hynynen *et al*., 2003; McDannold *et al*., 2005; McDannold *et al*., 2006). This enhancement is achieved similarly to sonophoresis, but this time by permeabilising the cell membranes or tissues through sonoporation. Depending on the ultrasound parameters such as acoustic pressure and pulse interval, the produced pores are usually on the nano- to micrometre scale in size, short-lived and enable the successful introduction of exogenous material into the cytoplasm (Mitragotri, 2005). This change in cell membrane permeability is influenced by the absolute and relative size of the bubbles compared to the vasculature and their shell composition (Fan, Kumon & Deng, 2014).

Combined with local release from encapsulated drug carriers, sonoporation makes for a very selective treatment method, thereby minimising exposure of healthy, non-target tissue to the drugs (Mitragotri, 2005). Ultrasound offers a high degree of activation localisation due to its ability to be tightly focussed. For example, preclinical studies have shown the release of doxorubicin encapsulated in micelles using ultrasound to treat cancer - thereby ensuring low systemic concentrations but high local concentrations at the tumour site (Nelson *et al*., 2002; Rapoport *et al*., 2004). Ultrasound has also been successfully implemented in gene therapy, enabling the delivery of DNA into various cells, both *in vitro* as well as *in vivo* (Anwer *et al*., 2000; Huber *et al*., 2003; Mead *et al*., 2016; Shapiro *et al*., 2016; Sakakima *et al*., 2005). Again, the underlying mechanism is based on increased cell membrane permeabilisation due to cavitation induced by ultrasound exposure.

As mentioned briefly in *Section 1.3.1*, ultrasound is also employed in sonodynamic therapy, which relates to the enhancement of the toxicity of certain compounds to treat various types of cancer (Costley *et al*., 2015; You *et al*., 2016; Canavese *et al*., 2018). For example, in the presence of the photosensitive drugs merocyanine 540 and photofrin, low-frequency ultrasound was shown to induce toxicity *in vitro* in leukaemia cells (Tachibana *et al*., 1997; Tachibana *et al*., 1999). This enhanced toxicity is primarily attributed to enhanced permeabilisation discussed above but may also be influenced by other effects, such as sonochemistry, including the generation of free radicals that induce peroxidation of lipids in cell membranes, the production of light, referred to as sonoluminescence, as recently shown by Beguin *et al*. (2019), or

increased susceptibility to shear forces induced by ultrasound due to the presence of drugs which act as so-called sonosensitizers (Tachibana *et al*., 1999; Rosenthal, Sostaric & Riesz, 2004).

The above brief review of the literature demonstrates the successful use of ultrasound in various experimental and medical applications. The ability of ultrasound to mediate multiple effects and the possibility of applying ultrasound locally and non-invasively to diseased tissue make it a very powerful tool in a clinical context. *Section 1.3.1.1* looks specifically and more in depth at the deposition of microbubble material on the lipid membrane known as sonoprinting, for its similarities with the proposed 'membrane tagging' in this *Thesis*. *Section 1.5* looks at the stimulation of the immune system using ultrasound, focusing on sonoporation-assisted immunotherapy in the presence and absence of cavitation agents.

1.3.3.1 Sonoprinting

Whereas the use of microbubbles and ultrasound focuses on two main avenues for drug delivery and intracellular uptake: (i) via temporary membrane pores and (ii) enhanced endocytosis, in 2016, De Cock *et al*. proposed a third application that relies on microbubble-cell interactions, so-called sonoprinting. Sonoprinting is the direct deposition of nanoparticles, loaded on microbubbles, in patches onto the cell membrane. In a precursor to this particular study, conducted by Lum *et al*. (2006), it was demonstrated that nanobeads loaded on microbubbles were deposited on the surface of a cellulose tube as a result of ultrasound exposure, and, more importantly, in the context of the work presented in this *Thesis*, this deposition of beads was shown to be co-localised with fluorescently-labelled components of the microbubble shell. This makes a case for the fact that not only the attached cargo but also lipid shell fragments transfer from the microbubbles to the cells, potentially via membrane fusion, a process in which the lipids of the nanoparticle are exchanged or mixed with lipids present in the cell membrane, as suggested by various studies (Crowder *et al*., 2005; Partlow *et al*., 2008; Lu *et al*., 2009).

However, the real-time confocal imaging performed in the 2016 study by De Cock *et al*. is not sufficiently fast to adequately capture which microbubble behaviour underlies the observed depositing of microbubble components. This was addressed in a follow-up study conducted in 2019 by Roovers *et al*., which focused on investigating the behaviour of nanoparticle-loaded microbubbles as a result of exposure to ultrasound and the resulting biophysical cell-microbubble interactions. Interestingly, they showed that

microbubbles released their cargo in the first few cycles of ultrasound exposure and that the release depended on the acoustic pressure the microbubbles were subjected to.

At low acoustic pressures (< 300 kPa), microstreaming caused the transportation of nanoparticles away from the cell membrane rather than towards it. Higher acoustic pressures (> 300 kPa) and longer ultrasound pulses (> 100 cycles) resulted in the generation of primary and secondary acoustic radiation forces and, subsequently, fast and prolonged spatial translation of microbubbles. This led to the observation of nanoparticles being transported along the cell membrane and, as a result, the elongated deposition of microbubbles on the cell membrane. The primary and secondary radiation forces cause microbubbles in close vicinity of each other to move closer (Postema *et al*., 2004 in Stride, 2009; Wang *et al*., 2015), a process that plays a larger role when longer cycles are being used (Dayton, 2002; Lum *et al*., 2006; Ferrera, Pollard & Borden, 2007).

In the 2019 study by Roovers *et al*., they employed three optical imaging techniques: (i) real-time confocal imaging to identify the minimum pressure and pulse length needed to observe 'sonoprinting', (ii) ultra-high-speed bright-field imaging to observe the release of nanoparticles from the microbubbles during the initial cycles of ultrasound exposure, and (iii) high-speed fluorescence imaging, to capture the transport of released nanoparticles in the medium surrounding the cells and microbubbles. Furthermore, a study conducted by Carugo *et al*. (2017) showed that the composition of the microbubble shell affects its lipid transfer efficiency and, potentially more importantly, that this transfer of lipids affects the organisation of lipid molecules within the cell membrane, specifically affecting the lipid order, a property that plays an important role in membrane protein and domain dynamics (McIntosh & Simon, 2006; Schäfer *et al*., 2011; Owen *et al*., 2012) and membrane permeability (Xia & Onyuksel, 2000).

Figure 1.2 (Carugo *et al*., 2017) shows that, as a result of exposure to ultrasound, DiO, a lipophilic carbocyanine dye, was transferred to the cell membranes for all three different microbubble formulations, either in a diffuse, *Figure 1.2.D*, or punctate, *Figure 1.2.E* and *1.2.F*, fashion, indicating integration within the membrane, and formation and transfer via lipid vesicles or aggregates, respectively. However, in the absence of ultrasound, significant DiO transfer was only observed for the DSPC microbubble formulation. The three-dimensional Costes' method for colocalisation of both DiO and CellMask shows extensive colocalisation of DiO with the cell membrane for DSPC-PEG40S microbubbles exposed to ultrasound. However, this method, even though supplemented by various other experiments supporting the hypothesis of

material transfer, only shows the transfer of the lipophilic dye DiO, not necessarily of the lipids within the microbubble shell.

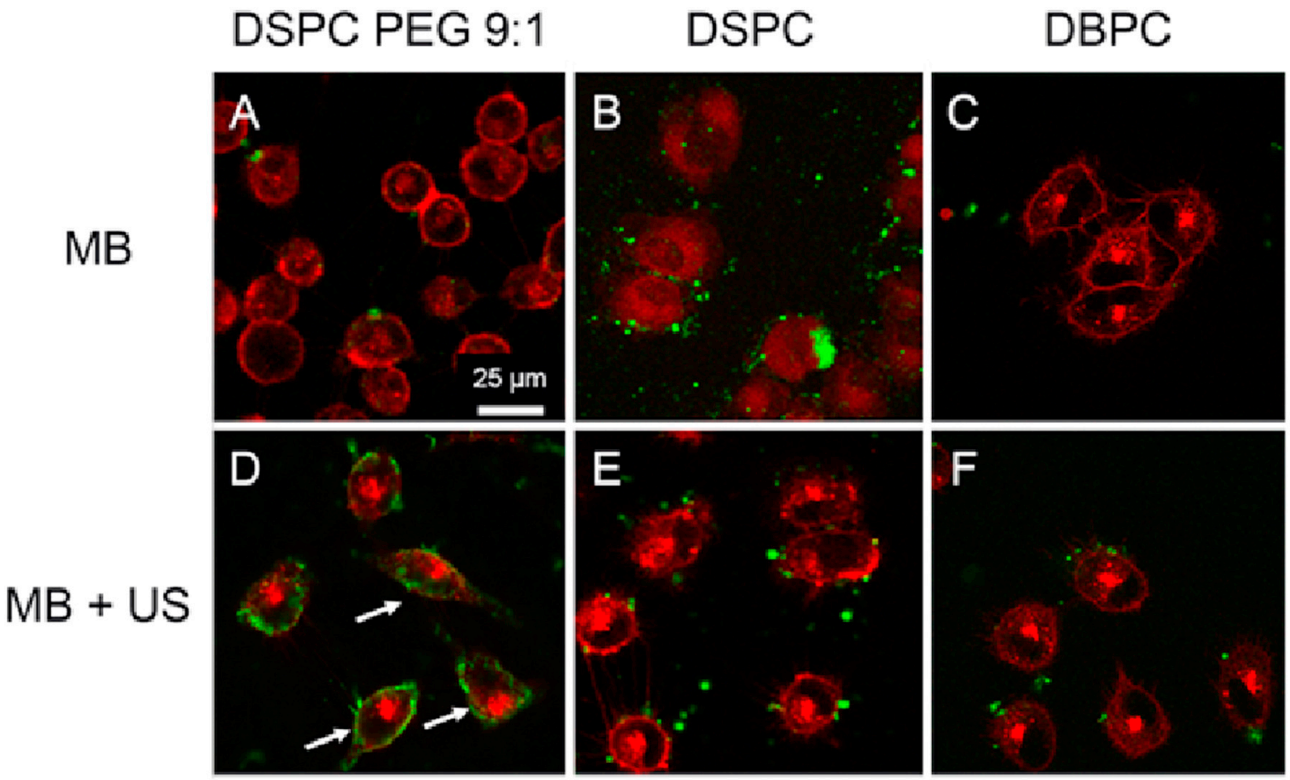


Figure 1.2. Confocal fluorescence images of the interactions of several microbubble formulations (DSPC-PEG40S, DSPC, and DBPC microbubbles), stained with DiO (green), and A549 cells, stained with CellMask (red), in the presence and absence of ultrasound. *Interaction is observed in a diffuse or punctate fashion for all three formulations following ultrasound exposure; however, without ultrasound, significant DiO transfer was only observed for DSPC microbubbles. Adapted from Carugo et al., 2017.*

1.4 Cancer and immunotherapy

Cancer is a disease affecting a large part of the population, with one in two people in the United Kingdom (UK) being diagnosed with some form of cancer in their lifetime. It is one of the leading causes of death, accounting for more than a quarter of all deaths in the UK, with lung, breast, prostate, and colorectal cancers being the most common types (Butterfield, 2015). For the last decades, the scientific community has put great efforts into improving cancer diagnosis and treatment (Cancer Research UK, 2019).

In January 2000, cancer researchers Douglas Hanahan and Robert Weinberg published a now well-cited, impactful article in the journal *Cell* regarding the underlying principles or hallmarks, a name proposed

by the authors, of cancer - a disease characterised by its extreme complexity. These hallmarks play a characteristic role in transforming normal cells into cancer cells. For example, cancerous cells stimulate their own growth, are insensitive to inhibitory anti-growth signals and programmed cell death, and have the ability to multiply indefinitely. In 2011, Hanahan and Weinberg published an updated version of the article. They proposed four more hallmarks, including active evasion by cancer cells from the attack and elimination by immune cells and inflammation (Hanahan & Weinberg, 2000; Hanahan & Weinberg, 2011). All hallmarks are illustrated in *Figure 1.3*.

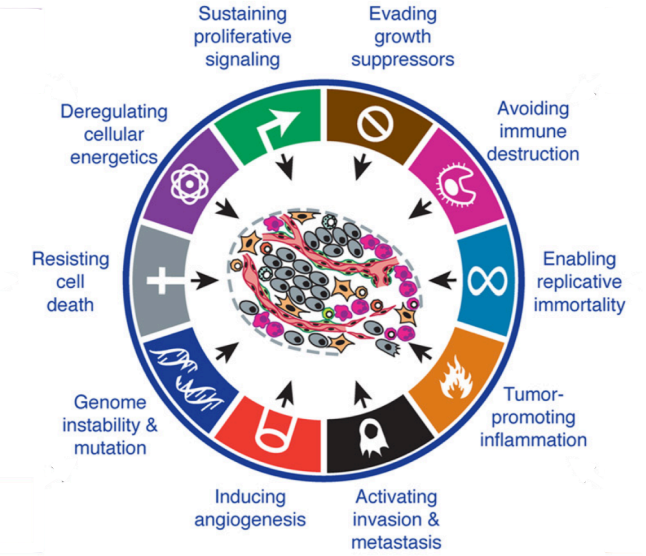


Figure 1.3. The Hallmarks of Cancer. *This illustration encompasses the six hallmarks of cancer as defined by Hanahan & Weinberg in 2000 and the four additional hallmarks from their 2011 paper, including cancer's ability to avoid immune destruction. Figure adapted from Hanahan & Weinberg, 2011.*

The immune response toward cancer cells is dynamic and complex. It is regulated by the dynamic spatiotemporal regulation of signalling proteins at the interface of interaction between immune cells and their targets. It is based on communication between membrane proteins on opposing surfaces: surface-presented antigens and ligands on antigen-presenting cells (APCs) that are recognised by immune cell receptors on, for example, T cells and mast cells (Jenkins *et al*., 2018). This interaction initiates intracellular signalling cascades that eventually lead to the formation of an immunological synapse (Dustin and Baldari, 2017).

Unfortunately, the response of the immune system to growing cancers is often weakened, as even though products of mutations in cancer cells would potentially be recognisable by the immune system as foreign antigens, they are, ironically, seen as 'self' (Schreiber, Old & Smyth, 2011 in Topalian, Weiner & Pardoll, 2011). The conceptual framework that is used to describe the complicated interactions between the immune system and developing cancer is called cancer immunoediting, where immunity promotes the growth of cancers capable of escaping the immune response. In this dual process, cancer cells evolve to avoid immune-mediated elimination by lymphocytes with anti-tumour properties (Schreiber, Old & Smyth, 2011) or recruit

immunosuppressive lymphocytes to create a tumour microenvironment that hinders an anti-tumour immune response (Ferrone & Dranoff, 2010).

However, tumour cells often (over)express proteins normally down-regulated in healthy somatic cells, such as the well-known overexpression of HER2 in breast cancer (Ross *et al*., 2009). Furthermore, the immune response is actively suppressed by the cancer milieu, which exploits the action of regulatory T cells and myeloid-derived suppressor cells, and by secretion of various immune suppressing substances, such as interleukin 6 (IL-6), interleukin 10 (IL-10) and vascular endothelial growth factors (Topalian, Weiner & Pardoll, 2011; Lindau *et al*., 2013). The broadened knowledge of immunology and antitumour immune responses has led to the development of a novel cancer therapy strategy called immunotherapy to complement standard therapies like chemotherapy, surgery and ablation, and radiotherapy (Arruebo *et al*., 2011). Immunotherapy focuses on counteracting the immunosuppressive effects of the tumour and enabling the patient's immune system to fight the disease.

1.4.1 Overview of cancer immunotherapy

Human cancer cells undergo various genetic and epigenetic mutations, resulting in the generation of neoantigens, which can be recognised by the immune system and instigate an immune response to the cancer cells. However, this response is not as effective as tumours become resistant, resulting in immune suppression, the onset of tolerance and systemic dysfunction in T cell signalling (Topalian *et al*., 2012). In 2004, Dunn, Old and Schreiber defined the mechanism of the immune response to cancer by the now prominent concept of the so-called three Es of cancer immunity: elimination, equilibrium and escape (Dunn, Old, Schreiber, 2004).

Firstly, developed cancerous cells are destroyed by a still adequate immune system in the elimination phase. There is evidence of this so-called cancer immunosurveillance in humans, as immunosuppressed transplant recipients display increased incidences of malignancies (Penn, 2000; Vajdic & Van Leeuwen, 2009), cancer patients show development of adaptive and innate immune responses to their tumours (Jiang *et al*., 2019), and the presence of tumor-infiltrating lymphocytes correlates with patient survival (Gooden *et al*., 2011). Secondly, tumour cells surviving this immune system attack end up in the second, or dynamic

equilibrium, phase, which is the most prolonged phase. In this phase, lymphocytes and IFN-γ continue to exert selection pressure on tumour cells, resulting in genetically unstable and mutating tumour cells, with variants arising that are increasingly resistant to immune attack.

Cells surviving this second phase enter the third and final phase, called the escape phase, characterised by progressive tumour growth and the development of an immunosuppressive tumour environment by elaboration of immunosuppressive cytokines, such as TGF-β and IL-10, or recruitment of immunosuppressive regulatory T cells (Sakaguchi *et al*., 2001; Mittal *et al*., 2014). Furthermore, it has been shown tumour cells show, e.g., loss of antigen expression, loss of MHC components and development of IFN-γ immunity. For example, it was shown that loss of MHC I antigen presentation is a frequent occurrence (40% - 90% of human tumours investigated) in many cancers (Algarra, Cabrera & Garrido, 2000; Dhatchinamoorthy, Colbert and Rock, 2021).

Immunotherapy employs activation or enhancement of the natural immune response of the patient to overcome disease (Unga & Hashida, 2014). It comprises several treatment approaches, which all build on both the specificity of the adaptive immune system and the diverse and potent action of the innate immune response. Treatment strategies include the administration of cancer vaccines (Butterfield, 2015; Banchereau & Palucka, 2018) such as the preventative human papillomavirus (HPV) vaccine (Arbyn, Xu, Simoens & Martin-Hirsch, 2018) or the therapeutic sipuleceucel-T vaccine for the treatment of advanced prostate cancer (Cheever & Higano, 2011), antitumour monoclonal antibodies or recombinant proteins that are known to either stimulate immune cells or block inhibitory pathways, called immune checkpoints, such as programmed death 1 (PD-1) checkpoint inhibitors (Keir *et al*., 2008; Weiner, Surana & Wang, 2010; Topalian *et al*., 2012), delivery of cytokines, such as interferon (IFN) and interleukins (ILs), and, lastly, adoptive cell transfer, including natural killer (NK) cells and regulatory T cells (Tu *et al*., 2018).

These agents prompt the immune response and have shown great potential in eradicating tumours, including non–small-cell lung cancer, melanoma and renal-cell cancer (Topalian *et al*., 2012). For example, PD-1 blockade with dostarlimab, an anti-PD-1 monoclonal antibody, has recently been shown in a phase 2 study to be highly effective in mismatch repair-deficient, locally advanced rectal cancer patients (Cercek *et al*., 2022). Cancers deficient for mismatch repair contain exceptionally high numbers of somatic mutations and have a large number of mutation-associated neoantigens (Le *et al*., 2017).

Unfortunately, only a minority of cancer patients respond positively to this form of treatment, possibly due to a low prevalence of tumour-associated antigen-specific T cells (Banchereau & Palucka, 2018). In some patients, treatment is even accompanied by a specific toxicity profile and severe side effects, such as autoimmune endocrinopathies, including hypophysitis, hypopituitarism, and thyroiditis, as well as autoimmune diabetes (Keir *et al*., 2008; Hughes *et al*., 2015). Elucidating the underlying mechanisms requires quantitative investigation of the immune cell-cell interactions involved, including the cell membrane receptors and their molecular behaviour upon cellular contact. It is essential to understand how immune cells process both activating and inhibitory signals (Jenkins *et al*., 2018). In practice, however, studying these factors in physiological systems remains challenging due to their enormous complexity and confounding factors such as protein-protein or protein-lipid interactions and the transient nature of these immune cell-cell interactions (Jenkins *et al*., 2018).

Any potentially gained immunity, defined here as the ability to resist a particular infection or toxin or, in fact, growth of cancer, by the action of specific antibodies or sensitised white blood cells, can be classified as either humoral immunity or cell-mediated immunity. The former results from antibodies produced by B lymphocytes, and the latter involves the activation of T lymphocytes. Both types of lymphocytes are activated by tumour-specific proteins and peptides, or tumour antigens (TAs). In 1994, the recognition of tumour antigens by T cells was first identified by Boon *et al*. in various solid tumours (Boon *et al*., 1994). T cells are activated when the antigen is presented by a major histocompatibility complex (MHC) molecule on the target cell's surface. More specifically, tumour antigens stimulate both cellular and humoral responses in cancer patients, with cytotoxic T cells, called $CD8^+$ T cells, being activated by antigens presented by the MHC I complex on tumour cells and T helper cells, called $CD4^+$ T cells, being activated by antigens presented by the MHC II complex expressed on antigen-presenting cells and tumour cells (Kirkwood *et al*., 2012).

$CD8^+$ T cells can directly destroy antigen-expressing cells, including tumour cells, by releasing cytotoxins that lead to the death of the diseased cell, whereas $CD4^+$ cells influence the strength, duration and efficacy of the immune reaction by releasing cytokines involved in cytotoxic T cell and B cell activation. Furthermore, another type of cell is involved in the humoral immune response called B cells, which produce antigen-specific antibodies (Reuschenbach *et al*., 2009). The role these various cell types play in the immune

response is illustrated in *Figure 1.4* in a simplified manner. Several of these tumour antigens have now been identified, characterised by their (over-)expression in tumour cells compared to healthy cells, and are capable of priming the immune system to recognise tumour cells (Smyth, Godfrey & Trapani, 2001; Turk *et al.*, 2002).

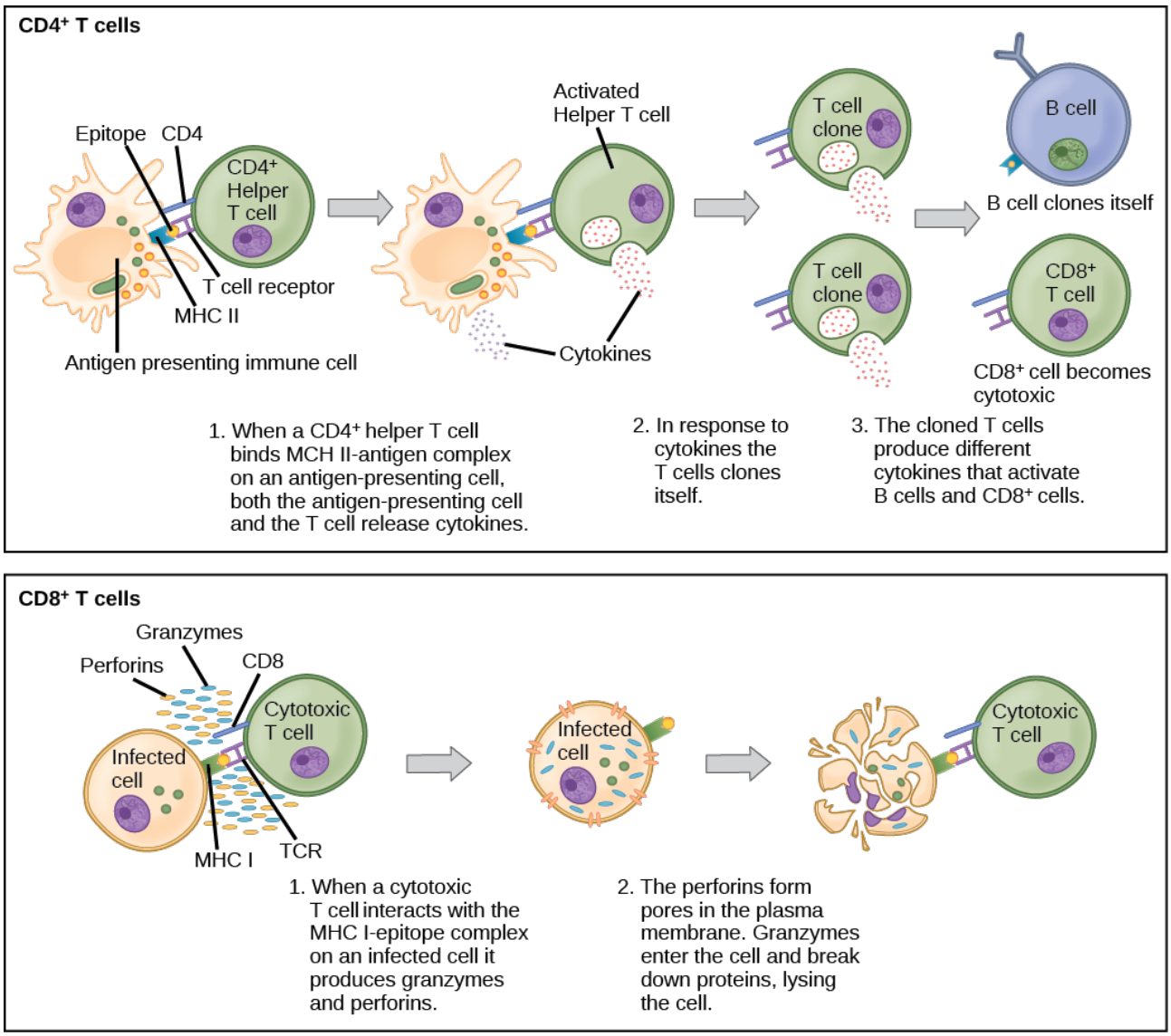


Figure 1.4. Illustration of the immune response to antigen-presenting cells. *It highlights the roles CD4+ T cells - T helper cells - and CD8+ T cells - cytotoxic T cells - play. T helper cells bind MCH II complexes on antigen-presenting cells (APCs), and subsequently, cytokines are released that activate B cells and cytotoxic T cells, as shown in the top panel. Cytotoxic T cells bind MCH I complexes on infected and cancer cells and can induce cell death by releasing cytotoxins, such as granzymes and perforins. Figure reproduced from Molnar & Gair, 2015.*

The most common form of immunotherapy treatment against cancer currently is the use of antibodies, with several products on the market, such as rituximab for the treatment of chronic lymphocytic leukaemia and

non-Hodgkin lymphoma through inducing cell lysis and apoptosis, cetuximab for the treatment of advanced bowel, and head and neck cancer, trastuzumab for the treatment of breast and stomach cancer, and lastly bevacizumab, an antibody that binds to vascular endothelial growth factor (VEGF) and in doing so significantly reduces the formation of new blood vessels and thus delivery of nutrients (Weiner, Murray & Shuptrine, 2012; Unga & Hashida, 2014). Antibodies can be designed to specially bind to targets on the cell surface and are, therefore, very attractive tools for targeted cancer treatment. They are used in various ways, including as tumour antigens by binding to cancer cells and, subsequently, being recognised as foreign by immune cells, as blocking agents for receptors involved in the downregulation of the activity of cytotoxic T cells, and as stimulatory agents acting positively on the receptors involved in immune cell responses (Scott, Wolchok & Old, 2012).

For example, CD20 monoclonal antibody therapies have significantly improved the survival in patients with B-cell malignancies. However, many patients do not achieve complete remission and malignancies develop resistance to these therapies. Monoclonal antibodies employ a variety of cell mechanisms to eradicate cancer, including induction of programmed cell death or Fc-mediated effector functions such as antibody-dependent cell-mediated cytotoxicity (ADCC), antibody-dependent cellular phagocytosis (ADCP) and complement-dependent cytotoxicity (CDC) (Oostindie *et al*., 2019). It was shown by De Jong *et al*. (2016), for example, that the natural process of antibody hexameter formation, i.e. Fc-Fc interactions that leads to Fc clustering, on targeted cells allows for the induction of complement-dependent cytotoxicity. In addition, Oostindie *et al*. (2019) showed that the concept of hetero-hexamer formation, i.e. Fc clustering with two monoclonal antibodies, CD20 and CD37, could induce superior and synergistic CDC and enhance subsequent tumour killing capacity.

In recent years, there have been various reports that ultrasound can be employed to boost the immune response to cancer. There are a few ways in which ultrasound can contribute to immunotherapy. The direct mechanical and thermal effects of (High-Intensity) Focussed Ultrasound (HIFU/FUS), with and without cavitation nuclei, have been shown to have an immunostimulatory effect, and ultrasound and cavitation have been used in combination with immune system-stimulating drugs, such as tumour antigens (Unga & Hashida, 2014; Tu *et al*., 2018; Yang *et al*., 2019). All of these approaches actively modulate the immune response, resulting in, for example, an increase in the $CD4^+/CD8^+$ ratio, infiltration by dendritic cells,

activated cytotoxic T cells and natural killer cells. Furthermore, they have a large effect on the expression of relevant proteins, such as signal transducer and activator of transcription 3 (STAT3), vascular endothelial growth factor (VEGF) and transforming growth factors β1 and β2, which are all involved in the development of tumours.

Ultrasound-mediated therapy is currently a widely studied treatment modality for various diseases, ranging from cancer and cardiovascular diseases to diseases of the central nervous system and skeletal muscle system (Escoffre *et al*., 2016; Yang *et al*., 2019). *Section 1.5* reviews the use of ultrasound in its various forms for immunotherapy.

1.5 Application of ultrasound for enhanced immunotherapy

1.5.1 Ultrasound tumour ablation and immunity

Ablation is a widely used technique in cancer treatment that specifically induces necrosis in tumour tissue without affecting the surrounding healthy tissue. There are several tumour ablation techniques, including radiofrequency and microwave ablation (Smith & Jennings, 2015; Facciorusso, Di Maso & Muscatiello, 2016), laser irradiation ablation (Mooney *et al*., 2017; Schena, Saccomandi & Fong, 2017), cryoablation (Sheen, Boston & Sherlock, 2002; Colangeli *et al*., 2018) and, lastly, high-intensity focussed ultrasound (HIFU). Most of these ablation techniques employ rapid heating of the target region to cause spatially localised necrosis, except cryoablation, which requires several longer cycles of freezing (van den Bijgaart *et al*., 2017). Out of these techniques, HIFU is the only non-invasive ablation technique and has been applied extensively to treat cancer of the prostate, breast, liver, kidney, bone and brain (Kennedy, 2005; Merckel *et al*., 2016).

For cryoablation, a strong connection has been observed with the immune response, with ablation causing the infiltration of immune cells in the tumour microenvironment and the maturation of dendritic cells (Den Brok *et al*., 2006; Matin *et al*., 2010). Tumour ablation generally generates a large quantity of tumour debris, accompanied by the release of tumour antigens and bioactive molecules such as damage-associated molecular patterns (DAMPs). However, the underlying mechanisms and exact nature and suitability of the

generated tumour debris to instigate the immune response are poorly understood. Tumour ablation as achieved by HIFU is based on either thermal or mechanical destruction of the tumour tissue. Raising the temperature of a tissue volume to at least 55 ˚C for at least one second leads to coagulation of the proteins and fusion of cell membranes and, therefore, immediate cell death (ter Haar & Coussios, 2007).

In contrast, mechanical destruction leads to the aforementioned fragmentation and generation of tumour debris. This mechanical destruction is known as histotripsy and is achieved using μs or ms acoustic pulses of high intensity, repeated with a low duty cycle to limit the increase in temperature. These high-pressure waves cause cavitation, a phenomenon detailed in *Section 1.3*. HIFU is performed using an ultrasound transducer placed outside the body, which focuses the incident ultrasound wave at a specific location in the body, leading to a local increase in energy density (ter Haar & Coussios, 2007), highlighting that the damage is, therefore, spatially confined, with no damage to the surrounding area.

Preclinical and clinical results of HIFU tumour ablation have shown that, as for cryoablation, infiltration and activation of T helper cells and cytotoxic T cells are enhanced (Wu *et al*., 2004; Hu *et al*., 2007; Lu *et al*., 2009; Haen *et al*., 2011). One of the first indications of a connection between HIFU ablation and an enhanced immune response was observed by Yang *et al*. in 1992. They observed a significant reduction in tumour growth following a second tumour challenge in previously HIFU cured animals (Yang *et al*., 1992). Furthermore, Rosberger *et al*. showed the ability of thermal HIFU to affect the $CD4^+/CD8^+$ T cell ratio. They demonstrated a general increase in $CD4^+$ T cells, indicating the immunomodulatory effect of ultrasonic treatment in choroidal melanoma (Rosberger *et al*., 1994).

This increase in immune response, however, is insufficient to achieve constant, protective antitumour immunity and needs to be complemented by other therapeutic approaches to achieve long-lasting tumour immunity, as providing this additional stimulus can help overcome immune tolerance and activate dendritic cells and T cells (Makkouk & Weiner, 2015; van den Bijgaart *et al*., 2017) - a topic explored extensively for thermal ablation approaches (Haen *et al*., 2011). Furthermore, the tumour debris generated from exposure to HIFU functions as a source of tumour antigens, possibly enabling the creation of an *in situ* systemic cancer vaccine, stimulating the immune response to other tumour lesions present elsewhere in the body (Prise, O'Sullivan, 2009). In response to cell debris as a result of HIFU, dendritic cells, which are known to function as antigen-presenting cells, show up-regulation of co-stimulatory molecules involved in the immune

response, such as IL-12, and macrophages show an increase in their secretion of tumour necrosis factor alpha (TNF-α), which is known to be critically involved in the regulation of infectious, inflammatory and autoimmune responses (Pasparakis *et al*., 1996; Hu *et al*., 2005 in Unga & Hashida, 2014). This effect is more pronounced in response to debris from mechanical HIFU than from thermal HIFU.

Moreover, HIFU has been shown to facilitate penetration of the tumour microenvironment by dendritic cells, activated cytotoxic T cells, and natural killer cells (Hu *et al*., 2007; Lu *et al*., 2009). In 2012, Huang *et al*. showed that mechanical HIFU complementing surgery in the treatment of prostate cancer led to inhibition of tumour growth by downregulation of the signal transducer and activator of transcription 3 (STAT3), as well as the enhancement of dendritic cell numbers and activity (Huang *et al*., 2012). Furthermore, a decrease in immunosuppressing cytokines, such as VEGF, β1 and β2, in blood circulation has been observed for patients treated with HIFU (Zhou *et al*., 2008).

In general, the literature shows a substantial role for HIFU ablation of tumours in inducing or modifying the immune response to cancer both *in vitro* and *in vivo*. However, HIFU treatment is not entirely without risks, as common complications involve skin redness, oedema pain and necrosis outside the target area, and metastases formation, as mentioned in several studies (Jung *et al*., 2011). Furthermore, treatment time is on the order of hours (1-3 hours for prostate HIFU treatment (Cordeiro *et al*., 2012)) and the cost of HIFU devices ranges from £257500 to £473,000, based on two devices: Ablatherm Integrated Imaging (EDAP TMS SA, France) and Sonablate 500 (Focus Surgery Inc, USA) (Warmuth *et al*., 2010).

1.5.2 Sonoporation-assisted immunotherapy

Another way in which ultrasound plays a role in immunotherapy is through one of its effects, as highlighted in *Section 1.3*: sonoporation. This *Section* focuses on the use of ultrasound without cavitation agents and its role in immunotherapy. Several theoretical studies (Wu, 2002; Sundaram, Mellein & Mitragotri, 2003; Doinikov & Bouakaz, 2010) have been performed that indicate that collapsing bubbles in close proximity to cell membranes are capable of inducing structural deformations in said membranes and subsequently enhance transport of molecules. The ultrasound energy used to achieve sonoporation is much lower than for ablation (Tachibana *et al*., 1999), even though higher than in the presence of exogenous cavitation nuclei.

The details of the underlying mechanisms remain unclear, but it is thought that heating of the tissue may increase the fluidity of lipid bilayers (Unga & Hashida, 2014). The result is reversible permeabilisation of the cell membrane, thereby facilitating the transport of drugs into cells and increased extravasation from the blood to surrounding tissue. In 2010, Casey *et al*. successfully delivered a therapeutic gene construct, coding for granulocyte-macrophage colony-stimulating factor (GM-CSF) and B7-1 costimulatory molecule, to solid tumours via ultrasound sonoporation (Casey *et al*., 2010). Several other studies report on sonoporation-assisted delivery of plasmid DNA to prostate cancer cells, both *in vitro* and *in vivo* (Huber & Pfisterer, 2000; Zarnitsyn & Prausnitz, 2004), as well as Interferon β (IFNβ)-loaded cationic liposomes to hepatic tumours (Hayashi *et al*., 2009). However, the effect of ultrasound on the increase of cell membrane permeability can be enhanced by the presence of cavitation nuclei, such as bubble liposomes, unilamellar vesicles and microbubbles, as will be elaborated upon in the following *Sections*.

1.5.3 Immunotherapy assisted by microbubbles and ultrasound

There have been several preclinical *in vitro* and *in vivo* studies, as outlined below, into the use of microbubbles combined with ultrasound to enhance the immune response. The presence of microbubbles, without any therapeutic agents, has been shown to trigger the immune response. Liu *et al*. exposed solid tumours in mice to low-pressure focussed ultrasound with SonoVue microbubbles. They observed suppressed tumour progression compared to ultrasound exposure on its own and an increase in infiltration of non-T regulatory tumour infiltrating lymphocytes (TILs) and cytotoxic T lymphocytes (Liu *et al*., 2012). Moreover, Alkins *et al*. showed that combined treatment of microbubbles and ultrasound could increase the permeability of the blood-brain barrier to injected immune cells. Natural killer cells were present in significantly higher numbers at the site of brain metastases after combined treatment (Alkins *et al*., 2013).

The study, as performed by Alkins *et al*., is a good example of co-injection of a bioactive substance, in this case, natural killer cells, with microbubbles, to increase the chances of successful delivery of said bioactive substance. There are several reports on the combination of microbubbles and ultrasound for the intracellular delivery of genes (Rong *et al*., 2018). For example, tumour growth in mice was significantly suppressed due to an increase in IFNβ expression after IFNβ pDNA transfection with the help of

perfluoropropane microbubbles (Sakakima *et al*., 2005). Delivery of pDNA encoding for Interleukin-27 (IL-27) with SonoVue microbubbles resulted in a substantial reduction in tumour volume and an increase in T lymphocytes in the tumour microenvironment - a good indication of activation of the immune system (Zolochevska *et al*., 2011).

One obvious downfall of co-injection is the inhomogeneous distribution of both the bubbles and the bioactive molecules throughout the body. Therefore, microbubble formulations were developed in which the active compound is incorporated within the microbubble, either enclosed within the microbubble shell, incorporated into the microbubble shell or attached to the surface of the microbubbles (Lentacker, De Smedt & Sanders, 2009). The efficacy of these drug-loaded microbubbles has been proven in several studies, both *in vitro* and *in vivo*, as outlined by Kooiman *et al*. (Kooiman *et al*., 2014).

For example, Lentacker *et al*. developed doxorubicin-containing liposome-coated microbubbles for drug delivery with therapeutic ultrasound, which resulted in the death of twice as many melanoma cells compared to doxorubicin-liposomes alone, probably due to the release of free doxorubicin as well as sonoporation of the cell membranes (Lentacker *et al*., 2010). In 2016, Zhu *et al*. developed paclitaxel-loaded microbubbles, capable of inducing lower viability in vascular smooth muscle cells upon exposure with ultrasound (Zhu *et al*., 2016).

Furthermore, Teupe *et al*. developed pDNA loaded albumin microbubbles (Teupe *et al*., 2002), and Zhao *et al*. successfully loaded microbubbles with the therapeutic protein Hirudin, which is capable of inhibiting thrombin (Zhao *et al*., 2005). Even more advanced drug-carrying microbubbles were developed by attachment of drug-loaded nanoparticles as well as bioactive ligands, using an avidin-biotin tagging strategy (Lum *et al*., 2006; Ottoboni *et al*., 2006; Kheirolomoom *et al*., 2007; Willmann *et al*., 2008) or via covalent binding (Alonso *et al*., 2007; Wheatley *et al*., 2007). It was shown by De Cock *et al*. (2016), who employed real-time swept field confocal microscopy imaging, that nanoparticle-loaded microbubbles deposit the attached nanoparticles onto the cell membrane in patches, a process they called ‘sonoprinting’, as elaborated upon in *Section 1.3.3.1*.

Thus far, the combined use of microbubbles and ultrasound, both to stimulate the immune response and combat other diseases, has been explored in this *Chapter*. However, Bioley *et al*. showed the potential of microbubbles to be phagocytosed by human and mouse dendritic cells without ultrasound (Boiley *et al*.,

2012a). For this purpose, microbubbles were fluorescently labelled, permitting the tracking of the binding to and rapid internalisation in dendritic cells of said microbubbles using confocal laser scanning microscopy. These results show the immense potential for microbubbles to serve as a delivery system for antigens, even without ultrasound. Their follow-up study (Boiley *et al*., 2012b) showed the successful delivery of the model antigen ovalbumin (OVA) without exposure to ultrasound.

Work like this demonstrates the suitability of microbubbles in a wide scope of applications, such as vaccination against infections and modulation of immune responses in allergies, cancer and other immune-related pathologies. It is well known that microbubble parameters such as size, charge and composition affect their ability to induce adaptive immunity (Boiley *et al*., 2012b). However, an all-around account and understanding of the underlying mechanisms are lacking. Before moving on to the objectives of this *DPhil Project*, alternatives to microbubbles such as liposomes and bubble-liposomes are briefly discussed in the next *Section*.

1.5.4 Liposomes and bubble-liposomes

Pharmaceutical cancer treatment often relies on the so-called enhanced permeability and retention (EPR) effect, which exploits the 'leaky' vasculature characteristic, e.g., inter-endothelial gaps of up to 2 μm, of the tumour microenvironment for passive delivery of drugs or particles (Maeda *et al*., 2000). However, recent challenging of this dogma by, e.g., Sindhwani *et al*. (2020), showed these inter-endothelial gaps are not responsible for the transport of nanoparticles into solid tumours and instead active trans-endothelial pathways, accompanied by rearranging of the cytoskeleton and cell membrane, are responsible for nanoparticle uptake. Sindhwani *et al*. (2020) showed this active process could occur due to the binding of nanoparticles to endothelial cells and subsequent uptake in vesicles or due to transport through transcellular channels which are formed through connecting vesicles and/or fenestrae - a process which could potentially be exploited in particle design, e.g., by specifically targeting the proposed microbubbles to induce this pathway to enhance uptake.

In addition to microbubbles as described above, liposomes and bubble liposomes have been used as drug carriers. Liposomes are predominantly spherical vesicles, consisting of an aqueous core surrounded by

a single or several lipid bilayer(s), which makes them well-suited for the delivery of drugs, small interfering RNA (siRNA), plasmid DNA, peptides, proteins, viruses and bacteria (Schroeder, Kost & Barenholz, 2009). Similar to microbubbles, the lipid shell consists primarily of phosphatidylcholines or sphingomyelins. In principle, liposomes are very similar to microbubbles, apart from their limited ability to fuse with the cell membrane (Wilschut & Hoekstra, 1984). Temperature-sensitive liposomes have been investigated as drug carriers in several studies, such as the targeted release of doxorubicin to solid liver tumours (Grüll & Langereis, 2012; Gray *et al*., 2019).

In 2009, Suzuki *et al*. showed the use of bubble liposomes, which are gas-entrapping liposomes, and ultrasound to deliver an exogenous antigen directly into the cytosol of dendritic cells, which was presented on an MCH class I complex and, subsequently, attracted and activated cytotoxic T lymphocytes. Dendritic cells are antigen-presenting cells and one of the most potent cell types to prime specific T cell responses via the presentation of these antigens on i) MHC class I complexes, via fusion with early endosomes, to $CD8^+$ cells and ii) MHC class II complexes, via fusion with late endosomes/lysosomes, to $CD4^+$ cells (Burgdorf et *al*., 2007; Bioley *et al*., 2012b). This process even resulted in the complete rejection of induced tumours (Suzuki *et al*., 2009). Furthermore, treating dendritic cells with tumour antigens derived from melanoma using bubble liposomes and ultrasound has shown a four-fold decrease in the frequency of melanoma-originated lung metastases (Oda *et al*., 2012).

1.6 Thesis overview and research objectives

The main aim of this *DPhil Project* is to design and develop microbubbles functionalised with a protein of choice to tag target cell membranes to (i) elucidate the underlying microbubble-cell interactions and (ii) exploit said knowledge to make diseased target cells, such as cancer cells, more visible to the immune system or immune cells more potent in detecting diseased cells.

Chapter 6 elaborates upon potential *in vivo* applications of the proposed protein-loaded microbubbles. In short, the microbubbles could be loaded with various antibodies that specifically target receptors present at high levels and (almost) exclusively on T cell membranes. Examples of these receptors that have been used in a variety of T-cell targeting nanoparticle studies include CD3 (Smith *et al*., 2017), CD4

(Ramishetti *et al*., 2015), CD7 (Lee *et al*., 2012; Kumar *et al*., 2008) and CD8 (Schmid *et al*., 2017; Yang *et al*., 2019).

To then subsequently direct these microbubble-targeted cells to diseased cells, a second protein or antibody can be loaded on the microbubble shell that targets cancer cells, similar to the multiple His-tagged entities on GUVs used by Jenkins *et al*. (2018) as discussed in *Chapter 2*. Relevant examples for this *Thesis* include CD19 for B-cell and follicular lymphoma or B-cell Maturation Antigen (BCMA) for multiple myeloma, which are two targets used in currently approved FDA CAR T cell therapies. This could potentially promote close proximity of immune cells with diseased cells and instigate an immune response.

Furthermore, another potential application could be the use of these microbubbles in anti-PD-1 immunotherapy, by not only loading a cancer-targeting protein/antibody (see *Chapter 6*), but also his-tagged anti-PD-1 antibodies on the nickelated microbubbles, which are explained in *Chapter 2*. This is illustrative of one of the advantages of the microbubbles proposed in this *Thesis*: the wide applicability of these microbubbles and thus their commercial potential, due to a plethora of commercially available His-tagged molecules. Lastly, there is potential for delivery of a transgene construct with microbubbles, similar to the latest CAR T cell therapy generations, where both CAR and cytokine transgenic cassettes are delivered.

As the first step of this research avenue, a novel microbubble has been designed to study the interactions of microbubbles with the cell membrane, employing confocal microscopy and flow cytometry. The role of microbubble and ultrasound properties in successfully tagging the cell membrane with microbubble components is explored. Lastly, this knowledge is applied to explore the possibility of using microbubbles in modulating the immune system based on their drug carrier properties and the possibility of incorporating surface membrane proteins in the lipid shell. To this end, the following **four objectives** have been formulated:

1. Development of functionalised microbubbles, using nickelated lipids and His-tagged proteins,
2. Conduction of qualitative proof-of-principle experiments to study the interactions of these custom-fabricated microbubbles with the cell membrane for adherent cells,
3. Conduction of quantitative experiments to study the interactions of these custom-fabricated microbubbles with the cell membrane for cells in suspension,

4. Further development of targeted functionalised microbubbles, using transferrin and human serum albumin as targeting proteins.

1.6.1 Research objectives

1. *Development of functionalised microbubbles, using nickelated lipids and His-tagged proteins.*

   Even though redistribution of a fluorescent lipid probe, as shown by Carugo *et al*. (2017), might serve as an indirect measure of lipid transfer, this, unfortunately, does not provide an insight into the processes occurring upon contact between the microbubble and the cell membrane. It is hypothesised that microbubbles will stochastically fuse with the cell membrane, even without the presence of a pressure field, such as provided by ultrasound. Therefore, the first objective aims to develop functionalised microbubbles with which it is possible to observe protein-lipid transfer from microbubbles to the cell membrane and visualise their interactions.

   Many antibodies, proteins and potential therapeutics are commercially available with a His-tag (Lee *et al*., 2006; Uchinomiya *et al*., 2009, Jenkins *et al*., 2018). Microbubbles complemented with lipids with an active nickel (Ni) head bind these His-tagged molecules. These nickelated microbubbles are developed as a novel platform for studying the non-invasive delivery of these molecules to target tissues, with and potentially without ultrasound, by means of transfer or fusion. This part of the *Thesis* concerns the stability and conjugation efficiency of a model His-tagged molecule, His-GFP, and its dynamics and kinetics in the microbubble shell, as investigated by fluorescence correlation spectroscopy (FCS), as well as the generation of general microbubble population statistics.

2. *Conduction of qualitative proof-of-principle experiments to study the interactions of these custom-fabricated microbubbles with the cell membrane for adherent cells*

   Subsequently, using these novel bubbles containing nickelated lipid conjugated with His-GFP or custom-made His-AF488, the aim of this objective, using a similar approach to Carugo *et al*. (2017), is to either confirm or rule out the fusion of microbubbles and/or transfer of lipids to the cell membrane. The hypothesised microbubble fusion/lipid transfer is studied with and without ultrasound, as there is

evidence in the literature that fusion, transfer and endocytosis can occur in certain cell types without ultrasound (Bioley *et al*., 2012; Carugo *et al*., 2017). This effect can nevertheless potentially be enhanced using ultrasound. This is interesting because it could provide further evidence for lipid transfer playing an important role in microbubble- (and ultrasound-)mediated drug delivery.

3. *Conduction of quantitative proof-of-principle experiments to study the interactions of these custom-fabricated microbubbles with the cell membrane for cells in suspension*

Following on from the qualitative proof-of-principle experiments in objective two, where His-GFP / His-AF488 functionalised lipid transfer and/or microbubble fusion with A549 cell membranes is observed qualitatively using confocal microscopy, this objective aims to explore this effect further, using a quantitative method called flow cytometry. Flow cytometry is a technique for rapidly analysing the optical characteristics of single particles or cells in suspension, e.g., uptake of fluorescent material. It allows for the analysis of thousands of cells on timescales on the order of minutes. Thus, it provides a means of determining the quantities and proportion of successfully tagged cells and the extent to which each positive cell is tagged, allowing a more definitive exploration of the ultrasound parameter space to optimise this 'membrane tagging' process.

Experiments were carried out with suspensions of either A549 or Jurkat cells, the latter of which were used as model immune cells and a preliminary assessment of increasing the potency of immune cells by tagging the membrane with relevant proteins. The His-AF488 functionalised microbubble behaviour across a part of the parameter space used in these experiments was investigated and compared to SonoVue microbubble behaviour and DPBS controls (Gray *et al*., 2021).

4. *Further development of targeted functionalised microbubbles, using transferrin and human serum albumin as targeting proteins*

To improve the specificity of the proposed 'membrane tagging' as a future therapy and limit off-target interactions by selectively directing microbubbles to structures of interest, such as the vasculature or cancer cells, microbubbles can be conjugated with targeting ligands, i.e. peptides and antibodies, on their surface. For example, Korpanty *et al*. produced microbubbles conjugated to monoclonal antibodies

against endoglin (CD105), VEGF receptor 2 and VEGF-activated blood vessels (the VEGF-VEGFR complex) to image and quantify the effects of antitumour therapies in pancreatic tumour-bearing mice (Korpanty *et al*., 2007). Similarly, vascular cell adhesion molecule 1 (VCAM-1) and intercellular adhesion molecule 1 (ICAM-1), which are upregulated in, e.g., atherosclerosis inflammation sites and brain metastases, have been targeted with microbubbles loaded with their respective antibodies (Ottoboni *et al*., 2006; Yan *et al*., 2018).

In 2021, research by Olsman *et al*. investigated the effect of blood-brain barrier (BBB) targeted liposomes compared to non-specific liposomes. They combined microbubble-enhanced ultrasound with both transferrin-loaded liposomes and control liposomes and observed a 40% increase in delivery of liposomes across the BBB. They hypothesised that combining ultrasound and microbubbles with the BBB-targeting liposomes might enhance endocytosis, which has great potential to improve drug delivery to the brain (Olsman *et al*., 2021). In this *Thesis*, lung carcinoma epithelial cells, A549 cells, are used as a model cell line which overexpresses transferrin receptors on the outer membrane. Microbubbles loaded with His-tagged transferrin are used to explore the targeting ability of the designed microbubbles compared to a control protein, His-tagged human serum albumin. Lastly, the targeting ability of these His-transferrin functionalised microbubbles to A549 cells, which had the transferrin receptors blocked using excess transferrin, is assessed to investigate the specific targeting of these microbubbles to the transferrin receptor.

Chapter 2 - The Design, Fabrication and Characterisation of Protein-Loaded Microbubbles

2.1 Introduction

This *Project* aims to eventually generate microbubbles that, in combination with ultrasound, can either make diseased cells more visible to the immune response or immune cells more potent against malfunctioning cells. Therefore, together with the 2017 study by Carugo *et al*. as elaborated upon in *Chapter 1*, inspiration is drawn from a 2018 study by Jenkins *et al*., in which they explored the use of Giant Unilamellar Vesicles (GUVs), as opposed to microbubbles, to study the interactions of live T cells, B cells and mast cells with signalling proteins usually present at immune cell-cell contacts. The authors observed dynamic spatiotemporal regulation of signalling proteins, including kinases, responsible for immune activation. To functionalise the GUVs with signalling proteins, Jenkins *et al*. incorporated nickel-nitrilotriacetic acid NTA(Ni)-functionalised lipids into these GUVs - the same strategy used in the microbubbles presented in this *Thesis*. These lipids are capable of binding directly to His-tagged surface proteins, as seen in *Figure 2.1.B*, which generally play a role in immune cell activation, such as peptide/major histocompatibility complex (pMHC), cluster of differentiation (CD) 45, intercellular adhesion molecule 1 (ICAM-1) and CD58, all of which are outlined in *Figure 2.1.C*.

Cell-GUV contacts were successfully established using GUVs functionalised with either fluorescent pMHC, which binds the T cell receptor (TCR), or fluorescent CD58, which binds the small adhesion protein CD2 on the surface of T cells, as shown for CD58 in *Figure 2.1.D*. One advantage of this binding complex of NTA(Ni) with histidine molecules over commonly used protein-ligand complexes, such as the (strept)avidin-biotin complex (Aron *et al*., 2019; Dewitte, Roovers, Smedt & Lentacker, 2019; Horsley *et al*., 2019), is its very low to no immunogenicity (Lukáč *et al*., 2011). The complex is most commonly used in protein purification protocols, especially for recombinant proteins with chromatography, due to nickel's high-affinity, rapid non-covalent binding to histidine residues.

Jenkins *et al*. (2018) have presented a free-standing GUV-based membrane system capable of providing important insights into the spatiotemporal basis of immune cell-cell interactions and lymphocyte activation. GUVs allowed for the unhindered diffusion of small and large proteins in their bilayer, more closely mimicking actual cells. By inserting key cell-surface proteins typically expressed by antigen-presenting cells and subsequently imaging the interaction between GUVs and live immune cells, including T

cells, B cells and mast cells, the large-scale spatial reorganisation of these proteins involved in the earliest stages of immune cell activation could be observed (Jenkins *et al*., 2018).

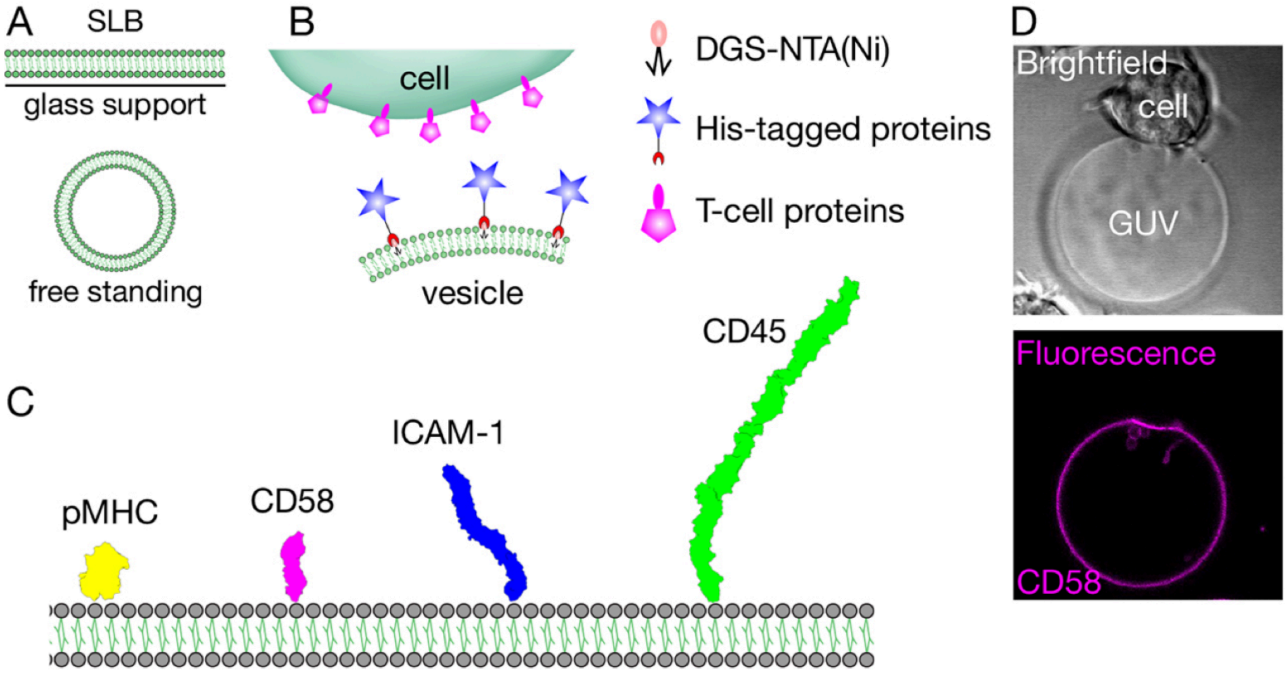


Figure 2.1. GUVs functionalised with His-tagged proteins. *(A) Illustration of a supported lipid bilayer (SLB) and a free-standing vesicle, such as a GUV, (B) Schematic showing the in vitro cell-GUV interaction, with His-tagged proteins binding specifically to DGS-NTA(Ni) lipid in the vesicle, and subsequently interacting with proteins expressed on the opposing T cell, (C) Illustration of the various molecules of interest to be attached to GUVs by Jenkins et al., (D) Example of a bright-field (top) and fluorescence (bottom) image of a GUV functionalised with CD58+ interacting with a CD2+ Jurkat cell. Adapted from Jenkins et al., 2018.*

Although studying live immune cells interacting with free-standing vesicles such as GUVs offers a way to elucidate passive and active processes involved in the immune response, these systems are limited in their use: GUVs cannot be used as drug carriers due to their inability to fuse with the cell membrane. Alternatively, small liposomes are often used as drug carriers, but they also exhibit poor fusion properties with the cell membrane. Encapsulated microbubbles on the other hand, widely used as contrast agents for ultrasound imaging and explored in areas of gene therapy and targeted drug delivery (Dijkmans *et al*., 2004; Ferrara, Pollard & Borden, 2007; O'Reilly & Hynynen, 2018), are known to fuse with the cell membrane and can, therefore, potentially be used as drug carriers (Carugo *et al*., 2017). Despite very promising preliminary data

(Lajoinie *et al*., 2016; Carugo *et al*., 2017), the underlying principles and mechanisms of the interactions with the target cell membrane are currently poorly understood.

In 2011, Lukáč *et al*. first showed the construction of what they referred to as surface-modified metallochelating microbubbles, or, in other words, microbubbles with a nickel-nitrilotriacetic acid (NTA(Ni))-functionalised lipid incorporated in the shell. They argued that the reversible bond, fast binding kinetics at room temperature, high affinity, and low if any immunogenicity made the Ni-His binding method a good candidate for use in microbubbles for *in vivo* drug delivery. Prior to their work, only a few papers used this binding method in particles, particularly in liposomes.

For example, Malliaros *et al*. (2004) developed a custom-made ISCOMATRIX™ vaccine, a particulate antigen delivery system usually composed of antigen, cholesterol, phospholipid and saponin, containing DPIDA, a chelating iminodiacetic acid (IDA). The authors exploited its metal-affinity chelating interactions to recombinant His-tagged antigens to improve cytotoxic T cell responses due to lower required doses of both the antigen and adjuvant to elicit an immune response. Mašek *et al*. (2011) also successfully fabricated and characterised so-called proteoliposomes with recombinant His-tagged proteins attached to a DOGS-NTA(Ni) lipid. However, their work focused primarily on optimising the liposome fabrication method. Another study showing recombinant proteins and synthetic peptides with poly-histidine residues binding to a metal ion chelating lipid, DOGS-NTA(Ni), is that of Chikh *et al*. (2002). They developed AntpHD-CW3- and AHNP-functionalised liposomes using this binding strategy for applications in vaccine production by inducing T cell responses and inhibition of tumour growth, respectively.

The work by Van Broekhoven *et al*. (2004), which shows a highly effective procedure for the induction of antitumor immunity by targeting dendritic cells with antigen-containing liposomes, demonstrates a biological effect of these metallochelating liposome-based structures both *in vitro* and *in vivo* in the mouse melanoma model. It is important to note that Van Broekhoven *et al*. used the three-functional chelating lipid NTA_3(Ni)-DTDA, which may have allowed for a higher *in vivo* stability, as studies shown by Rüger *et al*. (2006) and Mašek *et al*. (2011) found the single NTA(Ni) complex to be unstable in human plasma and serum, respectively, resulting in the detachment of the recombinant proteins. This may be important for translating the protein-functionalised microbubbles proposed in this *Thesis* to *in vivo* applications.

The work presented in this *Chapter* combines elements from the research avenues explored in this *Section* to create microbubbles reconstituted with proteins, varying from model fluorescent proteins, as presented here, to, for example, proteins normally found on antigen-presenting cells. Exploiting the potential of transfer of microbubble material to the cell membrane, as indicated by Carugo *et al*. (2017), these functionalised microbubbles could be used to study microbubble-cell interactions and potentially immune cell-cell interactions. They may provide an opportunity to modulate the immune response by turning any target cell, such as a cancer cell, into an antigen-presenting cell or make immune cells more potent in destroying diseased cells, similar to CAR T cell therapy. For example, these proteins can render the target cells more visible to immune cells, thus increasing the cytotoxic efficiency of immune cells against these target cells, as visually explained in the cartoon in *Figure 2.2*.

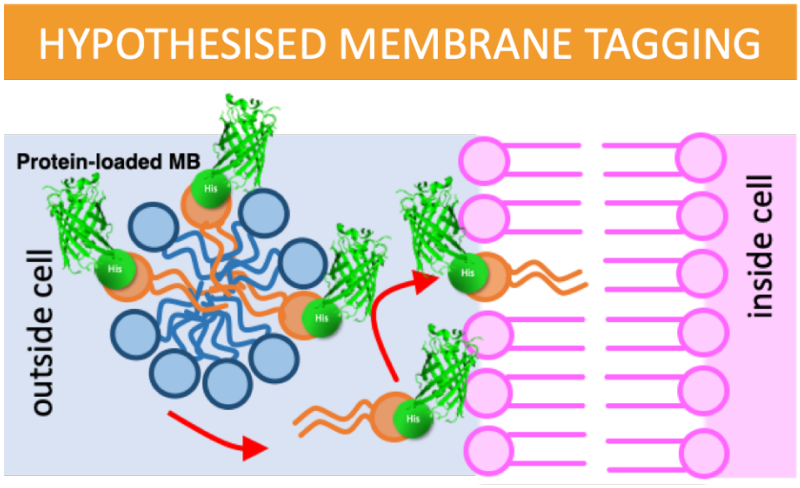


Figure 2.2. Schematic of the proposed microbubble and the hypothesised 'membrane tagging'*. The microbubble consists of DSPC, PEG40S and DGS-NTA(Ni), functionalised with proteins, e.g., His-GFP, to tag target membranes, with or without ultrasound. Adapted from Aron et al., 2019.*

2.2 Methods

2.2.1 Microbubble fabrication

A batch sonication protocol has been employed to prepare the microbubbles (Carugo *et al*., 2017). Functionalised microbubbles comprised of 1,2-distearoyl-sn-glycero-3-phosphocholine (18:0 PC, Avanti

Polar Lipids), commonly referred to as DSPC, polyoxyethylene (40) stearate (PEG40S, Sigma Aldrich, UK), and 18:1 or 16:0 nickel-nitrilotriacetic acid NTA(Ni)-functionalised lipids (*Table 2.1*) to which a protein modified with a polyhistidine tag, e.g., His-GFP, or a synthetic dye with a polyhistidine tag, e.g., His-AF488 (used as a model protein/dye compatible with fluorescence microscopy) can be attached.

In brief, the protocol is as follows: DSPC (18:0 PC, Avanti Polar Lipids), polyoxyethylene (40) stearate (PEG40S, Sigma Aldrich, UK), and 18:1 or custom-made 16:0 nickel-nitrilotriacetic acid (NTA(Ni))-functionalised lipids (DGS-NTA(Ni), Avanti Polar Lipids and Cambridge Research Biochemicals Ltd) were dissolved in chloroform (Sigma Aldrich, UK) and mixed in a glass vial at a molar ratio of 9 : 0.5 : 0.2, containing 20 mg of lipid constituents in total. The chloroform solution was covered with perforated parafilm (Bemis Company, Inc., Neenah, WI, USA) and subsequently either heated overnight on a hotplate set to 50 ˚C or dried under a vacuum at 60 ˚C for 45 minutes (Eppendorf, Concentrator plus, V-AQ), facilitating evaporation of chloroform and the formation of a homogenous lipid film.

The obtained dry lipid film was suspended in 5 mL of Dulbecco's phosphate-buffered saline (DPBS, pH 7.4, Life Technologies, Paisley, UK) and either stirred at 100 ˚C on a magnetic stirrer hotplate or shaken at 95 ˚C and 500 rpm in a mixer (Eppendorf, ThermoMixer C) for a minimum of 45 minutes. Phosphate-buffered saline consists of 137 mM NaCl, 2.7 mM KCl, 10 mM Na_2HPO_4, and 1.8 mM KH_2PO_4 in H_2O. Lipids were then homogeneously dispersed for 150 seconds using a sonicator (Microson XL 2000, probe diameter 3 mm, 20 W, 22.5 kHz, Misonix Incorporated, NY, USA or Qsonica Q125, probe diameter is 3.18 mm, 125 W, 20 kHz, Newtown, Ct, USA) with the tip completely immersed in the lipid solution (power setting 3 or 35%, respectively). Microbubbles were subsequently formed by placing the sonicator tip at the air-water interface under constant sulphur hexafluoride flow (The BOC Group plc, UK) and sonicated for 30 seconds to create a cloudy suspension of microbubbles (power setting 14 or 90%). Immediately after production, the vial with the microbubble suspension was capped and placed on ice for approximately 5 minutes. Microbubbles were kept on ice / at 4 ˚C during all subsequent steps except during ligand incubation.

Microbubbles were washed once to eliminate the excess of free NTA(Ni)-functionalised lipid. Microbubbles were washed using a centrifugation method without size isolation. In summary, microbubbles were loaded into a 2 or 5 mL syringe and centrifuged for 5 minutes at 300g (Denley, BR401). Following centrifugation, the subnatent was discarded, and microbubbles were resuspended in 1 mL of a DPBS solution

containing a His-tagged protein or dye, such as His_6-GFP (20 μg/mL, Stratech, UK, 27 kDa) or custom-made His_6-AF488 (4 μg/mL, Cambridge Research Biochemicals Ltd, UK, 1356.4 Da). After 8 minutes of incubation on a roller mixer (SRT6, Stuart, UK) at room temperature, centrifugation was performed, again for 5 minutes at 300g, to eliminate the excess unbound His-GFP/His-AF488 and improve the signal-to-noise ratio for fluorescence microscopy experiments, after which microbubbles were resuspended in 1 mL of fresh DPBS. The various microbubble components are shown in *Table 2.1*.

Appendix, *Section A.1* provides an insight into the effect and optimisation of the microbubble fabrication method on microbubble material transfer as investigated in *Chapters 3* and *4*.

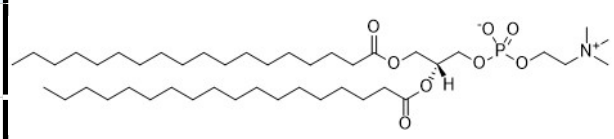
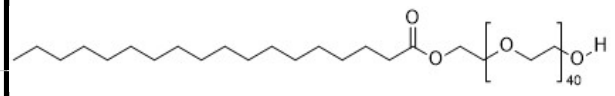
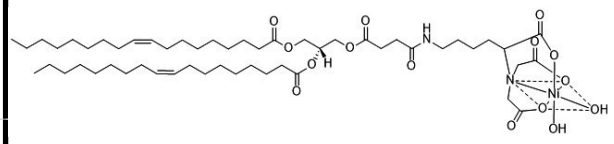
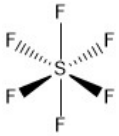
Short Name	**18:0 PC (DSPC)**	
Chemical name	1,2-distearoyl-sn-glycero-3-phosphocholine	
Molecular weight (g/mol)	790.145	
Molar fraction	9	
Short Name	**PEG40S**	
Chemical name	Polyoxyethylene glycol (40) stearate	
Molecular weight (g/mol)	2064.5	
Molar fraction	0.5	
Short Name	**18:1 DGS-NTA(Ni)**	
Chemical name	1,2-dioleoyl-sn-glycero-3-[(N-(5-amino-1-carboxypentyl)iminodiacetic acid)succinyl] (nickel salt)	
Molecular weight (g/mol)	1057.003	
Molar fraction	0.2	
Short Name	**SF_6**	
Chemical name	Sulfur hexafluoride (gas)	
Molecular weight (g/mol)	146.06	
Density (kg/m^3)	6.17	

Table 2.1. Microbubble components: DSPC, PEG40S, 18:1 DGS-NTA(Ni) and SF_6. *The table includes their chemical name, molecular weights, the density of SF_6, which is more than five times as high as the density of dry air, and molecular line drawings. It should be noted that 18:1 DGS-NTA(Ni) has two double bonds in its tail, potentially making incorporation in the microbubble shell more challenging.*

2.2.1.1 Saturated (16:0) and unsaturated (18:1) DGS-NTA(Ni)

As is apparent from the chemical structure of 18:1 DGS-NTA(Ni) in *Table 2.1*, this molecule contains two double bonds in its tails and is, therefore, referred to as the unsaturated form of DGS-NTA(Ni) used in this *Thesis*. Especially in the early stages of microbubble development, when small numbers of relatively unstable microbubbles were generated, the hypothesis was that this might be due to the unfavourable incorporation of the 'wide' double-bonded tail in the microbubble shell.

For example, most phospholipid chains in cell membranes are either saturated or monounsaturated hydrocarbon polymers. Previous work (Rawicz *et al*., 2000) into the effect of chain length and unsaturation of lipids on the elasticity of lipid bilayers suggests that polyunsaturated chain bilayers are thinner and more flexible than saturated/monounsaturated chain bilayers. They also observed an increase in chain repulsion and peaked stress distributions, affecting the lipid packing density: unsaturated lipids, with one or more kinks in the acyl chain, do not pack as well as their straight, saturated counterparts (Garg, Thomas & Borden, 2013). For this reason, microbubble formulations used in the clinic today contain saturated lipids.

In line with this, custom-made 16:0 DGS-NTA(Ni) was purchased from Cambridge Research Biochemicals Ltd. However, no apparent difference/improvement in microbubble stability or microbubble transfer/fusion was observed during this *Project*. However, an appropriate extensive investigation into the effect of the saturation of DGS-NTA(Ni) falls outside the current scope of this *Thesis*, and all subsequent experiments in this *Thesis* are performed with 18:1 DGS-NTA(Ni).

2.2.1.2 His-GFP and His-AF488

In this *Chapter*, both His-GFP and custom-made His-AF488, a synthetic fluorescent dye, were employed. As the *Project* aims to ultimately fabricate microbubbles functionalised with proteins normally present on the cell surface of antigen-presenting cells to instigate an immune response, a model fluorescent protein, GFP, was chosen to fabricate and characterise these novel microbubbles. However, due to its greater long-term storage stability and greater brightness and cost-effectiveness, initial experiments were also performed using the custom-made His-tagged green fluorophore Alexa Fluor 488 (AF488), as specified in the *Results*.

2.2.2 Microbubble characterisation

2.2.2.1 Brightfield microscopy

To quantify the microbubble size and concentration, 10 μL of the produced microbubble suspension was transferred onto a Neubauer improved cell counting chamber (Hausser Scientific Company) under a 24 mm × 24 mm glass coverslip (VWR International). Roughly 40 images of microbubbles were acquired at 40x magnification using a Leica DM500 microscope (Leica Microsystems GmbH, Germany) coupled with a CCD camera (Leica Microsystems GmbH, Germany). Microbubble sizing and counting were performed using purpose-written code in MATLAB® (Sennoga *et al*., 2010).

2.2.2.2 Multisizer

Population statistics, including microbubble concentration and mean diameter, were additionally collected using an electrozone sensing approach (Coulter Multisizer 4e, Beckman Coulter, Opa Locka, FI), as described by Feshitan *et al*. (2009). In brief, freshly prepared microbubbles were homogeneously dispersed by gentle agitation. Microbubbles (2 μL) were diluted into 10 mL of Isoton II in an Accuvette. Before each experiment in this and subsequent *Chapters*, microbubble samples were characterised three times, with thousands of events per repeat, as specified in the relevant figure descriptions. A 20 μm aperture (size range of 0.4–16 μm) was used. For the stability measurements, microbubbles were analysed over 3 hours in 30-minute intervals (N = 3 at each time point). The vials were capped and kept on ice to resemble the experimental conditions in the experiments in this *Chapter* and *Chapters 3*, *4* and *5*.

2.2.2.3 Confocal microscopy

The specificity of His-GFP for microbubbles was investigated using confocal fluorescence microscopy (LSM 780, Carl Zeiss AG, Germany), with magnifications varying from 20x to 63x. For this purpose, 2 μL of the microbubble sample was placed on a 75 mm × 25 mm × 0.17 mm glass coverslip (Logitech Ltd., Scotland). Excitation of both His-GFP and His-AF488 was achieved with a 488 nm laser line, and photomultiplier tube (PMT) reflections were simultaneously obtained to resemble brightfield images. Protein-functionalised

bubbles were compared to control DSPC-PEG40S bubbles (molar ratio: 9 : 0.5) made according to the protocol described in *Section 2.2.1*, but without the nickelated lipid, and thus also incubated with His-GFP.

2.2.2.4 Fluorescence Correlation Spectroscopy (FCS)

To investigate the potential for lipid transfer and/or fusion of the protein-loaded lipid from the microbubble shell to a target cell membrane, the diffusion characteristics of the His-GFP nickelated lipids within the lipid microbubble shell were quantified using Fluorescence Correlation Spectroscopy (FCS). FCS is, in short, a technique in which temporal fluctuations in fluorescence emitted by a sample of fluorescent molecules are analysed to obtain information about the processes that cause these fluctuations.

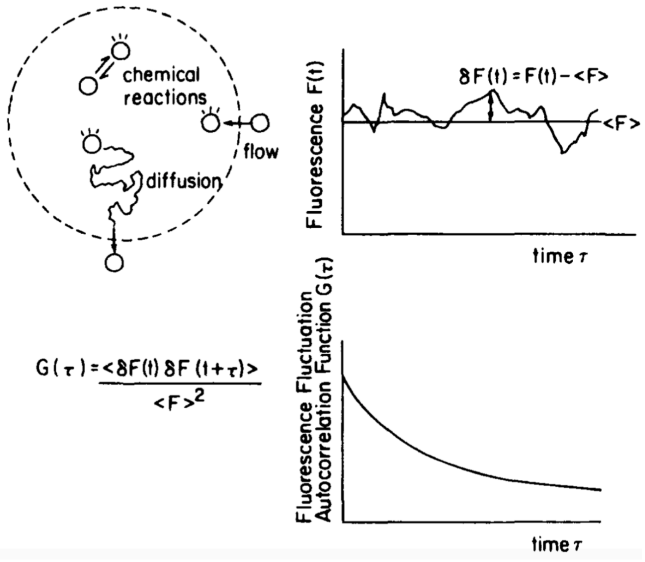


Figure 2.3. Schematic of the concepts of FCS. *Fluorescent particles diffuse or flow through the confocal volume, indicated by the dotted circle, or undergo transitions between states of different fluorescent yields (top left). This gives rise to fluctuations in the measured fluorescence intensity signal (top right). These fluctuations, denoted as δF(t), are autocorrelated as G(τ) (bottom left), which is shown as a function of lag time τ (bottom right) and has a characteristic rate and shape that yields both diffusion time τ_D and the average number of fluorescent particles in the confocal volume (Thompson, 2002, p. 338).*

Magde, Elson and Webb first applied FCS in 1972 as an analytical method for determining chemical dynamics of drug intercalation on DNA (Magde, Elson & Webb, 1972). Unfortunately, FCS was not frequently used due to a poor signal-to-noise ratio until it was combined with confocal microscopy, which greatly enhanced the detection efficiency, could handle large concentrations of dye molecules, and accurately suppressed the background fluorescence (Tian, Martinez & Pappas, 2011, p. 115). Over the years, FCS has proven to be a useful technique because of advantages such as high spatial and temporal resolution and short analysis time and has been used in several fields of study, for example, in measuring translational diffusion coefficients and chemical kinetic rate constants (Tian, Martinez & Pappas, 2011, p. 115; Thompson, 2002, p. 337). The conceptual basis of FCS is illustrated in *Figure 2.3*.

In general, fluorescent molecules move through a small confocal laser spot or undergo transitions between states of different fluorescent yields, which results in temporal fluctuations in the fluorescence intensity signal obtained from that area. The temporal autocorrelation of these fluctuations is the cross-correlation of the signal with itself but shifted in time by lag time τ. It represents the average duration of such a fluctuation and decays with time (Thompson, 2002, p. 338). As shown in *Figure 2.3*, the fluorescence $F(t)$ is measured as a function of time. The deviation of the measured fluorescence $F(t)$ from the temporal average value $< F >$ is defined as:

$$\delta F(t) = F(t) - < F > \tag{1}$$

The normalised autocorrelation function $G(\tau)$ is then given by:

$$G(\tau) = \frac{< \delta F(t+\tau) \cdot \delta F(t) >}{< F(t) >^2} \tag{2}$$

The rate and shape of the autocorrelation function reveal some information regarding the processes that cause the fluorescence fluctuations. Small values of τ yield a relatively high autocorrelation since time is limited for fluorescent particles to diffuse out of the focal volume or undergo a transition to a state of lower or higher fluorescent yield, while for large values of τ, the autocorrelation decreases because of fluorescent particles moving in and out of the focal volume and transitions taking place.

Furthermore, the rate of the fluctuations in the fluorescence intensity is inversely proportional to the decay time τ_D, which is the characteristic lag time τ at half maximum of $G(\tau)$, as can be seen in *Figure 2.4*. The magnitude at $\tau = 0$ yields the average number of fluorescent particles, $< N >$, in the sample area. With knowledge of the size of the observed volume, the mean concentration can be calculated by (Thompson, 2002, p. 341):

$$G(0) = \frac{1}{< N >} = \frac{1}{V_{eff} * < C >} \tag{3}$$

The effective volume in the case of the confocal microscopy performed in this *Chapter* is given by integrating the Gaussian form of the point spread function (PSF) of the focal volume:

$$V_{eff} = \pi^{\frac{3}{2}} \omega_{xy}^2 \omega_z \quad (4)$$

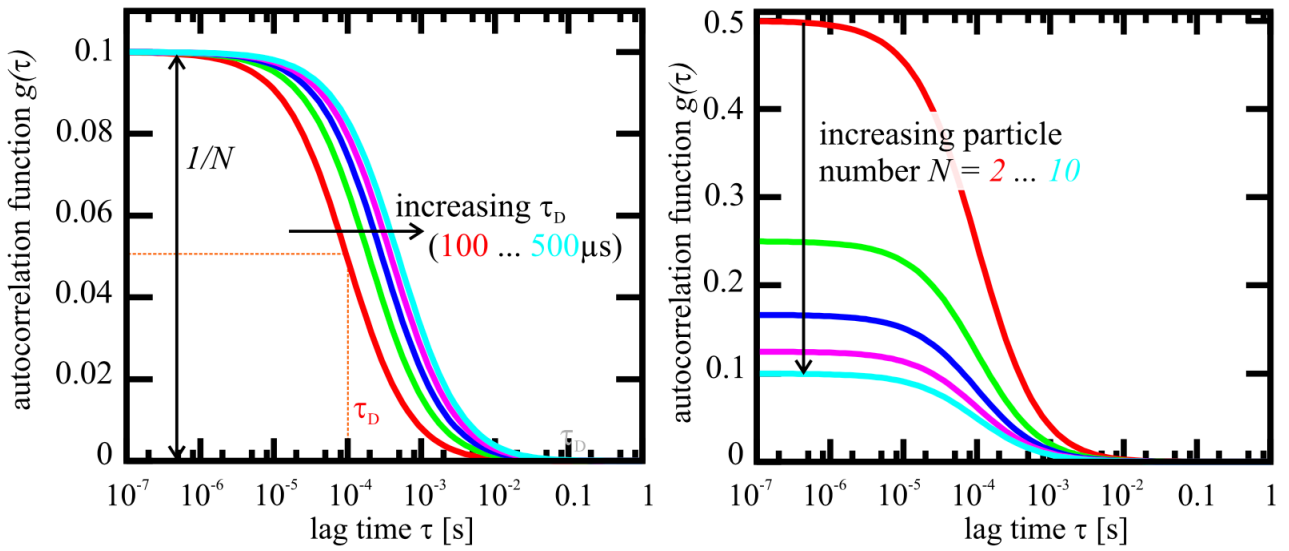


Figure 2.4. For illustrative purposes, this figure shows the autocorrelation functions for the process of simple diffusion. *It illustrates the effect of both the diffusion time τ_D (left) and the average number of fluorescent particles in the focal volume (right) on the autocorrelation function $G(\tau)$. Adapted from Krieger, Tódt and Langowski, accessed June 2017.*

To obtain the diffusion time and other variables, one needs to fit the appropriate model function to the experimental data. For the experiments in this *Chapter*, the diffusion type of the NTA(Ni)-His lipid-protein complexes was approximated to be 2D diffusion with a triplet state. The triplet state is a photophysical phenomenon in which molecules are trapped in a dark state for a few microseconds. Ignoring this state in the model can cause distortion of the FCS curves and, consequently, wrong values for diffusion times and diffusion coefficients, especially if the fraction of molecules in the triplet state is high or diffusion times are short (Sezgin & Schwille, 2011). Assuming that singlet-triplet transitions take place at a time scale much faster than the diffusion time, the fluctuations can be treated separately in a fast time range, i.e. in the order of μs (Widengren, Mets & Rigler, 1995). Therefore, the fitting function used to obtain τ_D is as follows (Sezgin & Schwille, 2011):

$$G_{Tr}(\tau) = G(\tau)[1 + T(1-T)^{-1} exp(\frac{-\tau}{\tau_{Tr}})] \quad (5)$$

, where T is the fraction of molecules occupying the triplet state, τ_{TR} is the rate of relaxation in the triplet state, and $G(\tau)$ equals the diffusion fitting function for simple 2D diffusion (Sezgin & Schwille, 2011):

$$G(\tau) = \frac{1}{N}(1 + \frac{\tau}{\tau_D})^{-1} \tag{6}$$

Once the diffusion time τ_D is obtained by fitting the experimental data to equation (5) using FoCuS-point software, developed by Waithe *et al*. (2016) for super-resolution STED-FCS and time-gated single-photon counting, the diffusion coefficient D can be calculated as follows:

$$D = \frac{\omega_{xy}^2}{8ln(2)\tau_D} \tag{7}$$

where ω_{xy} is the radial distance of the optical axis, or, in other words, the full-width half maximum of the focal volume.

In this *Chapter*, FCS was employed to study the diffusion characteristics of the NTA(Ni)-His-GFP complex in comparison to the same characteristics in GUVs. GUVs were produced by Dr Erdinc Sezgin according to a protocol as described by Jenkins *et al*. (2018), with 5 : 5 of POPC and cholesterol. Biological membranes are inherently dynamic, and fluidity in microbubble shells can similarly promote both His-tagged protein attachment, as it allows for poly non-covalent binding between histidine residues and NTA(Ni), leading to higher stability of the complex (Nye & Groves, 2008), and potentially improved microbubble-cell membrane transfer/fusion. To this end, confocal microscopy (LSM 780, Carl Zeiss AG, Germany) was performed to obtain the experimental FCS curves for both GUVs and microbubbles using a 40x water 1.2 NA objective.

After collecting the fluorescence intensity for 10 seconds with N = 3 per microbubble, using sensitive photodetectors, a hardware correlator correlated the signal from subsequent time points according to the correlation function described in equation (2) to obtain these experimental FCS curves. These curves were subsequently fitted with equation (5) using the FoCuS-point software to eventually obtain diffusion coefficients for the NTA(Ni)-His lipid-protein complex in the GUVs and microbubbles. To calculate D,

however, ω_{xy} needs to be resolved, which was done by performing a control experiment for the diffusion of freely diffusing Alexa Fluor 488 dye with known diffusion coefficient D = 430 μm²/s at room temperature and measurable τ_D, according to the 3D diffusion model (Sezgin & Schwille, 2011):

$$G(\tau) = \frac{1}{N}(1 + \frac{\tau}{\tau_D})^{-1}\frac{1}{\sqrt{1 + \omega_{xy}^2\frac{\tau}{\tau_D}}} \quad (8)$$

2.2.2.5 Serum and temperature incubation

To investigate the effect of 'physiological conditions' on both the stability and loading capacity of His-AF488-functionalised DGS-NTA(Ni) microbubbles, functionalised microbubbles were incubated in DPBS and Gibco Dulbecco's Modified Eagle Medium (DMEM) supplemented with 10% Fetal Bovine Serum (FBS), both on ice and at 37 ˚C for 10 minutes in a mixer (Eppendorf ThermoMixer C, Germany). Microbubbles were subsequently imaged using confocal fluorescence microscopy (LSM 780, Carl Zeiss AG, Germany) at 40x (EC Plan-NeoFluar 40x/1.3 Oil DIC M27) magnification by placing 2 μL of the microbubble sample on a 75 mm × 25 mm × 0.17 mm glass coverslip (Logitech Ltd., Scotland). Excitation of His-AF488 was achieved with a 488 nm laser line, and photomultiplier tube (PMT) reflections were simultaneously obtained to resemble brightfield images.

2.2.2.6 Binding of a variety of His-tagged entities

To demonstrate the applicability of DGS-NTA(Ni) microbubbles to bind a variety of His-tagged dyes and proteins and, therefore, its translational potential, DGS-NTA(Ni) microbubbles were incubated with 4 μg/mL of His-AF488 (Cambridge Research Biochemicals Ltd, UK, 1356.4 Da), 20 μg/mL of His-GFP (Stratech, UK, 27 kDa), 20 μg/mL of His-PAmCherry (Abcam, UK, 29 kDa), 100 μg/mL of His-transferrin (SinoBiological, UK, 76.6 kDa) or 100 μg/mL His-human serum albumin (Abcam, UK, 67 kDa), according to the protocol described in *Section 2.2.1*. The protocol for the fluorescent labelling of His-transferrin and His-human serum albumin can be found in *Chapter 5*, *Section 5.2.1*. The microbubble samples were subsequently analysed using confocal microscopy, and their population statics were obtained, as described in *Sections 2.2.2.2* and *2.2.2.3*.

2.2.2.7 Statistical analysis

For the FCS diffusion experiment, statistical analysis was performed using Prism (GraphPad Software, San Diego, USA). The data, diffusion coefficients for the NTA(Ni)-His lipid-protein complex in both GUVs and microbubbles, are shown in boxplots to demonstrate the locality, spread and skewness of the data in each group. The Mann-Whitney test, the nonparametric alternative to the independent t-test, was performed to assess statistical significance, as the data do not satisfy the assumptions of the independent t-test, including normality. The difference was considered to be statistically significant when the p value was less than 0.05.

2.3 Results

2.3.1 Microbubble population characterisation: concentration and size

Using a Leica brightfield microscope, as described in *Section 2.2.2.1*, population statistics were obtained for His-GFP and His-AF488 microbubbles. It should be noted that the histograms, as shown in *Figures 2.5* and *2.6,* show a skewed distribution to the smaller diameters due to an initial non-optimised fabrication process used, which was subsequently optimised in *Appendix*, *Section A.1*. In subsequent experiments, the brightfield imaging combined with MATLAB analysis was, in favour of speed, substituted by Multisizer analysis, as shown in *Figures 2.7*, *2.13* and *2.14*. Furthermore, it can be observed that the dye-coating in the confocal image in *Figure 2.6* appears to be 'cleaner' than the protein-coating in *Figure 2.5*, which is possibly due to the formation of protein aggregates in the sample shown in *Figure 2.5*.

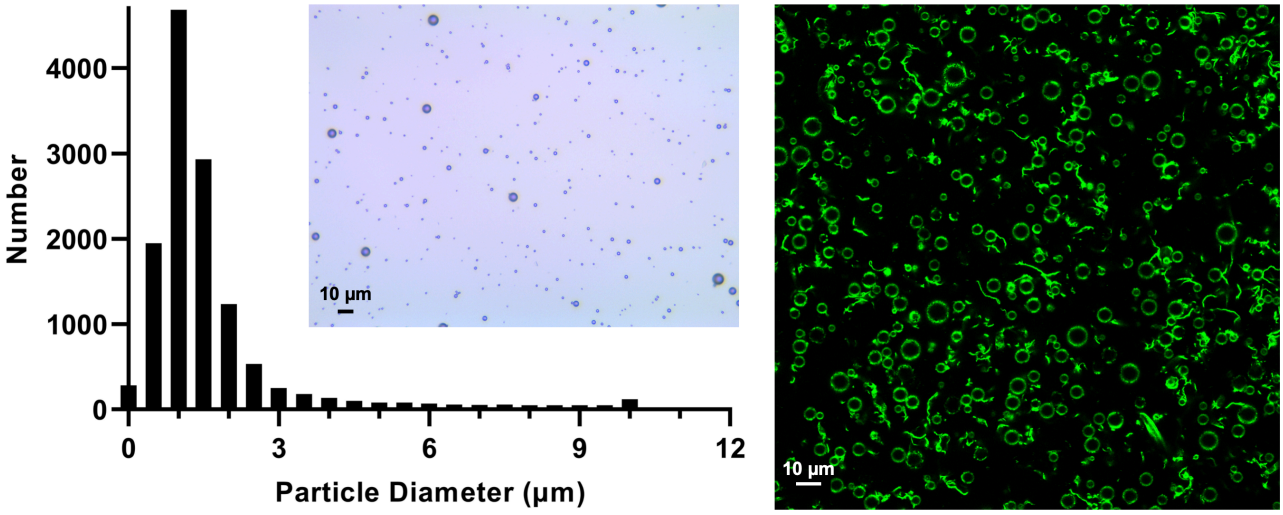


Figure 2.5. His-GFP functionalised DSPC-PEG40S-DGS-NTA(Ni) microbubbles, fabrication and characterisation. *To the left: microbubble size distribution histogram (number of events = 12145), showing a mean diameter of 1.62 ± 1.36 µm and a concentration of 2.56 x 10^8 bubbles per mL, with inserted a representative brightfield microscopy image, fed into a custom-written MATLAB programme to obtain the statistics. To the right: a representative confocal fluorescence microscopy image of His-GFP-loaded microbubbles (green) obtained at 40x magnification. The data shown are representative of 1 microbubble sample.*

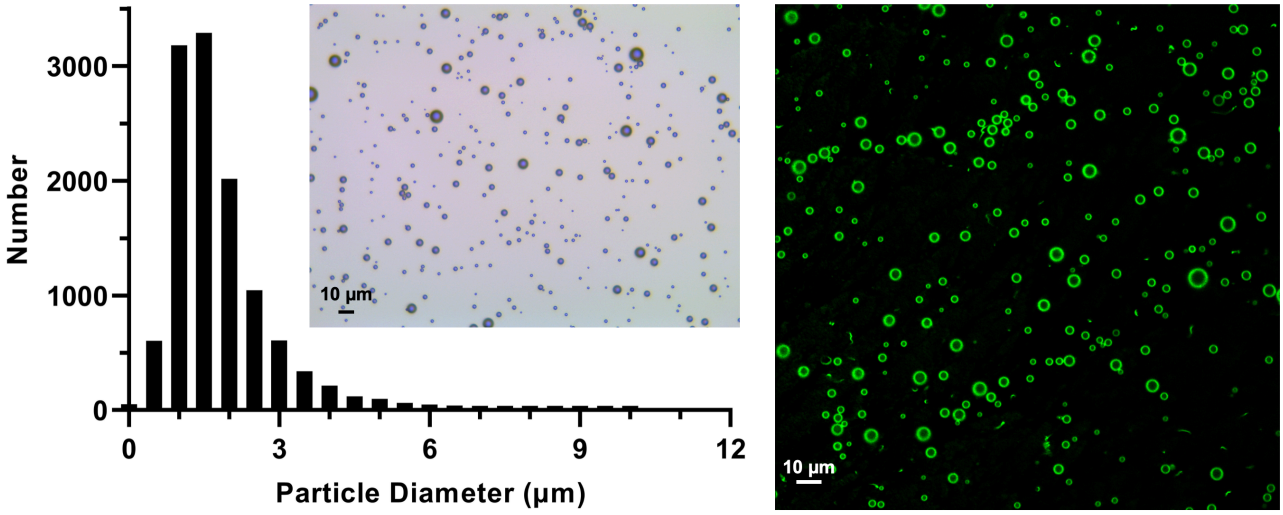


Figure 2.6. His-AF488 functionalised DSPC-PEG40S-DGS-NTA(Ni) microbubbles, fabrication and characterisation. *To the left: microbubble size distribution histogram (number of events = 11809), showing a mean diameter of 1.82 ± 1.50 µm and a concentration of 5.0*10^8 bubbles per mL, with inserted a representative brightfield microscopy image, fed into a custom-written MATLAB programme to obtain the statistics. To the right: a representative confocal fluorescence microscopy image of His-AF488-loaded microbubbles (green) obtained at 40x magnification. The data shown are representative of 1 microbubble sample.*

2.3.2 Microbubble population stability

To obtain microbubble population stability statistics, the Multisizer was chosen as the method going forward, as both the speed and the number of particles analysed were greater than could be obtained with microscopy. To illustrate the raw data obtained with this method, *Figure 2.7* shows histograms obtained for DGS-NTA(Ni) microbubbles functionalised with His-AF488 at t = 0 and t = 180 minutes, the endpoint of this stability study. It should be noted that this method can reliably detect smaller structures, resulting in higher values for the concentration measured compared to the brightfield method, in which they are missed due to limits on the camera resolution and the MATLAB algorithm. However, it should also be noted that it is not possible to optically verify that the counted structures are, in fact, microbubbles. Furthermore, rather than a bin size of 0.5 μm as in *Figures 2.5* and *2.6*, a bin size of 0.03 μm is achieved using the Multisizer, generating a more accurate representation of the size distribution.

Figure 2.7 shows the mean diameter and concentration changes for DGS-NTA(Ni) microbubbles between t = 0 and t = 180 minutes (N = 3). *Figure 2.8* shows the stability results in terms of mean diameter (A) and concentration (B) for DGS-NTA(Ni) microbubbles functionalised with His-AF488 (N = 3), obtained over three hours, demonstrating negligible changes over the course of a three-hour experiment.

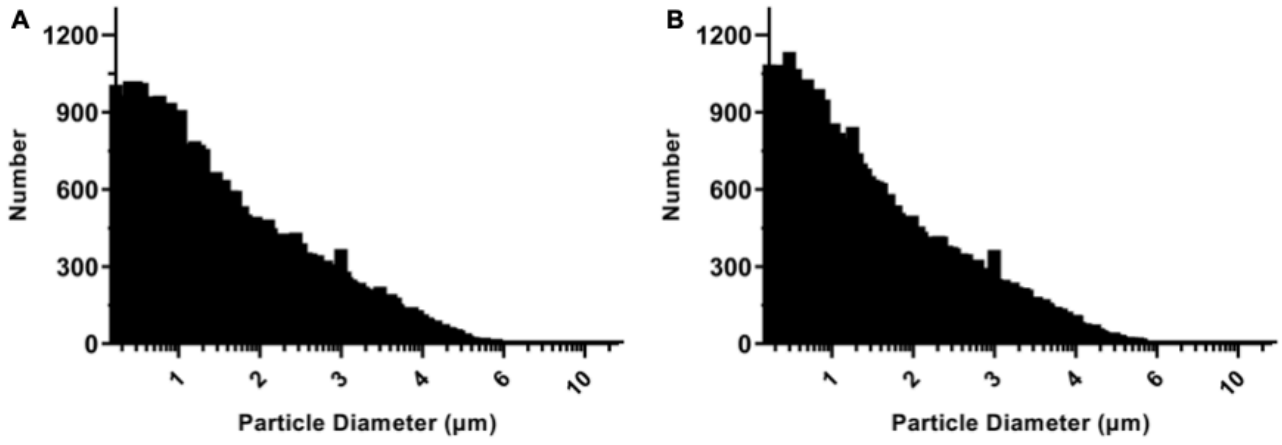


Figure 2.7. Microbubble size distribution histograms at t = 0 minutes (A) and t = 180 minutes (B) for DGS-NTA(Ni) microbubbles functionalised with His-AF488. *It shows a mean diameter of 1.99 ± 1.21 µm and a concentration of 4.82 x 10^9 bubbles per mL (number of events = 48244), and a mean diameter of 1.94 ± 1.19 µm and a concentration of 4.81 x 10^9 bubbles per mL (number of events = 44276), respectively.*

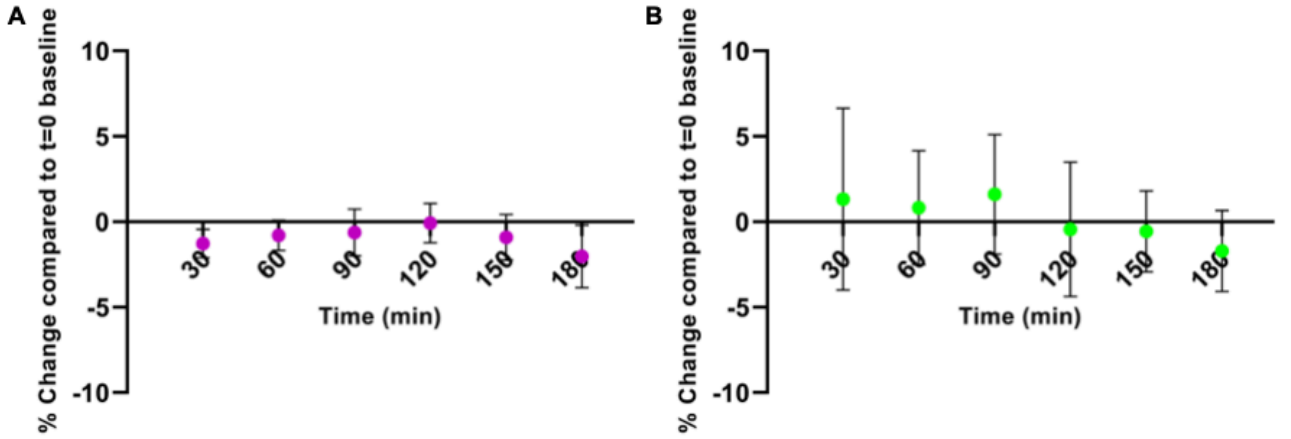


Figure 2.8. Stability results in terms of mean diameter (A) and concentration (B) for DGS-NTA(Ni) microbubbles functionalised with His-AF488 (N=3). *Stability statistics were obtained at 30-minute intervals for a duration of 180 minutes. Shown is the percentage deviation from the baseline (t = 0 minutes) mean diameter (A) or concentration (B) histograms, respectively.*

2.3.3 Specificity

Specificity of His-GFP for microbubbles containing DGS-NTA(Ni) was investigated using confocal fluorescence microscopy, where nickelated bubbles were compared to DSPC-PEG40S bubbles, which were made according to the same protocol as the DGS-NTA(Ni) functionalised microbubbles, with a molar ratio of 9 : 0.5, respectively.

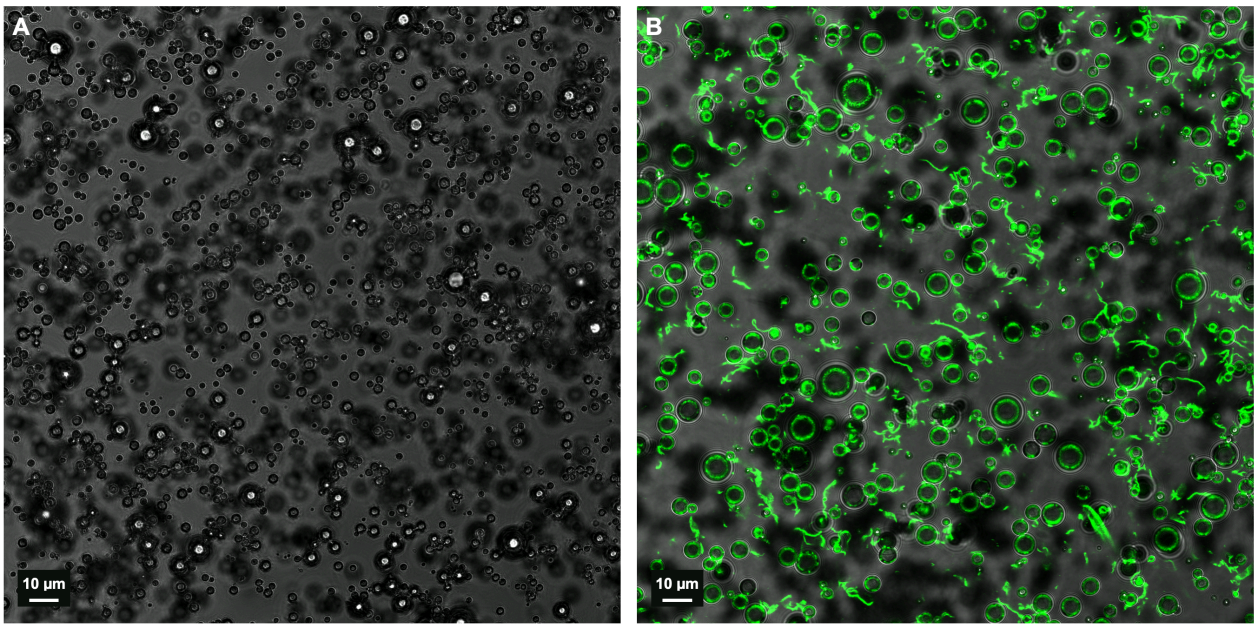


Figure 2.9. Confocal fluorescence microscopy images of His-GFP incubated (A) control DSPC-PEG40S microbubbles and (B) functionalised DSPC-PEG40S-DGS-NTA(Ni) microbubbles. *As can be observed, there is no non-specific binding of His-GFP (green) to microbubbles lacking nickelated lipid (A). In contrast, His-GFP binds specifically to nickelated microbubbles (B).*

The results are shown in *Figure 2.9*. As can be observed, His-GFP (green) binds to microbubbles containing nickelated lipid (*B*), whereas no binding can be observed for the control bubbles without nickelated lipid (*A*).

2.3.4 Diffusion: Fluorescence Correlation Spectroscopy (FCS)

Compared to the same conjugated protein-lipid complex embedded in GUVs (D = 7.5 ± 0.9 $\mu m^2/s$), diffusion of the His-GFP conjugated lipids in the protein-functionalised microbubbles is slower, as can readily be observed in *Figure 2.10*. However, the His-GFP conjugate in microbubbles still has a diffusion coefficient substantially different from zero (D = 3.2 ± 1.2 $\mu m^2/s$), meaning it is mobile on the microbubble surface. Mobility in the microbubble surface is required for lipid transfer/fusion with a target cell plasma membrane, which is fluid too. Immobile proteins on microbubbles would get stuck onto the cell membrane and presumably would not fuse with it. Moreover, bilayer fluidity is key for a potentially stronger binding due to the formation of polyvalent bonds between histidine residues and Ni head groups (Nye & Groves, 2008).

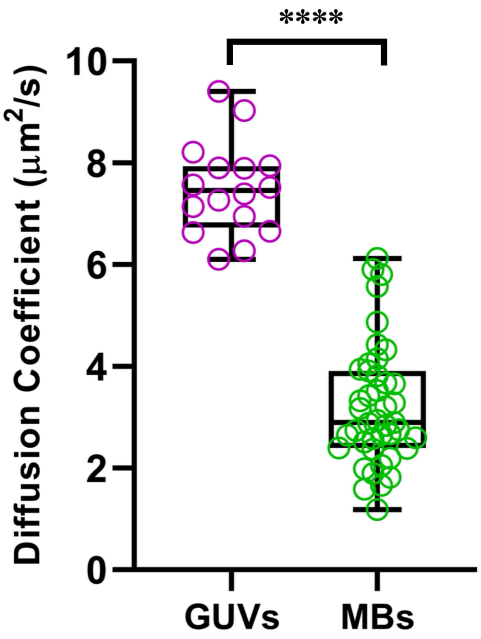


Figure 2.10. Using FCS, the diffusion of the His-GFP Ni-lipid conjugate in microbubbles was investigated and compared to the diffusion of the same conjugate in giant unilamellar vesicles (GUVs). *The conjugate is mobile in both GUVs and microbubbles, though slower in microbubbles (Mann Whitney Test, p<0.0001).*

2.3.5 Domains

Through serendipity, upon qualitative characterisation of DGS-NTA(Ni)-incorporated microbubbles functionalised with both His-GFP (*Figure 2.11*) and His-AF488, so-called domains were observed, as indicated by the black patches rather than homogenous green fluorescent coating in *Figure 2.11*. This indicates that the constituents of the microbubbles are not homogeneously dispersed throughout the lipid

shell. This is a phenomenon observed and characterised previously by, *inter alia*, Borden *et al*. (2006), Owen *et al*. (2019) and Langeveld *et al*. (2021).

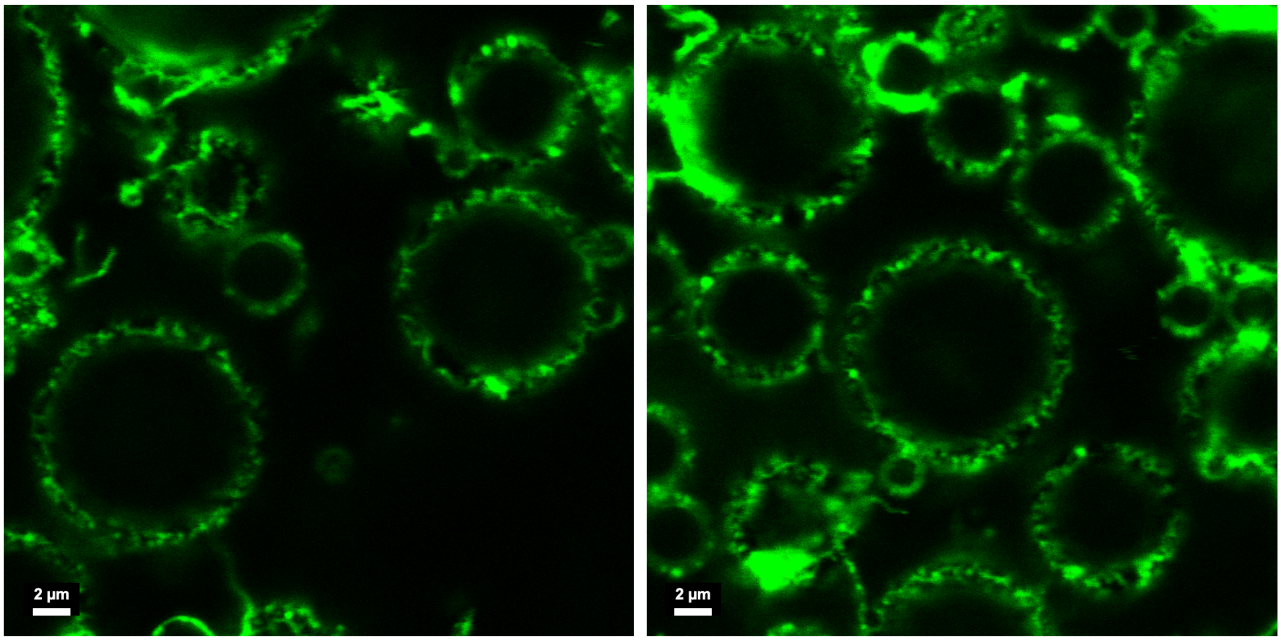


Figure 2.11. Representative images of domain formation in His-GFP-functionalised DGS-NTA(Ni) microbubbles at 63x. *They were acquired by confocal microscopy (LSM 780, Carl Zeiss AG, Germany), showing a heterogenous coating of the fluorescent protein on the microbubble shells.*

The lipid distribution is important as it dictates properties important in drug delivery or, in this case, microbubble-cell membrane transfer/fusion, such as the location and local concentration of the ligand/drug and PEG brush coverage, which may affect the accessibility of the ligand/drug and physiological clearing from *in vivo* systems (Borden *et al*., 2006).

Owen *et al*. (2019) showed that domain formation was mainly observed in larger microbubbles, consistent with the results shown in *Figure 2.11*. Those larger microbubbles happened to contain a larger concentration of PEG40S.

Langeveld *et al*. (2021) investigated the effect of lipid handling via a direct (immediate lipid resuspension in an aqueous solution) and indirect method (as used in this *Thesis*, by drying off the organic solvent to obtain a lipid film, which subsequently is resuspended in an aqueous solution), and lipid phase transitions on the microbubble coverage, showing that various lipids, such as DPPC and DSPC, and emulsifiers, such as PEG40S, are present in different phases: a liquid expanded (LE) and a liquid condensed

(LC) phase. PEG40S exists in the LE phase, whereas DSPC is always in the LC phase at room temperature. They found that microbubbles made by the indirect method had a significantly larger LC phase area than microbubbles made by the direct method and a homogenous ligand distribution. They used a DSPE-PEG2000 lipid as a model ligand.

This contrasts with the preliminary data in *Figure 2.11*, which shows that the ligand in this thesis, the His-tagged protein-lipid complex, appears to be heterogeneously distributed and, therefore, is unlikely to exist in both the LE and LC phase of the microbubbles. Further investigation is required into both the effect of lipid handling prior to microbubble formation and the role of the various microbubble components in the creation of these domains in the developed protein-functionalised microbubbles.

2.3.6 Loading capacity of His-AF488-functionalised DGS-NTA(Ni) microbubbles

As stated in the *Methods* section, DGS-NTA(Ni) microbubbles were incubated with 4 μg/mL of His-AF488. This *Section* explores the theoretical maximum loading capacity and takes a preliminary look at the loading capacity as measured immediately after incubation of the microbubbles. There are two approaches to this theoretical calculation: 1) using the molar concentration of the nickelated lipid used in the microbubble formulation, and 2) using the total surface area that the His-tagged dye can occupy.

Considering that DGS-NTA(Ni) has a molecular weight of 1057 g/mol, the first method gives a total of 0.19 μmol of DGS-NTA(Ni) in the microbubbles' volume of 2 mL. This means that, for His-tagged AF488 (1356.4 g/mol), no more than 260 μg could bind to NTA(Ni) lipids in the microbubbles. However, this estimate hinges on the assumption that all of the NTA(Ni) lipid is incorporated into the microbubbles, a vast overestimation, as not all lipid is incorporated into the shell, which is why the first washing step takes place to remove excess lipid.

The second method uses the surface area. A typical concentration of 3 x 10^9 MBs/mL and a typical surface mean diameter (D20 or D[2,0]) of 2 μm are used for this calculation. The surface mean diameter is the diameter of a hypothetical particle having a surface area equal to the mean surface area of the particles in a sample. This diameter can be calculated from the size distribution as:

$$D_{20} = \frac{\int_0^\infty D^2 p(D) dD}{\int_0^\infty p(D) dD} \quad (9)$$

, where D equals the particle diameter, and $p(D)$ is the probability density function of the size distribution, used to calculate the total surface area (Filippa, Trento & Álvarez, 2012). Using the molecular footprint of a typical phospholipid or the His-tagged payload - whichever is larger, the total number of payload molecules that can fit on the microbubble surface area can be estimated. Using a typical phospholipid molecular area of 50 $Å^2$, or 5 x 10^{-19} m^2, and a total surface area of 3 x 10^9 4π $(D_{20}/2)^2$ which equals 0.04 m^2/mL, gives a total number of phospholipids equal to 2.4 μmol in 2 mL of microbubble suspension. If 2% of those are DGS-NTA(Ni), the upper bound on the amount of bound His-tagged AF488 is 6 μg.

Experimentally, the loading was measured immediately after the fabrication of the microbubbles. Using a fluorescence plate reader, a standard curve was obtained for His-AF488, as shown in *Figure 2.12*. After microbubble fabrication and centrifugation, the fluorescence of the microbubble-free subnatent was measured to obtain the concentration of unbound His-AF488. By subtracting this concentration from the total His-AF488 concentration of 4 μg/mL with which the microbubbles were incubated, the amount of His-AF488 present on the microbubble shell after fabrication and centrifugation can be estimated. This results in 2.1 ± 0.2 μg/mL remaining on the microbubbles immediately after fabrication (N = 3).

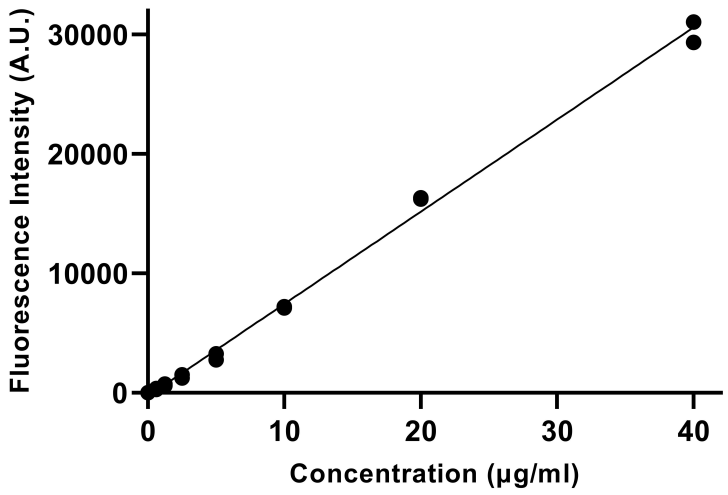


Figure 2.12. The standard curve for fluorescence of His-AF488. *The data (N = 2) were obtained using a fluorescence plate reader (gain 600, excitation 490 ± 10 nm, emission 520 nm). The corresponding linear relationship is defined as y = 772.07x - 278.8 with an R^2 value of 0.9976.*

Caution should be taken in interpreting this data, as the effect of resuspending the microbubbles prior to their use is not considered. The binding between mono-NTA(Ni) and a His_6-tag is relatively weak, with a K_D of

$13 \pm 5 \times 10^3$ nM, and the dissociation kinetics fast, with a k_{off} of $(1800 \pm 400) \times 10^{-3}$ s^{-1}, corresponding to a complex half-life of 0.39 seconds (Lata *et al*., 2005). Consequently, when a microbubble cake containing only bound His-tagged molecules is resuspended, a new equilibrium will be established on a timescale of a few seconds, with a substantial decrease in the amount of bound His-tagged molecules on the microbubbles.

2.3.7 Effect of physiological conditions on His-AF488-functionalised DGS-NTA(Ni) microbubbles

To test the feasibility of translating this technique of protein-loaded microbubbles to *in vivo* applications, the effect of Gibco Dulbecco's Modified Eagle Medium (DMEM) supplemented with 10% Fetal Bovine Serum (FBS) was investigated. Moreover, this effect was examined after 10 minutes of incubation at 4 ˚C or 37 ˚C.

In a different context, NTA(Ni) is often used for high-level purification of His_6-tagged proteins. In those protocols (e.g., the QIAexpressionist™), a word of caution is ushered regarding the presence of serum proteins in mammalian cell culture, e.g., amino acids with electron-donating groups, such as glutamine or histidine, which compete with the His_6-tagged protein for NTA(Ni) binding sites. The same can be said for metal ions in the cell culture medium that compete with Ni for NTA.

Secondly, clinical use of microbubbles takes place at body temperature (~37 ˚C). Guiot *et al*. (2006) showed strong fluctuations in the echogenicity of SonoVue with changing temperature, with a peak in scattering energy observed at 40 ˚C. In 2008, Vos, Emmer and De Jong investigated the effect of the physiological temperature on both SonoVue and Definity microbubbles. For both microbubble formulations, they showed a larger expansion at higher temperatures and a two-fold decrease in the acoustic pressure threshold at physiological temperature (Vos, Emmer & De Jong, 2008).

Figure 2.13 shows the results, with (*A*) and (*C*) corresponding to His-AF488 microbubbles in DPBS at respectively 4 and 37 ˚C, and (*B*) and (*D*) corresponding to His-AF488 microbubbles in DMEM with 10% FBS at respectively 4 and 37 ˚C. *Figure 2.13.E* and *2.13.F* show the corresponding population statistics. The microbubble size distribution for 4 ˚C in DPBS, which equals most of the conditions used for experiments in subsequent *Chapters*, is shown in black as the baseline, with the shift shown for both microbubbles in DPBS (*E*) and DMEM with 10% FBS (*F*) in grey. Interestingly, while both microbubble populations, regardless of

the surrounding medium, shifted to the left, i.e. much smaller diameters, the dye loading on the microbubbles was very differently affected.

Initially, in DPBS at 4 ˚C - the baseline condition at which the microbubbles are stored during experiments - the microbubble concentration is 4.25 x 10^9 MBs/mL, and the mean diameter is 1.84 μm (number of events = 37031). Upon incubation in PBS at 37 ˚C - the condition at which experiments are performed in *Chapters 3*, *4* and *5*, this shifts to 0.51 x 10^8 MBs/mL with a mean diameter of 1.07 μm (number of events = 25520), as shown in *Figure 2.13.E*. Upon incubation in DMEM + 10% FBS at 37 ˚C - , this equally shifts down, compared to the microbubble statistics obtained at the storage conditions (4 ˚C, in DPBS), to 0.47 x 10^8 microbubbles/mL and a mean diameter of 0.96 μm (number of events = 23547). This constitutes a ~85-fold decrease in microbubble concentration and a ~2-fold decrease in microbubble size after 10 minutes at 37 ˚C.

Figure 2.13.E and *2.13.F*, therefore, show the changes in microbubble population statistics compared to the storage conditions at 37 ˚C in both DPBS (E), the experimental conditions used in this *Thesis*, and in DMEM + 10% FBS (F), to resemble 'physiological conditions' and assess the impact of serum proteins on the His-AF488 functionalised microbubbles. Whereas His-AF488 remains on the microbubble shell in DPBS (*C*), regardless of temperature, it is observed primarily in the surrounding medium for microbubbles incubated in DMEM with 10% FBS (*D*) at 37 ˚C.

2.3.8 Applicability of 2%-18:1 DGS-NTA(Ni) microbubbles to bind a variety of His-tagged entities

To demonstrate the broad applicability of DGS-NTA(Ni) functionalised microbubbles, *Figure 2.14* shows His-GFP, His-AF488, His-PAmCherry, His-human serum albumin and His-transferrin functionalised microbubbles. The latter two are labelled using CF™660C, elaborated upon in *Chapter 5*, *Section 5.2.1*. Even though the degree of labelling obtained for both His-human serum albumin and His-transferrin is similar, as confirmed by absorption using a fluorescence plate reader, the His-transferrin microbubbles are significantly less bright, indicating a smaller amount of protein loaded on the microbubble shells.

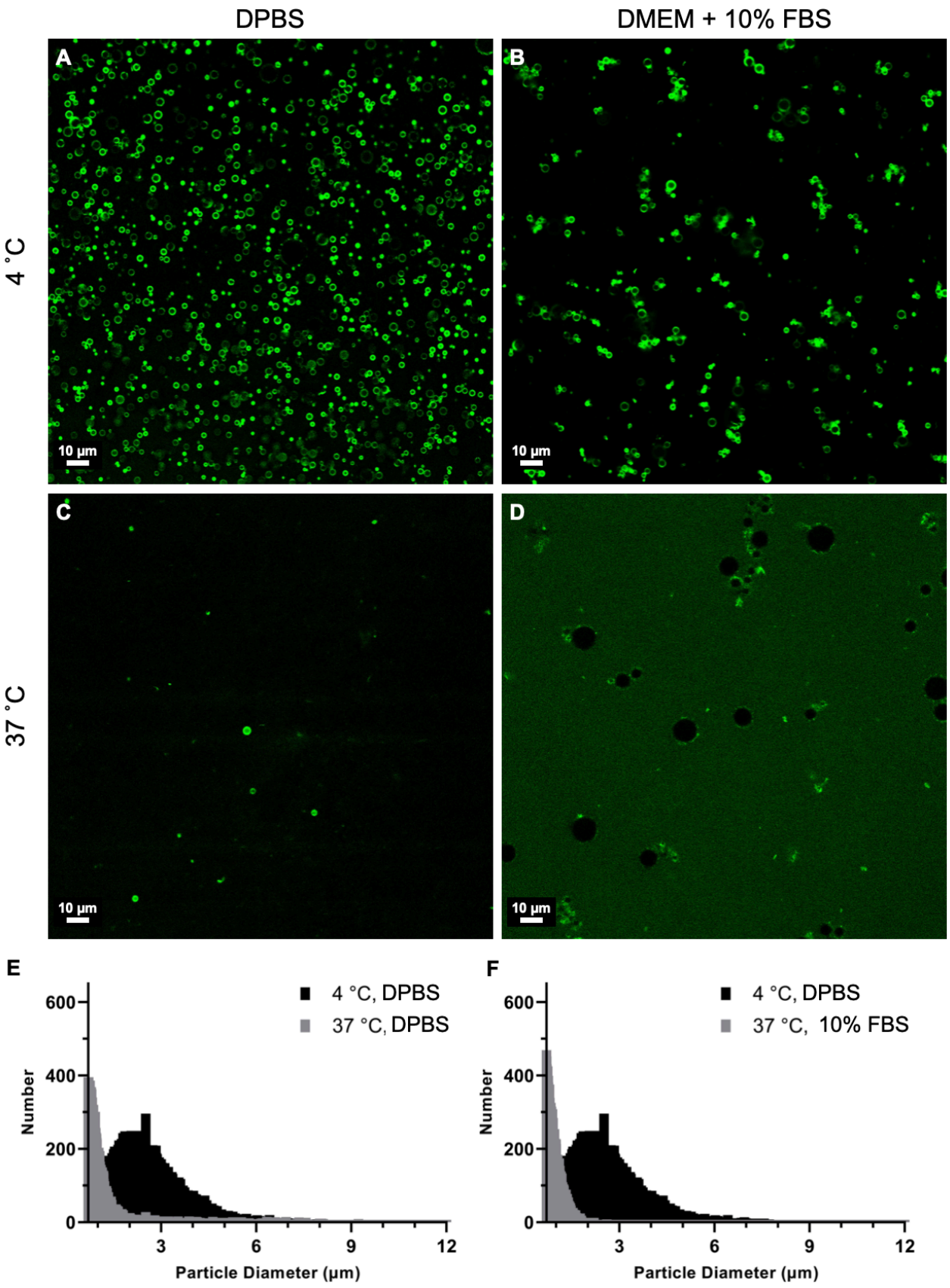


Figure 2.13. His-AF488 microbubbles in DPBS at respectively 4 ˚C (A) and 37 ˚C (C), and His-AF488 microbubbles in DMEM with 10% FBS at respectively 4 ˚C (B) and 37 ˚C (D). *Corresponding population statics are shown in (E) with microbubbles in DPBS at 4 ˚C (A) in black and DPBS at 37 ˚C (C) in grey, and (F) with microbubbles in DPBS at 4 ˚C (A) in black and DMEM with 10% FBS at 37 ˚C (D) in grey.*

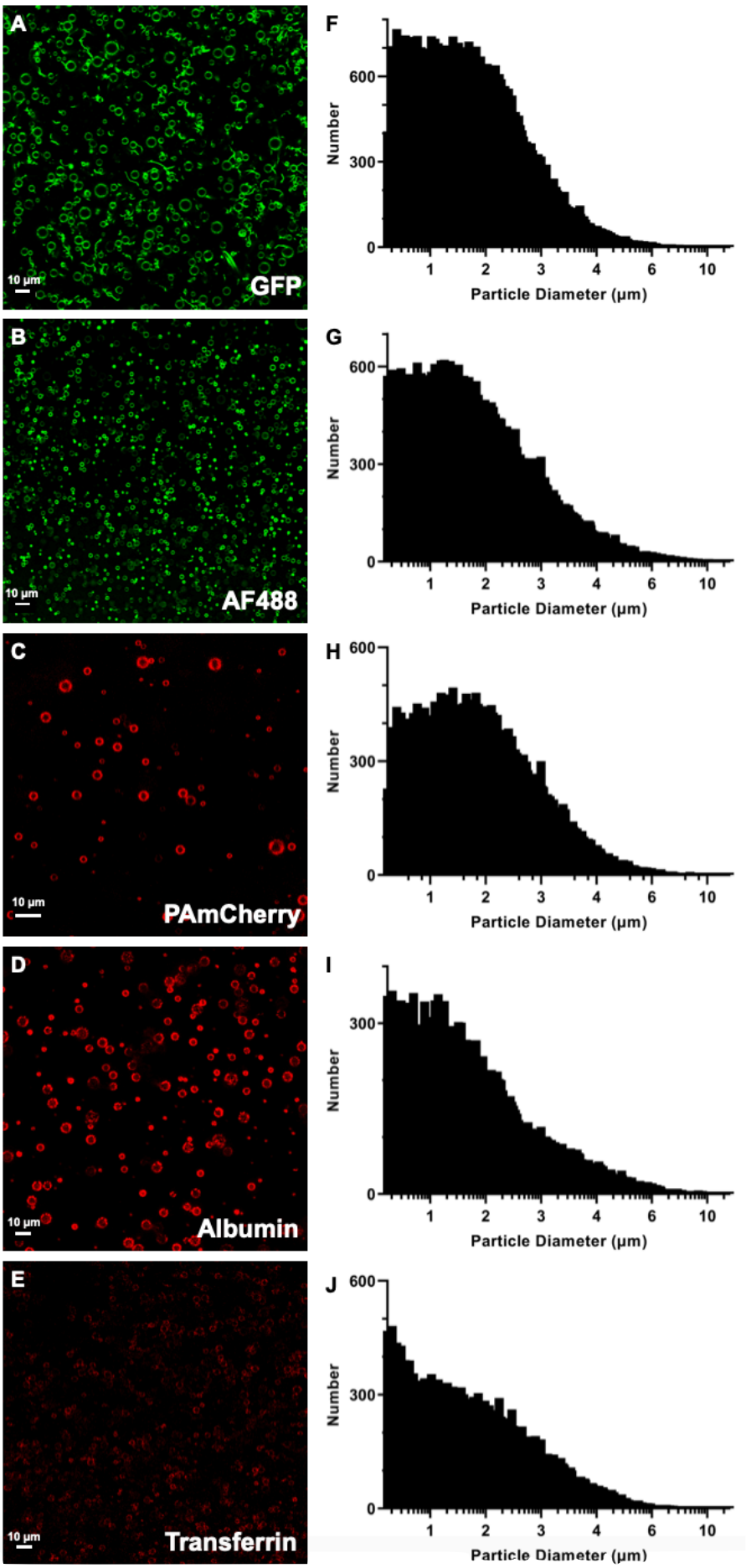


Figure 2.14. Confocal fluorescence images of microbubbles which are functionalised with His-GFP (A), His-AF488 (B), His-PAmCherry (C), His-human serum albumin (D) and His-transferrin (E) and microbubble size distributions (not corresponding to the confocal images on the left) obtained using the Multisizer, for microbubbles functionalised with His-GFP (F), His-AF488 (G), His-PAmCherry (H), His-human serum albumin (I) and His-transferrin (J). *The statistics are His-GFP: 4.78 x 10^9 MBs/mL, 2.01 µm mean diameter; His-AF488: 4.32 x 10^9 MBs/mL, 1.92 µm mean diameter; His-PAmCherry: 3.48 x 10^9 MBs/mL, 2.20 µm mean diameter; His-human serum albumin: 2.08 x 10^9 MBs/mL, 1.89 µm mean diameter; His-transferrin: 2.49 x 10^9 MBs/mL, 2.19 µm mean diameter.*

2.4 Discussion

2.4.1 Microbubble population characterisation: concentration and size

The work in this *Chapter* meets the first objective of this *Thesis*, which is the successful fabrication and characterisation of protein-functionalised microbubbles using a metallochelating complex through an NTA(Ni) and histidine residues interaction. The results are shown in *Figures 2.5* and *2.6*. This is one of the smallest high-affinity binding units, therefore hypothesised to minimise disruption to microbubble formation and stability. Its use has been widely explored in particular in recombinant protein purification.

Advantages over other microbubble ligand-loading methods of the NTA(Ni)-His complex, such as streptavidin/avidin-biotin and maleimide-thiol (Lux *et al*., 2017; Punjabi *et al*., 2019; Omata, Unga, Suzuki & Maruyama, 2020), include site-specific binding, the reversibility of the reaction, for example, through the addition of EDTA, and limited to no immunogenicity.

Notable downsides to this strategy include the potentially limited *in vivo* stability due to the competition of histidine-rich serum proteins with the His-tagged protein of choice initially incubated with the microbubbles, potential toxicity of the nickel headgroup and pH sensitivity, with a decreasing pH causing a decrease in Ni-His complexes.

However, this *Chapter* confirmed the successful fabrication of these surface-modified protein-loaded microbubbles by using a fluorescent protein and dye as a model, which was easily detected by fluorescence microscopy. The fact that the fluorescence was not affected by the binding indicates that the native conformation of the fluorescent protein is undisturbed.

2.4.2 Microbubble population stability

For the application of these microbubbles in protein-lipid complex transfer and/or fusion to target cell membranes, both *in vitro* and *in vivo*, the first steps were taken in characterising their stability. Microbubble stability can be assessed in different ways: (i) the stability of the microbubbles themselves, in their production conditions, and (ii) the effect of biological conditions, such as proteins and ions present in

biological fluids, on the stability of the NTA(Ni)-His binding. Regarding (i), the results in *Figure 2.8* generally make a good case for both concentration and mean diameter size to remain within acceptable deviation from the baseline when stored at 4 ˚C over up to three hours. However, their stability in *in vivo* conditions is limited, as shown in *Figure 2.13*, with the His-tagged entity detaching from the microbubbles, not helped by the weak binding and quick dissociation, as discussed in *Section 2.3.6*. This can be improved by using tris-NTA, with three active NTA(Ni) binding locations or 10 or 12 His-tags on the proteins of interest, as elaborated upon in *Section 2.4.7*.

2.4.3 Diffusion: Fluorescence Correlation Spectroscopy (FCS)

Another area that requires further investigation is the binding kinetics and dynamics of the His-tagged entities to the NTA(Ni) lipids. The Fluorescence Correlation Spectroscopy experiment, as shown in *Figure 2.10*, gives some insight into the diffusion dynamics in the microbubble shell, giving a positive indication of the potential for strong poly-histidine NTA(Ni) bonds as well as favourable lipid transfer to / microbubble fusion with cell membranes when exposed to ultrasound, as further explored in *Chapter 3*. As Nye and Groves discussed in their 2008 paper, the histidine bond to chelator lipids likely occurs in two steps: (i) monovalent binding and (ii) polyvalent binding due to bilayer fluidity, causing each His-tagged entity to interact with multiple chelating binding sides. However, it is not known whether these steps occur for the His-tagged protein/dye decoration on the custom-made microbubbles. Nye and Groves concluded that short incubations at high His-tagged protein/dye concentrations lead to primarily monovalently bound ligands, most of which desorb within minutes. In contrast, long incubations at low His-tagged protein/dye concentrations lead to primarily polyvalently bound ligands, which show little desorption on timescales as long as hours.

From experimental evidence to be shown in *Chapter 3*, it is known that the microbubbles produced in this *Chapter* maintain their fluorescent His-tagged protein/dye decoration for several hours during the transfer/fusion experiments, even after a short incubation time of merely 8 minutes, compared to the hours or days required to reach true equilibrium according to Nye and Groves (2008). Therefore, the exact nature of the bond of the lipid-protein complex or the desorption kinetics of these protein-loaded microbubbles

remains unknown and provides an interesting avenue for further optimisation of loading efficiency and minimising microbubble production costs.

2.4.4 Domains

Another interesting avenue to explore would be the formation of the domains, as observed in *Figure 2.11,* and how they correlate with the proposed transfer/fusion, as elaborated upon in *Chapter 3*. For example, does the heterogeneity in ligand coating cause any problems or irregularities in protein-tagging target membranes? And in which phase, LE or LC phase, does the protein-lipid complex exist, and is that influenced by the other components present in the microbubbles or the production protocol? Sadly, though very interesting and important, these questions fall outside the current scope of this thesis.

2.4.5 Loading capacity of His-AF488-functionalised DGS-NTA(Ni) microbubbles

The amount of ligand present on the microbubbles was preliminarily investigated both through a theoretical approximation and a measure of the fluorescence in the subnatent of the microbubbles directly after fabrication. As discussed briefly in *Section 2.3.6*, the mono-NTA(Ni)-His_6 binding is a weak binding with quick dissociation upon disturbance of the equilibrium. Every disturbance of the equilibrium, i.e. washing and resuspending of the microbubbles, leads to a loss of dye/protein to the surrounding medium. With this specific system, no conditions exist in which there are no or negligible amounts of free dye/protein in the surrounding medium. This could potentially cause binding of free dye/protein in solution in the targeting experiments, as elaborated upon in *Chapter 5*, and, more generally, requires incubation with larger amounts of dye/protein to achieve sufficient loading capacity. A potential solution to this problem again involves modifying the microbubble shell by incorporating a lipid with either tris-NTA(Ni) or an anti-His_6 antibody head group rather than mono-NTA(Ni).

Regarding loading efficiency, this *Chapter* has not dealt with the experimental composition of the microbubbles, e.g., how much of each component (DSPC, PEG40S and DGS-NTA(Ni)) ends up in the microbubble shell. A first attempt was made to tackle this issue by using High-Performance Liquid

Chromatography (HPLC) and Mass Spectrometry (MS) to separate and quantify the various lipid and protein/dye components. Successful separation was achieved for DSPC and PEG40S, and the fluorescent protein/dye could be identified using its absorbance, but quantification of DGS-NTA(Ni) content remains to be achieved.

2.4.6 Effect of physiological conditions on His-AF488-functionalised DGS-NTA(Ni) microbubbles

The microbubbles developed in this *Chapter* show promising stability under experimental conditions, i.e. capped and on ice (~ 4 ˚C). However, exposing them for prolonged times (10 minutes) to mammalian cell culture medium supplemented with bovine serum at 37 ˚C negatively impacts their stability and potentially causes the His-tagged entity to desorb from the membrane. Furthermore, the microbubbles became smaller, as seen in *Figure 2.13.E* and *2.13.F*, which is an effect observed previously by Mulvana *et al*. (2010). Interestingly, Shekhar *et al*. (2018) observed similar size distributions for Definity® at 25 ˚C and 37 ˚C. Not only does the increase in temperature to a physiological temperature affect the size of the microbubbles, it also affects ultrasound performance, with both Definity and SonoVue showing an increase in their radius upon expansion due to insonation and a decrease in the cavitation threshold at physiological temperatures (Mulvana *et al*. 2010; Vos, Emmer & De Jong, 2008). These are things to keep in mind for cell experiments in *Chapters 3*, *4* and *5*, which were performed at 37 ˚C.

2.4.7 Improvements and future in vivo work

The above opens up the general quest to optimise these microbubbles for stability and applicability. As mentioned in the introductory *Section 2.1*, Van Broekhoven *et al*. (2004) showed a highly effective procedure for the induction of antitumor immunity by targeting dendritic cells with antigen-containing liposomes, for which they used a three-functional chelating lipid NTA_3(Ni)-DTDA. In a follow-up study (Van Broekhoven & Altin, 2005), they showed that this molecule, with three NTA moieties in its head group instead of one, is several-fold more effective than its one NTA moiety counterpart at (i) establishing a stable His-tagged protein binding to liposomes, and (ii) binding to target T cells, both *in vivo* and *in vitro*. Whereas mono-NTA

had a dissociation constant of 13 ± 5 x 10^3 nM (Lata *et al*., 2005), for triple-NTA, this is reduced by a factor of ~6000 to 2.1 ± 0.8 nM, indicating a much stronger biding for triple-NTA than mono-NTA. The dissociation rate constant k_{off} is (0.34 ± 0.01) x 10^{-3} s^{-1} (Lata *et al*., 2005), resulting in a half-life of 2039 seconds. This indicates that the steady-state is reached after 8155 to 10193 seconds, or 136 to 170 minutes, compared to a few seconds for mono-NTA(Ni).

Secondly, rather than using NTA(Ni)-His as a binding strategy, another potential avenue would be the use of His-tag antibody-modified lipids, which are specific for the His_6-tag, and, therefore, would reduce the non-specific binding of histidine residues without affecting the commercial potential of binding a variety of commercially available His-tagged molecules. These antibodies are also commercially available from, e.g., Abcam (UK) or Sigma-Aldrich (UK). A few different options to modify the lipid to recognise the anti-His_6 antibody are 1) the use of maleimide, which is thiol reactive, in, e.g., DSPE-PEG-Maleimide bubbles, which can be subsequently incubated with a pre-treated antibody which contains maleimide-reactive cysteine residues (Yeh *et al*., 2015; Della Martina *et al*., 2008; Geers *et al*., 2011, Klibanov, 2005), 2) the use of strained alkyne lipids, e.g., DSPE-PEG-DBCO, which could react to azide-modified antibodies (Liu *et al*., 2018; Slagle *et al*., 2018; Liu *et al*., 2019), and 3) the use of the aforementioned biotin-avidin tagging strategy, e.g., DSPE-PEG-Biotin lipids, coated with avidin, and subsequently incubated with biotinylated antibody (Korpanty *et al*., 2005; Bayer *et al*., 1976). The last strategy, though criticised above for its more complicated process, immunogenicity and non-specific binding (Paganelli *et al*., 1992), remains a feasible option, especially by making use of neutravidin, which has shown improvements in immunogenicity and non-specific binding (Yumura *et al*., 2013; Jain *et al*., 2017).

The first successful attempt at producing metallochelating microbubbles by Lukáč *et al*. (2011) does not use any emulsifier in the microbubble composition, such as PEG40S. PEG40S has been hypothesised to increase the stability of microbubbles *in vitro* and *in vivo* due to aiding microbubble formation and providing protection from clearing via the immunogenic pathways (Yang *et al*., 2014; Upadhyay, Dalvi, Gupta & Khanna, 2017; Owen *et al*., 2018). The ability to resist protein adsorption and evade clearance by immune cells is generally thought to require, at minimum, PEG coverage of the microbubble to occur at a density corresponding to the mushroom/brush transition. The ‘brush’ confirmation, in which the PEG chains are densely packed compared to the collapsed ‘mushroom’ confirmation, may provide a sterically protected layer

against uptake by immune cells. However, the PEG 'brush' confirmation may simultaneously hinder the accessibility of the NTA(Ni) binding sites for His-tagged cargo and decrease the cell-specific targeting ability, as investigated in *Chapter 5*. A possible way to tackle this issue is the synthesis of a PEGylated lipid with an NTA(Ni), tris-NTA(Ni) or an anti-His_6 antibody head group, circumventing the possible 'shielding' of NTA(Ni) from histidine residues and, therefore, increasing loading efficiency.

So, potential avenues to be explored to improve the NTA(Ni)-functionalised microbubbles are (i) the use of different chelating metal ions in addition to nickel (II), such as cobalt (II) and zinc (II), (ii) the physicochemical character of the metallochelating lipid used, such as the chain length, saturation, potential PEG linker, use of NTA_3, and use of an anti-His_6 antibody head group (iii) the ligand loading efficiency and optimal surface density through ligand incubation protocols, such as variations in the concentration of both the His-tagged protein/dye and the chelating lipid, and (iv) the strengthening of the histidine-tag by moving to ten or twelve histidine residues, rather than the six histidine residues present in all His-tagged entities used in this *Thesis*.

2.5 Conclusion

This *Chapter* demonstrates the successful design, fabrication and characterisation of protein/dye-functionalised microbubbles using a metallochelating complex through an NTA(Ni) and histidine residues interaction, with a fluorescent model protein/dye, and discusses potential avenues for their optimisation. The objective was to design a new microbubble functionalised with proteins to tag target membranes, using ultrasound, to either make them more visible to the immune system or make immune cells more potent to destroy diseased cells.

To this end, *Chapter 3* shows results from proof-of-principle experiments to show protein-lipid complex transfer to and/or protein-functionalised microbubble fusion with the cell membrane in adherent A549 cells using confocal microscopy. *Chapter 4* uses flow cytometry to explore this 'membrane tagging' bioeffect quantitatively with A549 and Jurkat T cells in suspension. *Chapter 5* subsequently elaborates on targeting specific cell membranes through microbubble shell loading with the His-tagged targeting proteins

transferrin and human serum albumin, in addition to the His-tagged fluorescent protein/dye used in this *Chapter*.

Chapter 3 - Proof-of-Concept: Qualitative Assessment of His-Functionalised Microbubble-Cell Membrane Interactions

3.1 Introduction

After the successful fabrication and characterisation of the protein/dye-functionalised microbubbles in *Chapter 2*, this *Chapter* investigates the potential of utilising these bubbles to tag cell membranes. The results from proof-of-principle experiments are presented and discussed in the context of previous work, in particular the fusion experiments carried out by Carugo *et al*. (2017), sonoprinting experiments (De Cock *et al*., 2016; Roovers *et al*., 2019b) and the GUVs and immune cell experiments (Jenkins *et al*., 2017), as discussed in both *Chapter 1* and *2*.

To optimise and tune microbubble-membrane 'tagging', it is important to develop an experimental protocol that can be used to perform real-time measurements of microbubble/cavitation activity and correlate these with the desired biological effect. To this end, the first step in this *Chapter* was to identify and design a suitable system. The two most widely applied methods for monitoring cavitation activity are i) optical, which uses ultra-high-speed video microscopy and is generally not feasible *in vivo*, and ii) acoustic, which records the re-radiated sound fields produced by oscillating and/or collapsing bubbles. Both the amplitude and frequency components of the acoustic signal contain information on bubble behaviour. Low concentrations of bubbles at low incident ultrasound amplitudes have been shown to produce predominantly harmonic emissions (integer multiples of the driving frequency) (Stride & Coussios, 2010). As driving pressures increase, the bubble emission spectrum may also contain fractional components known as subharmonics and ultraharmonics (Stride & Coussios, 2019), indicating stronger nonlinear behaviour and broadband noise indicative of inertial cavitation. Integer harmonics are a primary indicator of bubble oscillation but can also be caused by non-linearities anywhere in an experimental system, e.g., due to non-linear propagation. By contrast, fractional harmonics and broadband noise strongly correlate with bubble dynamics.

The relationship between bubble behaviour and the detected acoustic emissions may be complicated by factors including the incident ultrasound field, the nucleation environment, and the characteristics of the detection pathway (Stride & Coussios, 2019). Nevertheless, important information about bubble behaviour and their interactions with cells can be gained by discerning trends in frequency and energy in the acoustic

spectrum. To fully exploit this information, robust, translatable, and reproducible experimental methods are required.

Currently, there is substantial variation in reported protocols for designing systems and conducting studies to support the development of cavitation-assisted therapies. A range of design approaches has been undertaken in terms of the apparatus. Several groups have used parallel-plate chambers (De Cock *et al*., 2016; Dong *et al*., 2017; van Rooij *et al*., 2017; Duan *et al*., 2019), either custom-built or commercially available (e.g., OptiCell, ThermoFisher Scientific, UK). Hu *et al*. (2013) developed a cell chamber coupled with an ultrasound sonication module and real-time confocal imaging. Carugo *et al*. (2015) used a system comprising a commercially available cell culture dish with a custom-made PDMS lid to allow submersion in a water bath during ultrasound exposure. Pereno *et al*. (2018) used a device consisting of layered acoustofluidic resonators that allow for simultaneous optical and acoustic characterisation of bubble dynamics and bubble-cell interactions.

The use of custom-fabricated and application-specific designs complicates the characterisation of the ultrasound field and other environmental exposure conditions, making cross-study comparisons challenging. For example, there is considerable variation in the ultrasound parameters identified for achieving successful sonoporation, which include centre frequencies ranging from 0.02 to 15 MHz, duty cycles varying from 1 percent to continuous wave, and rarefactional pressures ranging from 0.1 to 20 MPa (Hu *et al*., 2013; De Cock *et al*., 2015; Fan *et al*., 2012; Helfied *et al*., 2016; Helfield *et al*., 2017; Aron *et al*., 2019), as summarised in *Table 3.1*. There is similarly considerable variation in the spectral components (harmonics, sub-harmonics) that have been identified as being associated with particular bioeffects.

Parameter	Unit	Minimum	Maximum
Frequency	MHz	0.02	15
Pressure (PNP)	MPa	0.1	20
Pulse Length	Cycles	1	CW
Duty Cycle	%	1	CW
Exposure Time	s	10	1000

Table 3.1. Summary of the range of reported parameters facilitating sonoporation in vitro.

This *Chapter* qualitatively investigates protein/dye-lipid complex transfer to or microbubble fusion with the cell membrane in three Systems for Acoustic Transfection (SAT): SAT2, Mini-SAT and SAT3, each with unique geometries and ultrasound hardware specifics. In short, each system consists of a cell exposure compartment, an ultrasound source (0.5 or 1 MHz), and a single element transducer functioning as a passive cavitation detector (PCD), all of which are integrated into a benchtop test chamber. These designs build upon the prior system development described in Carugo *et al*. (2015) and are elaborated upon further in *Section 3.2*. The His-AF488 functionalised microbubble behaviour across a part of the parameter space used in the experiments in this and subsequent *Chapters* was also investigated and compared to SonoVue microbubble behaviour and DPBS controls (Gray *et al*., 2021). Lastly, the effect of modifying the microbubble fabrication protocol on 'membrane tagging' and comparing this 'membrane tagging' with 'internalisation' achieved with 18:1 Lyso PE microbubbles are shown in *Appendix A.1* and *A.2*, respectively.

3.2 Methods

3.2.1 Microbubble fabrication

A batch sonication protocol was employed to prepare the microbubbles, as described in *Chapter 2*. Functionalised microbubbles comprised of DSPC (18:0 PC, Avanti Polar Lipids, USA), polyoxyethylene (40) stearate (PEG40S, Sigma Aldrich, UK), and 18:1 nickel-nitrilotriacetic acid NTA(Ni)-functionalised lipids to which a protein modified with a polyhistidine tag, e.g., His-GFP, or synthetic peptide with a polyhistidine tag, e.g., His-AF488, used as a model protein/peptide compatible with fluorescence microscopy, can be attached. The protocol is elaborated upon in detail in *Chapter 2*, *Section 2.2.1*. For this *Chapter*, following centrifugation, microbubbles were loaded with His_6-GFP (20 μg/mL, Stratech, UK, 27 kDa) or custom-made His_6-AF488 (4 μg/mL, Cambridge Research Biochemicals Ltd, UK, 1356.4 Da). All microbubbles were characterised using brightfield microscopy and/or the Beckman Coulter Multisizer as described in *Sections 2.2.2.1* and *2.2.2.2* in *Chapter 2*.

3.2.2 Cell culture

Immortalised human alveolar adenocarcinoma cells (A549s) were cultured in T-75 flasks and passaged at 80% confluence (ATCC, UK). A549 growth medium consisted of Dulbecco's Medium-Eagle Medium (DMEM) supplemented with 10% fetal bovine serum (FBS). Cells were grown in a temperature- and CO_2-controlled incubator at 37°C and 5% CO_2. Cells were removed from T-75 culture flasks by exposure to 0.25% trypsin/EDTA for approximately 5 minutes. Cells were then suspended in 10 mL culture medium to deactivate the trypsin and subsequently centrifuged for 5 minutes at 300g to form a pellet. Cells were then re-suspended in 10 mL fresh culture medium. Cell concentration and viability were measured using trypan blue and a Countess® Automated Cell Counter (Invitrogen, UK). Unless stated otherwise, all cell culture materials were purchased from ThermoFisher Scientific (UK).

For experiments in the SAT2, ~0.2 x 10^6 cells were seeded in 35 mm diameter tissue culture-treated Ibidi μDishes (Ibidi, Germany) in 2 mL of the growth medium, 48 hours prior to exposure, to obtain near 80% confluence. For experiments in the Mini-SAT, 48 hours prior to exposure, approximately 0.4 x 10^6 cells were seeded on a single, plasma-cleaned 75 mm x 25 mm #1.5 glass coverslip (Logitech Ltd., Scotland) in 2 mL growth medium, supplemented with 1x penicillin-streptomycin (pen/strep). These coverslips were placed in 80 mm diameter Petri dishes, and, after 10 minutes to let the cells settle, an extra 8 mL of growth medium with 1x pen/strep was added. On the coverslips, an 8 by 8 mm square was drawn to indicate the region of interest for ultrasound exposure and subsequent microscopy analysis. Coverslips were sterilised in 70% ethanol for 30 minutes and exposed to UV for 30 minutes prior to seeding. Cells grown to ~80% confluence on glass coverslips were carefully transported to the Mini-SAT using tweezers. Lastly, for experiments in the SAT3, 0.01 x 10^6 cells were seeded approximately 48 hours prior to imaging in 6.5 mm diameter transwells in 24-well plates (Corning®, Sigma Aldrich, UK) in 100 μL growth medium.

In all cases, cells were washed twice with DPBS and incubated with a plasma membrane stain (1 μg/mL CellMask Deep Red) for 8 minutes. Subsequently, cells were washed twice before incubation with lyso-microbubbles (*Appendix*, *Section A.2*), DSPC-PEG40S-DGS-NTA(Ni)-His-GFP or -His-AF488 microbubbles at various concentrations and exposed to a variety of ultrasound conditions, as specified in the corresponding *Results* sections below.

3.2.3 Ultrasound set-up

3.2.3.1 SAT2

Each SAT consists of a cell exposure compartment, an ultrasound source, and a single element transducer that functions as a passive cavitation detector (PCD) integrated into a benchtop test chamber, as shown in Figure *3.1.A* to *3.1.C* for the SAT2. For the SAT2, a culture dish (35 mm diameter, of which a 21 mm diameter area is observable) is used to ensure compatibility with existing cell culture techniques and imaging systems. The SAT2 cell exposure compartment is formed by press-fitting a flexible polymer lid over the culture dish (Carugo *et al*., 2015). As seen in *Figure 3.1*, the lid has a pair of 1.2 mm diameter holes that allow filling the compartment with an 18 G blunt needle syringe. After filling, these ports are sealed with short plastic rods. The holder for the cell exposure compartment was built into the chamber lid, where a light press-fit is sufficient to ensure proper alignment.

In the SAT2, a 1.0 MHz centre frequency ultrasound source (Imasonic 8233 A101, 40 mm diameter, 120 mm radius of curvature) was used with a field that spans the cell attachment area, ensuring minimal spatial variability by using the pre-focal region of the large focused source. The ultrasound source was driven by a radio frequency amplifier (1020L, E&I Ltd., 200 W power amplifier), with the input signal generated by a waveform generator (33250, Agilent).

The SAT2 internal volume is approximately 0.8 L. The acoustic field is terminated in a fixed boundary to eliminate variability from air-water interfaces in partially filled chambers. In SAT2 and 3, this was accomplished by installing an acoustic absorber (1 cm thickness, APTFlex F28, Precision Acoustics) on the chamber lid to further reduce the field complexity that may arise from boundary reflections. The filtered water in the chamber was degassed for at least 2 hours to minimise the likelihood of cavitation and/or scattering from pre-existing bubbles in the propagation path.

The re-radiated sound field was picked up by a PCD (7.5 MHz centre frequency, V320 Panametrics, Olympus) fitted into the chamber lid. The response of the PCD to the ultrasound source was minimised by selecting a PCD with a centre frequency at least five times that of the ultrasound source and passing the signal through a 1.8 MHz high pass filter (E508, Thorlabs, UK). The signal was then passed through a pre-amplifier (SR445A, Stanford Research Systems, used for either 5x or 125x amplification to ensure capture of

the smallest expected signals and improve the signal-to-noise ratio of the final result. A digitiser was employed as a 12-bit streaming USB oscilloscope (HS5-110-XM, TiePie Engineering) to record the signal after it was passed through a 50 ohms impedance matching network. The paths for signal conditioning and recording are shown in *Figure 3.2*.

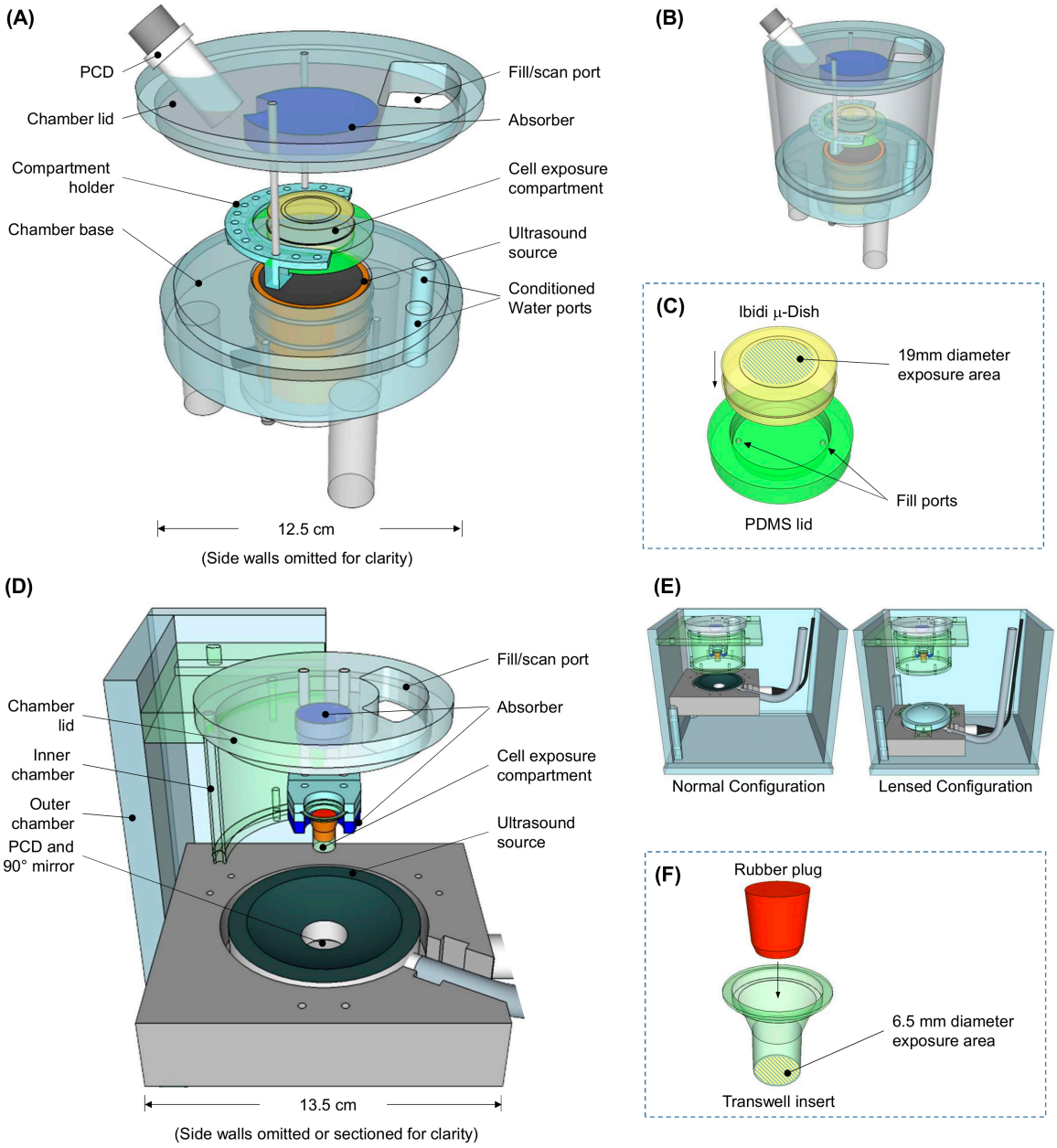


Figure 3.1. Illustrations of two ultrasound exposure system designs incorporating cavitation monitoring: SAT2 (A - C) and SAT3 (D - F). *(A) SAT2 annotated assembly with the side wall removed for clarity. (B) SAT2 with side wall intact. (C) SAT2 cell exposure compartment, disassembled. (D) SAT3 annotated assembly. (E) SAT3 in normal (left) and lensed (right) configurations for beam width matching at different frequencies. (F) SAT3 cell exposure compartment, disassembled. Adapted from Gray et al., 2021.*

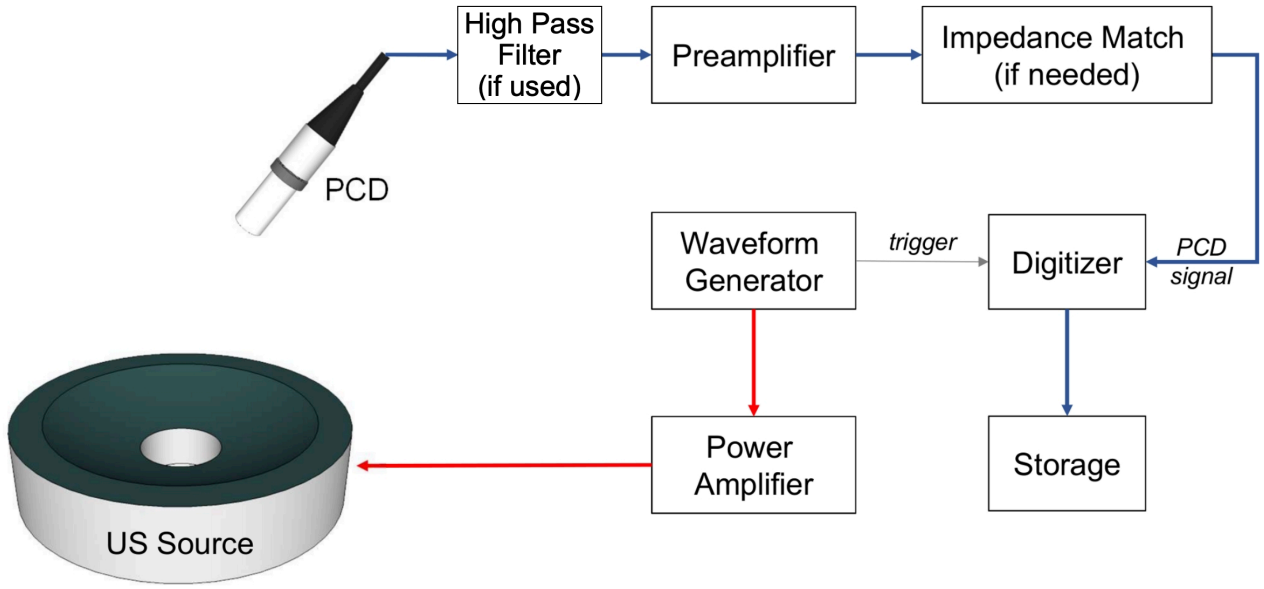


Figure 3.2. Instrumentation for cavitation signal conditioning and recording (blue arrows), ultrasound source excitation (red lines), and data acquisition triggering. *Adapted from Gray et al., 2021.*

3.2.3.2 Mini-SAT

The Mini-SAT, as shown in *Figure 3.3*, is built on the same principles as the SAT2. The cells are grown on a #1.5 glass coverslip (75 x 25 mm), which is placed, upside down, in the chamber filled with culture media or DPBS. It should be noted that the sample is exposed in a parallel configuration, with the ultrasound source (0.5 MHz centre frequency, 40 mm spherical focus, 1.5" diameter, Olympus NDT) placed in parallel with the glass slide. Again, a PCD (3.5 MHz centre frequency, unfocussed, 1/4" diameter, Olympus NDT) was used to record the reradiated sound field produced by the microbubbles.

Contrary to SAT2 and SAT3, the signal was not passed through a 1.8 MHz high pass filter to obtain whole spectrum data in the first experiments in this set-up. Otherwise, the signal conditioning and recording followed the schematic shown in *Figure 3.2*. The Mini-SAT internal volume is approximately 1.8 L, with a sample compartment chamber insert of 0.3 L to minimise the disposable volume and allow biologically relevant fluids other than the tank fill water (e.g., cell culture media or DPBS) to be used. As in the SAT2 and SAT3, an absorber was used to reduce the field complexity from boundary reflections. The glass coverslip is not acoustically transparent, which is why this side-on ultrasound exposure configuration was chosen. The changes in the ultrasound field due to the presence of the coverslip were investigated using a needle hydrophone by Dr Michael Gray and deemed to be minimal in the central region.

3.2.3.3 SAT3

The SAT3, as shown in *Figure 3.1.D* to *3.1.F*, is also built on the same principles as the SAT2 and Mini-SAT and was designed to obtain small working volumes of ~150 μL per sample. Rather than a μDish as in the SAT2, for SAT3, a transwell insert is used (6.5 mm diameter, Corning). The transwells have a permeable membrane and must be placed in cell media or DPBS rather than water. The SAT3 internal volume is approximately 7.6 L. An internal chamber of 0.3 L was added to minimise the disposable volume and allow biologically relevant fluids other than the tank fill water to be used (e.g., cell culture media or DPBS). The internal chamber bottom is made from a 30 μm thick mylar sheet to allow maximum acoustic transmission. The SAT3 compartment is filled by syringe or pipette and sealed by press-fitting a rubber stopper/bung (6 mm bottom diameter and 8 mm top diameter, 391-2101, VWR).

The ultrasound source used in the SAT3 is a 0.5 MHz focused source with a main lobe width that matches the diameter of the cell attachment area (0.5 MHz, H107 with central hole, Sonic Concepts), and requires an impedance matching network (H-107, Sonic Concepts) between the amplifier and the transducer. In contrast to the SAT2 and Mini-SAT, experiments in the SAT3 were performed at 37 ˚C to mimic physiological conditions, established by using an aquarium heater (EasyHeater, 100 W, Aquael).

To allow for compact configuration in the SAT3, the PCD (5 MHz centre frequency, IBHGO54, Olympus NDT) is integrated into the ultrasound source base. The reradiated field is picked up using a 90˚ reflector (F-102, Olympus NDT). The paths for signal conditioning and recording are otherwise the same as for the SAT2, as shown in *Figure 3.2*. For all the above mentioned SATs, the resultant PCD traces were processed using custom-written MATLAB code, courtesy of Dr Michael Gray, to obtain power spectra and an indication of the various components, e.g., broadband, harmonics and ultraharmonics, making up the signal. *Table 3.2* provides an overview of the ultrasound source and PCD hardware used in each set-up.

Parameter	SAT2	Mini-SAT	SAT3
US source centre frequency	1	0.5	0.5
PCD	7.5 MHz, focussed	3.5 MHz, unfocussed	5 MHz, focussed
Cell orientation	Upside down	Upside down	Right side up
Cell surface adherence material	Polymer	Glass	Polyester

Table 3.2. Ultrasound hardware and cell culture parameters for the three different set-ups.

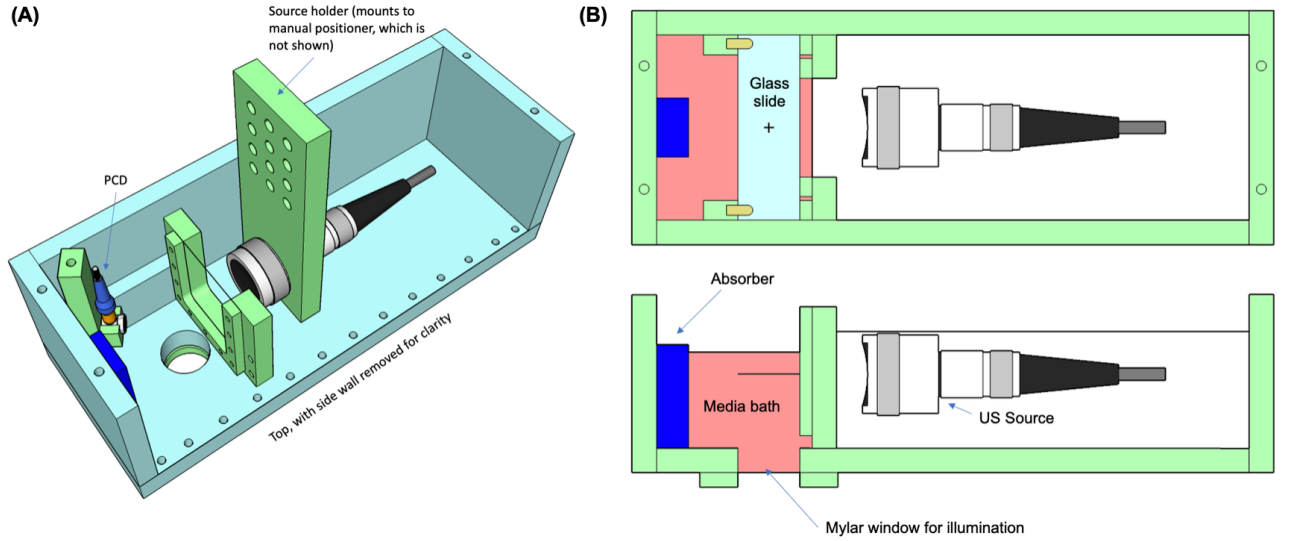


Figure 3.3. Illustrations of the Mini-SAT ultrasound exposure system designs incorporating cavitation monitoring. *(A) Mini-SAT annotated assembly with the side wall removed for clarity. (B) Mini-SAT schematic, which shows the alignment of a glass slide and culture media compartment. Figure courtesy of Dr Michael Gray.*

3.2.3.4 Ultrasound Experimental Protocol

The following protocol was used in all three SATs. To minimise the likelihood of cavitation in the propagation path, the filtered water, functioning as the fill liquid, was degassed under a pressure of -10^5 Pa for at least two hours. For the SAT2 and Mini-SAT, the test chamber was filled slowly to minimise the re-introduction of air into the degassed liquid, whereas the water in the SAT3 was degassed *in situ*. All residual bubbles were cleared from the transducer and media container surfaces immediately after filling and again just before initiating exposure experiments. For the SAT3, the chamber was given sufficient time to heat up to 37 ˚C, verified with a thermometer, before commencing experiments. The ultrasound source power amplifier was allowed to warm up so that the gain and output were stable with respect to time.

For the SAT2, the microbubble suspension was diluted prior to injection, to concentrations specified in the *Results* section, and withdrawn and dispensed slowly using an 18 G blunt fill needle to minimise the destruction of microbubbles during the loading process. The PDMS lid was rinsed with DPBS before press-fitting the lid to the μDish containing washed A549s. The needle was inserted through one of the PDMS fill holes to fill the sample chamber slowly. When filled, the holes were closed by inserting a short (4-5 mm) polymer rod (PTFE monofilament, Zeus). The compartment was visually checked for evidence of entrapped macrobubbles, and if present, the above steps were repeated. The compartment was then press-fitted into the compartment holder in the chamber lid and subsequently placed in the SAT2 chamber, lowering the lid at an

angle to avoid the formation of macrobubbles on top of the absorber and holder. It is important to know that in the SAT2, the cells are at the top of the chamber, with the microbubble suspension underneath, allowing the microbubbles to float up towards the cell layer.

For the Mini-SAT, the coverslip was carefully placed with the cells facing down in the media compartment, as shown in *Figure 3.3.B*. Microbubbles were injected using a pipette inserted beneath the glass slide and allowed to float up towards the cell layer. A square was pre-marked on the slide prior to seeding to guide this process, but it should be noted that this method does not allow for exact control over the microbubble concentration in contact with the cells.

For the SAT3, the transwell with cells grown on the membrane was filled with 200 µL of microbubble suspension. The cell exposure compartment was formed by carefully sealing the transwell with a rubber plug, removing any overflow liquid with a clean paper towel or wipe. As with the SAT2, the compartment was checked for evidence of entrapped macrobubbles, and if present, the above steps were repeated. The cell exposure compartment was then press-fitted in the compartment holder in the chamber lid and subsequently placed in the SAT3 chamber, lowering the lid at an angle to avoid the formation of macrobubbles on top of the absorber and holder. It is important to know that in the SAT3, the cells are at the bottom of the chamber, with the microbubble suspension above the cell layer, causing the microbubbles and cell layer to separate over time due to the natural buoyancy of the microbubbles.

Ultrasound parameters were initially based on previous experiments as performed by Carugo *et al*. (2017) and Aron *et al*. (2019), e.g., 200 kPa peak negative pressure, continuous wave, 60-second total exposure duration, after which the parameter space was explored using flow cytometry, as described in *Chapter 4*.

3.2.3.5 Data Collection

The following steps apply to all three SATs. Firstly, background PCD response levels were established by conducting initial experiments with the cell exposure compartment filled with a control liquid, e.g., DPBS, as common laboratory liquids such as DPBS or cell media will exhibit cavitation at moderate pressures (e.g., 0.5 MPa at 0.5 MHz) if not degassed. Examples in the SAT3 for various microbubbles and DPBS controls are shown in *Chapter 3*, *Section 3.3.4*. Furthermore, PCD data were recorded without driving the ultrasound

source for 5 seconds prior to each ultrasound exposure to establish background electronic noise levels and ensure the first exposures were not missed. Experiments were monitored in real-time in the time and frequency domain using the TiePie software. The time-domain monitoring is important to ensure appropriate sizing of the signal and no leaking of cavitation agent from the cell exposure compartment. The frequency-domain monitoring indicates the type of bubble behaviour, e.g., the presence of broadband emissions.

Simultaneously, the amplifier output signal that drives the ultrasound source was monitored throughout the experiment to ensure the ultrasound source generated the desired pressures. For this purpose, a high voltage probe (PP019 10:1, 250 MHz 12 pF, Lecroy, Teledyne) and an oscilloscope (T3DSO1104 Digital Storage Oscilloscope, Teledyne) were used to visualise the amplifier output. As mentioned in *Section 3.2.3.1*, signals were recorded using the TiePie digitiser, and the resultant PCD traces were processed using custom-written MATLAB code provided by Dr Michael Gray.

After ultrasound exposure, samples were carefully removed from the test chamber and transferred as required for further analyses, e.g., confocal microscopy as described in this *Chapter* or flow cytometry as described in *Chapter 4*. The PDMS lid (SAT2) or rubber plug (SAT3) were cleaned in preparation for subsequent use. In the case of the Mini-SAT, the sample chamber was drained after a small number of exposures to minimise contamination of the chamber media.

3.2.4 Confocal microscopy

For all three SATs, further analysis of microbubble-cell interactions was performed using confocal fluorescence microscopy (LSM 780, Carl Zeiss AG, Germany), with magnifications including 10x (EC Plan-NeoFluar 10x/0.3 M27), 20x (Plan-Apochromat 20x/0.8 M27), 40x (EC Plan-NeoFluar 40x/1.3 Oil DIC M27) and 63x (Plan-Apochromat 63x / 1.40 Oil DIC M27). For this purpose, µDishes (SAT2), glass slides (Mini- SAT) or porous transwells placed on glass slides (SAT3) were analysed.

Cells were stained with a plasma membrane stain, 1 µg/mL CellMask Deep Red (C10046, Thermofisher, UK), with its excitation maximum at 649 nm and its emission maximum at 666 nm. On the Zeiss LSM 780 system, it is excited by the 633 nm laser, and the emitted signal is picked up between 638 and 755 nm. His-GFP, His-AF488 and 18:1 NBD Lyso PE (*Appendix*, *Section A.2*) are excited by the 488 nm

laser, and the emitted signal is picked up between 493 and 598 nm. Photomultiplier tube (PMT) reflections were simultaneously obtained to resemble brightfield images.

Due to the porous membrane of the SAT3 transwells, the obtained images contained considerable amounts of noise in both channels and generally showed a reduced sharpness. To combat this, the SAT3 images were processed in ImageJ (Schindelin *et al*., 2012) to reduce this noise by despeckling. All images obtained in the SAT2 and Mini-SAT are shown here as recorded without post-processing.

3.2.5 Microbubble behaviour - ultrasound exposure parameter study

To get a better idea of the behaviour of the His-AF488 functionalised microbubbles in response to ultrasound exposure, His-AF488 microbubbles and SonoVue microbubbles were compared to DPBS controls across an extensive parameter space. SonoVue (Bracco, Italy) was chosen because of its widespread use as a diagnostic contrast agent, increased use in therapeutic ultrasound applications and ease of use (Stride & Coussious, 2019). SonoVue microbubbles were prepared as per the manufacturer's instructions. The ultrasound driving conditions are summarised in *Table 3.3*, for His-AF488 functionalised microbubbles, SonoVue and the DPBS controls. The ultrasound exposure protocol was as described in Gray *et al*. (2021).

MB type	US centre frequency (MHz)	Peak negative pressure (kPa)	Duty cycle (%)	Duration of exposure (s)
His-AF488 Fabrication method 2	0.5	200	1	50
	0.5	400	1	50
	0.5	700	1	50
SonoVue	0.5	200	1	50
	0.5	400	1	50
	0.5	700	1	50
DPBS	0.5	200	1	50
	0.5	400	1	50
	0.5	700	1	50

Table 3.3. Ultrasound driving conditions for the comparison between His-AF488 functionalised microbubbles, SonoVue and the DPBS controls. *Similar to the data as shown in Gray et al. (2021).*

3.3 Results and Discussion

Lipid transfer from His-GFP/AF488 functionalised microbubbles to cell membranes and/or whole microbubble-cell fusion was observed in all three SATs, to different degrees depending on the SAT specifications and, therefore, ultrasound conditions, bubble manufacturing method and microbubble composition. The results shown below are arranged as follows:

1. The qualitative observation of functionalised lipid transfer and/or microbubble fusion in the SAT2 (*Figure 3.4 and 3.5*),
2. The qualitative observation of functionalised lipid transfer and/or microbubble fusion in the Mini-SAT (*Figures 3.6* to *3.8*),
3. The qualitative observation of functionalised lipid transfer and/or microbubble fusion in the SAT3 (*Figures 3.9* and *3.10*).

Appendix A.1 and *Appendix A.2* show the results of supporting studies in which the effect of both the microbubble manufacturing method and microbubble composition, respectively, were investigated.

3.3.1 The qualitative observation of functionalised microbubble material transfer in the SAT2

His-GFP microbubbles (~1 x 10^7 MBs/mL) were employed for the first proof-of-principle study investigating the effect of these novel functionalised microbubbles with ultrasound (1.0 MHz, 200 kPa PNP, continuous wave, 15 and 30 seconds total exposure) on microbubble material transfer to the cell membrane. The geometry of the SAT2, where the microbubbles naturally float up towards the cell layer due to their buoyancy, was hypothesised to potentially help the transfer and/or fusion of these microbubbles with the membrane, even without ultrasound exposure. The results are shown in *Figures 3.4* and *3.5*.

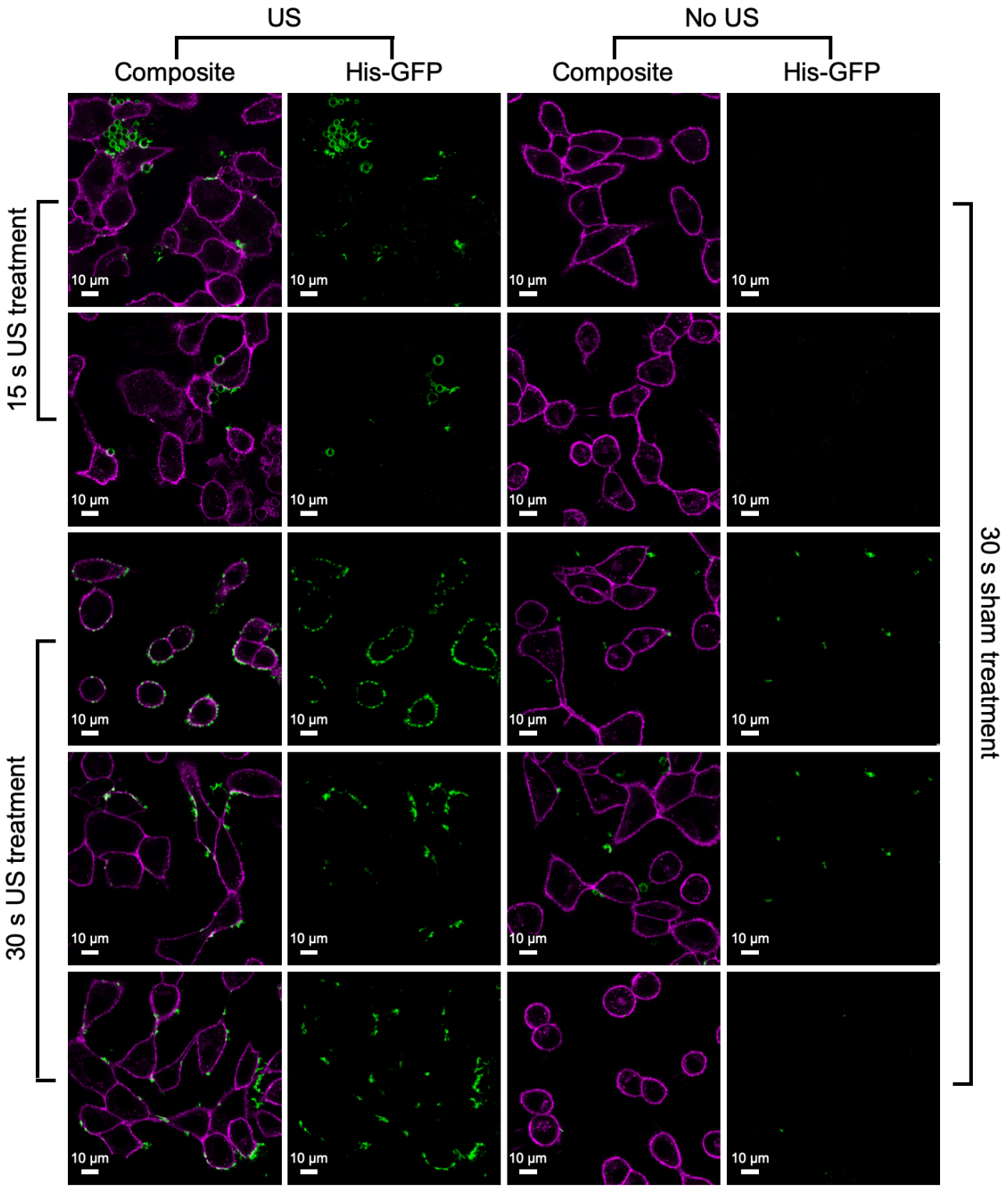


Figure 3.4. 'Membrane tagging' observed in the SAT2. *Confocal microscopy images of A549 cells stained with Cell Mask Deep Red (magenta) and His-GFP NTA(Ni) lipids and microbubbles (green) for 15s (N = 2) and 30s of ultrasound exposure (N = 3) (1.0 MHz, 200 kPa PNP, CW) in the SAT2 on the left, and corresponding no ultrasound 30 second sham treatment controls (N = 3) on the right. A distinct qualitative difference in the amount and pattern of transfer/fusion of His-GFP NTA(Ni) lipid to the cell membranes can be observed.*

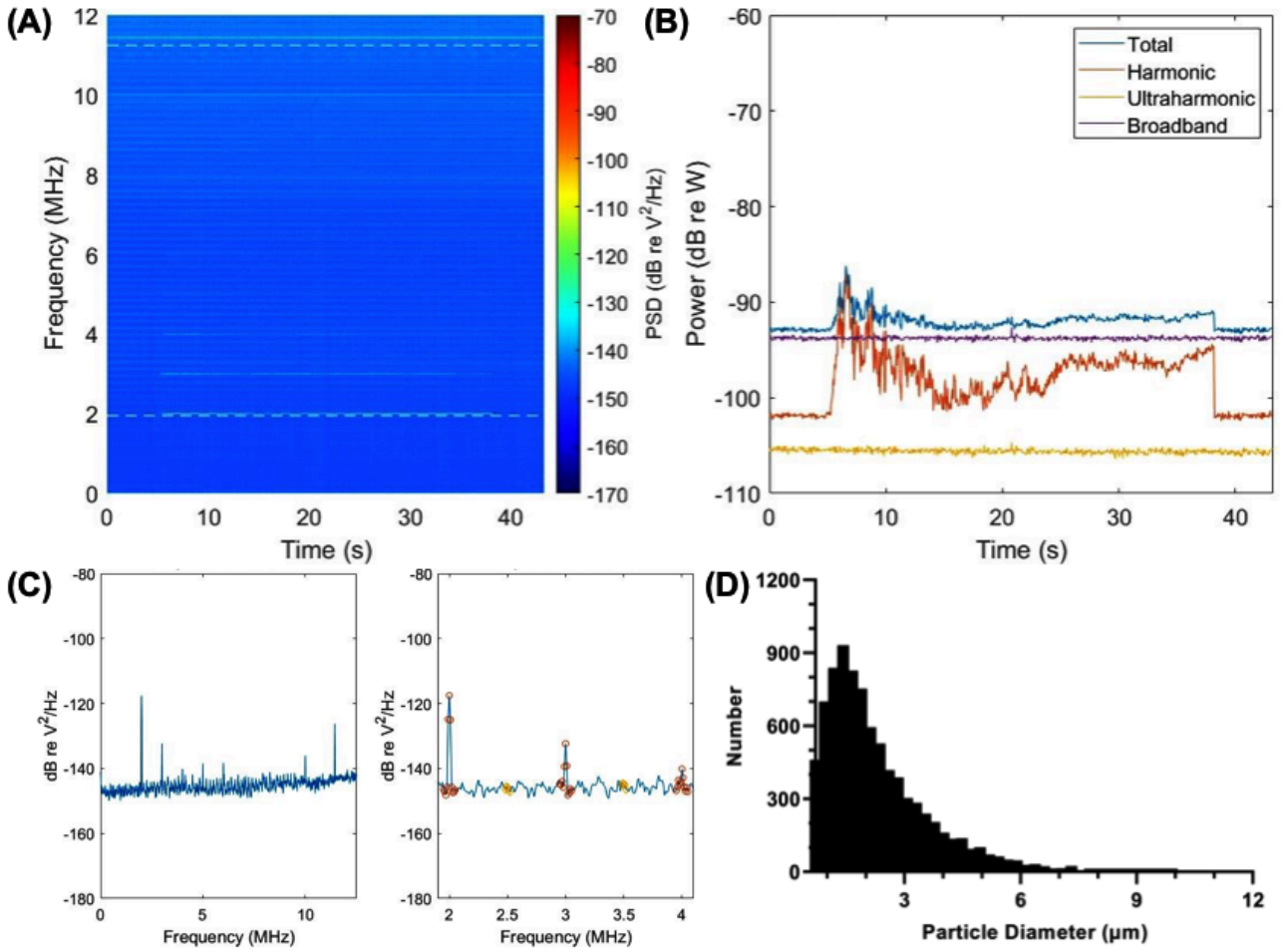


Figure 3.5. Example spectrum histories over a 30-second exposure of a suspension of His-GFP microbubbles at 1 x 10^7 MBs/mL. *(A) Full spectra and (B) total, harmonic, ultraharmonic and broadband signal powers, all as a function of time. (C) Frequency domain PCD trace corresponding to the onset of the ultrasound signal (left), zoomed in (right), showing harmonics (orange) and ultraharmonics (yellow). Drive conditions: 1.0 MHz, 0.2 MPa PNP, continuous wave, 30 seconds total duration. (D) Microbubble size distribution histogram (number of events = 8535), with a mean diameter of 2.31 µm and a concentration of 4 x 10^8 MBs/mL, for centrifuged microbubbles as used in the experiment in Section 3.3.1.*

In the SAT2, as shown in *Figure 3.4*, an increase in His-GFP functionalised NTA(Ni) lipid can be observed in the selection of fields of view. However, only in the case of a 30-second ultrasound exposure does this His-GFP functionalised NTA(Ni) lipid appear to be deposited on or within the cell membrane. For 15-second ultrasound exposures, His-GFP functionalised NTA(Ni) microbubbles seem to still be present, without much transfer of material to and/or fusion with the plasma membrane. The small amounts of transferred and/or fused His-GFP functionalised NTA(Ni) lipid in the control samples indicate limited spontaneous transfer, e.g., without the aid of ultrasound. All samples were washed twice after treatment - either with or without ultrasound, allowing for the elimination of non-attached microbubbles.

Looking at the example acoustic traces in *Figure 3.5*, corresponding to the confocal microscopy data in *Figure 3.4*, a trend can be observed in the frequency domain PCD trace in (*C*). Interestingly, when looking at the signal powers in (*B*) to those obtained in other set-ups, e.g., *Figures 3.7* and *3.10*, the total power recorded is lower, and there is little to no broadband noise. A possible reason for this is that the bubble concentration was low, at 1 x 10^7 MBs/mL, due to the larger total volume of ~10 mL, which leads to a lower probability of bubble coalescence and subsequent broadband noise. Please note that various interferences may have caused the high background noise levels observed in *Figure 3.5*, but most likely a defective cable.

3.3.2 The qualitative observation of functionalised microbubble material transfer in the Mini-SAT

Preliminary experiments were performed in the Mini-SAT, with A549 cells grown on glass slides. Apart from the different geometry, with the ultrasound source positioned in line with the glass slide, the centre frequency of both the Mini-SAT and SAT3 systems is 0.5 MHz, compared with 1 MHz in the SAT2. In both the SAT2 and SAT3, a 3D volume of microbubbles is exposed to the incident ultrasound wave, but in the Mini-SAT, the microbubbles form a plane/sheet against the glass slide. The lipid transfer/microbubble fusion results in the Mini-SAT are shown in *Figures 3.6* and *3.7*.

In *Figure 3.6*, His-GFP functionalised NTA(Ni) lipid transfer to and/or His-GFP functionalised NTA(Ni) microbubble fusion with the cell membrane can be observed following ultrasound exposure, as in the SAT2 (0.5 MHz centre frequency, 200 kPa PNP, continuous wave, 60 seconds total exposure duration).

As shown in *Figure 3.7*, the corresponding ultrasound analysis shows distinct broadband and ultraharmonic signals, which subside over the course of the 60-second exposure. This decrease in signal power might be caused by the destruction of microbubbles in the acoustic focus. Compared to experiments in the SAT3, as discussed below, the quick decline in signal powers may be due to a lower microbubble concentration in the focal volume, as discussed in *Section 3.4*, in the mini-SAT compared to the SAT2. The limited broadband component may also be caused by different PCDs, with different sensitivities, or suboptimal alignment, for which a complete system calibration is required.

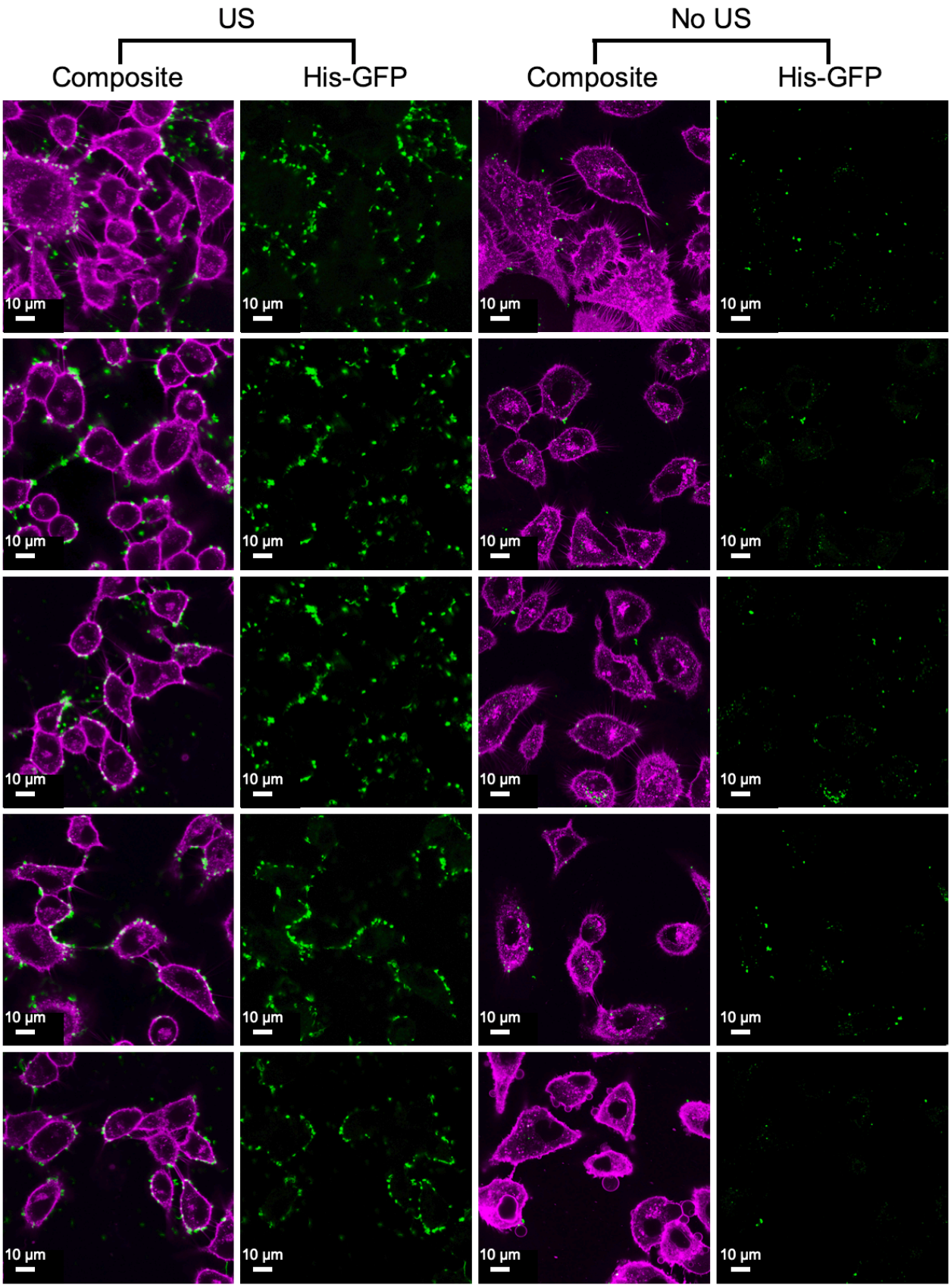


Figure 3.6. 'Membrane tagging' observed in the Mini-SAT. *Confocal microscopy images of A549 cells stained with Cell Mask Deep Red (magenta) and His-GFP NTA(Ni) lipids and microbubbles (green) 60s of ultrasound exposure (N = 2) (0.5 MHz, 200 kPa PNP, CW) in the Mini-SAT on the left, and corresponding no ultrasound controls (N = 2) on the right. A distinct qualitative difference in the amount and pattern of transfer/fusion of His-GFP NTA(Ni) lipid to the cell membranes can be observed.*

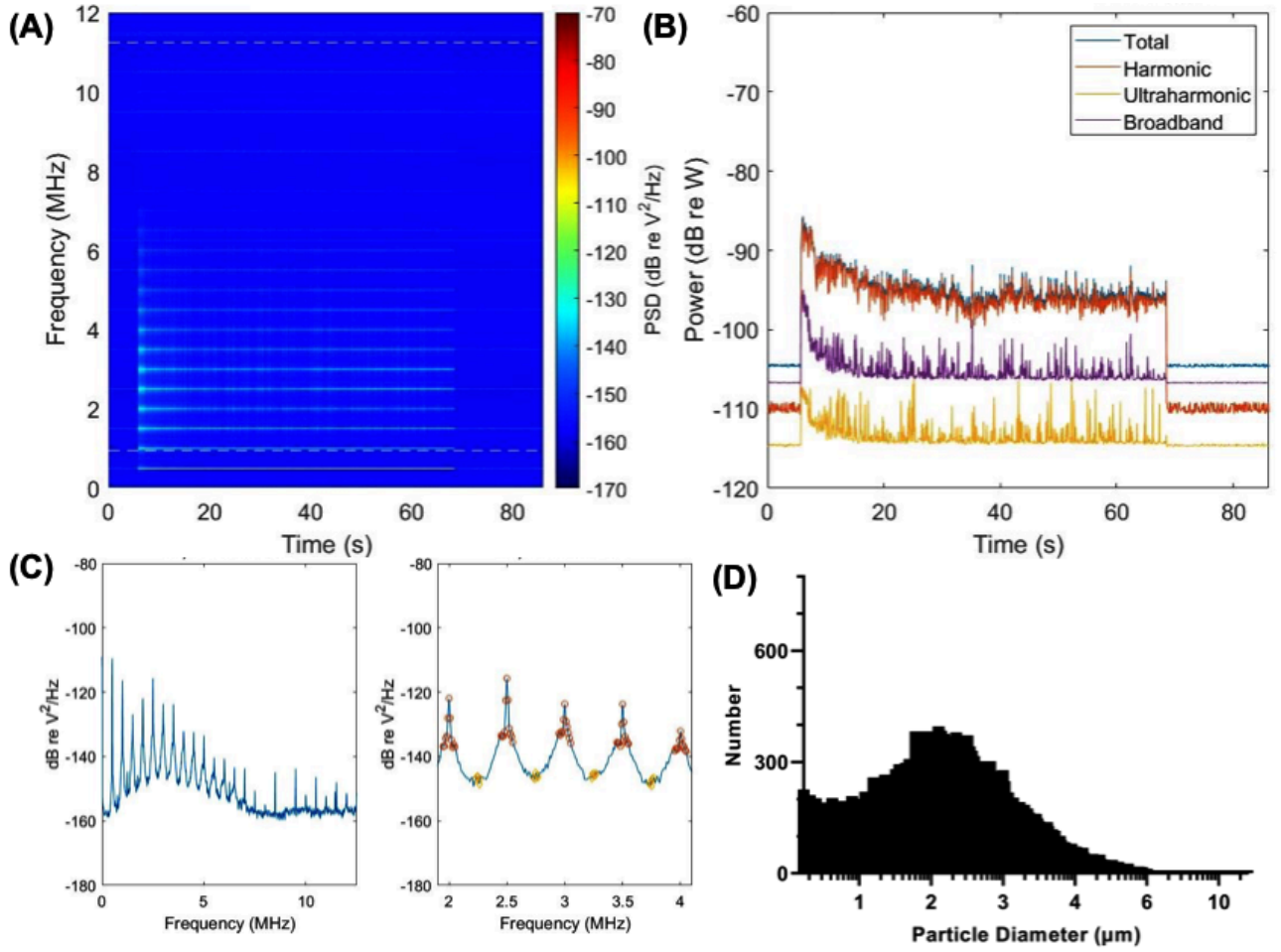


Figure 3.7. Example spectrum histories over a 60-second exposure of a suspension of His-GFP microbubbles injected underneath the glass slide in the Mini-SAT. *(A) Full spectra and (B) total, harmonic, ultraharmonic and broadband signal powers, all as a function of time. (C) Frequency domain PCD trace corresponding to the onset of the ultrasound signal (left), zoomed in (right), showing harmonics (orange) and ultraharmonics (yellow). Drive conditions: 0.5 MHz, 0.2 MPa peak negative pressure, continuous wave, 60 seconds total exposure. (D) Microbubble size distribution histogram (number of events = 28286), with a mean diameter of 2.35 µm and a concentration of 2.8 x 10⁹ MBs/mL, for centrifuged microbubbles as used in the experiment in Section 3.3.2.*

Membrane blebbing, an indicator of cellular stress, was observed in *Figure 3.8* in these and other experiments described in later *Chapters*. Membrane blebbing in response to ultrasound was described as a potential recovery mechanism in site-specific sonoporation by Leow *et al*. (2015), albeit at different, single-shot ultrasound parameters (1 MHz centre frequency, 0.45 MPa PNP, 30 μs pulse duration) and with a different cell line (human breast carcinoma cells CCL-1505). Leow *et al*. looked at the effect of a single microbubble.

They showed that blebbing would occur both at the sonoporation site and elsewhere along the cell membrane after resealing of the pore. Interestingly, the size of the bleb was correlated with the diameter of

the microbubble that caused the pore. In 99% of the cases, blebbing occurred in response to sonoporation due to cavitating microbubbles with a minimum diameter of 1.5 μm. Leow *et al*. concluded that the bleb served to accommodate the increase in cytoplasmic Ca^{2+} brought on by sonoporation (Zhou *et al*., 2008; Kumon *et al*., 2009; Fan *et al*., 2012). However, it should be noted that cellular blebbing can be induced in response to various mechanical and chemical stimuli (Khajah & Luqmani, 2016). Therefore, more investigation is required into the effect of ultrasound and, specifically, His-GFP functionalised NTA(Ni) microbubbles on this observed bleb formation, which falls outside the scope of this *Thesis*.

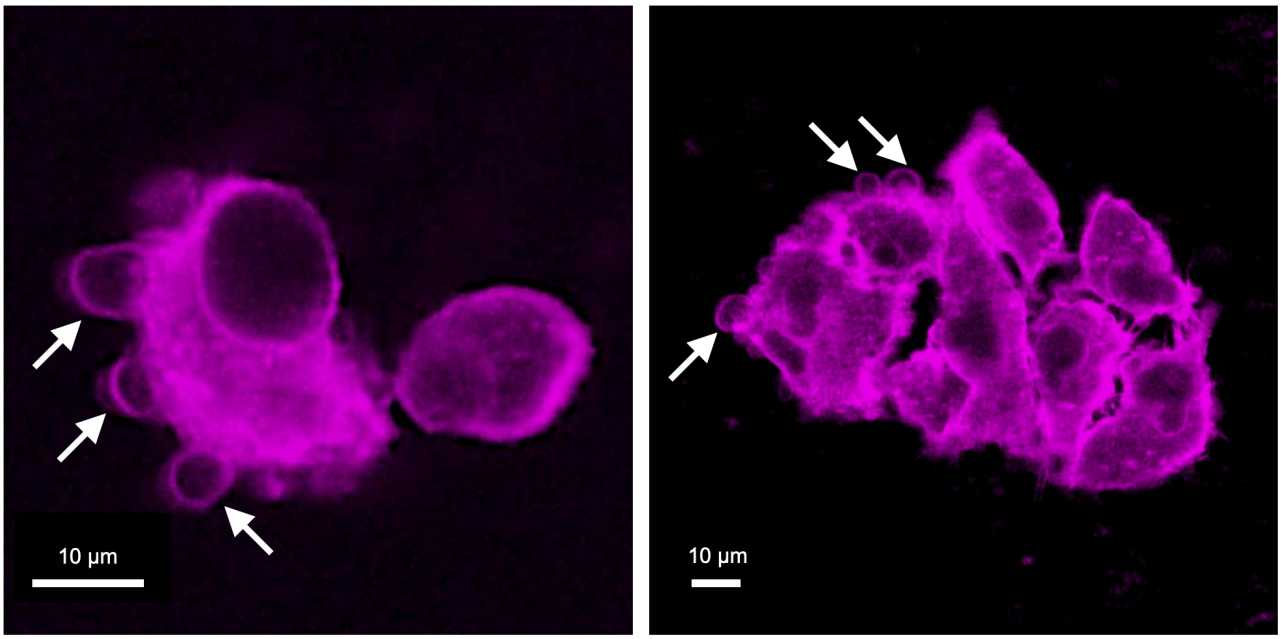


Figure 3.8. Cell blebbing in response to ultrasound exposure. *Example confocal microscopy images of A549 cells stained with Cell Mask Deep Red (magenta) after 60 seconds of ultrasound exposure (0.5 MHz, 200 kPa PNP, CW) with His-GFP NTA(Ni) microbubbles in the Mini-SAT, which show observations of membrane blebbing as indicated by the white arrows.*

3.3.3 The qualitative observation of functionalised microbubble material transfer in the SAT3

In both the SAT2 and Mini-SAT, the microbubbles were situated below the cell layer. Thus, interaction may occur between the microbubbles and cells unaided by ultrasound, simply due to the buoyancy of the bubbles. In the SAT3, the cell layer was situated below the microbubbles, reducing the likelihood of the interaction between microbubbles and the cell layer in the absence of ultrasound. *Figures 3.9* and *3.10* show the lipid transfer/microbubble fusion and acoustic emissions observed in the SAT3, respectively.

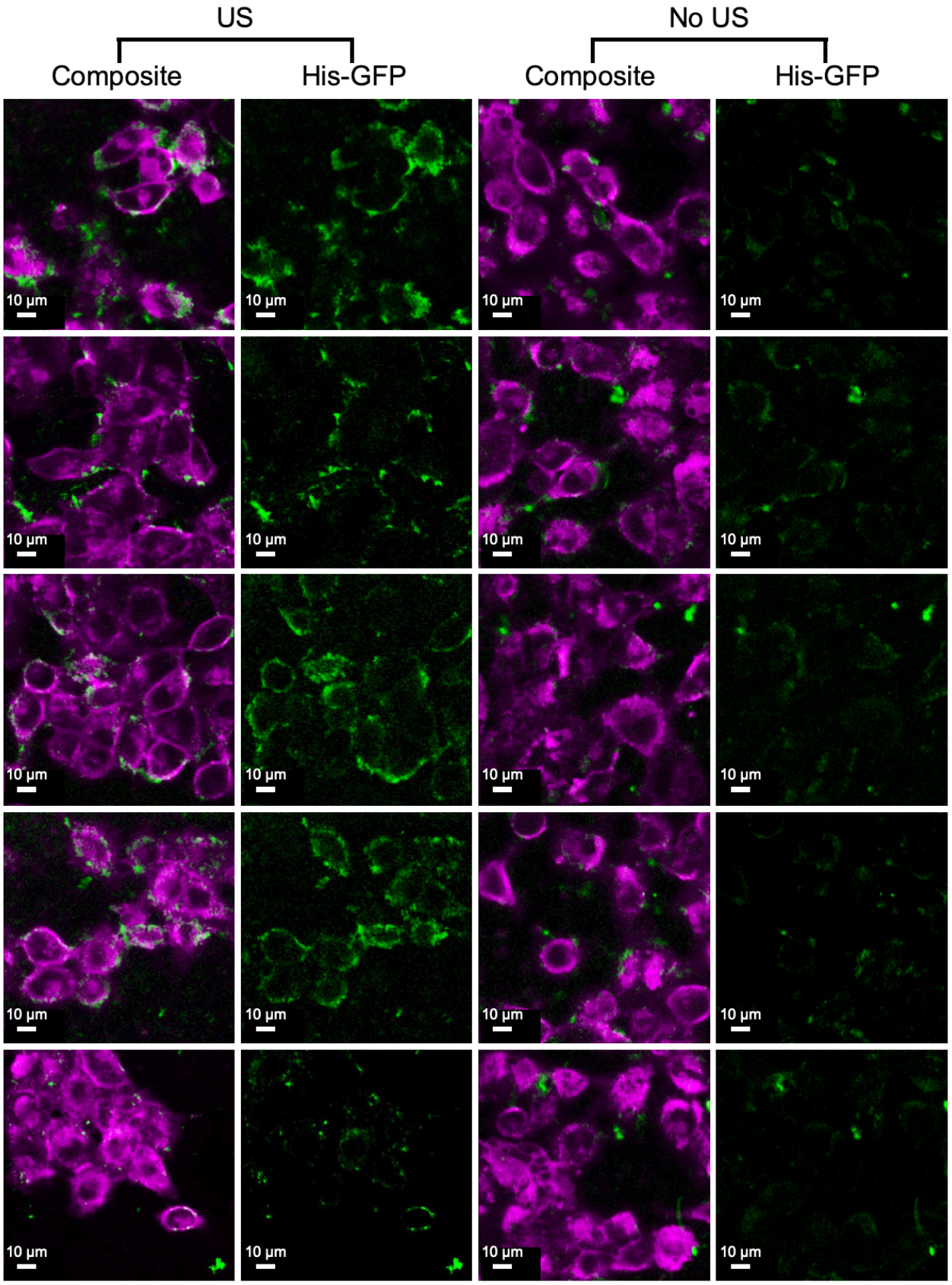


Figure 3.9. 'Membrane tagging' observed in the SAT3. *Confocal microscopy images of A549 cells stained with Cell Mask Deep Red (magenta) and His-GFP NTA(Ni) lipids and microbubbles (green) 60s of ultrasound exposure (N = 3) (0.5 MHz, 200 kPa PNP, CW) in the SAT3 on the left, and corresponding no ultrasound controls (N = 3) on the right. A distinct qualitative difference in the amount and pattern of transfer/fusion of His-GFP NTA(Ni) lipid to the cell membranes can be observed.*

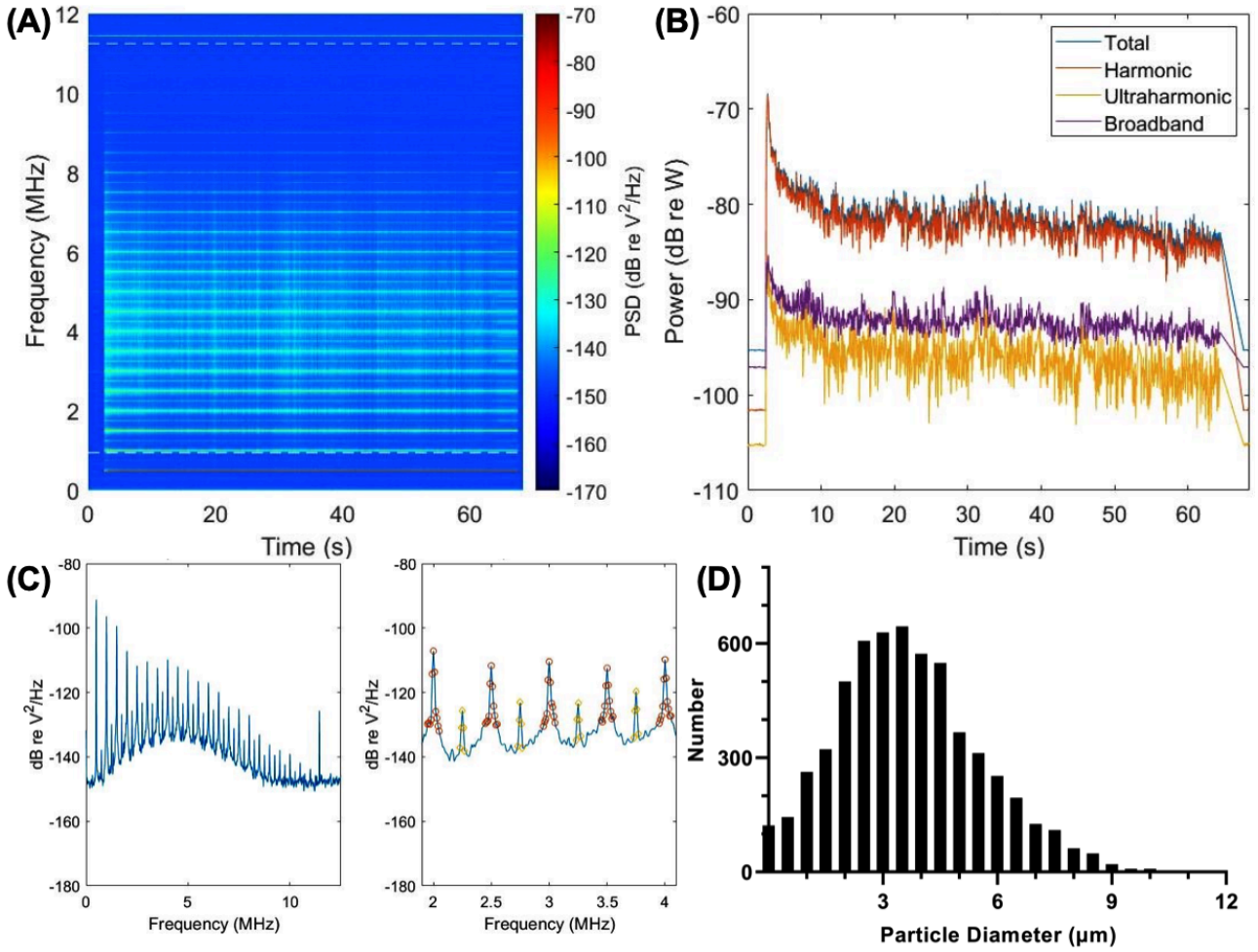


Figure 3.10. Example spectrum histories over a 60-second exposure of a suspension of His-GFP microbubbles at 1 x 10^8 MBs/mL in the SAT3. *(A) Full spectra and (B) total, harmonic, ultraharmonic and broadband signal powers, all as a function of time. (C) Frequency domain PCD trace corresponding to the onset of the ultrasound signal (left), zoomed in (right), showing harmonics (orange) and ultraharmonics (yellow). Drive conditions: 0.5 MHz, 0.2 MPa peak negative pressure, continuous wave, 60 seconds total exposure. (D) Microbubble size distribution histogram (number of events = 5860), with a mean diameter of 3.7 μm and a concentration of 2 x 10^7 MBs/mL, for centrifuged microbubbles as used in the experiment in Section 3.3.3.*

Figure 3.9 shows that His-GFP functionalised NTA(Ni) lipid transfer to and/or microbubble fusion with the cell membrane did still occur following ultrasound exposure, albeit in a smoother, less punctate fashion. This change in the pattern of the His-GFP functionalised NTA(Ni) lipid might be due to the geometry of the set-up or could potentially be an optical effect, as the confocal images were taken through the porous transwell membrane. Interestingly, for the no ultrasound controls in this set-up, some lipid transfer and/or microbubble fusion was observed, albeit to a lesser degree than in the ultrasound-treated samples, in contrast to the no ultrasound controls in either the SAT2 or Mini-SAT, which show little to no spontaneous transfer/fusion.

These results align with previous work, as demonstrated by Carugo *et al*. (2017), which showed limited DiO lipid transfer/microbubble fusion for both DSPC : PEG40S and DSPC microbubbles in the absence of ultrasound.

The example spectrum histories in *Figure 3.10*, corresponding to the confocal microscopy data in *Figure 3.9*, show a large broadband component (*A*). This elevated and prolonged broadband might have contributed to the more diffuse than punctate His-GFP functionalised NTA(Ni) lipid deposition on the cell membranes in *Figure 3.9*. However, no comparison can be made between microbubble behaviour in response to ultrasound in the different set-ups without a complete system calibration.

Lastly, examples of the response of various microbubbles - His-AF488 functionalised microbubbles made with fabrication methods 1 and 2 as specified in the *Appendix*, *Section A.1*, and SonoVue - to a range of ultrasound driving conditions are visualised in *Figures 3.11* to *3.13*.

3.3.4 Comparison of His-AF488 and SonoVue microbubble behaviour under ultrasound exposure

To understand the properties of the His-AF488 functionalised NTA(Ni) microbubbles, their behaviour was compared to that of clinically used SonoVue microbubbles, as well as DPBS controls, with the following ultrasound driving parameters in the SAT3: 0.5 MHz centre frequency, 200, 400 and 700 kPa peak negative pressure, 1% duty cycle (200 ms pulse repetition period. 2.0 ms pulse duration), for a 50-second total exposure.

Figure 3.11 shows the PCD responses as a function of time. In the left panels, full spectra are shown over a 50-second exposure time, during which the source emitted 2.0 ms pulses every 0.20 seconds. Corresponding total, harmonic and broadband powers are shown in the right panels. All data were collected at a final concentration of ~2 x 10^7 MBs/mL. The signal recordings began ~5 seconds before the start of the ultrasound pulse. For both His-AF488 functionalised and SonoVue microbubbles, at the lowest incident pressure, the PCD response shows the lowest total signal power with a minimal contribution from the broadband signal. An increase from 200 kPa to 400 kPa results in increased signal powers and a corresponding increase in broadband signal.

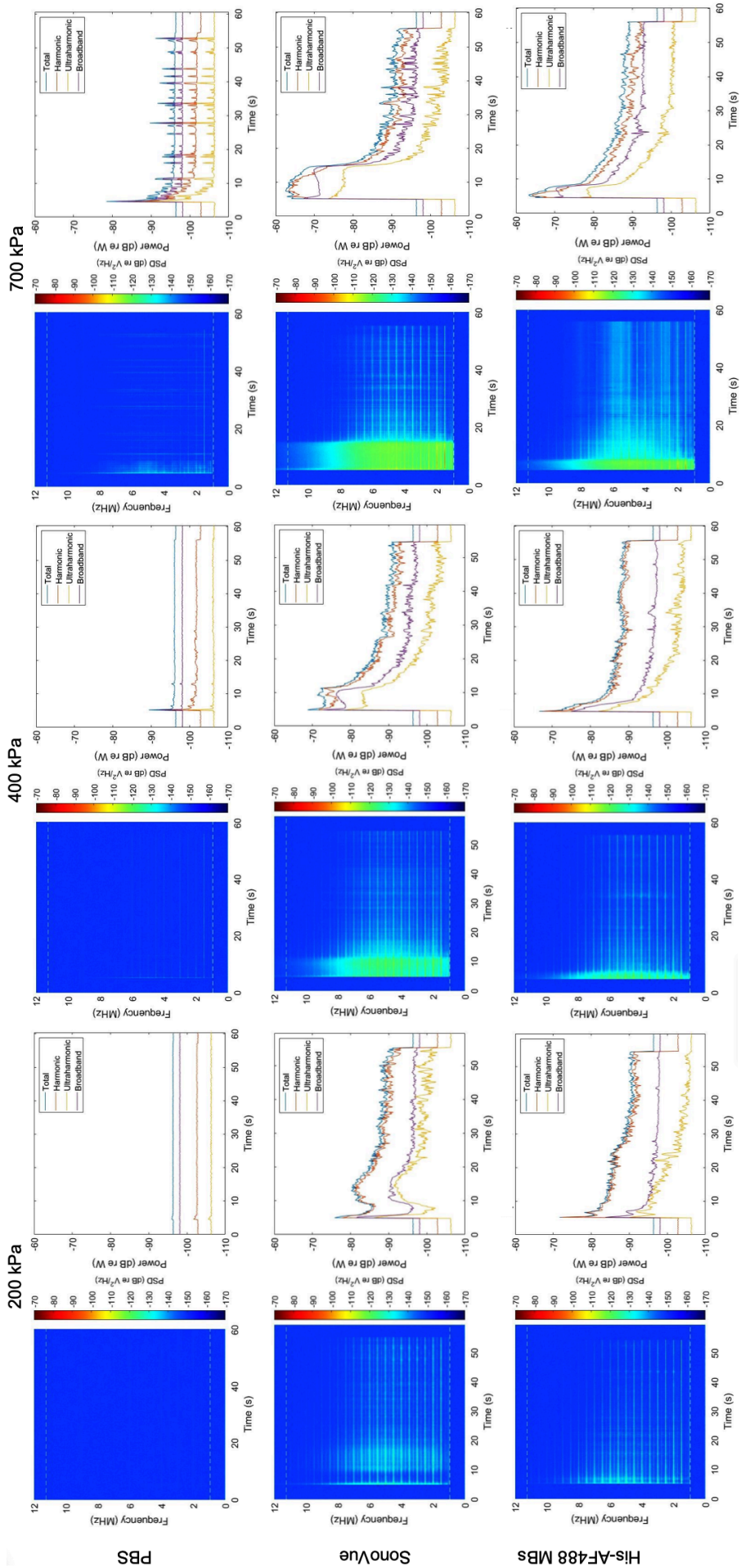


Figure 3.11. Example spectrum histories over a 50 second exposure of suspension of His-GFP microbubbles, SonoVue microbubbles at 2 x 10⁷ MBs/mL and DPBS controls. *Full spectra and total, harmonic, ultraharmonic and broadband signal powers, all as a function of time, are shown. US conditions were 0.5 MHz, 200, 400 and 700 kPa peak negative pressure, 1%, 50-second total exposure duration.*

At the highest pressure, the time domain waveform amplitude has grown nonlinearly relative to the lower pressures due to elevated broadband noise visible in the spectrum. This noise is commonly considered to be a result of inertial cavitation and, in this example, corresponds to the destruction of microbubbles. The initial spike corresponds to the destruction of the largest bubbles in the suspension (as His-AF488 microbubbles and SonoVue are polydisperse) and is a common observation in cavitation experiments with shelled bubbles. After a few seconds, the broadband response rapidly diminished, likely due to bubble destruction, and the signal became predominantly comprised of harmonics. This suggests that the freed gas and remaining microbubbles mainly vibrate stably and non-inertially. At t equals ~50 seconds, the broadband component has fallen close to the level of the original background noise.

Interestingly, even though maximum signal powers reached are comparable between His-AF488 functionalised and SonoVue microbubbles, this high signal power plateau is maintained for longer for the SonoVue microbubbles, indicating a reduced rate of destruction of these microbubbles compared to the His-AF488 microbubbles. Exposure tests like this give a good understanding of the timescales during which different bubble effects may be acting upon the cells in the chamber and how the experiments with His-AF488 functionalised microbubbles might compare to experiments with commercial microbubbles, such as SonoVue.

Figure A.1.5 in Appendix, *Section A.1* shows representative microbubble size distributions histograms of SonoVue microbubbles and His-GFP microbubbles.

3.4 Limitations and Future work

This *Chapter* demonstrates the transfer to and/or microbubble fusion with the cell membranes for His-GFP functionalised NTA(Ni) microbubbles and A549 cells in three different SATs.

Since the SATs were designed for real-time monitoring of acoustic emissions, with biological assays being performed outside of the acoustic experiment, it is impossible to directly relate local microbubble behaviour to local biological effects. However, modifying the SATs would be relatively simple to enable direct optical observation of the sample chamber via a microscope objective. In particular, the mini-SAT was designed with precisely this purpose in mind. The microscope objective could be coupled to a fluorescence

and/or high-speed microscopy system to observe drug uptake and bubble dynamics - an ongoing project in the BUBBL group.

The PCD output as currently presented in terms of voltage indicates: i) the types of cavitation behaviour and their relative proportions, ii) how long these cavitation behaviours persist, iii) whether the observed time-cumulative exposure characteristics are correlated to a particular bioeffect, and iv) whether the relative levels and time-dependent behaviours are consistent with previous experiments in the exposure system. Whilst the receive sensitivity of the PCD can be quantified, additional spatial information is required to characterise the acoustic emissions in terms of absolute energy reliably. This could be achieved by replacing the PCD with an array probe to implement passive acoustic mapping (PAM) (Coviello *et al*., 2015). This would, however, increase the complexity of signal processing and the computational time and power required.

All experiments in this *Chapter* were performed with cells adherent on either a glass or polymer membrane boundary. It is known that the presence of a boundary affects the response of microbubbles (Li *et al*., 2010; Helfield, Leung & Goertz, 2014; Dzaharudin, Ooi & Manasseh, 2017; Ali, Dzaharudin & Alias, 2020). Microbubble behaviour near a surface includes asymmetric oscillations, microstreaming and microjetting at sufficiently high pressures. Moreover, the reradiated sound field from the bubbles can reflect off the surface, causing both a pressure gradient in the medium and secondary radiation forces acting on the microbubbles. The phase difference between the reradiated sound field and the sound field reflected of the boundary, and thus the net direction of the microbubble movement, is determined by the elasticity of said boundary (Stride & Coussios, 2019). For this reason, observations made in conventional *in vitro* set-ups, like those presented in this *Chapter*, may not represent the additional complexities of *in vivo* situations, such as the heterogeneous nature of tissues, which does not allow for predictions of microbubble behaviour.

Lastly, the limiting factors of the experiments presented in this *Chapter* are i) the low *N* number (*N* equals 2 or 3) for each condition due to the labour-intensive nature of these experiments and procedure times, and ii) the lack of quantitative data as the results as presented here are all qualitative. To increase the *N* number and obtain quantitative data and assess the lipid transfer to and/or microbubble fusion with the cell membranes in a potentially more clinically relevant setting, flow cytometry is used in *Chapter 4* for both A549 and Jurkat T cells in suspension. This rapid quantitative analysis allows, furthermore, for an

exploration of the ultrasound parameter space to optimise the ultrasound conditions to achieve the 'membrane tagging' in suspension.

3.5 Conclusion

Previous work, both in the BUBBL group and the wider community, has focussed on optimising microbubbles for intracellular drug delivery (Aron *et al*., 2019; Horsley *et al*., 2019; Stride, 2019). For example, Aron *et al*. *(*2019) showed a ~5-fold increase in sonoporation for DBPC : PEG40S microbubbles containing 16:0 lyso-PC compared to control DBPC : PEG40S microbubbles containing 16:0 PC. *Appendix*, *Section A.2*, equally shows an increased internalisation of 18:1 NBD Lyso PE - a fluorescent equivalent - with ultrasound. However, to modulate the immune response, there is a need for a microbubble that does not deliver lipids or other cargo intracellularly but 'tags' the cell membrane with a relevant protein, as immune signalling starts at the cell membrane rather than intracellularly. The results from this *Chapter* make the novel His-GFP NTA(Ni) functionalised microbubbles a promising candidate for this purpose.

In conclusion, this *Chapter* shows the transfer of material from the microbubbles to the cell membrane for His-GFP NTA(Ni) microbubbles and A549 cells. As shown in the *Results* section, there is a clear indication of microbubble material transfer of His-GFP NTA(Ni) functionalised microbubbles to A549 cell membranes, as seen in the confocal images. These results lay the groundwork for the quantitative analysis conducted in *Chapter 4*, as this phenomenon referred to as 'membrane tagging' can be observed across three different set-ups and is, therefore, likely independent of ultrasound equipment and specific set-up geometries.

Chapter 4 - Quantitative Assessment of His-Functionalised Microbubble-Cell Membrane Interactions

4.1 Introduction

Following on from the pilot experiments in *Chapter 3*, where His-GFP functionalised lipid transfer and/or microbubble fusion with A549 cell membranes was observed qualitatively using confocal microscopy, this *Chapter* aimed to investigate this process quantitatively using flow cytometry.

Flow cytometry is a technique for rapidly analysing the optical characteristics of single particles or cells in suspension, e.g., the uptake of fluorescent material. It allows for the analysis of thousands of events (10,000 cells or microbubbles in the experiments in this *Chapter*) on timescales on the order of minutes, as compared to the approximately 20 minutes per sample achieved in *Chapter 3* using confocal microscopy. It thus provides a means of determining the quantities of cells successfully tagged and exploring the ultrasound parameter space to optimise the process. In addition to the adherent A549 cells used in *Chapter 3*, in this *Chapter*, A549 cells and Jurkat T cells, used as a model immune cell and a preliminary assessment of increasing the potency of immune cells by tagging the membrane with relevant proteins, were used in suspension.

4.2 Methods

4.2.1 Microbubbles

The microbubble fabrication protocol is described in detail in *Chapter 2*, *Section 2.2.1*. For this *Chapter*, following centrifugation, microbubbles were loaded with His_6-AF488 (4 μg/mL, Cambridge Research Biochemicals Ltd, UK, 1356.4 Da), apart from the control microbubbles in *Section 4.3.2.1*, which were simply DSPC : PEG40S : 18:0 DGS-NTA(Ni), without His_6-AF488. Microbubbles were characterised using the Beckman Coulter Multisizer as described in *Section 2.2.2.2* in *Chapter 2*. Final microbubble concentrations were achieved of (0.2, 0.6, 1) x 10^8 microbubbles per mL, as specified in the *Results* section. The 1 x 10^8 microbubbles per mL concentration corresponds to the conditions used in the same ultrasound set-up (SAT3) in *Chapter 3*, *Section 3.3.3*, and was subsequently lowered to assess the effect of microbubble concentration on the 'membrane tagging' process. For the experiment described in *Section 4.3.2.1*, control

microbubbles were fabricated, according to the same protocol, with DSPC : PEG40S : DGS-NTA(Ni) but without incubation of His-AF488.

4.2.2 Cell culture

In this *Chapter*, two cell lines were used: 1) immortalised human alveolar adenocarcinoma cells (A549 cells), as elaborated upon in *Chapter 3*, and 2) immortalised human T lymphocyte cells (Jurkat cells). A549 cells represent solid tumours, while Jurkat cells represent either suspension tumours or suspension immune cells. The protocol for the A549 cells can be found in *Chapter 3*. For Jurkat cells, the growth medium consisted of Roswell Park Memorial Institute (RPMI) 1640 medium supplemented with 10% fetal bovine serum (FBS). Cells were grown in suspension in a temperature- and CO_2-controlled incubator at 37°C and 5% CO_2, upright in T-75 culture flasks. Cells were passaged 1 : 4 every two days. Cell concentration and viability were measured using trypan blue and a Countess® Automated Cell Counter (Invitrogen, UK).

Both A549 and Jurkat cells were made up to 2 x 10^6 per mL in T-25 cells culture flasks to achieve 4 x 10^5 cells per SAT3 transwell during experiments. A549 cells were made up to a concentration of 2.5 * 10^5 per mL in a total volume of 500 μL for the preliminary experiment in the pilot experiment set-up, as elaborated upon below. A549 cells were kept on ice to avoid adherence to the culture flask, whereas Jurkat cells were kept in a temperature- and CO_2-controlled incubator at 37°C and 5% CO_2. Unless stated otherwise, all cell culture materials were purchased from ThermoFisher Scientific (UK).

4.2.3 Ultrasound set-up

4.2.3.1 SAT3

For the majority of the experiments, the SAT3 set-up was used as described in *Chapter 3*, *Section 3.2.3.3*. A range of pressures - 0, 50, 100, 140, 150 and 200 kPa - and a range of duty cycles - 0, 1, 5, 10, 20, 40, 80, 100 % - were investigated with varying microbubble concentrations - (0.2, 0.6, 1) x 10^8 microbubbles per mL, to optimise His-AF488 lipid transfer and/or microbubble fusion to both cell types. The two lower microbubble concentrations, compared to the 1 x 10^8 microbubbles/mL in *Chapter 3*, were chosen to both

minimise the effect on the morphology of the cells, as elaborated upon in the *Results*, and resemble *in vivo* conditions better. After exposure, samples were split out two ways for flow cytometry analysis corresponding to t equals 0 and 35 minutes post exposure (70 μL in 430 μL of DPBS). The experimental protocol and data collection and analysis were performed as described in *Chapter 3*, *Sections 3.2.3.4* and *3.2.3.5*.

4.2.3.2 Pilot Experiment Set-Up

For the experiment corresponding to the results in *Figures* 4.*3* to *4.6*, a preliminary experiment was conducted in a variation of the experimental set-up described in Smith & Coussios (2020), which was designed specifically for use with suspended cells. Eppendorf tubes (Eppendorf LoBind microcentrifuge tubes, 2 mL total volume; Sigma-Aldrich, Germany) containing samples of 500 μL of A549 cells at a concentration of 2.5 x 10^5 per mL in DPBS were mixed with His-AF488 functionalised microbubbles at a concentration of 1 x 10^8 per mL, corresponding to ~400 microbubbles per cell.

These Eppendorf tubes were placed at the focus of a 0.5-MHz therapeutic transducer (H-107 D SN12; Sonic Concepts, USA) with an effective diameter of 64 mm and a focal length of 62.6 mm, and, subsequently, placed in a large water tank of degassed, filtered water. One L7-4 linear array (L7-4, Verasonics, USA) was used to simultaneously and passively capture acoustic emissions from cavitation. The driving conditions were 0.5 MHz centre frequency, 200 kPa peak negative pressure, continuous wave, for a total exposure duration of 60 seconds. After this 60-second exposure, the Eppendorf was carefully removed, and the sample was split out three ways for flow cytometry analysis immediately or 35 minutes post exposure (200 μL each in 2 mL Eppendorf tube, made up to 500 μL with DPBS), as well as for confocal microscopy analysis (100 μL in an 8 well μ-Slide (Ibidi, Germany)). Due to the preliminary nature of this experiment, the ultrasound data could not be acquired.

4.2.4 Confocal microscopy

As in *Chapter 3*, further analysis of the bioeffects associated with the microbubble-cell interactions and microbubble acoustic activity in the pilot experiment set-up with A549 cells was performed using confocal fluorescence microscopy (LSM 780, Carl Zeiss AG, Germany) at 20x (Plan-Apochromat 20x/0.8 M27).

His-AF488 was excited by the 488 nm laser, and the emitted signal was picked up between 493 and 598 nm. Photomultiplier tube (PMT) reflections were simultaneously obtained to resemble brightfield images to locate the cells. Due to the cells being in suspension, the cells were not stained with Cell Mask Deep Red as in *Chapter 3*.

4.2.5 Flow cytometry

Flow cytometry (Beckman Coulter CytoFLEX, USA) was employed to quantify the degree of lipid transfer, microbubble fusion and/or internalisation, and the viability of the cells after treatment.

Each cell was analysed for visible light scatter and two fluorescence parameters, specifically the presence of His-AF488 (ex/em: 448/519) and Propidium Iodide (PI) (ex/em: 535/615). PI (P4170, Sigma-Aldrich, 5 μg/mL) was used as a live/dead stain and indicator of permeabilisation. PI is typically cell-impermeant and thus widely used as a model drug, as its uptake indicates membrane permeabilisation (Riccardi & Nicoletti, 2006). The visible light scatter was measured in two different directions: 1) the forward scatter (FCS), which is indicative of the size of the particle, and 2) the side scatter (SCC), which is indicative of the internal complexity or granularity of the particle (McKinnon, 2018). These parameters provide an insight into the effect of the microbubble and ultrasound treatments on cell morphology.

All biological samples were analysed both at 5 and 35 minutes after ultrasound exposure, after being split out two ways for flow cytometry analysis (70 μL in 430 μL of DPBS). This extra 5-minute interval from t equals 0 and 35 minutes allowed for incubating the cells with 5 μL of 5 μg/mL PI for 5 minutes. These two time points were chosen to observe any direct effects of the ultrasound treatment and any effects occurring on the order of minutes, e.g., the potential resealing of membrane pores due to sonoporation or death (Helfield *et al*., 2016). Samples were kept on ice immediately after treatment to slow down degradation and enzymatic activity.

For each sample, 10,000 events (microbubbles or cells) were analysed, and appropriate controls (live cells, heated and thus dead/dying cells, and microbubbles) were carried out prior to commencing the experiment. The FITC, corresponding to His-AF488, and ECD, corresponding to PI, channel gatings, as shown in the *Results* section, were chosen based on the live cell control sample, which was negative for both

His-AF488 and PI. 'Membrane tagging' was identified to have occurred for those cells that were positive for His-AF488 and negative for PI at t = 5 minutes, as the latter indicates an intact cell membrane. However, it should be noted that flow cytometry, as used in this *Chapter,* gives a yes/no answer as to whether a fluorophore is present. So, while PI is a good indicator of permeabilisation of the cells, the exact location of said fluorophore cannot be established with certainty. Given the low numbers and high variability, the mean fluorescence intensity, an indicator of how many fluorescent molecules are present, of the cells positive for AF488 but negative for PI were not analysed.

4.3 Results and Discussion

4.3.1 Overview

The results below are summarised first per cell type: A549 and Jurkat cells. For all experiments, the figures show the i) cell population statistics, ii) microbubble material transfer, iii) the corresponding viability data, and iv) the corresponding ultrasound analysis and microbubble population statistics. The cell population statistics are important as an introduction of His-AF488 microbubbles, even in the absence of ultrasound exposure, causes a shift from population 1, which is predominant in the live cells control sample, towards a second smaller population, population 2, in the forward scatter versus side scatter plots, indicating a change in cell morphology. An example of this for both A549 and Jurkat cells is shown in *Figure 4.1*. The forward scatter versus side scatter plots for three repeats of His-AF488 microbubbles are shown in *Figure 4.2*.

The microbubble material transfer is assessed based on the fraction of cells that are positive for His-AF488 and negative for PI in both populations. In population 1, which shows limited to no uptake of PI, it is hypothesised that the cells in that fraction are surface-tagged. In population 2, which shows a large uptake of PI that seems to decrease over time, cells are potentially both surface-tagged and have His-AF488 internalised through sonoporation. Flow cytometry as used in this *Chapter*, however, does not elucidate the way in which His-AF488 is incorporated in the cells. The PI data provide insight into the effects of ultrasound, such as sonoporation or potential cell death, as prolonged PI-positive cells are likely dead, and a reduction of the PI-positive cell fraction might indicate a cell recovery mechanism.

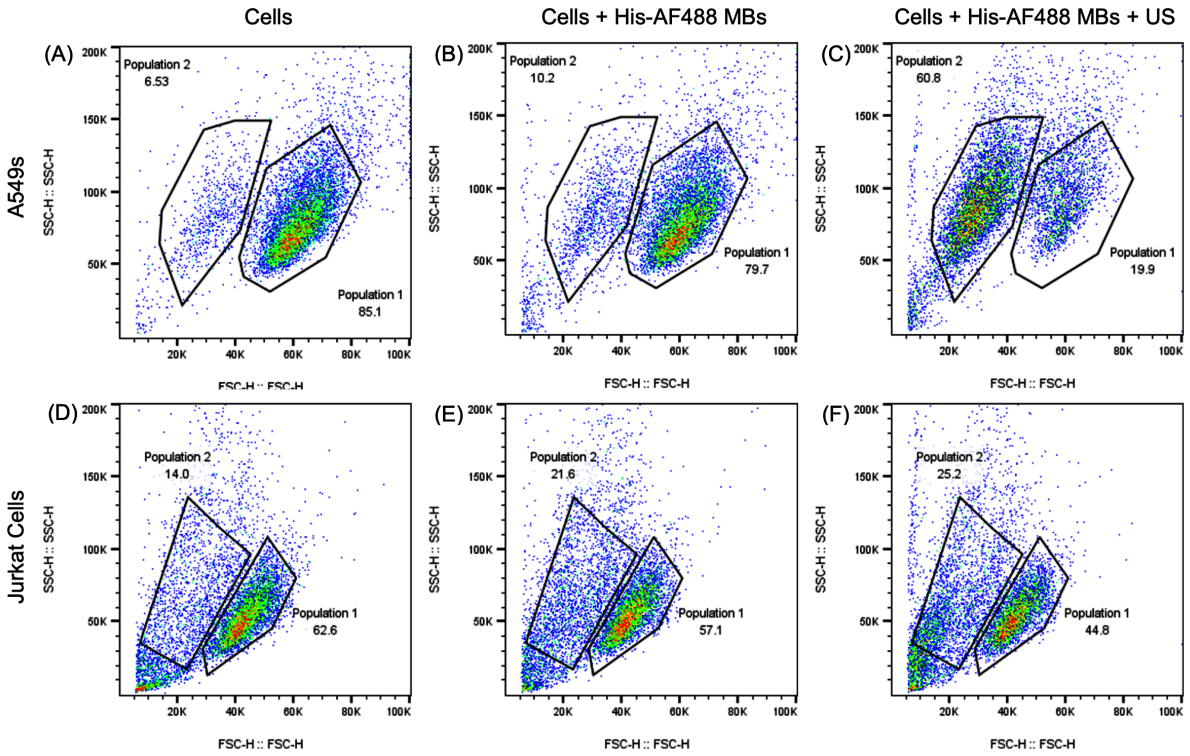


Figure 4.1. Flow cytometry analysis of both A549 (A - C) and Jurkat Cells (D - F) used in the experiments in this Chapter. *It shows the forward vs side scatter plots for healthy control cells (A, D), cells incubated with His-AF488 microbubbles (B, E) and cells incubated with His-AF488 microbubbles exposed to ultrasound (C, F), showing a shift from population 1 to population 2.*

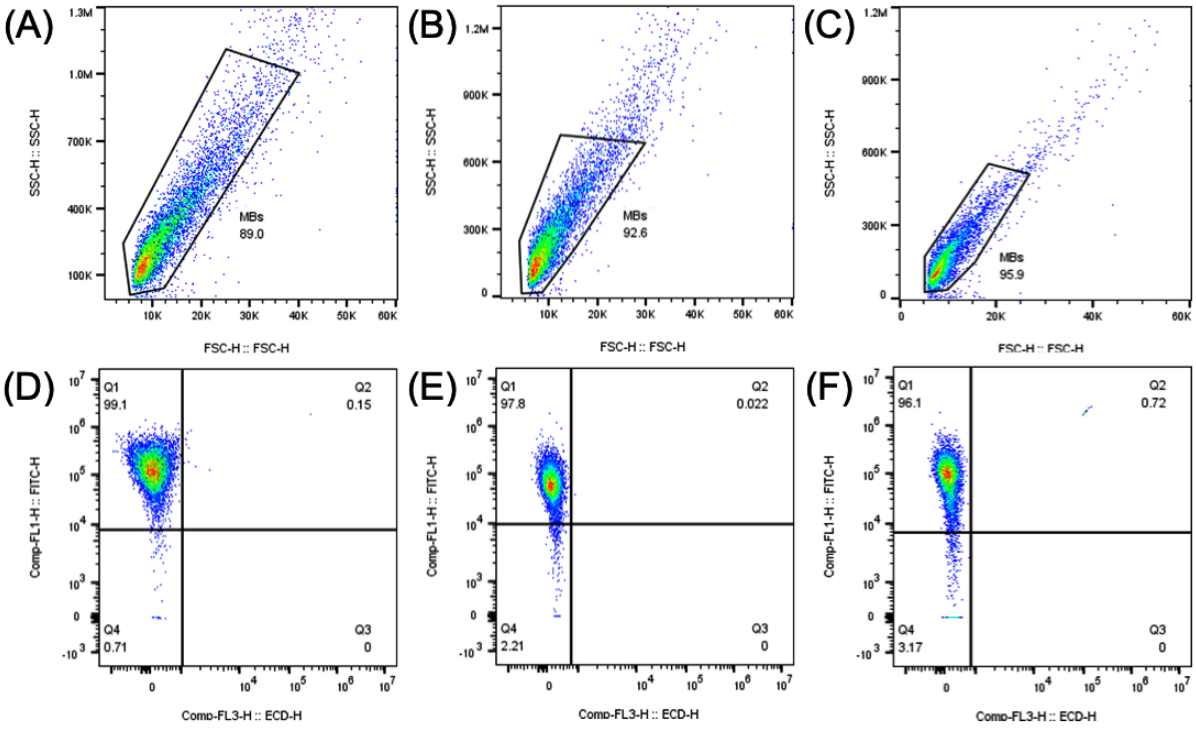


Figure 4.2. Flow cytometry analysis of three examples of His-AF488 microbubbles used in the experiments in this Chapter. *It shows the forward vs side scatter plots (A - C) and corresponding FITC (His-AF488) vs ECD (PI) plots (D - F), compensated for spectral mixing of His-AF488 into the PI channel.*

For the A549 cells, the experiments conducted and corresponding figures are respectively:

1. His-AF488 functionalised microbubbles versus control microbubbles at ultrasound driving conditions of 0.5 MHz centre frequency, 200 kPa PNP and 60s continuous exposure (*Figures 4.3-4.6*, *4.19a*),
2. His-AF488 functionalised microbubbles at varying pressures (0, 100, 150 and 200 kPa PNP) and two microbubble concentrations (6 x 10^7 and 1 x 10^8 MBs/mL) (*Figures 4.7-4.14*, *4.19b*),
3. His-AF488 functionalised microbubbles at varying duty cycles (0, 10, 20, 40, 80 and 100%) (*Figures 4.15-4.18*, *4.19c*).

For the Jurkat cells, the experiments conducted and corresponding figures are respectively:

1. His-AF488 functionalised microbubbles at varying pressures (0, 140 and 200 kPa PNP) and three microbubble concentrations (2 x 10^7, 6 x 10^7 and 1 x 10^8 MBs/mL) (*Figures 4.20-4.23*, *4.36a*),
2. His-AF488 functionalised microbubbles at varying pressures (0, 50, 100, 150 and 200 kPa PNP), and two microbubble concentrations (6 x 10^7 and 1 x 10^8 MBs/mL) (*Figures 4.24-4.31*, *4.36b*),
3. His-AF488 functionalised microbubbles at varying duty cycles (1, 5, 10, 20, 40, 80 and 100%) (*Figures 4.32-4.35*, *4.36c*).

4.3.2 Quantitative observation of functionalised lipid transfer and/or microbubble fusion in A549 cells

4.3.2.1 Pilot study: His-AF488 functionalised microbubbles versus control microbubbles

Samples were analysed quantitatively using flow cytometry and confocal microscopy. In the preliminary A549 and Jurkat cell experiments, two populations could be readily identified in the FSC vs SSC plots: i) a population overlapping with the live control cells, named 'population 1', and ii) a population that appears to grow after exposure to both microbubbles alone and microbubbles with ultrasound treatment, therefore named 'population 2', as shown in *Figure 4.1*. It is important to note that this second population is also present in healthy controls, albeit to minimal levels.

In this pilot experiment, both His-AF488 functionalised NTA(Ni) microbubbles and DSPC : PEG40S : DGS-NTA(Ni) control microbubbles were tested with and without ultrasound. Firstly, the confocal imaging shows two interesting observations: i) the way in which AF488 shows up in cells exposed to

ultrasound is very different than in the absence of ultrasound, and ii) the morphology of the cells in response to ultrasound changes, regardless of bubble type, as seen in the PMT images. The results can be seen in *Figure 4.3*.

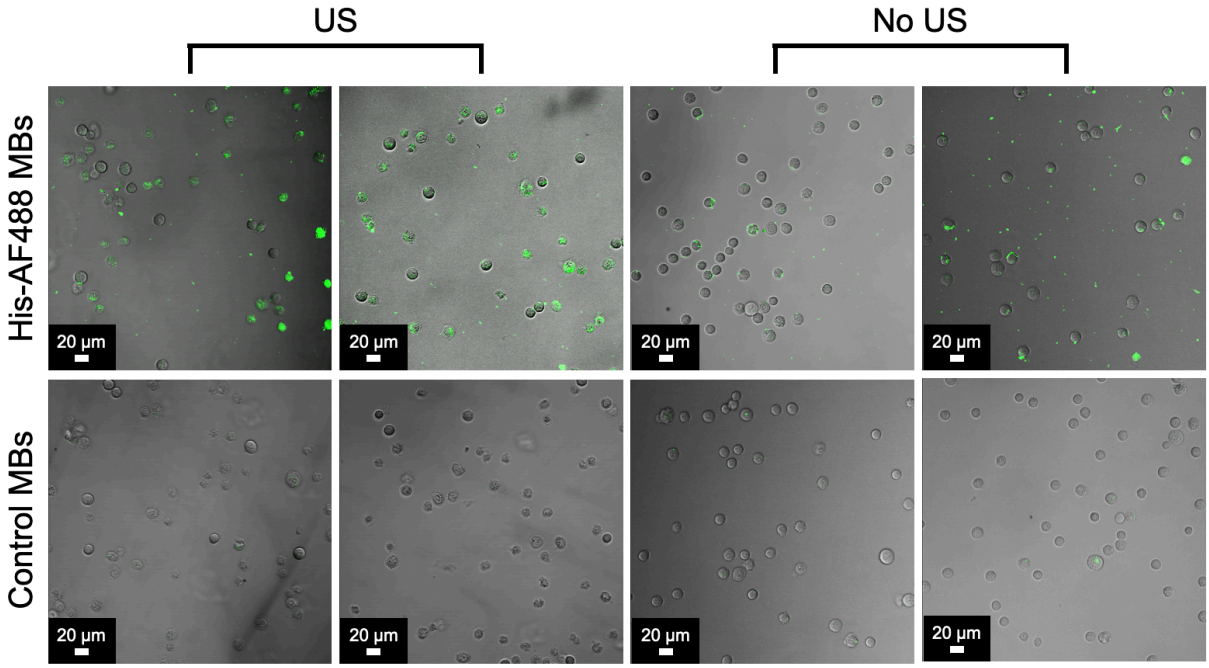


Figure 4.3. Confocal microscopy images of A549 cells (PMT) and His-AF488 lipids (green) for four conditions: His-AF488 microbubbles or DSPC : PEG40S : DGS-NTA(Ni) control microbubbles exposed to ultrasound, His-AF488 microbubbles or control microbubbles without ultrasound (N = 2 for all). *A distinct qualitative difference can be observed in the amount as well as the pattern of transfer/fusion of His-GFP NTA(Ni) lipid to the cell membranes between ultrasound and no ultrasound conditions, as well as a difference in the cells as shown on the PMT images between ultrasound and no ultrasound conditions, regardless of microbubble type.*

With ultrasound, the pattern of His-AF488 transfer seems to be that of internalisation, comparable to what was observed with lyso-microbubbles in the *Appendix*, *Section A.2*, rather than the desired 'membrane tagging'. The large fraction of PI-positive cells under ultrasound treatment (*Figure 4.6*) aligns with this observation, as it can indicate permeabilisation of the cell membrane, as elaborated upon below. The His-AF488 microbubbles, in the absence of ultrasound, show a pattern closer to the desired 'membrane tagging'. Even though the results in *Figure 4.5* show the largest fraction of AF488-positive and PI-negative cells in the absence of ultrasound, this is not apparent from the confocal images in *Figure 4.3*.

Explanations for this might simply be the sensitivity of the confocal microscope versus the flow cytometer, allowing the latter to pick up the AF488 signal that would lie below the noise threshold on the confocal

microscope or the exclusion of PI-positive cells in *Figure 4.5*. The second interesting observation, which aligns with the shift in populations observed upon ultrasound treatment using flow cytometry, as shown in *Figure 4.4*, is the change in morphology observed on the PMT reflections in *Figure 4.3* between ultrasound and non-ultrasound treated samples with both His-AF488 functionalised microbubbles and DSPC : PEG40S : DGS-NTA(Ni) control microbubbles.

From *Figure 4.4*, it is clear that upon ultrasound exposure, regardless of the type of microbubbles used, the majority of cells (~76% for His-AF488 and ~79% for control microbubbles) exist in population 2 at t = 5 minutes, with no observable change at t = 35 minutes (~78% for His-AF488 and ~79% for control microbubbles). A small shift from cells in population 1 to population 2 could be discerned for the cells treated with either type of microbubble but no ultrasound. At t = 5 minutes and at t = 35 minutes, for both His-AF488 functionalised microbubbles and control microbubbles, differences were observed between ultrasound and non-ultrasound treated samples. In summary, microbubbles, regardless of type, cause a morphological change in the cells, which was substantially enhanced by ultrasound.

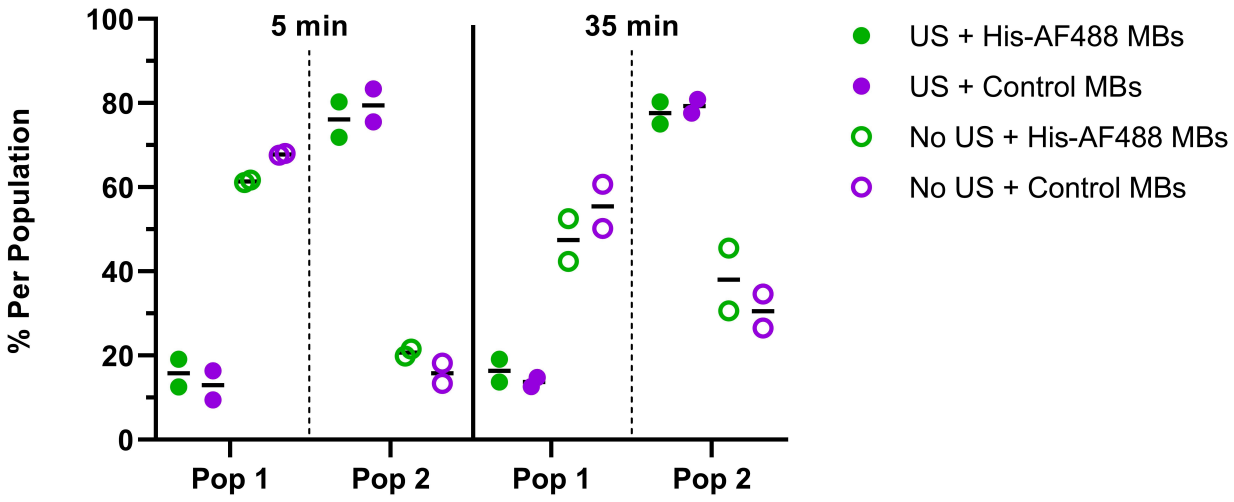


Figure 4.4. Population statistics for A549 cells in the pilot experiment. *The % of A549 cells in population 1 (pop 1), overlapping with the healthy control cells, and shifted cell population named population 2 (pop 2) for four conditions: His-AF488 microbubbles exposed to ultrasound (green, solid), control microbubbles exposed to ultrasound (magenta, solid), His-AF488 microbubbles (green, open) and control microbubbles (magenta, open) (N = 2 for all), at t = 0 and t = 35 minutes.*

Exploring the biological effect of interest, the 'membrane tagging', *Figure 4.5* summarises the results for each population at t = 0 and t = 35 minutes for all four sample conditions. This *Figure* shows the percentage

of cells positive for AF488 and negative for PI, indicating no compromise of the cell membrane. As expected, no His-AF488 signal was picked up in samples treated with control microbubbles. For samples treated with His-AF488 functionalised microbubbles, a greater effect was observed in population 2 in the absence of ultrasound (green, open) than after ultrasound treatment (green, closed) at t = 35 minutes.

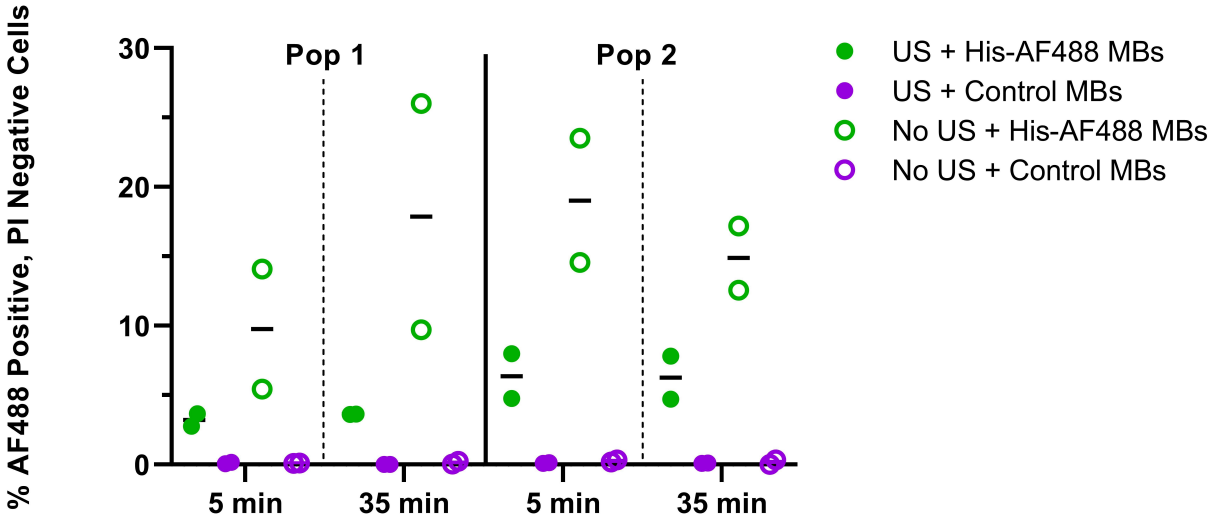


Figure 4.5. 'Membrane tagging' with and potential internalisation of His-AF488 for A549 cells in the pilot experiment. *The fraction of cells in population 1 (pop 1), overlapping with the healthy control cells, and shifted cell population named population 2 (pop 2) that are positive for His-AF488, either due to lipid transfer or internalisation, and PI-negative, for four conditions: His-AF488 microbubbles exposed to ultrasound (green, solid), control microbubbles exposed to ultrasound (magenta, solid), His-AF488 microbubbles (green, open) and control microbubbles (magenta, open) (N = 2), at t = 0 and t = 35 minutes.*

Figure 4.6 shows that the cells present in population 1 show no uptake of PI, meaning those cells have not experienced permeabilisation, sonoporation or cell death. However, cells in population 2, which is substantially larger in the case of ultrasound treatment, show a large uptake of PI at t = 5 minutes for all four conditions, varying from ~38% to ~66%. This PI uptake in cells in population 2 is greatly reduced at t = 35 minutes, ranging from ~2% to ~11%. This result indicates that cells previously positive for PI - an indication of cell death or permeabilisation - at t = 5 minutes no longer are positive for PI at t = 35 minutes. The hypothesis is that rather than being dead or dying at t = 5 minutes, the majority of PI-positive cells in this population might be permeabilised. Most surprising is the fact that this is also seen in the absence of ultrasound, indicating a possible effect of the microbubbles themselves. The data in *Figure 4.6* furthermore

show that cells that are not morphologically altered, i.e. the cells that are present in population 1, show no uptake of PI.

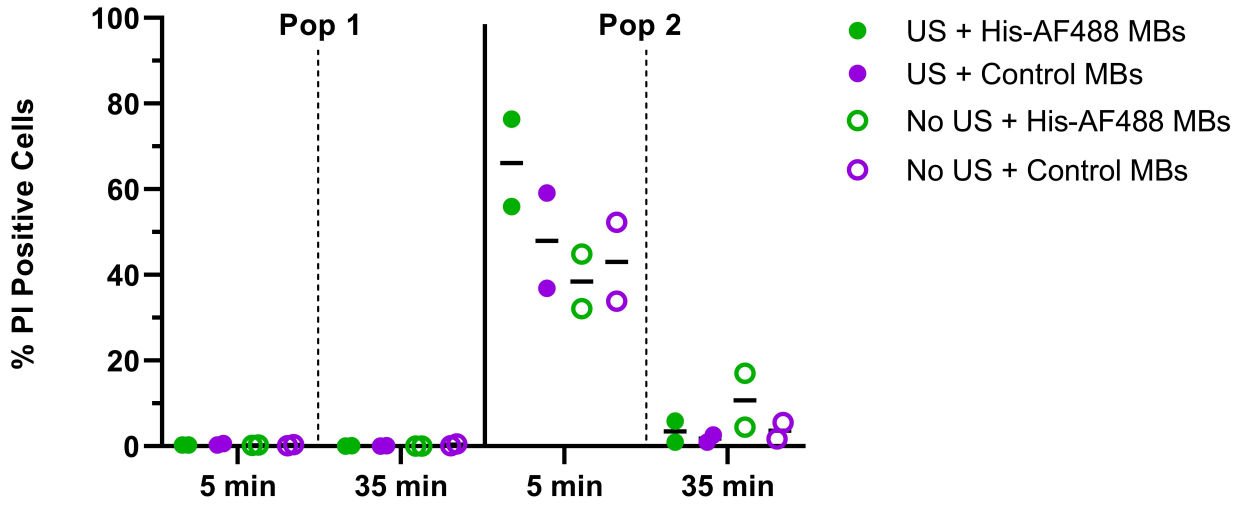


Figure 4.6. PI analysis, an indicator of cell death or permeabilisation, of A549 cells in the pilot experiment. *The fraction of cells in population 1 (pop 1), overlapping with the healthy control cells, and shifted cell population named population 2 (pop 2) that are positive for PI, an indicator of cell death or permeabilisation, for four conditions: His-AF488 microbubbles exposed to ultrasound (green, solid), control microbubbles exposed to ultrasound (magenta, solid), His-AF488 microbubbles (green, open) and control microbubbles (magenta, open) (N = 2), at t = 0 and t = 35 minutes.*

However, it is important to interpret all these results in comparison to each other. For example, nearly 20% of the cells in population 1 were AF488-positive and PI-negative for cells treated with His-AF488 microbubbles without ultrasound at t = 35 minutes. This population 1 constituted ~48% of all cells analysed, so approximately 10% of all 10,000 events analysed were AF488-positive and PI-negative for this sample condition. In comparison, at t = 5 minutes, population 1 constituted ~61% of all cells analysed, with 10% being AF488-positive and PI-negative when cells were treated with His-AF488 microbubbles, in the absence of ultrasound. This means approximately 6% of all 10,000 events analysed were AF488-positive and PI-negative for this sample condition.

4.3.2.2 Varying pressures: 0, 100, 150 and 200 kPa PNP, and two microbubble concentrations

In *Section 4.3.2.1*, a change in morphology in A549 cells was observed in response to ultrasound treatment (0.5 MHz, 200 kPa, continuous wave, 60 seconds total exposure duration), as well as the largest percentage of cells positive for His-AF488 and negative for PI, in the samples without ultrasound.

This *Section*, therefore, explores the effect of three different pressures and two microbubble concentrations on precisely these two observations: morphology and membrane tagging. The ultrasound driving conditions were 0.5 MHz centre frequency, 0, 100, 150 and 200 kPa peak negative pressure, 10% duty cycle (rather than 100% as in the *Section* above), and a 60-second total exposure duration. Furthermore, samples were treated in suspension in the SAT3 rather than in the pilot experiment set-up from here on.

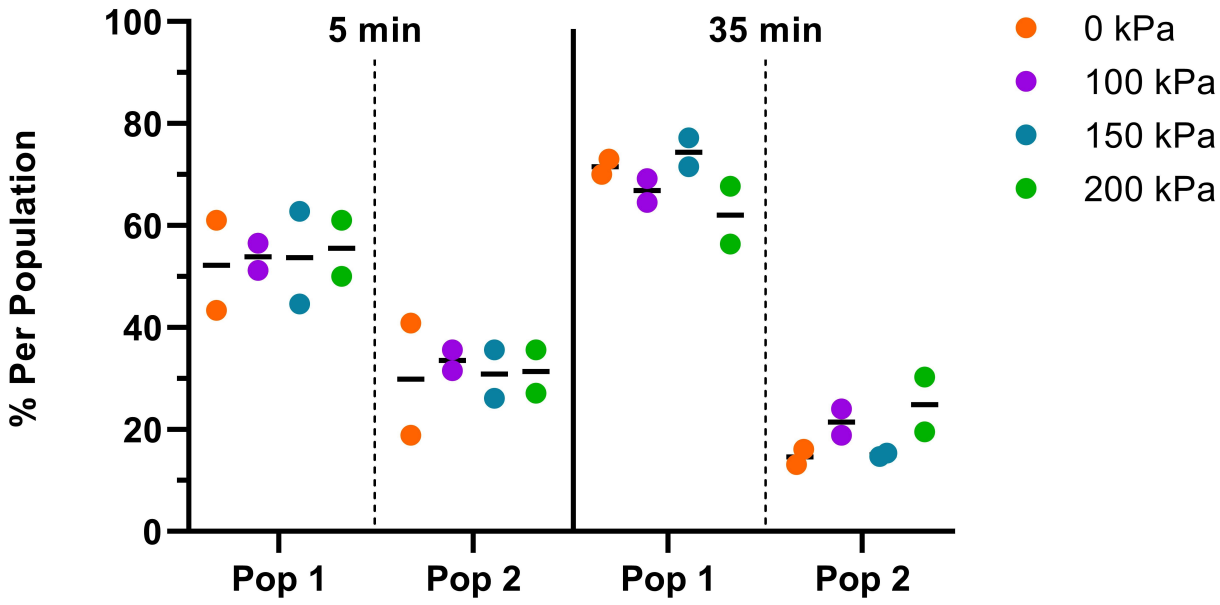


Figure 4.7. Population statistics for A549 cells in response to varying peak negative pressures at 1 x 10^8 MBs/mL. *It shows the % of A549 cells in population 1 (pop 1), overlapping with the healthy control cells, and shifted cell population named population 2 (pop 2) for four conditions: 0 (orange), 100 (magenta), 150 (blue) and 200 (green) kPa PNP (N = 2 for all), at t = 0 and t = 35 minutes.*

For both microbubble concentrations, 6 x 10^7 and 1 x 10^8 MBs/mL, as shown in *Figures 4.7* and *4.8*, respectively, the number of cells in population 1 was larger (~60%) than in the pilot experiment outlined above (~15%). This could be due to a variety of reasons, e.g., i) the less strenuous ultrasound conditions with a 10% duty cycle rather than 100% duty cycle, ii) the difference between 50 microbubbles per cell in this experiment rather than 400 microbubbles per cell as in the previous experiment, or iii) the different geometry

and exposed volumes of the two set-ups. At 5 minutes, there was no observable difference in these population statistics when a bubble concentration of 1 x 10^8 MBs/mL was used regardless of the pressure applied, and, similarly, at 6 x 10^7 MBs/mL, only a slight impact of pressure could potentially be observed. For 1 x 10^8 MBs/mL, an increase in the fraction of cells in population 1 and a corresponding decrease in the fraction of cells in population 2 might be discerned over time. This could indicate a recovery process occurring after ultrasound exposure, as the PI data in *Figure 4.6* also suggested. This effect, however, was not observed for the 6 x 10^7 MBs/mL, as shown in *Figure 4.8*, which showed the same split over time, potentially due to the lower microbubble concentration causing smaller changes that are more difficult to observe over time.

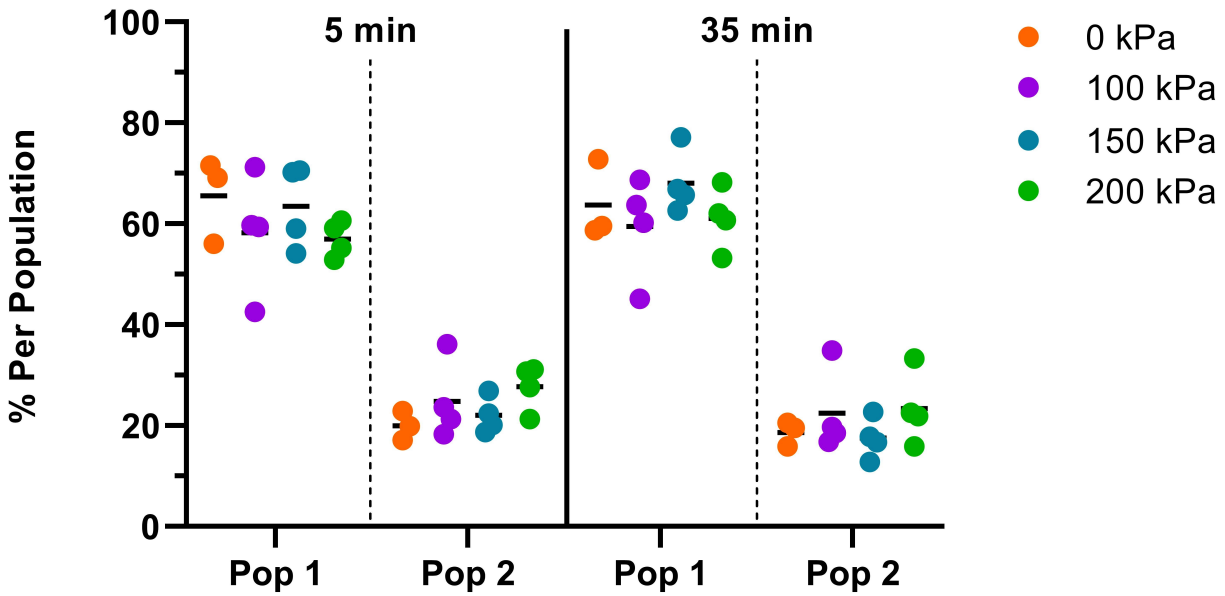


Figure 4.8. Population statistics for A549 cells in response to varying peak negative pressures at 6 x 10^7 MBs/mL. *The % of A549 cells in population 1 (pop 1), overlapping with the healthy control cells, and shifted cell population named population 2 (pop 2) for four conditions: 0 (orange), 100 (magenta), 150 (blue) and 200 (green) kPa PNP (N = 2 for all), at t = 0 and t = 35 minutes.*

The study of the effect of pressure on the fraction of PI-negative cells in both cell populations positive for His-AF488 shows a similar pattern as the experiment above, as can be seen in *Figures 4.9 and 4.10* for 1 x 10^8 MBs/mL and 6 x 10^7 MBs/mL, respectively.

In population 1, both pressure and microbubble concentration had an effect on the 'membrane tagging'. Specifically, in *Figure 4.10*, a difference was observed between 0 and 150 kPa, and 0 and 200 kPa, at t = 35 minutes. Comparing the two microbubble concentrations, a difference can be observed at t = 35

minutes and 100 kPa peak negative pressure. In population 2, both microbubble concentration and time had an effect on the 'membrane tagging'. Specifically, comparing the two microbubble concentrations, a difference can be observed at t = 35 minutes and 0 kPa peak negative pressure. Furthermore, time has an effect on the 0 kPa, 1 x 10^8 MBs/mL condition.

For the 6 x 10^7 MBs/mL condition, the no ultrasound condition caused a larger fraction of cells in population 1 to be His-AF488-positive while being PI-negative, indicating a potentially higher degree of 'membrane tagging' due to the lack of internalisation of PI. This could be due to the milder or no ultrasound conditions allowing microbubbles to persist for longer rather than being immediately destroyed. As shown in *Figures 4.13* and 4.*14*, the ultrasound data support this hypothesis, as they show lower signal powers for the 100 kPa than the 150 and 200 kPa pressure conditions. The cells in population 1 are particularly of interest, as they show no morphological change compared to the live controls, as can be seen in *Figure 4.1* and *Figures A.3.1* and *A.3.3* in the *Appendix*, *Section A.3*, and are, therefore, less like to have been functionally altered.

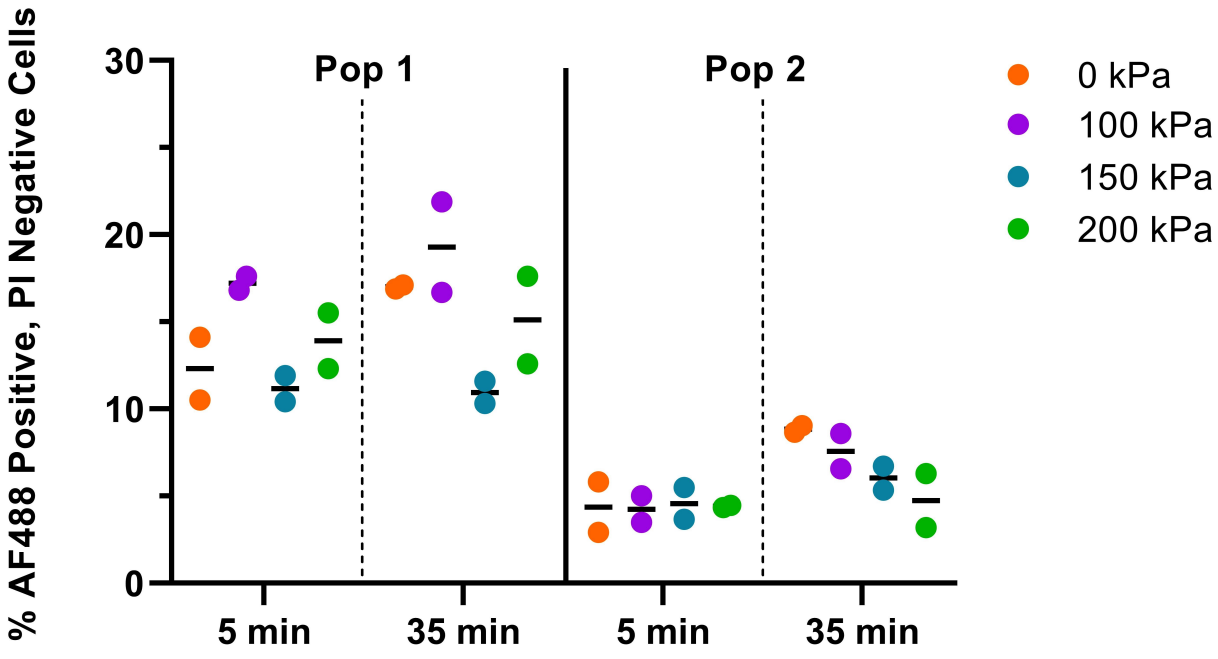


Figure 4.9. 'Membrane tagging' with and potential internalisation of His-AF488 for A549s in response to varying peak negative pressures at 1 x 10^8 MBs/mL. *The fraction of cells in population 1 (pop 1), overlapping with the healthy control cells, and shifted cell population named population 2 (pop 2) that are positive for His-AF488, due to lipid transfer or internalisation, and negative for PI, for four conditions: 0 (orange), 100 (magenta), 150 (blue) and 200 (green) kPa PNP (N = 2 for all) at t = 0 and t = 35 minutes.*

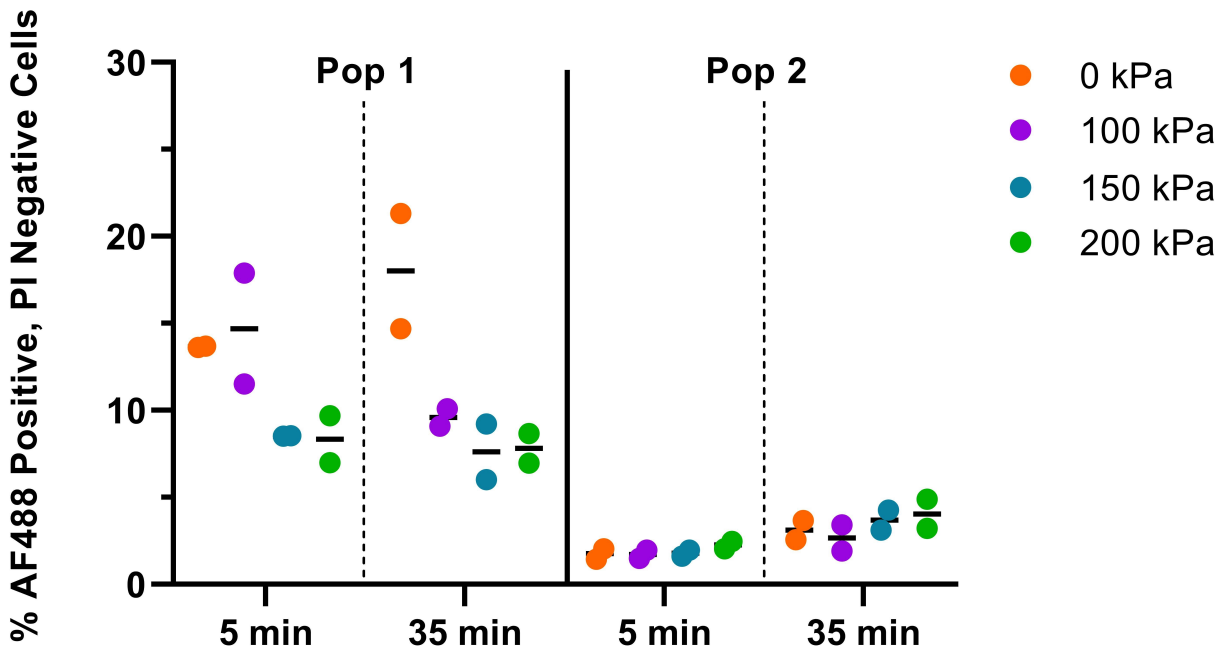


Figure 4.10. 'Membrane tagging' with and potential internalisation of His-AF488 for A549s in response to varying peak negative pressures at 6 x 10^7 MBs/mL. *The fraction of cells in population 1 (pop 1), overlapping with the healthy control cells, and shifted cell population named population 2 (pop 2) that are positive for His-AF488, due to lipid transfer or internalisation, and negative for PI, for four conditions: 0 (orange), 100 (magenta), 150 (blue) and 200 (green) kPa PNP (N = 2 for all) at t = 0 and t = 35 minutes.*

In the pilot experiment in *Section 4.3.2.1*, cells in population 2 appear to show a negative trend over the course of 35 minutes with a decrease in PI uptake. *Figures 4.11* and 4.*12* did not show the same trend over time, especially for the 6 x 10^7 MBs/mL condition, as shown in *Figure 4.12*. The majority of cells initially positive for PI remained PI-positive at 35 minutes. For this reason, those cells were excluded from the His-AF488 analysis, as PI-positive cells 35 minutes after treatment are less likely to be sonoporated - a process with known timescales on the order of seconds to minutes (Gelderblom *et al*., 2013; Helfield *et al*., 2016; Helfield *et al*., 2017) - and more likely to be dead or dying. However, an effect of microbubble concentration on the fraction of PI-positive cells in population 2 may be observed, with the 6 x 10^7 MBs/mL condition leading to a higher percentage of PI-positive cells in population 2.

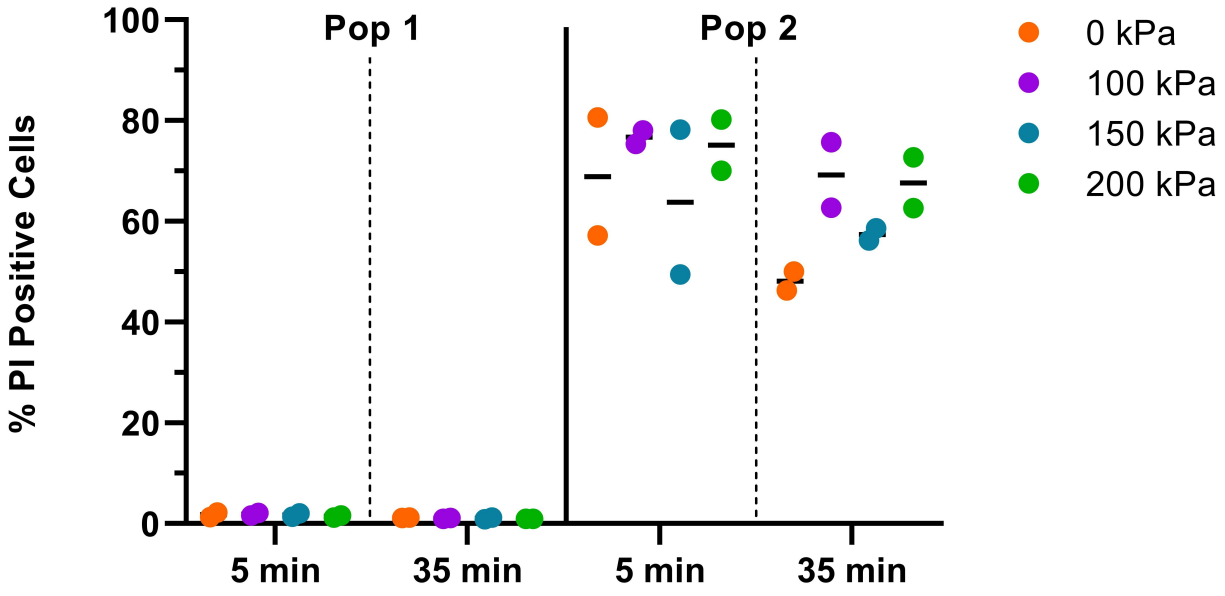


Figure 4.11. PI analysis, an indicator of cell death or permeabilisation, of A549 cells in response to varying peak negative pressures at 1 x 10^8 MBs/mL. *The fraction of cells in population 1 (pop 1), overlapping with the healthy control cells, and shifted cell population named population 2 (pop 2) that are positive for PI, an indicator of cell death or permeabilisation, for four conditions: 0 (orange), 100 (magenta), 150 (blue) and 200 (green) kPa PNP (N = 2 for all) at t = 0 and t = 35 minutes.*

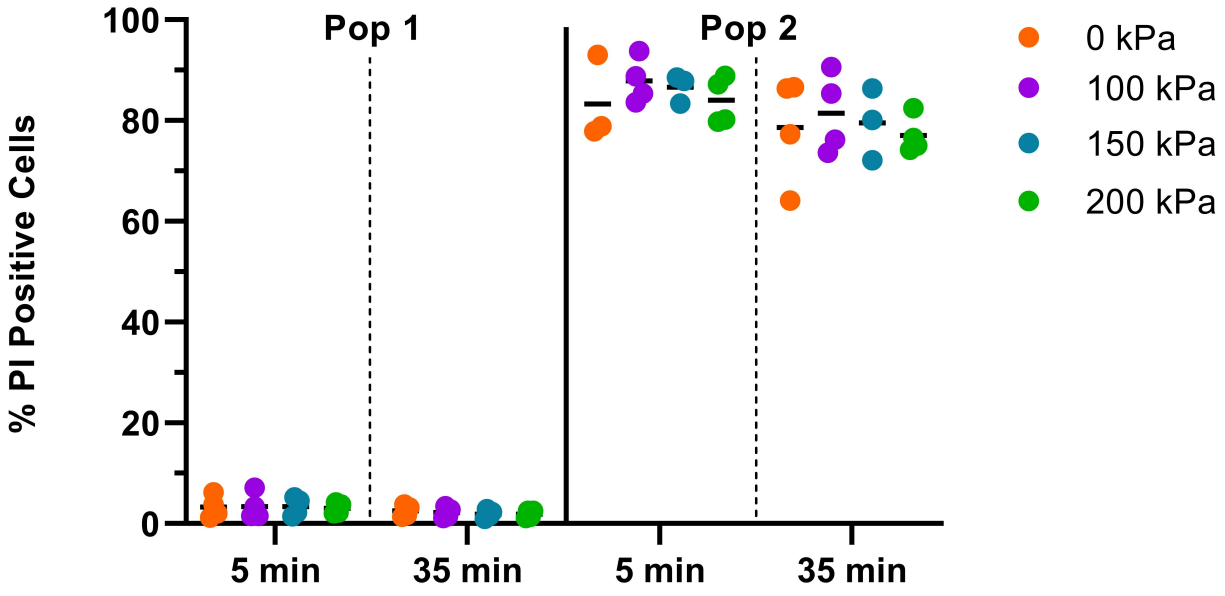


Figure 4.12. PI analysis, an indicator of cell death or permeabilisation, of A549 cells in response to varying peak negative pressures at 6 x 10^7 MBs/mL. *The fraction of cells in population 1 (pop 1), overlapping with the healthy control cells, and shifted cell population named population 2 (pop 2) that are positive for PI, an indicator of cell death or permeabilisation, for four conditions: 0 (orange), 100 (magenta), 150 (blue) and 200 (green) kPa PNP (N = 2 for all) at t = 0 and t = 35 minutes.*

To reiterate, the data in *Figures 4.11* and 4.*12* should be considered in the context of *Figures 4.7* and 4.*8*, respectively. For example, for 1 x 10^8 MBs/mL, 15% of all recorded cells were located in population 2 for the 0 kPa condition at t = 35 minutes, as shown in *Figure 4.7*. Of those cells, ~50% were PI-positive, as shown in *Figure 4.11*, corresponding to 750 cells, or ~7.5% of the analysed cells. In contrast, for the 200 kPa condition at t = 35 minutes, this was 1675 cells, or ~17% of the total analysed cells. So, it is important to keep in mind that while the PI data in *Figures 4.11* and 4.*12* showed large fractions of PI-positive cells in population 2 for the 0 kPa no ultrasound conditions, this was offset by the smaller fraction of cells in population 2 for the 0 kPa no ultrasound conditions.

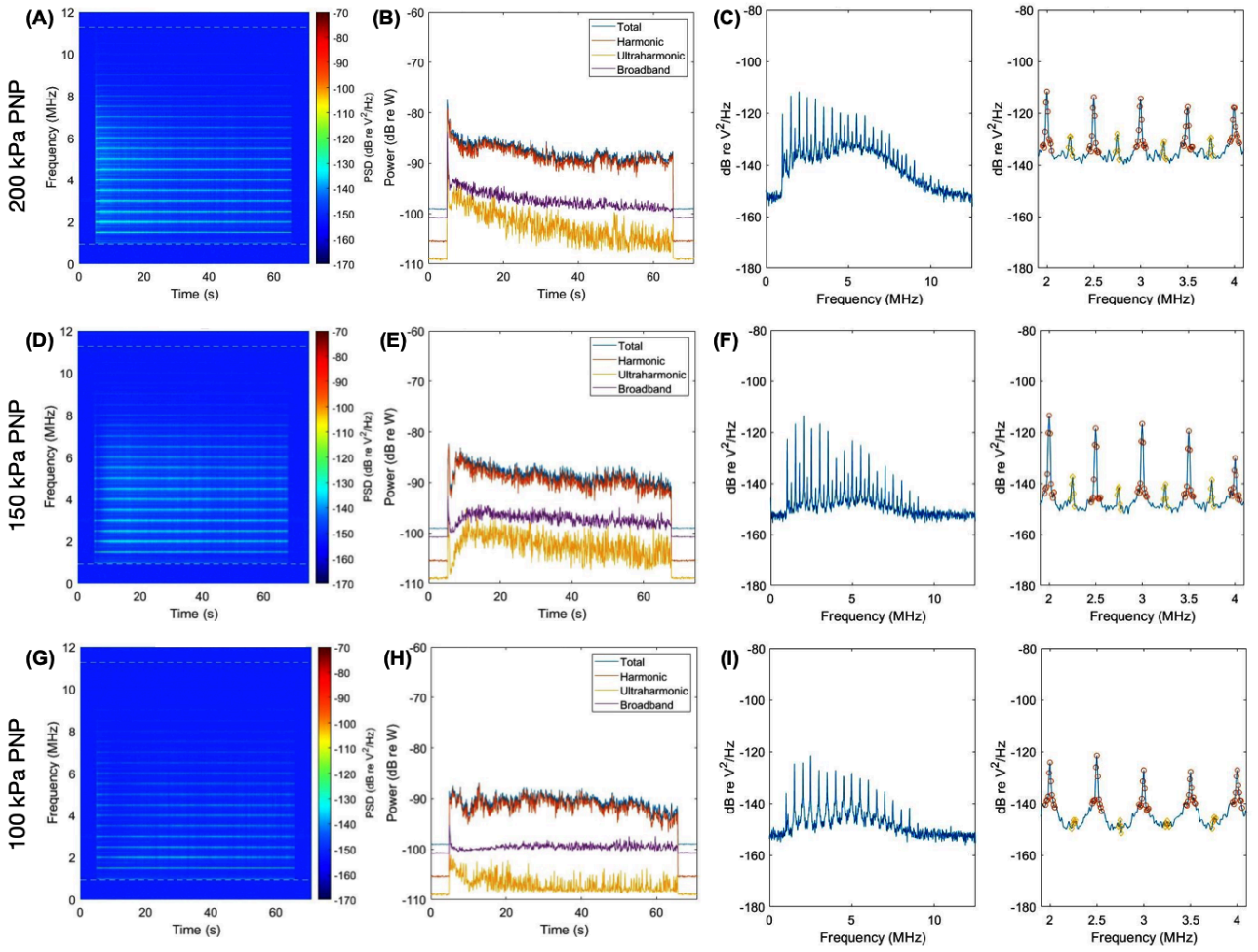


Figure 4.13. Example spectrum histories over a 60-second exposure of a suspension of His-AF488 microbubbles at 1 x 10^8 MBs/mL. *(A, D, G) Full spectra and (B, E, H) total, harmonic, ultraharmonic and broadband signal powers, all as a function of time. (C, F, I) Frequency domain PCD trace corresponding to the onset of the ultrasound signal (left), zoomed in (right), showing harmonics (orange) and ultraharmonics (yellow). Drive conditions were 0.5 MHz, 200 (A, B, C), 150 (D, E, F) and 100 (G, H, I) peak negative pressure, continuous wave, and a 60-second total exposure duration.*

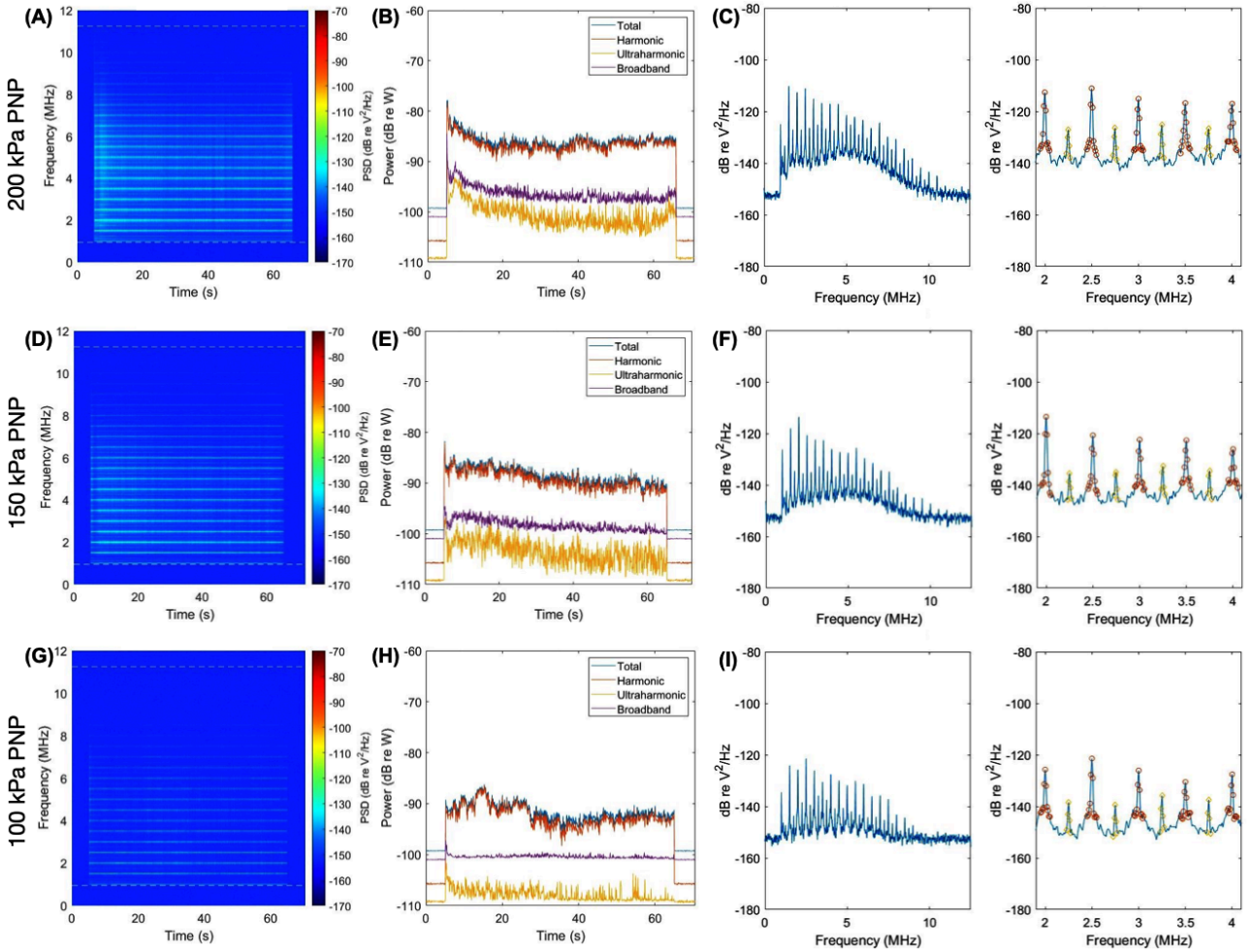


Figure 4.14. Example spectrum histories over a 60-second exposure of a suspension of His-AF488 microbubbles at 6 x 10⁷ MBs/mL. *(A, D, G) Full spectra and (B, E, H) total, harmonic, ultraharmonic and broadband signal powers, all as a function of time. (C, F, I) Frequency domain PCD trace corresponding to the onset of the ultrasound signal (left), zoomed in (right), showing harmonics (orange) and ultraharmonics (yellow). Drive conditions were 0.5 MHz, 200 kPa (A, B, C), 150 (D, E, F) and 100 (G, H, I) peak negative pressure, continuous wave, and a 60-second total exposure duration.*

4.3.2.3 Varying duty cycles: 0, 10, 20, 40, 80 and 100%

The experiment in *Section 4.3.2.2* showed that the number of cells in population 1 was larger (~60%) than in the pilot experiment in *Section 4.3.2.1* (15%). The duty cycle - 10% rather than 100% - was one of the differences between these two experiments. To this end, the effect of the duty cycle was investigated on both the morphology and membrane tagging of A549 cells.

Where the difference in pressure and microbubble concentration in *Section 4.3.2.2* had minimal effect on the population statistics, the variation in duty cycle, i.e. the amount of time the ultrasound is 'on', has a dramatic effect, as can readily be observed in *Figure 4.15*. The ultrasound driving conditions were 0.5

MHz centre frequency, 200 kPa PNP, varying duty cycle, and a total exposure duration of 60 seconds at a microbubble concentration of 1 x 10^8 MBs/mL. *Figure 4.15* shows a shift from population 1 to the morphologically different population 2 with increasing duty cycle, from ~80% of the cells being present in population 1 at 0% duty cycle, i.e. no ultrasound, to ~22% of the cells being present in population 1 at 100% duty cycle, i.e. continuous wave ultrasound. This was accompanied by an increase in the fraction of cells present in population 2 from ~10% at 0% duty cycle to 57% at 100% duty cycle. This shift did not fully match up in both populations, which might be due to the destruction of a fraction of the cells at higher duty cycles. This pattern was observed at t = 5 minutes and t = 35 minutes.

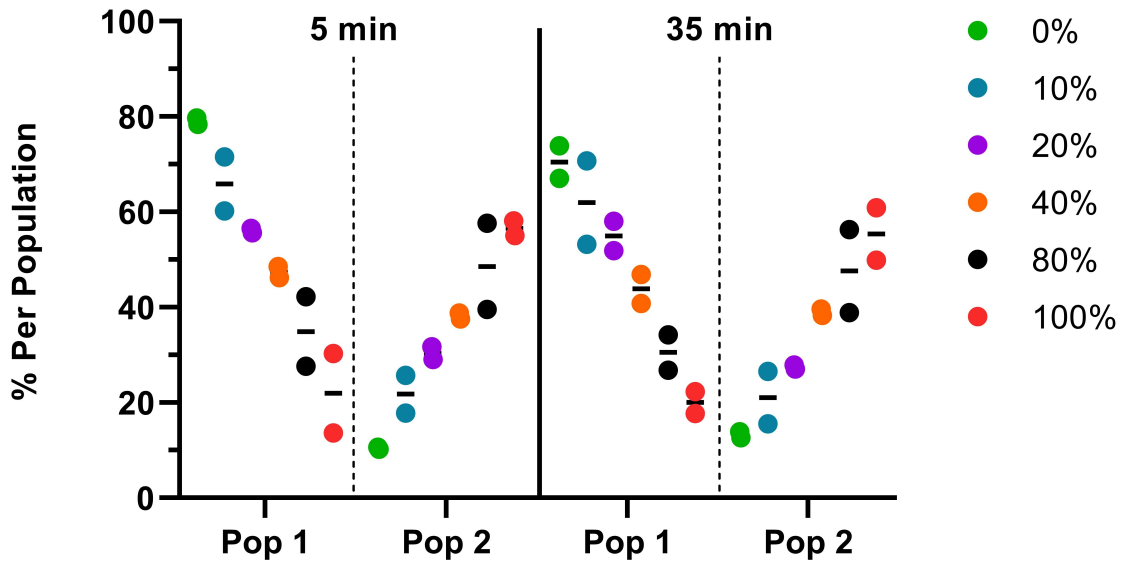


Figure 4.15. Population statistics for A549 cells in response to varying duty cycles at 1 x 10^8 MBs/mL. *It shows the % of A549 cells in population 1 (pop 1), overlapping with the healthy control cells, and shifted cell population named population 2 (pop 2) for six conditions: 0 (green), 10 (blue), 20 (magenta), 40 (orange), 80 (black) and 100 (red) % DC (N = 2 for all), at 0.5 MHz, 200 kPa PNP, and a 60-second total exposure duration. The effects are shown at t = 0 and t = 35 minutes.*

Regarding the 'membrane tagging' bioeffect, it can be observed in *Figure 4.16* that the PI-negative cells in the morphologically altered group, population 2, show negligible AF488 signals. This is an interesting observation since the two previous experiments, and corresponding *Figures 4.5*, *4.9* and *4.10*, did show uptake at both no ultrasound and ultrasound conditions. In population 1, it is notable that both the no ultrasound group (0% duty cycle, green) and the continuous ultrasound group (100% duty cycle, red) seemed to show the largest fraction of AF488-positive and PI-negative, albeit no more than 10% of cells. It is important to bear in mind that this constitutes roughly 8% of the total number of cells analysed, being

AF488-positive and PI-negative for the 0% duty cycle and 3% for the 100% duty cycle. However, no meaningful differences could be observed between different duty cycle conditions, as all means fall within each other's variance.

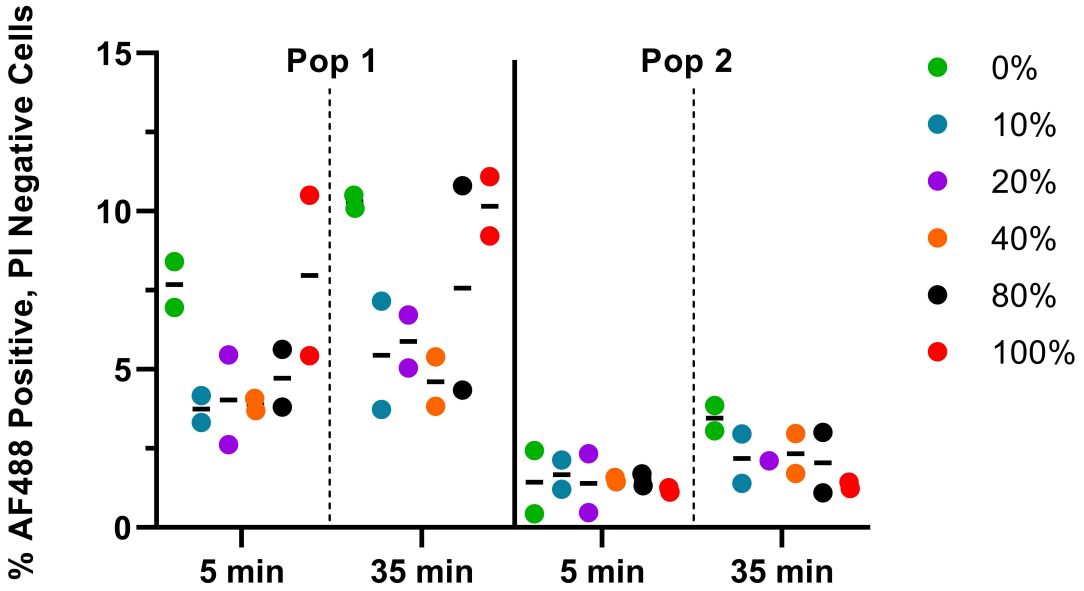


Figure 4.16. 'Membrane tagging' with and potential internalisation of His-AF488 for A549s in response to varying duty cycles at 1 x 10^8 MBs/mL. *It shows the fraction of cells in population 1 (pop 1), overlapping with the healthy control cells, and shifted cell population named population 2 (pop 2) that are positive for His-AF488, either due to lipid transfer or internalisation, and negative for PI, for six conditions: 0 (green), 10 (blue), 20 (magenta), 40 (orange), 80 (black) and 100 (red) % DC (N = 2 for all), at 0.5 MHz, 200 kPa PNP, and a 60-second total exposure duration. The effects are shown at t = 0 and t = 35 minutes.*

Interesting to note in *Figure 4.17* is the high percentage of PI-positive cells in population 2 for the no ultrasound control (0% duty cycle, green), and a general decreasing trend in PI uptake with increasing duty cycle might be discerned. In absolute numbers, this graph would show the opposite trend, as, for example, even though 'only' ~66% of the cells in population 2 are PI-positive at t = 35 minutes for 100% duty cycle (red), as this population constitutes ~55% of the total cells analysed, this constitutes ~36% of all cells analysed. In comparison, only ~13% of all cells fall in population 2 for 0% duty cycle, and with 72% of those being PI-positive, this constitutes ~9% of all cells analysed.

It was again observed that there was limited recovery of cells over time, i.e. no strong decrease in PI-positive cells over the course of the 35 minutes, especially for the higher duty cycle conditions, which raises the question as to why this was indicated in the first experiment. Possible reasons include i) different experimental characteristics, e.g., an Eppendorf tube versus a transwell, ii) different volumes, e.g., 500 μL

versus 150 μL, iii) different cell concentrations, e.g., 5 x 10^5 versus 2 x 10^6 cells/mL, and iv) thus a different bubble to cell ratio: 400 versus 50 microbubbles per cell. The higher cell concentration, and thus the smaller number of microbubbles per cell, was necessary due to the smaller exposure volume in the SAT3, as enough intact cells had to be guaranteed for flow cytometry analysis. High bubble concentrations in such a small volume could cause acoustic shielding and, therefore, a dampened acoustic response.

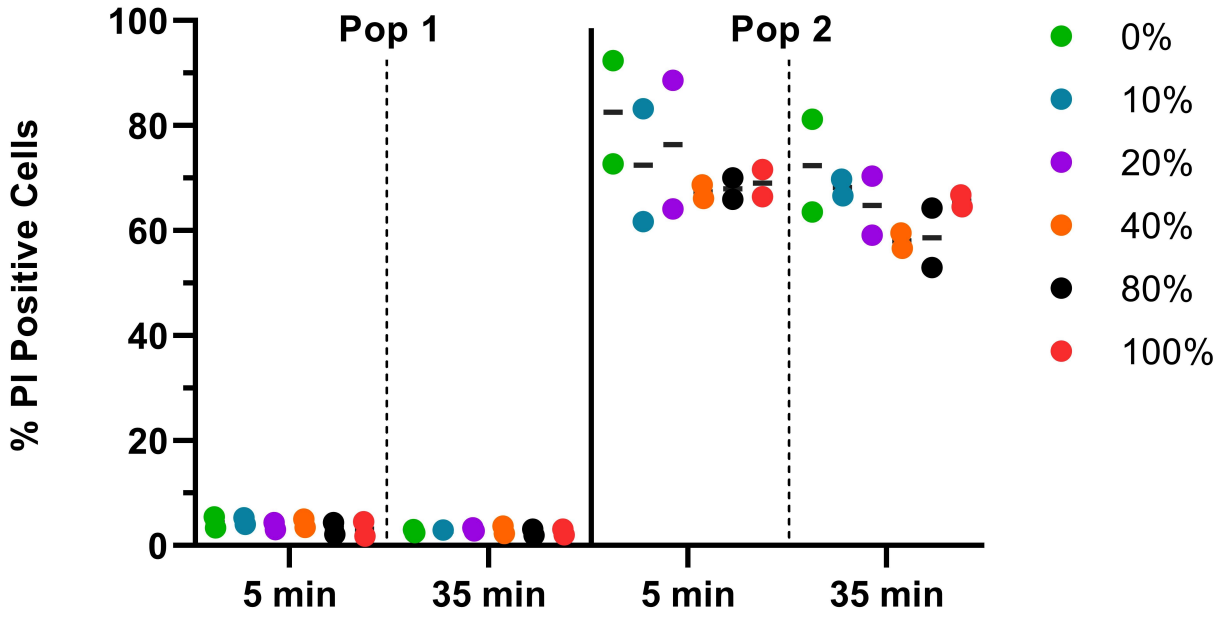


Figure 4.17. PI analysis, an indicator of cell death or permeabilisation, of A549 cells in response to varying duty cycle at 1 x 10^8 MBs/mL. *The fraction of cells in population 1 (pop 1), overlapping with the healthy control cells, and shifted cell population named population 2 (pop 2) that are positive for PI, an indicator of cell death or permeabilisation, for six conditions: 0 (green), 10 (blue), 20 (magenta), 40 (orange), 80 (black) and 100 (red) % DC (N = 2 for all), at 0.5 MHz, 200 kPa PNP, and a 60-second total exposure duration. The effects are shown at t = 0 and t = 35 minutes.*

Examples of the accompanying ultrasound analysis are shown in *Figure 4.18*, with decreasing duty cycle from the top to the bottom of the figure, from 100% to 0% duty cycle. From both the example spectrum histories as well as the frequency domain PCD traces, it can be observed that the broadband component, and therefore violent microbubble behaviour, decreases with a decrease in duty cycle, which matches the increase in the fraction of cells in the morphologically altered population 2 with increasing duty cycle. In *Figure 4.19*, example microbubble size distributions are shown for the microbubbles used in the experiments in *Sections 4.3.2.1* to *4.3.2.3*.

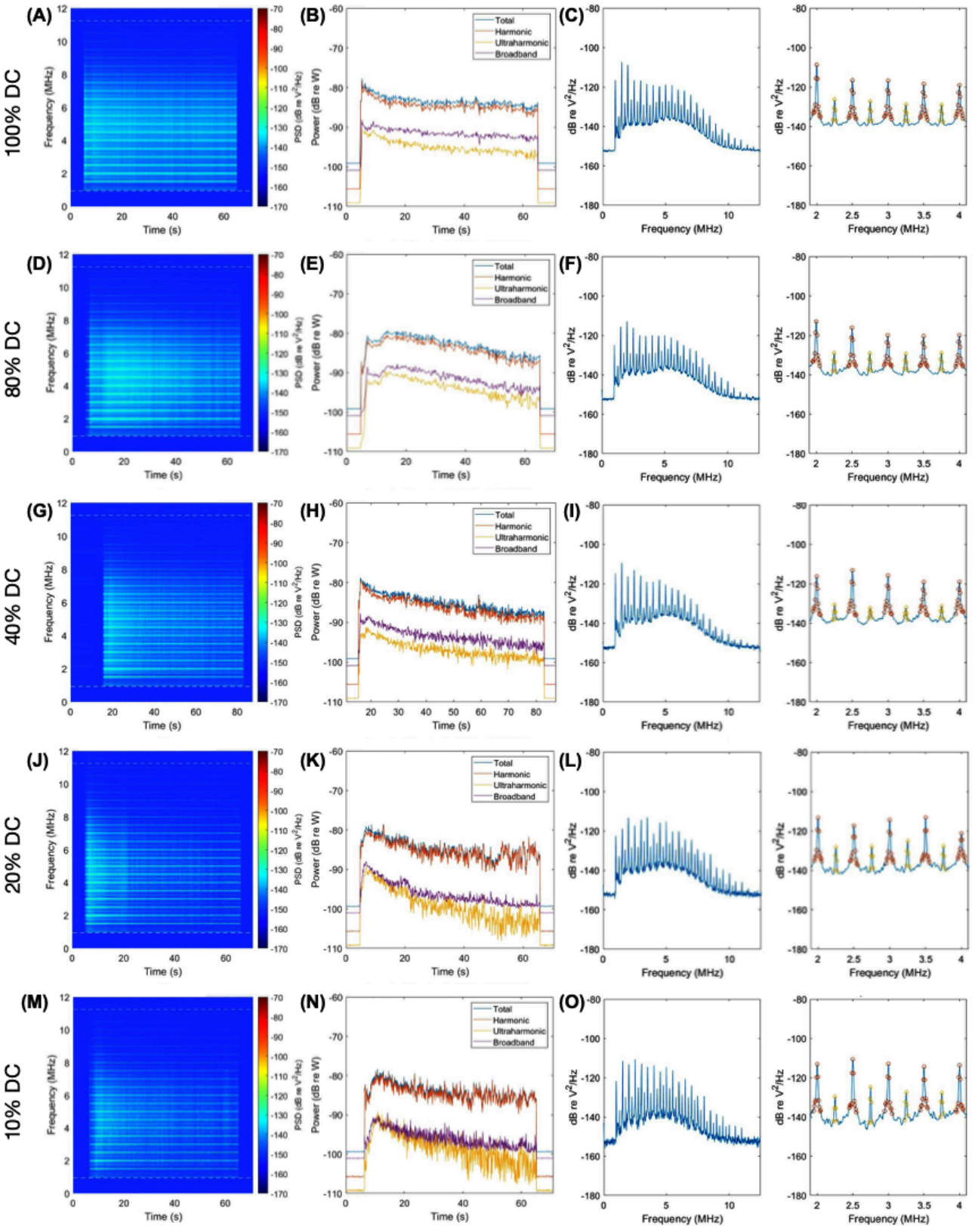


Figure 4.18. Example spectrum histories over a 60-second exposure of a suspension of His-GFP microbubbles at 1 x 10^8 MBs/mL. *(A, D, G, J, M) Full spectra and (B, E, H, K, N) total, harmonic, ultraharmonic and broadband signal powers, all as a function of time. (C, F, I, L, O) Frequency domain PCD trace corresponding to the onset of the ultrasound signal (left), zoomed in (right), showing harmonics (orange) and ultraharmonics (yellow). Drive conditions were 0.5 MHz, 200 kPa peak negative pressure, for six DC: 10 (M, N, O), 20 (J, K, L), 40 (G, H, I), 80 (D, E, F) and 100 (A, B, C) %, 60 seconds total exposure duration.*

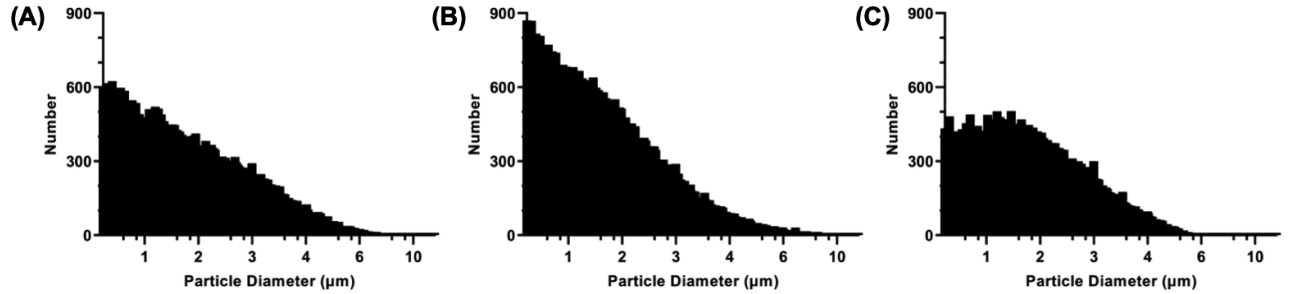


Figure 4.19. Microbubble size distribution histograms for microbubbles used in the experiments in Sections 4.3.2.1 (A), 4.3.2.2 (B) and 4.3.2.3 (C). *Microbubble size distribution histograms for His-AF488 microbubbles used in experiments corresponding to (A), with a mean diameter of 2.32 µm and a concentration of 3.9 x 10^9 MBs/mL (number of events = 38739), (B), with a mean diameter of 1.80 µm and a concentration of 4.4 x 10^9 MBs/mL (number of events = 44331), and (C), with a mean diameter of 2.08 µm and a concentration of 3.4 x 10^9 MBs/mL (number of events = 33894).*

4.3.3 Quantitative observation of functionalised lipid transfer and/or microbubble fusion in Jurkat cells

A similar parameter space was explored for Jurkat T cells, looking at the effects of varying peak negative pressure, duty cycle and microbubble concentration.

4.3.3.1 Varying pressures: 0, 140 and 200 kPa PNP, and three microbubble concentrations

The effect of varying pressure - 0, 140 and 200 kPa PNP - at three microbubble concentrations - 2 x 10^7, 6 x 10^7 and 1 x 10^8 MBs/mL - on the population statistics of Jurkat cells is shown in *Figure 4.20*. It shows again two populations, one that overlaps with the live Jurkat control cells, shown as population 1 in *Figure 4.1*, and *Figures A.3.2* and *A.3.4* in the *Appendix*, *Section A.3*, and one towards the left of that on the FSC axis denoted 'population 2'. The latter fraction increased in response to His-AF488 microbubbles and ultrasound exposure.

Figure 4.20 shows the fraction of cells in population 1 decreasing with increasing ultrasound pressure. This was combined with a reverse trend for the cells in population 2. A second possible trend within each pressure group was one regarding the microbubble concentration, as the fraction of cells in population 1 seemed to decrease further with increasing microbubble concentration.

Figure 4.21 shows again that the no ultrasound control condition seemed to produce the most 'membrane tagging' at the highest microbubble concentration of 1 x 10^8 MBs/mL in population 1. The

fraction of His-AF488-positive and PI-negative cells in population 1 seemed to increase with microbubble concentration for the 0 kPa PNP ultrasound condition at t = 0 and 35 minutes.

An interesting phenomenon can be observed for the cells in population 2 in *Figure 4.21*. The fraction of cells positive for AF488 and negative for PI is negligible at t = 5 minutes. However, this fraction grows, to different extents, at t = 35 minutes. In the *Appendix*, *Section A.3*, *Figure A.3.4.C* and *A.3.4.F*, and *A.3.4.I* and *A.3.4.L* are paired comparisons over time of Jurkat cells incubated with 1 x 10^8 His-AF488 microbubbles per mL and either exposed to ultrasound (200 kPa peak negative pressure) or not, respectively. As can be observed, there was a shift from PI-positive to PI-negative over 35 minutes for both conditions, causing a larger fraction of Jurkat cells to be simultaneously positive for His-AF488 and negative for PI.

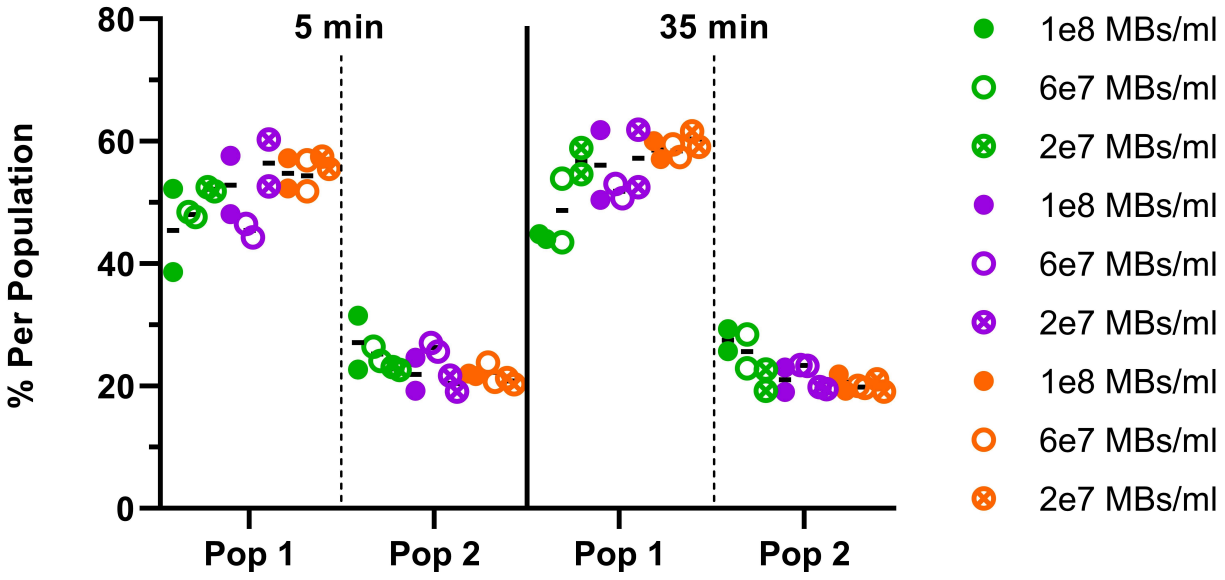


Figure 4.20. Population statistics for Jurkat cells in response to varying peak negative pressures at three microbubble concentrations. *The % of Jurkat cells in population 1 (pop 1), overlapping with the healthy control cells, and shifted cell population named population 2 (pop 2) for three microbubble concentrations condition: 1 x 10^8 (solid), 6 x 10^7 (open) and 2 x 10^7 (cross) MBs/mL, at three peak negative pressures: 0 (orange), 140 (magenta) and 200 (green) kPa (N = 2 for all), at t = 0 and t = 35 minutes. Ultrasound driving conditions were 0.5 MHz, 10% DC, and a 60-second exposure duration.*

This explains the results as seen in *Figure 4.21* and is a good indicator of a recovery mechanism present in Jurkat cells, like in the A549 experiments. This also aligns with the PI results shown in *Figure 4.22*, which indicate a decrease in PI-positive cells in population 2 over the course of the 35 minutes. Furthermore, it is

also a good indication of the internalisation of His-AF488 lipid in the cells, possibly due to sonoporation and material from His-AF488 microbubbles being deposited on the Jurkat cell membrane.

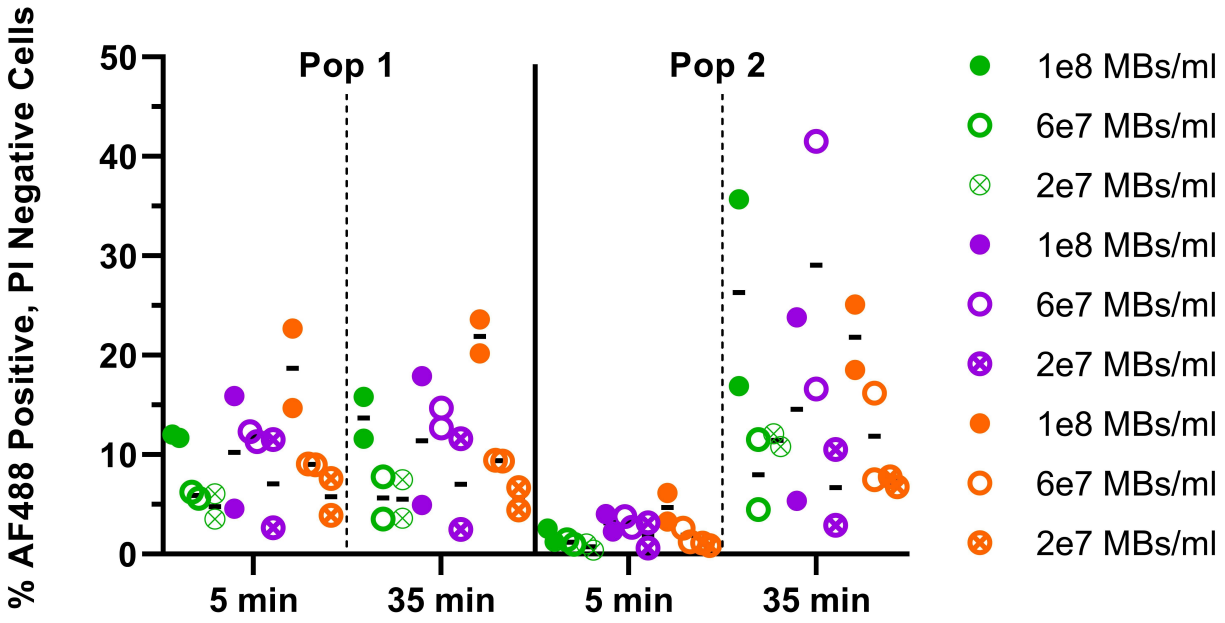


Figure 4.21. 'Membrane tagging' with and potential internalisation of His-AF488 for Jurkat cells in response to varying peak negative pressures at three microbubble concentrations. *The % of Jurkat cells in population 1 (pop 1), overlapping with the healthy control cells, and shifted cell population named population 2 (pop 2) that are positive for His-AF488, either due to lipid transfer or internalisation, and negative for PI, for three microbubble concentrations condition: 1 x 10^8 (solid), 6 x 10^7 (open) and 2 x 10^7 (cross) MBs/mL, at three peak negative pressures: 200 (green), 140 (magenta) and 0 (orange) kPa (N = 2 for all), at t = 0 and t = 35 minutes. Ultrasound driving conditions were 0.5 MHz, 10% DC, and a 60-second exposure duration.*

The highest fraction of AF488-positive and PI-negative cells in population 2 at t = 35 minutes corresponded to the '6 x 10^7 MBs/mL with 140 kPa' condition. This group also showed the lowest PI uptake, as seen in *Figure 4.22*, and a relatively small fraction of cells in population 1, as can be seen in *Figure 4.20*, compared to other ultrasound and microbubble conditions. It should be noted that the variances, especially for this sample in *Figure 4.21* at t = 35 minutes, were large. However, analysis of the acoustic emissions data, an example of which is shown in *Figure 4.23*, revealed no grounds for the exclusion of data from either sample.

Figure 4.22 shows that the highest concentration of microbubbles, 1 x 10^8 MBs/mL, at 200 kPa caused the highest fraction of the cells in population 2 to be PI-positive. It can be observed in *Figure 4.23* that a lower concentration of microbubbles led to a less sustained microbubble response, based on both the

broadband (purple) and ultraharmonic (yellow) traces, and that the total signal power was lower for the lower peak negative pressure.

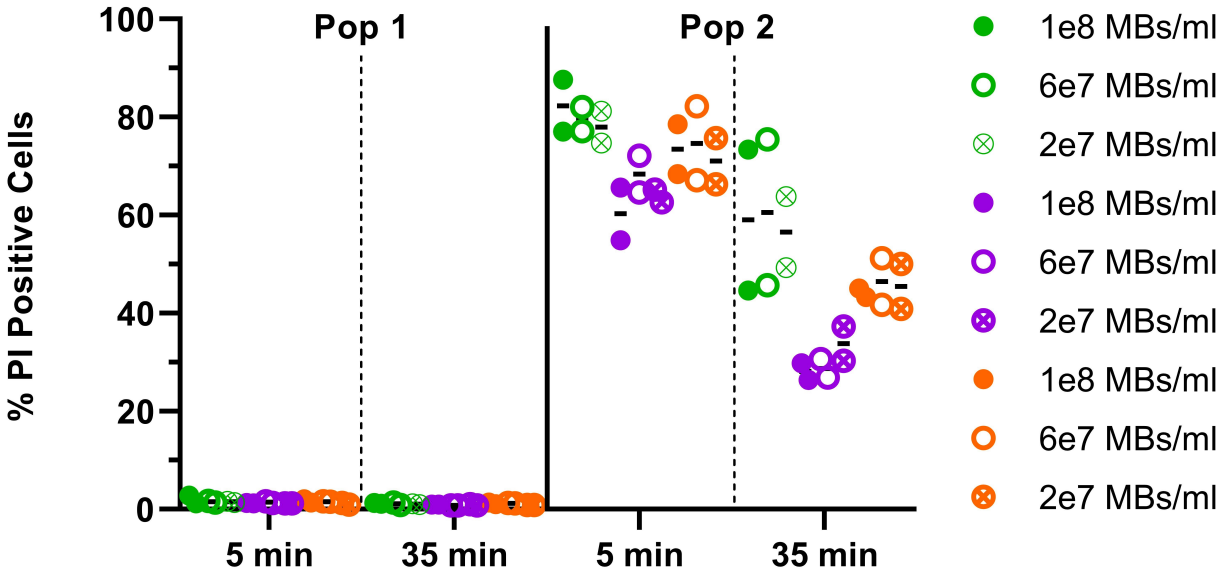


Figure 4.22. PI analysis, an indicator of cell death or permeabilisation, of Jurkat cells in response to varying peak negative pressures at three microbubble concentrations. *The % of Jurkat cells in population 1 (pop 1), overlapping with the healthy control cells, and shifted cell population named population 2 (pop 2) that are positive for PI, an indicator of cell death or permeabilisation, for three microbubble concentrations condition: 1 x 10^8 (solid), 6 x 10^7 (open) and 2 x 10^7 (cross) MBs/mL, at three peak negative pressures: 200 (green), 140 (magenta) and 0 (orange) kPa (N = 2 for all), at t = 0 and t = 35 minutes. Ultrasound driving conditions were 0.5 MHz, 10% DC, and a 60-second total exposure duration.*

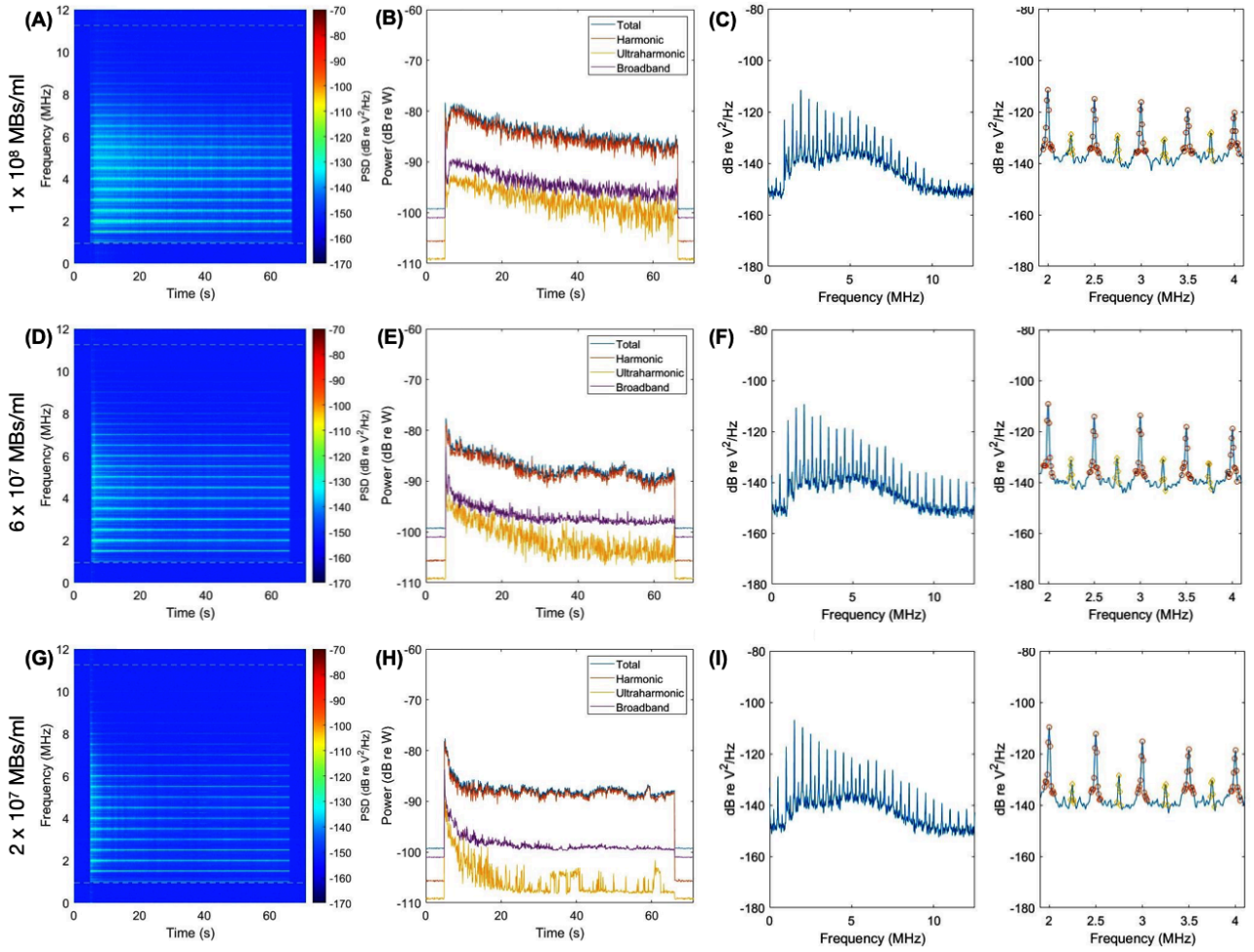


Figure 4.23a. Example spectrum histories over a 60-second exposure of a suspension of His-AF488 microbubbles at 1 x 10⁸ (A-C), 6 x 10⁷ (D-F) and 2 x 10⁷ (G-I) MBs/mL and 200 kPa peak negative pressure. *(A, D, G, J, M, P) Full spectra and (B, E, H, K, N, Q) total, harmonic, ultraharmonic and broadband signal powers, all as a function of time. (C, F, I, L, O, R) Frequency domain PCD trace corresponding to the onset of the ultrasound signal (left), zoomed in (right), showing harmonics (orange) and ultraharmonics (yellow). Drive conditions were 0.5 MHz, 200 kPa peak negative pressure, 10% DC, and a 60-second total exposure duration.*

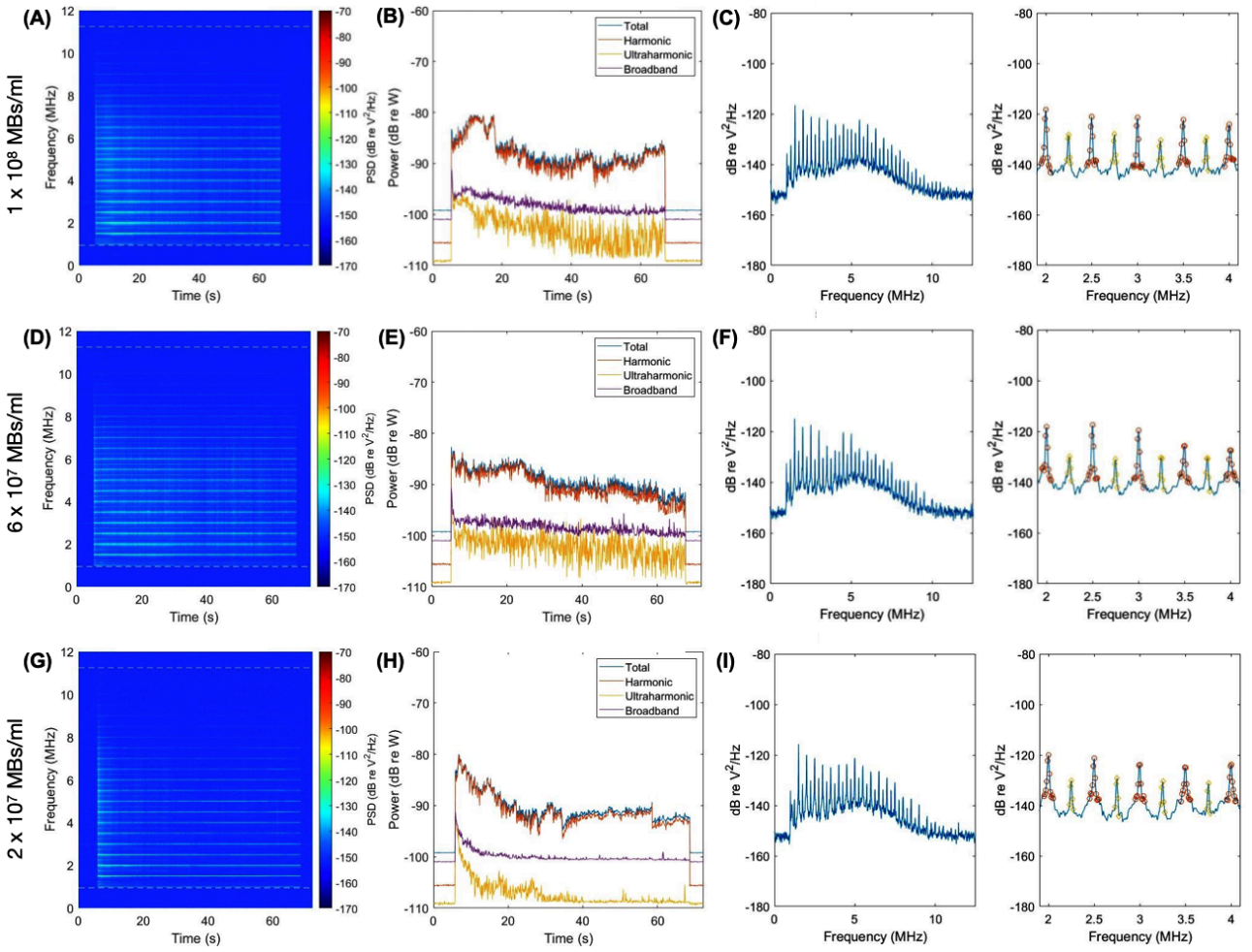


Figure 4.23b. Example spectrum histories over a 60-second exposure of a suspension of His-AF488 microbubbles at 1 x 10⁸ (J-L), 6 x 10⁷ (M-O) and 2 x 10⁷ (P-R) MBs/mL and 200 kPa peak negative pressure. *(A, D, G, J, M, P) Full spectra and (B, E, H, K, N, Q) total, harmonic, ultraharmonic and broadband signal powers, all as a function of time. (C, F, I, L, O, R) Frequency domain PCD trace corresponding to the onset of the ultrasound signal (left), zoomed in (right), showing harmonics (orange) and ultraharmonics (yellow). Drive conditions were 0.5 MHz, 140 kPa peak negative pressure, 10% DC, and a 60-second total exposure duration.*

4.3.3.2 Varying pressures: 0, 50, 100, 150 and 200 kPa PNP, and two microbubble concentrations

The previous experiment was extended to include a wider pressure sweep at only the two highest microbubble concentrations: 1 x 10^8 and 6 x 10^7 MBs/mL. Interestingly, for the pressure and microbubble concentration conditions that match with the previous experiment in *Section 4.3.3.1*, in this experiment, a larger fraction of cells was present in population 1 than in the experiment in *Section 4.3.3.1*, and a corresponding smaller fraction of cells in population 2. The population statistics seem to otherwise follow the same trend with a decrease in the fraction of cells in population 1 for higher ultrasound pressures and higher microbubble concentrations.

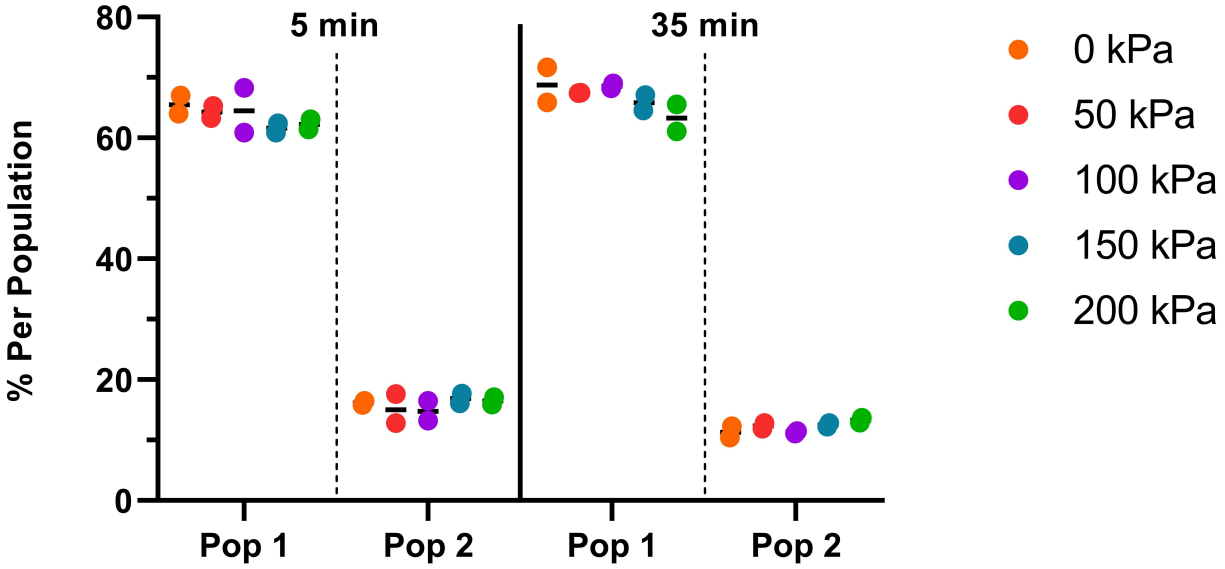


Figure 4.24. Population statistics for Jurkat cells in response to varying peak negative pressures at 1 x 10^8 MBs/mL. *The % of Jurkat cells in population 1 (pop 1), overlapping with the healthy control cells, and shifted cell population named population 2 (pop 2), at five peak negative pressures: 0 (orange), 50 (red), 100 (magenta), 150 (blue) and 200 (green) kPa (N = 2 for all), at t = 0 and t = 35 minutes. Ultrasound driving conditions were 0.5 MHz, 10% DC, and a 60-second exposure duration.*

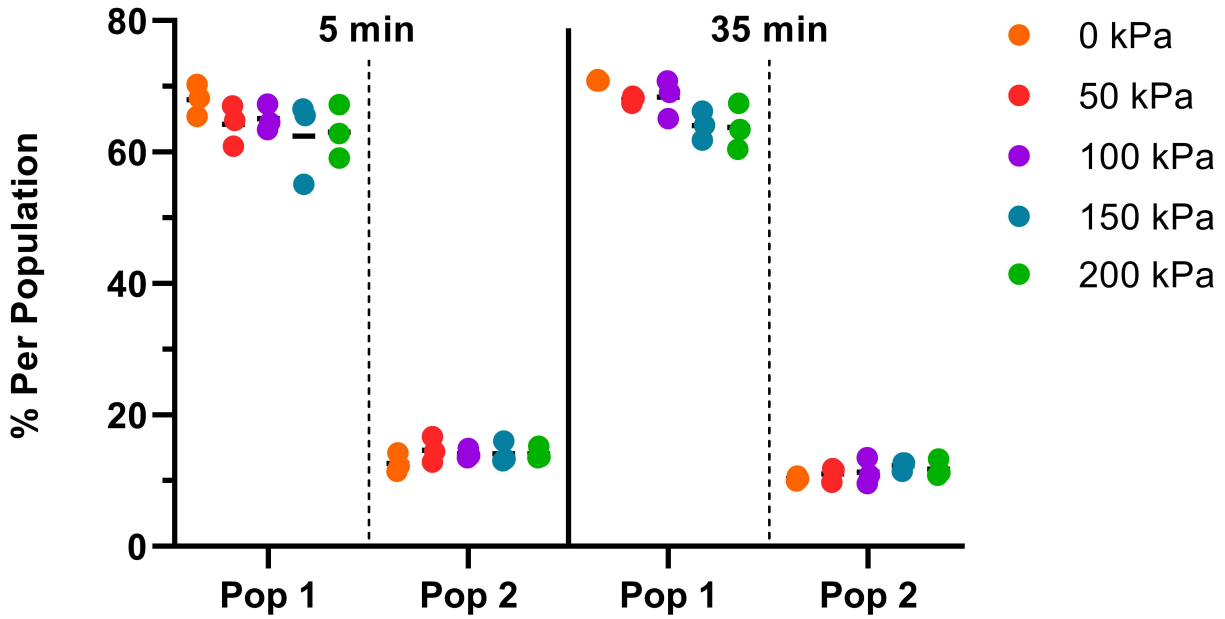


Figure 4.25. Population statistics for Jurkat cells in response to varying peak negative pressures at 6 x 10^7 MBs/mL. *The % of Jurkat cells in population 1 (pop 1), overlapping with the healthy control cells, and shifted cell population named population 2 (pop 2), at five peak negative pressures: 0 (orange), 50 (red), 100 (magenta), 150 (blue) and 200 (green) kPa (N = 3 for all), at t = 0 and t = 35 minutes. Ultrasound driving conditions were 0.5 MHz, 10% DC, and a 60-second exposure duration.*

An explanation for the generally raised level of the fraction of cells found in population 1 may be found when looking at the ultrasound data, as shown in *Figures 4.30* and 4.*31* for 1 x 10^8 and 6 x 10^7 MBs/mL, respectively. The example spectrum histories and signal power intensities look different from those observed for the previous experiment, as shown in *Figure 4.23*. Broadband signal was only briefly present for both microbubble concentrations at 200 (A - C) and 150 kPa (D - F) pressures. The broadband signal quickly falls back to the level of the background noise. *Figure 4.23* shows a slower decline in broadband signal power for the same conditions, potentially contributing to the cells in the experiment in *Section 4.3.3.1* being affected more by the ultrasound exposure, resulting in the lower fraction of cells present in population 1. As for the A549 cells in *Section 4.3.2.2*, the pressure did not seem to substantially affect the population statistics of Jurkat cells, as shown in *Figure 4.24* for 1 x 10^8 MBs/mL and *Figure 4.25* for 6 x 10^7 MBs/mL.

As in previous experiments, the highest fraction of 'membrane tagged' cells in population 1, i.e. cells positive for AF488 and negative for PI, occurred for the no ultrasound condition and high microbubble concentration condition of 1 x 10^8 MBs/mL, as shown in *Figure 4.26*. Consistently, regardless of pressure, the high microbubble concentration, shown in *Figure 4.26*, seems to have led to a higher fraction of cells presenting 'membrane tagging' compared to the low microbubble concentration, as shown in *Figure 4.27*. In most cases, it is seen that this was not improved over the course of 35 minutes. Interestingly, in population 2, the 200 kPa peak negative pressure condition caused the highest fraction of cells to be AF488-positive and PI-negative. This population was increasingly altered in response to ultrasound, and the higher AF488 signal might be caused by increased permeabilisation due to sonoporation at higher ultrasound pressures.

In both *Figures 4.26* and 4.*27*, and *Figures 4.28* and 4.*29*, there was no apparent effect of time on either the 'membrane tagged' or 'PI' fractions. The effect of time seemed more pronounced in the previous experiment in *Section 4.3.3.1*, indicating a potential recovery mechanism presented by the cells in response to microbubbles and ultrasound. There was no indication of such a mechanism in this experiment. Again, this could be due to the different ultrasound treatments received by the cells in this experiment; less effect of the ultrasound means less need and opportunity for recovery. Why the ultrasound treatment differs between this and the previous experiment is unclear. The microbubbles shown in *Figure 4.36* show a similar microbubble size distribution, ultrasound driving conditions were always verified, and the incident voltage and thus pressure was adjusted accordingly, using a high-voltage probe.

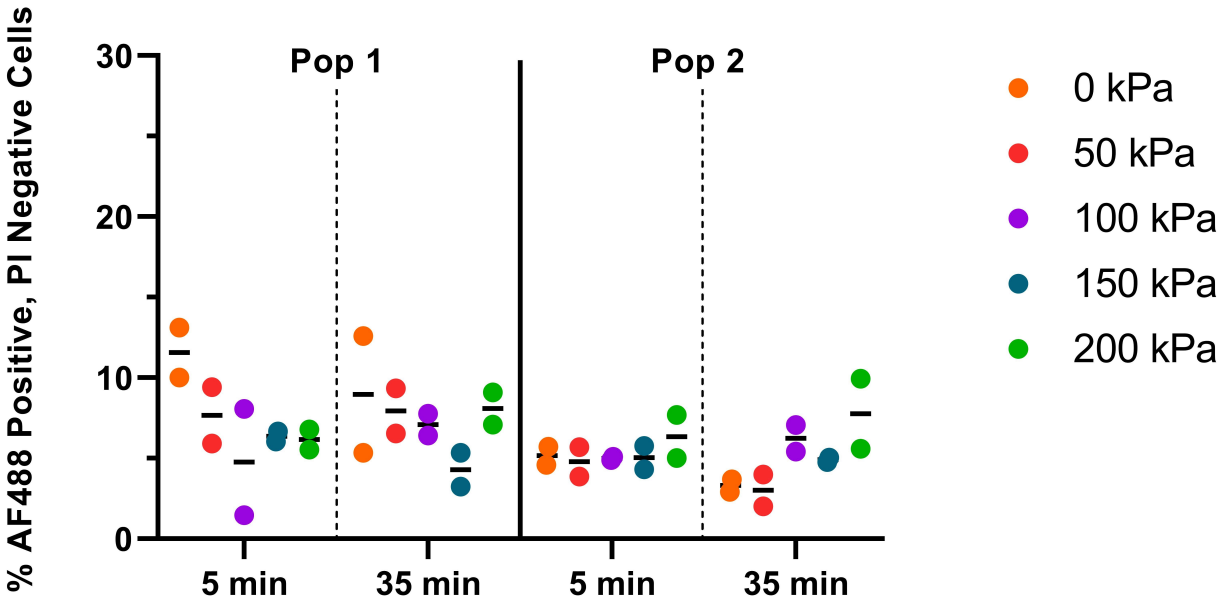


Figure 4.26. 'Membrane tagging' with and potential internalisation of His-AF488 for Jurkat cells in response to varying peak negative pressures at 1 x 10^8 MBs/mL. *The % of Jurkat cells in population 1 (pop 1), overlapping with the healthy control cells, and shifted cell population named population 2 (pop 2) that are positive for His-AF488, either due to lipid transfer or internalisation, and negative for PI, at five peak negative pressures: 0 (orange), 50 (red), 100 (magenta), 150 (blue) and 200 (green) kPa (N = 2 for all), at t = 0 and t = 35 minutes. Ultrasound driving conditions were 0.5 MHz, 10% DC, and a 60-second exposure duration.*

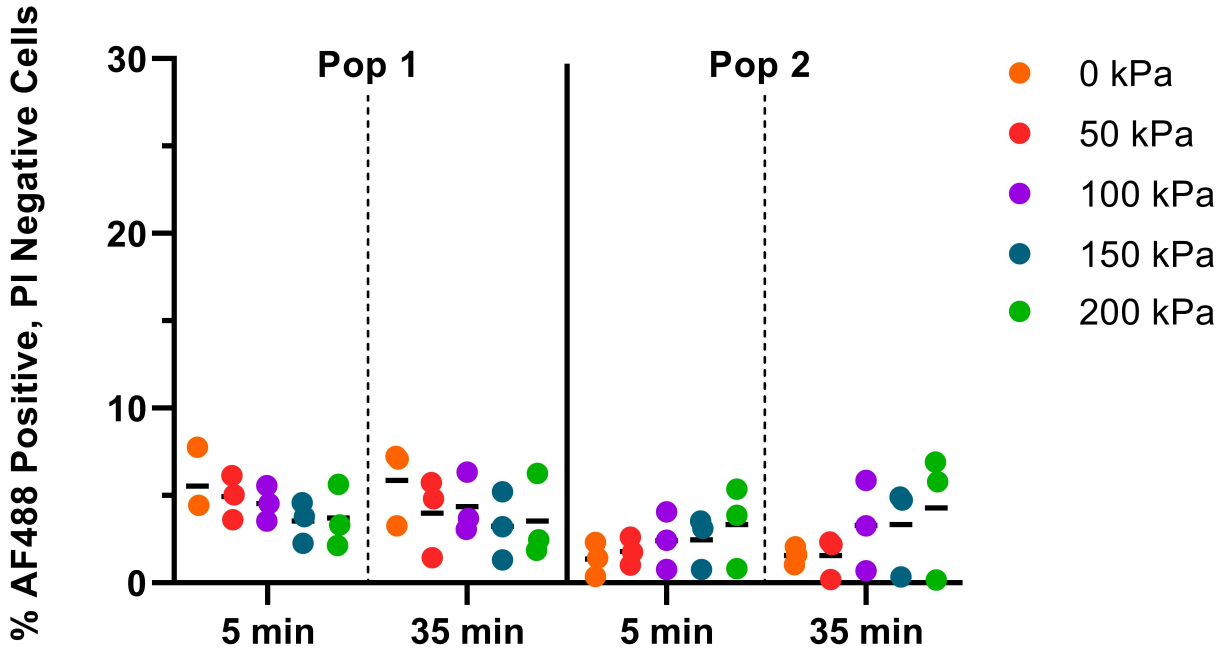


Figure 4.27. 'Membrane tagging' with and potential internalisation of His-AF488 for Jurkat cells in response to varying peak negative pressures at 6 x 10^7 MBs/mL. *The % of Jurkat cells in population 1 (pop 1), overlapping with the healthy control cells, and shifted cell population named population 2 (pop 2) that are positive for His-AF488, either due to lipid transfer or internalisation, and negative for PI, at five peak negative pressures: 0 (orange), 50 (red), 100 (magenta), 150 (blue) and 200 (green) kPa (N = 3 for all), at t = 0 and t = 35 minutes. Ultrasound driving conditions were 0.5 MHz, 10% DC, and a 60-second exposure duration.*

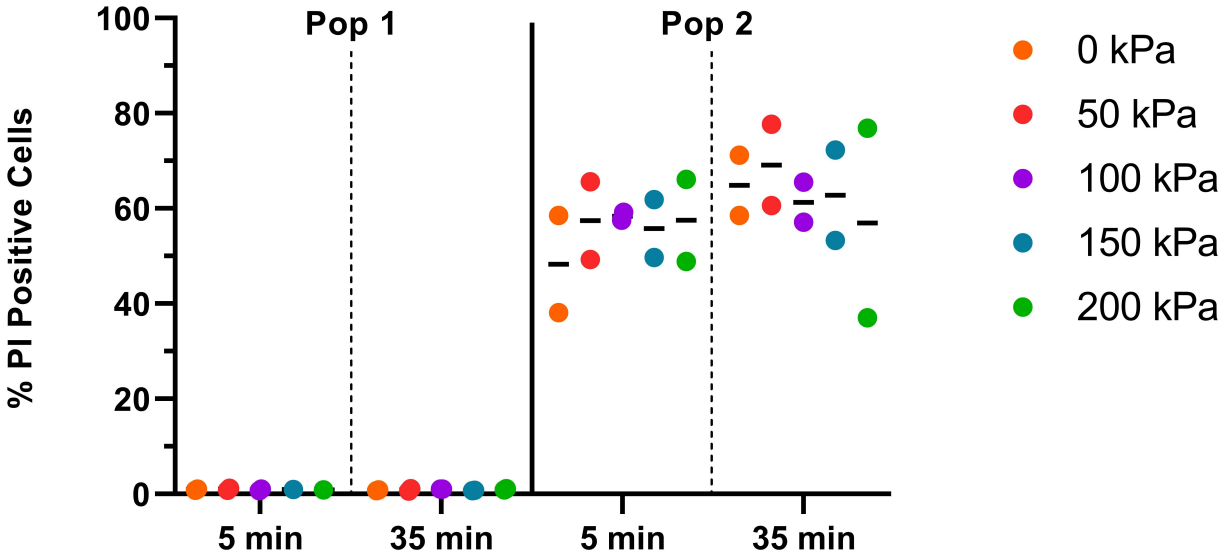


Figure 4.28. PI analysis, an indicator of cell death or permeabilisation, of Jurkat cells in response to varying peak negative pressures at 1 x 10^8 MBs/mL. *The % of Jurkat cells in population 1 (pop 1), overlapping with the healthy control cells, and shifted cell population named population 2 (pop 2) that are positive for PI, an indicator of cell death or permeabilisation, at five peak negative pressures: 0 (orange), 50 (red), 100 (magenta), 150 (blue) and 200 (green) kPa (N = 2 for all), at t = 0 and t = 35 minutes. Ultrasound driving conditions were 0.5 MHz, 10% DC, and a 60-second exposure duration.*

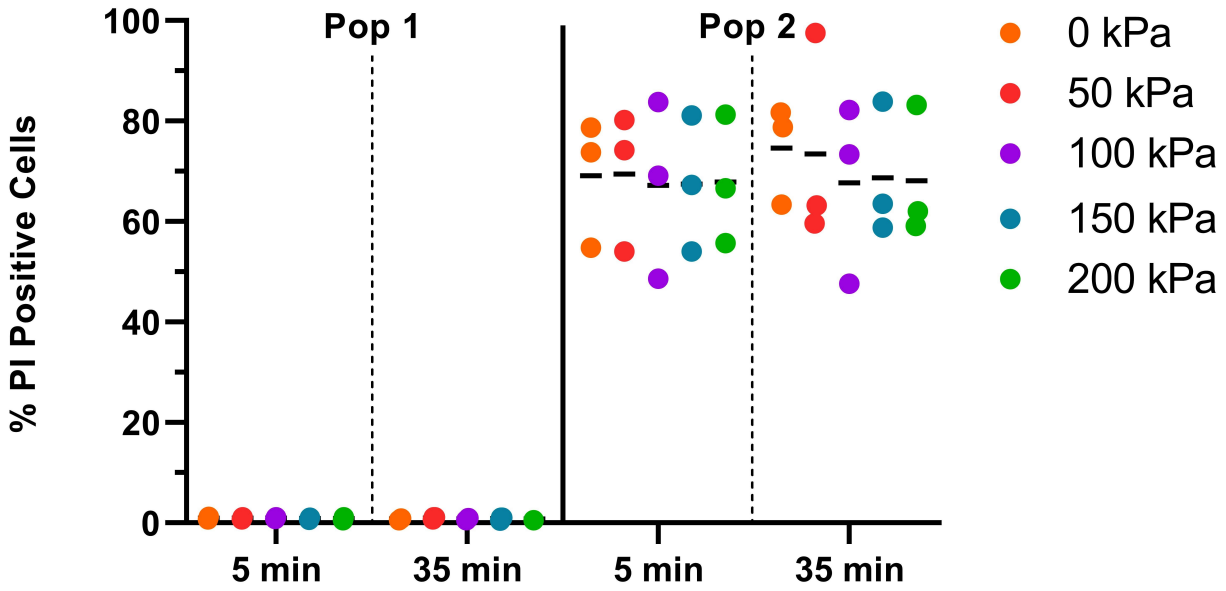


Figure 4.29. PI analysis, an indicator of cell death or permeabilisation, of Jurkat cells in response to varying peak negative pressures at 6 x 10^7 MBs/mL. *The % of Jurkat cells in population 1 (pop 1), overlapping with the healthy control cells, and shifted cell population named population 2 (pop 2) that are positive for PI, an indicator of cell death or permeabilisation, at five peak negative pressures: 0 (orange), 50 (red), 100 (magenta), 150 (blue) and 200 (green) kPa (N = 3 for all), at t = 0 and t = 35 minutes. Ultrasound driving conditions were 0.5 MHz, 10% DC, and a 60-second exposure duration.*

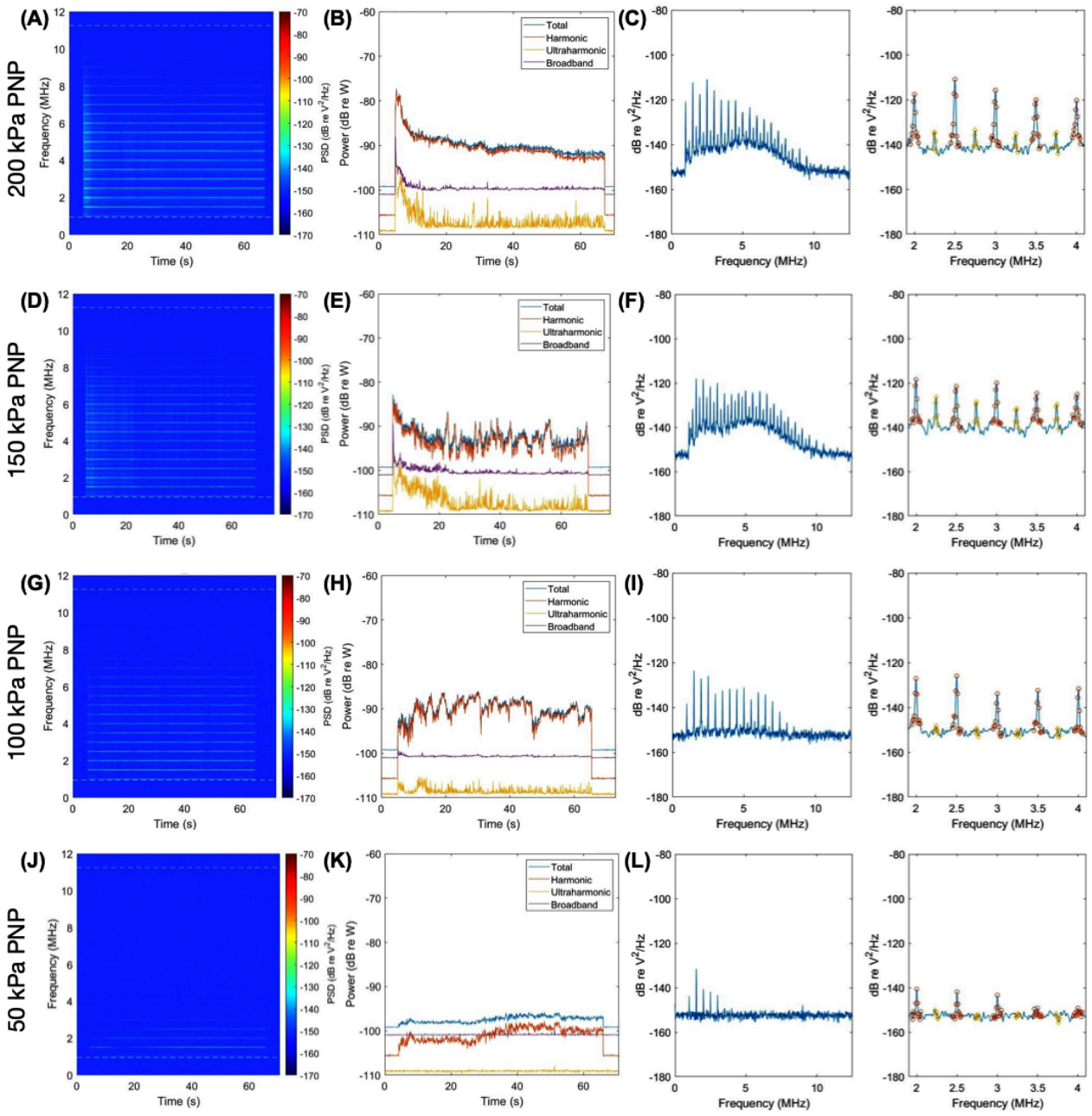


Figure 4.30. Example spectrum histories over a 60-second exposure of a suspension of His-AF488 microbubbles at 1 x 10^8 MBs/mL. *(A, D, G, J) Full spectra and (B, E, H, K) total, harmonic, ultraharmonic and broadband signal powers, all as a function of time. (C, F, I, L) Frequency domain PCD trace corresponding to the onset of the ultrasound signal (left), zoomed in (right), showing harmonics (orange) and ultraharmonics (yellow). Drive conditions were 0.5 MHz, 200 (A-C), 150 (D-F), 100 (G-I), 50 (J-L), 10% DC, and a 60-second total exposure duration.*

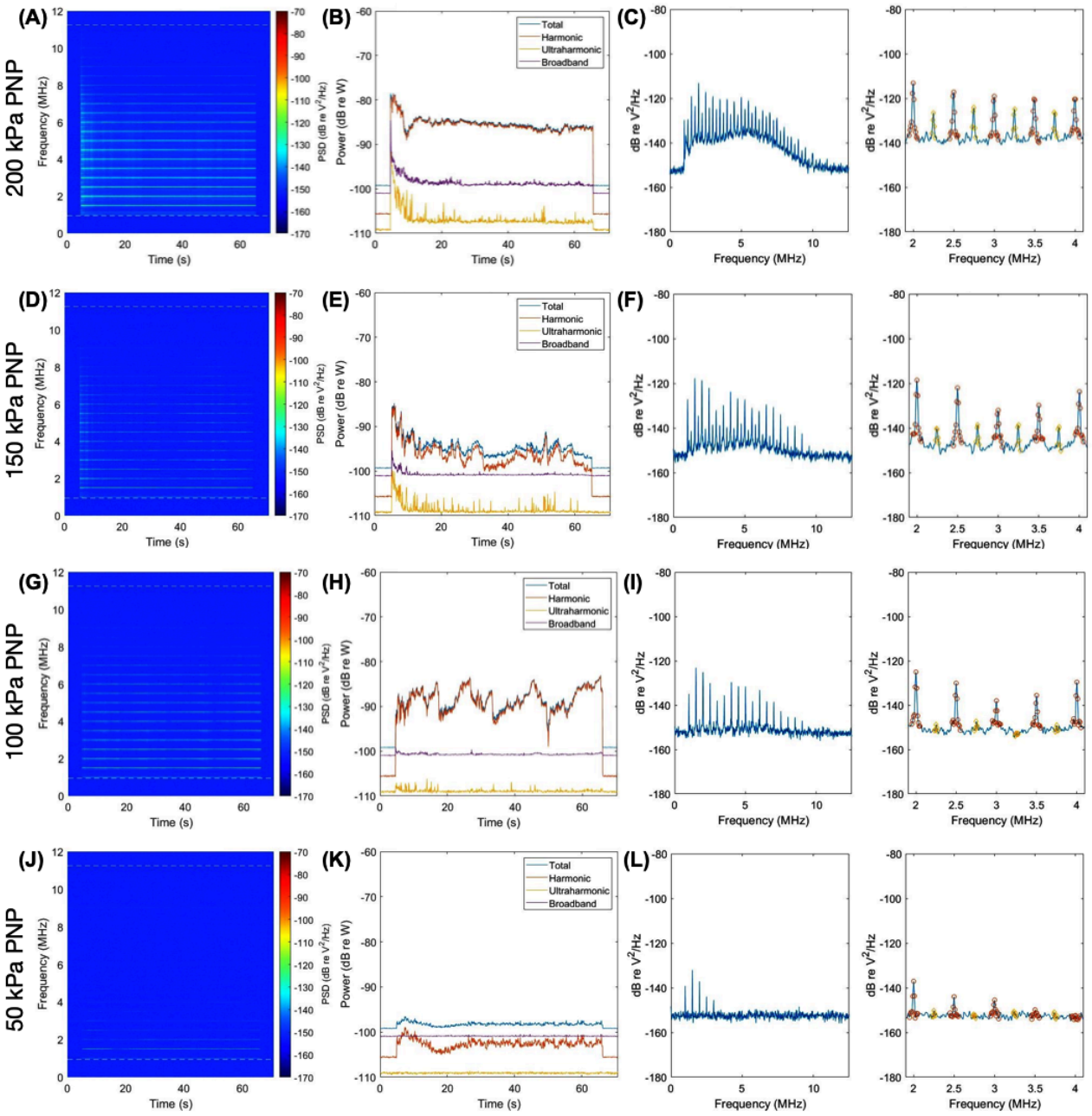


Figure 4.31. Example spectrum histories over a 60-second exposure of a suspension of His-AF488 microbubbles at 6 x 10⁷ MBs/mL. *(A, D, G, J) Full spectra and (B, E, H, K) total, harmonic, ultraharmonic and broadband signal powers, all as a function of time. (C, F, I, L) Frequency domain PCD trace corresponding to the onset of the ultrasound signal (left), zoomed in (right), showing harmonics (orange) and ultraharmonics (yellow). Drive conditions were 0.5 MHz, 200 (A-C), 150 (D-F), 100 (G-I), 50 (J-L), 10% DC, and a 60-second total exposure duration.*

It should be emphasised again that the proportion of cells that were positive for AF488 and negative for PI, as shown in *Figures 4.26* and 4.*27*, as well as the proportion of cells that were PI-positive, as shown in *Figures 4.28* and 4.*29*, should be interpreted in terms of the fraction of cells in each population as shown in *Figures 4.24* and 4.*25*. One more observation is that the lower concentration of microbubbles of 6 x 10⁷

MBs/mL, as shown in *Figure 4.29*, caused a higher uptake of PI in population 2 compared to the higher microbubble concentration of 1 x 10^8 MBs/mL. Even with a marginally lower fraction of cells present in population 2 for each pressure for the 6 x 10^7 MBs/mL condition, as shown in *Figure 4.25*, compared to the 1 x 10^8 MBs/mL condition, as shown in *Figure 4.24*, this still constitutes to more PI-positive cells as a function of the total of cells analysed. It is an interesting observation that may be relevant to finding ideal sonoporation parameters, rather than membrane tagging, for Jurkat cells, but further research regarding this falls outside of the scope of this *Thesis*.

4.3.3.3 Varying duty cycles: 1, 5, 10, 20, 40, 80 and 100%

For the A549 cells, at the pressures and microbubble concentrations tested these factors had minimal effect on the population statistics. However, the variation in duty cycle, i.e. the amount of time the ultrasound is 'on', had a dramatic impact, as shown in *Figure 4.15*. For Jurkat cells, previous experiments described in *Sections 4.3.3.1* and *4.3.3.2* show the effect of pressure and microbubble concentration, so the next step was to investigate the impact of the duty cycle on the population statistics, shown in *Figure 4.32*, 'membrane tagging', shown in *Figure 4.33*, and PI uptake, shown in *Figure 4.34*.

Figure 4.32 shows a similar trend for Jurkat cells as for A549 cells for the fraction of cells present in population 1, with this fraction decreasing with increasing duty cycle from ~60% at 1% duty cycle to 29% at 100% duty cycle at t = 5 minutes and from 62% at 1% duty cycle to 35% at 100% duty cycle at t = 35 minutes. However, rather than the stark increase in the fraction of cells present in population 2 with increasing duty cycle as seen for A549 cells in *Figure 4.15*, the fraction of Jurkat cells in population 2 seemed to only marginally increase. This may be due to Jurkat cells being more sensitive to prolonged ultrasound exposure than A549 cells, causing the destruction of cells rather than morphological alteration. This cellular debris was gated out in flow cytometry analysis, as shown in *Figures 4.1*, and *Figures A.3.2* and *A.3.4* in the *Appendix*, *Section A.3*, by leaving the bottom left corner - small values for both FSC and SSC - out of the analysis gates.

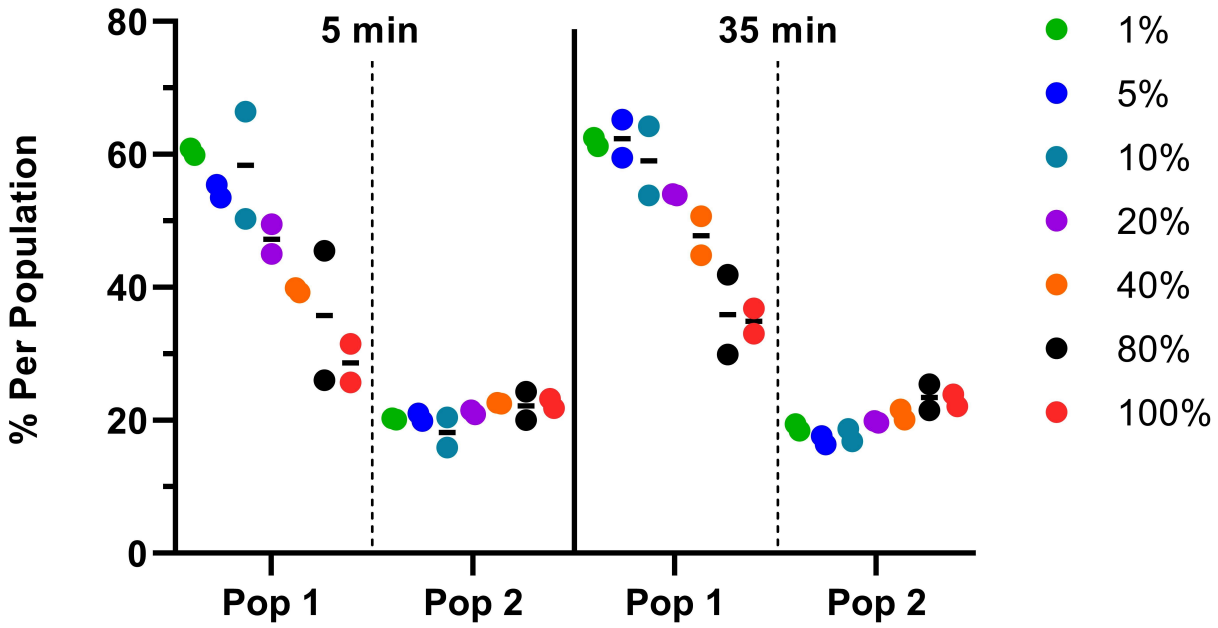


Figure 4.32. Population statistics for Jurkat cells in response to varying duty cycles at 1 x 10⁸ MBs/mL. *It shows the % of Jurkat cells in population 1 (pop 1), overlapping with the healthy control cells, and shifted cell population named population 2 (pop 2) for seven duty cycle conditions: 1 (green), 5 (cobalt), 10 (blue), 20 (magenta), 40 (orange), 80 (black) and 100 (red) % (N = 2 for all), at 0.5 MHz, 200 kPa PNP, for a total exposure duration of 60 seconds. The effects are shown at t = 0 and t = 35 minutes.*

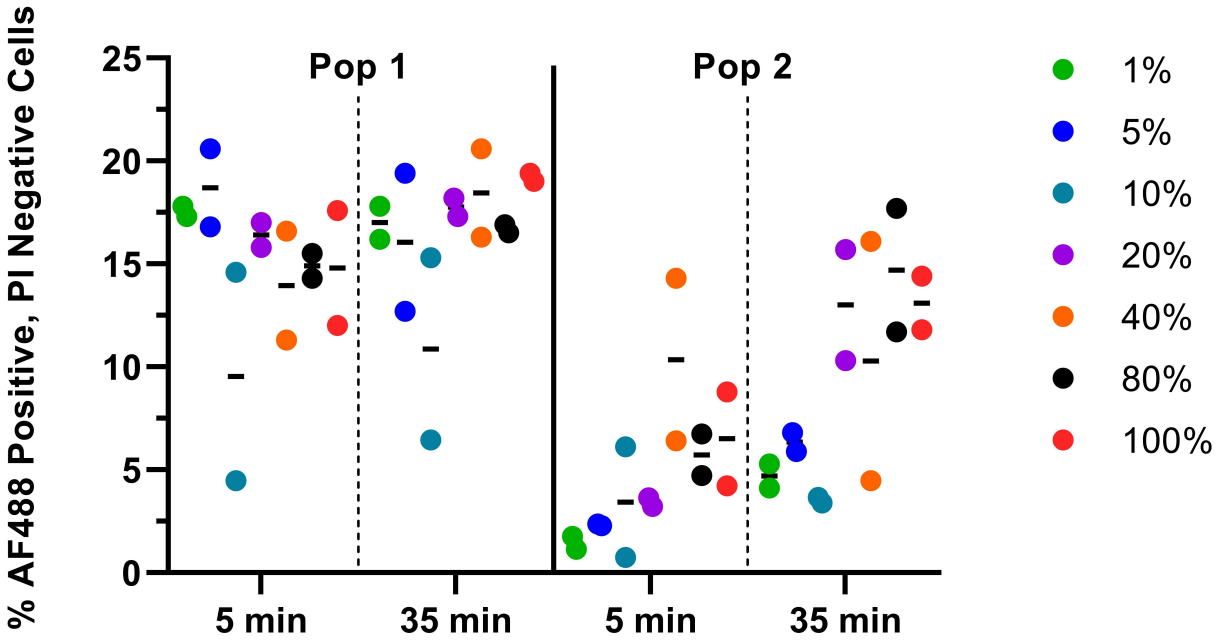


Figure 4.33. 'Membrane tagging' with and potential internalisation of His-AF488 for Jurkat cells in response to varying duty cycles at 1 x 10⁸ MBs/mL. *It shows the fraction of cells in population 1 (pop 1), overlapping with the healthy control cells, and shifted cell population named population 2 (pop 2) that are positive for His-AF488, either due to lipid transfer or internalisation, and negative for PI, for seven duty cycle conditions: 1 (green), 5 (cobalt), 10 (blue), 20 (magenta), 40 (orange), 80 (black) and 100 (red) % (N = 2 for all), at 0.5 MHz, 200 kPa PNP, for a total exposure duration of 60 seconds at t = 0 and t = 35 minutes.*

When looking at the 'membrane tagging' bioeffect, *Figure 4.33* shows large variances, making drawing conclusions challenging. At t = 5 minutes, a small decreasing trend in population 1 might be discerned with an increase in duty cycle, which seems to plateau at 40% duty cycle. Combined with the information in *Figure 4.34*, this increase does not seem to come from a decrease in PI-positive cells with duty cycle in this population. In population 2, an increase in AF488-positive and PI-negative cells can be discerned with an increase in duty cycle and time, as can be seen in *Figure 4.33*. This shows again evidence of a potential recovery mechanism of the Jurkat cells in response to ultrasound.

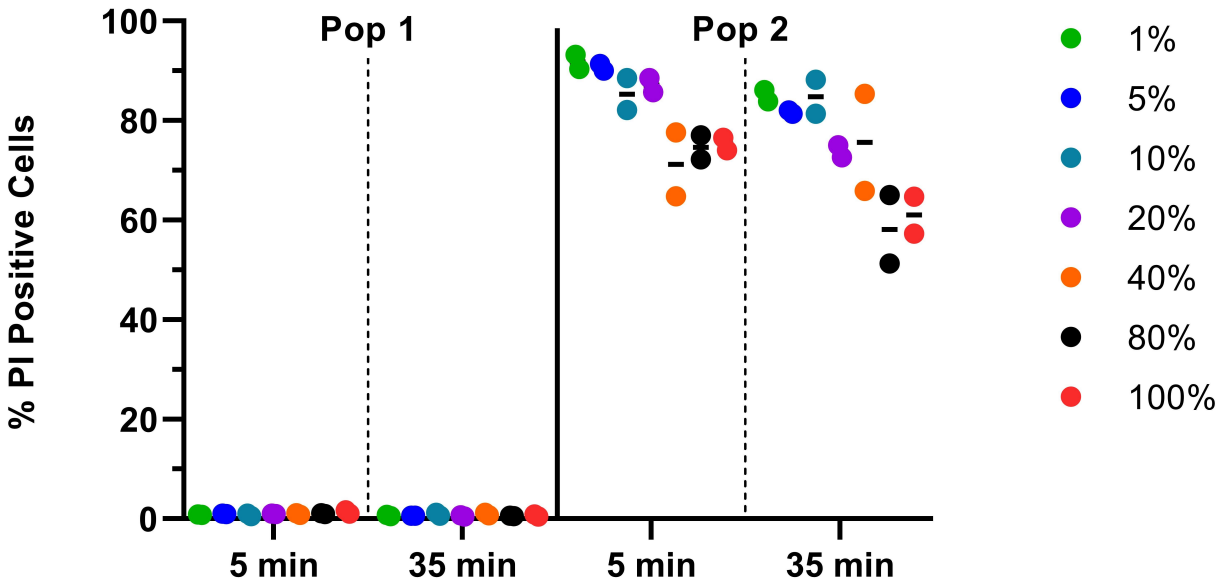


Figure 4.34. PI analysis, an indicator of cell death or permeabilisation, of Jurkat cells in response to varying duty cycles at 1 x 10^8 MBs/mL. *It shows the fraction of cells in population 1 (pop 1), overlapping with the healthy control cells, and shifted cell population named population 2 (pop 2) that are positive for PI, an indicator of cell death or permeabilisation, for seven duty cycle conditions: 1 (green), 5 (cobalt), 10 (blue), 20 (magenta), 40 (orange), 80 (black) and 100 (red) % (N = 2 for all), at 0.5 MHz, 200 kPa PNP, for a total exposure duration of 60 seconds, at t = 0 and t = 35 minutes.*

As with the A549 cells, for the cells in population 2, *Figure 4.34* shows an interesting trend with relative uptake of PI being highest in the lowest duty cycle group and decreasing with increasing duty cycle, e.g., from ~85% for 1% duty cycle to ~61% for 100% duty cycle at t = 35 minutes. Considering the population statistics, at t = 35 minutes, in absolute numbers, this corresponds to 1607 out of 10,000 cells positive for PI for the 1% duty cycle condition and 1400 out of 10,000 cells positive for PI for the 100% duty cycle. This could be explained by the observation that the harsher ultrasound conditions caused population 1 to decrease,

but this decrease was not matched in population 2, possibly due to cell destruction. Hence, cells that would have been PI-positive for the higher duty cycle ultrasound conditions may be disproportionally destroyed, as they are likely to experience the strongest cavitation effects linked to PI uptake.

Examples of the accompanying ultrasound analysis are shown in *Figure 4.35*, with decreasing duty cycle from the top to the bottom of the figure. From both the example spectrum histories as well as the frequency domain PCD traces, it can be observed that the broadband component, and therefore violent microbubble behaviour, decreases with a decrease in duty cycle, which matches the decrease in the fraction of cells in population 1 with increasing duty cycle, as shown in *Figure 4.32*.

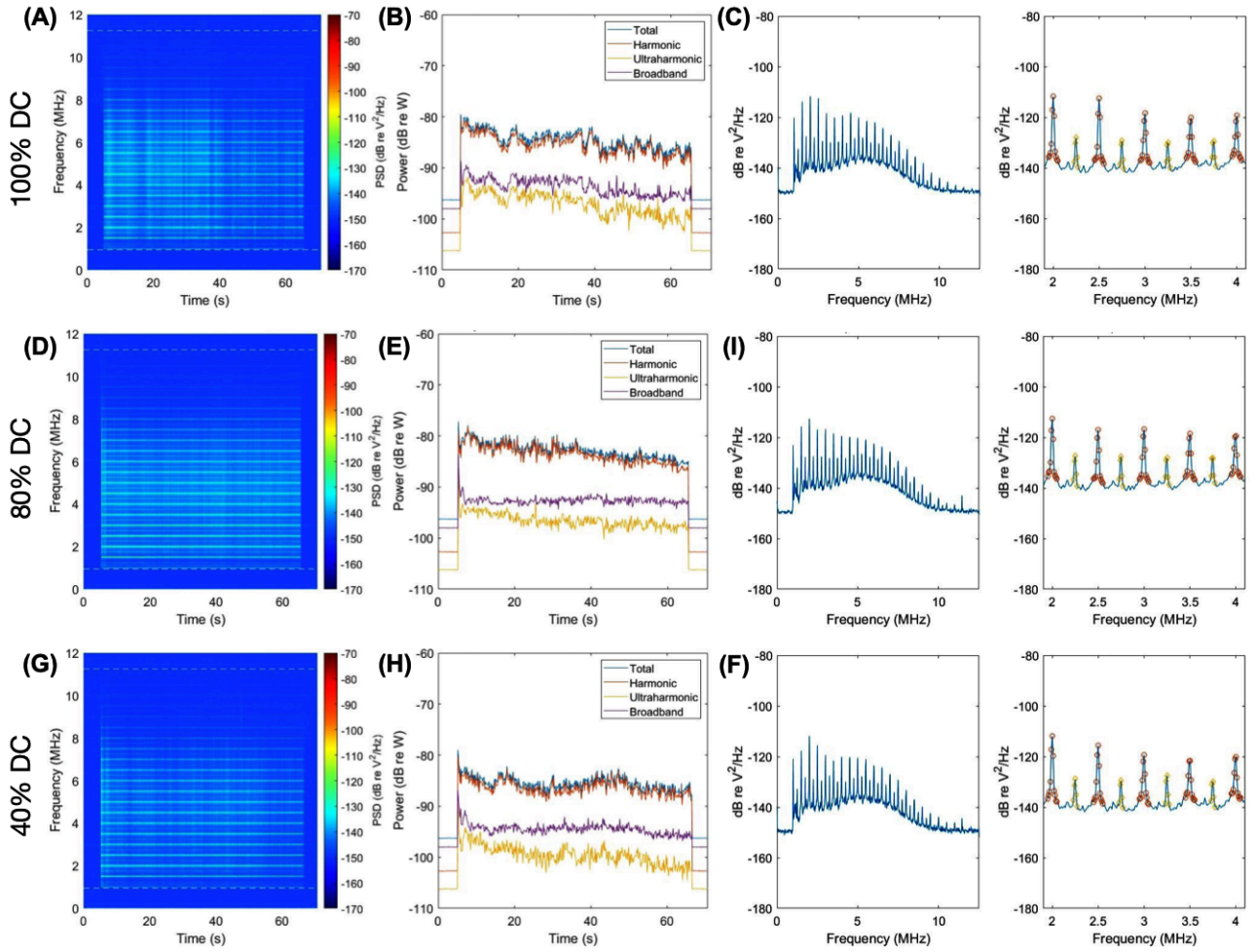


Figure 4.35a. Example spectrum histories over a 60-second exposure of a suspension of His-AF488 microbubbles at 1 x 10⁸ MBs/ mL. *(A, D, G) Full spectra and (B, E, H) total, harmonic, ultraharmonic and broadband signal powers, all as a function of time. (C, F, I) Frequency domain PCD trace corresponding to the onset of the ultrasound signal (left), zoomed in (right), showing harmonics (orange) and ultraharmonics (yellow). Drive conditions were 0.5 MHz, 200 kPa peak negative pressure, for three DC: 40 (G, H, I), 80 (D, E, F), and 100 (A, B, C) %, and a 60-second total exposure duration.*

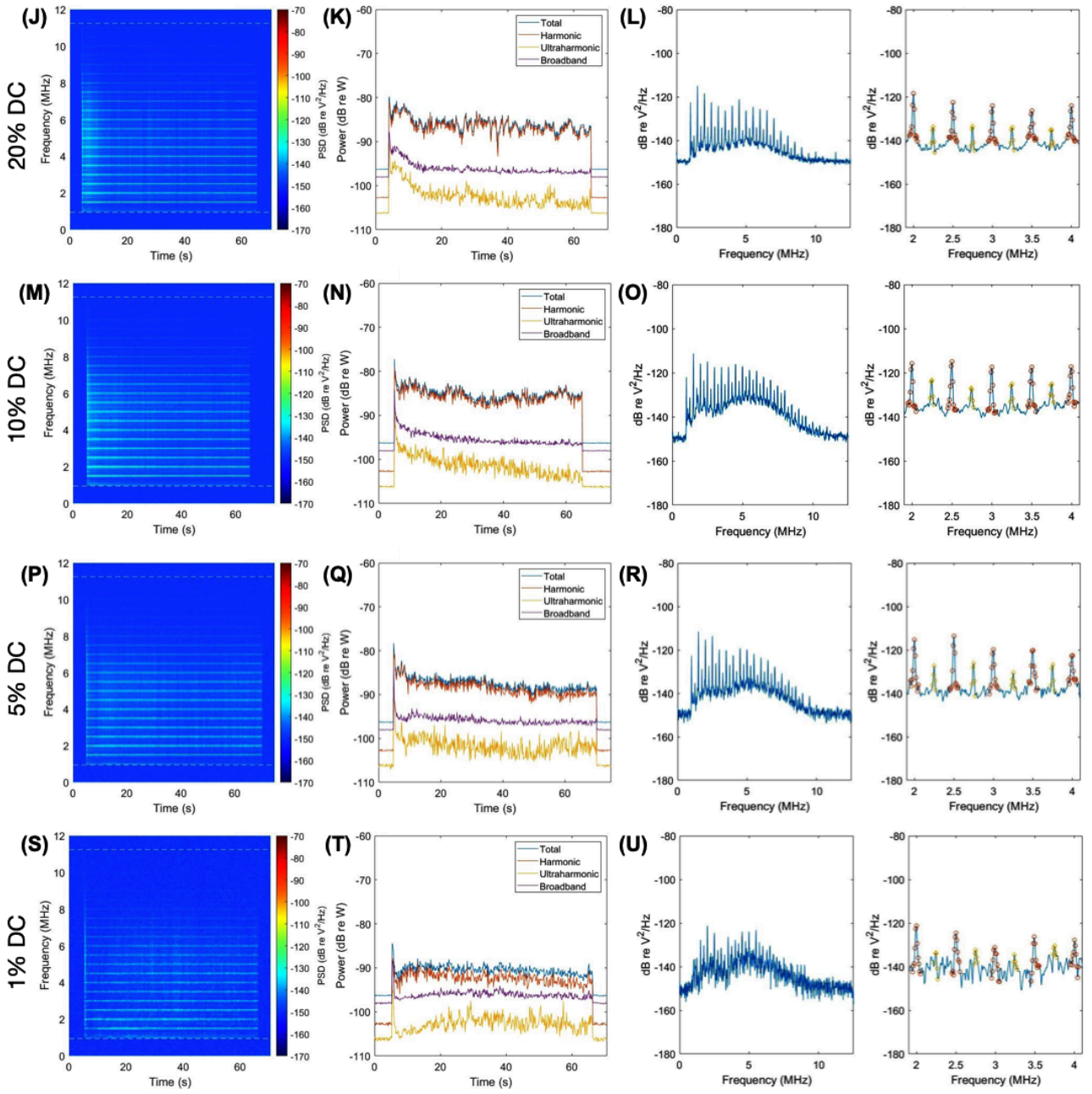


Figure 4.35b. Example spectrum histories over a 60-second exposure of a suspension of His-AF488 microbubbles at 1 x 10⁸ MBs/mL. *(J, M, P, S) Full spectra and (K, N, Q, T) total, harmonic, ultraharmonic and broadband signal powers, all as a function of time. (L, O, R, U) Frequency domain PCD trace corresponding to the onset of the ultrasound signal (left), zoomed in (right), showing harmonics (orange) and ultraharmonics (yellow). Drive conditions were 0.5 MHz, 200 kPa peak negative pressure for four DC: 1 (S, T, U), 5 (P, Q, R), 10 (M, N, O) and 20 (J, K, L) %, and a 60-second total exposure duration.*

In *Figure 4.36*, example microbubble size distributions are shown for the microbubbles used in the experiments in *Sections 4.3.3.1* to *4.3.3.3*.

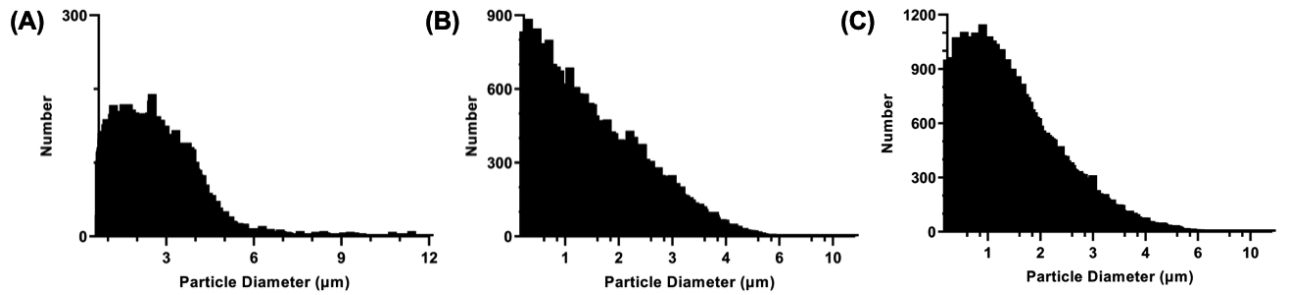


Figure 4.36. Microbubble size distribution histograms for microbubbles used in the experiments in Sections 4.3.3.1 (A), 4.3.3.2 (B) and 4.3.3.3 (C). *Microbubble size distribution histograms for His-AF488 microbubbles used in experiments corresponding to (A), with a mean diameter of 1.81 µm and a concentration of 3.0 x 10^9 MBs/mL (number of events = 30338), (B), with a mean diameter of 1.86 µm and a concentration of 3.7 x 10^9 MBs/mL (N = 30341), and (C), with a mean diameter of 1.80 µm and a concentration of 5.1 x 10^9 MBs/mL (number of events = 51226).*

4.4 Conclusion

In *Chapter 3*, His-GFP functionalised lipid transfer and/or microbubble fusion with A549 cell membranes was observed qualitatively in response to ultrasound exposure using confocal microscopy. This *Chapter* aimed to investigate this process quantitatively using flow cytometry. A549 cells, naturally adherent cells, and Jurkat T cells, suspension cells, were both investigated in suspension. The latter was used as a model immune cell to enable a preliminary assessment of increasing the potency of immune cells by tagging the membrane with relevant proteins. Flow cytometric analysis showed two predominant gates on the forward scatter versus side scatter plot, the first gate (denoted 'population 1') overlapped with live healthy cells, the second gate (denoted 'population 2) was most likely comprised of damaged and dieing cells. For both A549 cells and Jurkat T cells the experimental procedure lead to an increase in the proportion of cells aligned with population 2. This shift, corresponding to morphological changes, was increasingly observed for higher pressures and duty cycles, albeit to a lesser extent for the former. For Jurkat cells at high duty cycle conditions, as shown in *Figure 4.32*, while the fraction of cells in population 1 decreased, the fraction of cells in population 2 increased a disproportional amount compared to A549 cells, as shown in *Figure 4.15*. This might be due to Jurkat cells being more susceptible to the effects of ultrasound, leading to the destruction of cells rather than morphological changes. For both cells, this shift was largely maintained over the course of 35 minutes.

For the primary biological effect of interest - ‘membrane tagging’ - it was observed, generally, that the no or mild ultrasound conditions contributed to the largest fraction of cells being AF488-positive and PI-negative in population 1, i.e., thereby providing the ideal scenario of being 'membrane tagged’ but non-permeabilised. This might be due to the microbubbles only partially being destroyed or not at all, and, therefore, being able to either transfer material to or fuse with the cell membrane.

Interestingly, in contrast to the A549 cells, for the Jurkat cells, an increase over time was observed in this AF488-positive and PI-negative fraction of cells in population 2. This suggests that, while the cells remain morphologically different, a recovery mechanism occurs with a decreasing fraction of cells being permeable to PI at t = 35 minutes. This is corroborated by the findings in the PI graphs, which show a decrease in PI uptake for Jurkat cells over the course of 35 minutes. For A549 cells, especially the first experiment in *Section 4.3.2.1* showed a pronounced decrease in PI uptake - a decrease much less pronounced in the two subsequent experiments in *Sections 4.3.2.2* and *4.3.2.3*. This is possibly due to the use of a different set-up and, hence, different ultrasound and microbubble conditions.

For Jurkat cells, the no to low ultrasound conditions resulted in the most AF488 transfer to PI-negative cells for the cells in population 1, but the more intense ultrasound conditions – either higher pressure or duty cycle - resulted in the most AF488 transfer to PI-negative cells for cells in population 2, at t = 35 minutes. For A549 cells, minimal AF488-positive and PI-negative cells are found in population 2. Low pressures and low duty cycles are generally favourable for His-AF488 tagging in PI-negative cells in population 1 - similar to Jurkat cells. However, it is important to note that flow cytometry as employed in this *Chapter* only gives a simple yes/no answer as to whether His-AF488 is present. Therefore, it does not elucidate in which way His-AF488 is present, i.e. through membrane tagging or internalisation. The PI and the confocal microscopy results shown in *Figure 4.4* indicate internalisation after ultrasound treatment, as well as the desired ‘membrane tagging’.

The observations in this *Chapter* raise the question of why the results in *Chapter 3* showed greatly enhanced ‘membrane tagging’ using ultrasound in adherent A549 cells, while the results in this *Chapter* for A549 cells in suspension do not. A possible explanation could be the fact that microbubble behaviour and subsequent ‘membrane tagging’ affect cells differently in suspension conditions, in which free mixing occurs due to the ultrasound field and secondary microbubble effects such as microstreaming, compared to adherent

conditions, in which the cells are stationary and cannot 'escape' oscillating microbubbles, as is further speculated upon in *Chapter 6*. A potential avenue to address this would be the specific targeting of microbubbles to the cells prior to ultrasound exposure. This would improve the specificity of this mechanism, and thus of any potential future therapies, and limit off-target interactions by selectively directing microbubbles to structures of interest. It may also improve the 'membrane tagging' though microbubble material transfer, as observed in *Chapter 3*. To this end, *Chapter 5* explores the use of His-Transferrin functionalised microbubbles, as A549 cells exhibit overexpressed transferrin receptors on their outer membrane.

Chapter 5 - Targeting of His-Functionalised Microbubbles to Cell Membranes

5.1 Introduction

To improve the specificity of therapy and limit off-target interactions by selectively directing microbubbles to structures of interest, such as the vasculature or cancer cells, microbubbles can be conjugated with targeting ligands, e.g., peptides and antibodies, on their surface (Bracco Diagnostics Inc., NCT02142608).

Several strategies have been employed to target microbubbles to regions of interest. The most straightforward approach relies on the microbubble shell's inherent chemical or electrostatic properties. For example, albumin microbubbles used for contrast echocardiography have been shown to persist within the myocardial microcirculation after ischemia/reperfusion. Lindner *et al*. (2000a) found this to be due to inflammation-induced β_2-integrin– and complement-mediated binding of these microbubbles to activated leukocytes adherent to the venular wall. Another example is the incorporation of phosphatidylserine, a phospholipid, into the microbubble shell, as for the ultrasound contrast agent Sonazoid (perfluorobutane, GE Healthcare, Oslo, Norway). Phosphatidylserine has been shown to increase phagocytosis, and thus uptake, of cells and liposomes by Kupffer cells and macrophages (Allen *et al*., 1988; Nakano *et al*., 2008). These microbubbles have been shown to accumulate in Kupffer cells in the liver (Yanagisawa *et al*., 2007) and active neutrophils in areas of inflamed vascular walls (Linder *et al*., 2000b).

A more selective targeting strategy involves the conjugation of targeting ligands to the microbubble shell that bind to diseased cells. There is a variety of methods through which this conjugation can take place. For example, the targeting ligand can be attached via a poly(ethylene glycol) (PEG) tether, often prior to microbubble fabrication. With this technique, however, as little as 10% of the functionalised lipids may be incorporated into the microbubble shell. Subsequent “washing” of the bubbles can even cause further loss of lipids (Stride *et al*., 2020). One of the most widely used techniques to overcome this issue is the use of the non-covalent (strept)avidin binding to biotin. A variety of options is available for incorporating biotin into the microbubble shell, with a biotinylated lipid being the most common. The resulting biotinylated microbubble can be used as a carrier platform for a variety of either avidinated or biotinylated targeting ligands on the microbubble surface, the latter through dual binding to (strept)avidin, which functions as a bridge (Korpanty *et al*., 2005; Lentacker *et al*., 2007; Wang *et al*., 2012; McEwan *et al*., 2015; Nesbitt *et al*., 2018).

For example, Korpanty *et al*. produced microbubbles conjugated to monoclonal antibodies against endoglin (CD105), VEGF receptor 2 and VEGF-activated blood vessels (the VEGF-VEGFR complex) to image and quantify the effects of antitumour therapies in pancreatic tumour-bearing mice (Korpanty *et al*., 2007). Similarly, vascular cell adhesion molecule 1 (VCAM-1) and intercellular adhesion molecule 1 (ICAM-1), which are upregulated at, e.g., atherosclerosis inflammation sites and brain metastases, have been targeted with microbubbles presenting their respective antibodies (Ottoboni *et al*., 2006; Yan *et al*., 2018). The main advantage of this technique is its universal applicability to load a variety of targeting ligands, but one of its main downsides is the introduction of a foreign protein, (strept)avidin, and the consequent risk of immunogenicity of these microbubbles.

Another coupling strategy involves covalent chemistry reactions, such as aldehyde-amine or thiol-maleimide, forming a thioether bond (Wheatley *et al*., 2007; Myrset *et al*., 2011; Sirsi *et al*., 2012; Nakatsuka *et al*., 2012; Yeh *et al*., 2015). One of the advantages of this technique is the simplicity of the ligand coupling: one ligand has a single thiol group, present in the amino acid cysteine, which attaches to a single maleimide residue on the microbubbles (Unnikrishnan & Klibanov, 2012). Unfortunately, there is a risk of side effects caused by any exposed maleimide groups *in vivo*, and the possibility of non-specific binding to cysteine residues of proteins present in the blood (Stride *et al*., 2020).

In this *Chapter*, A549 cells were again used as a model cell line for consistency. As a lung cancer cell line, A549 cells express a high level of the transferrin receptor (Muralidharan *et al*., 2016), providing an excellent target for functionalised microbubbles. Transferrin (Tf) and the transferrin receptor (Trf) play a critical role in cellular iron uptake, which is required for various processes involved in cell proliferation. For this reason, cancer cells often overexpress the transferrin receptor, and their overexpression is often associated with a poor prognosis. For example, increased expression of the transferrin receptor is seen in certain types of breast cancer (Habashy *et al*., 2010), ovarian cancer (Basuli *et al*., 2017), and lung cancer (Kondo *et al*., 1990), as well as blood malignancies such as leukaemia (Shah, 1990; Patil & Shah, 1996).

To this end, the transferrin receptor has been identified as a universal cancer marker (Essaghir & Demoulin, 2012). The overexpression of the transferrin receptor on malignant cells, its role in cancer cell pathology, the extracellular accessibility and the receptor's role in internalisation make the transferrin receptor an excellent target for antibody-mediated cancer therapy and a target for delivery purposes. For

example, Candelaria *et al*. (2021) used a variety of (human) antibodies that target the transferrin receptor 1 as direct anti-cancer agents in mice. They showed that various anti-transferrin receptor 1 antibodies exhibited anti-cancer activity, with a manageable toxicity profile. This anti-tumour activity was particularly prevalent in malignancies in the blood - an easily accessible target for microbubbles. The main aim of these therapies is to inhibit the function of the transferrin receptor, leading to cancer cell death (White *et al*., 1990; Ng *et al*., 2002; Callens *et al*., 2008).

The other way in which the transferrin receptor can be targeted in cancer therapy is through the use of transferrin, ferritin (Chiou & Connor, 2018) or antibody-drug conjugates to deliver chemotherapeutics such as doxorubicin and cisplatin (Elliot, Stjernholm & Elliot, 1988; Singh, Atwal & Micetich, 1998; Kratz *et al*., 1998), proteins such as toxins (Raso & Basala, 1984; Chignola *et al*., 1995; Jiang *et al*., 2007), oligonucleotides with polylysine and polyethyleneimine as linkers (Wagner *et al*., 1990; Zatloukal *et al*., 1992) and viral vectors (Wightman *et al*., 1999; Kircheis *et al*., 1999).

In 2021, research by Olsman *et al*. investigated the effect of blood-brain barrier (BBB) targeted liposomes compared to non-specific liposomes. They combined microbubble-enhanced ultrasound with both transferrin-loaded liposomes and control liposomes and observed a 40% increase in delivery of transferrin-liposomes across the BBB compared to controls. They hypothesised that combining ultrasound and microbubbles with the BBB-targeting liposomes might enhance endocytosis, which has great potential to improve drug delivery to the brain (Olsman et al., 2021). This observation aligns with research by Fekri *et al*., who observed that ultrasound in combination with microbubbles acutely enhanced clathrin-mediated endocytosis, by tracking the abundance of the transferrin receptor on the cell surface and the internalisation of its ligand transferrin (Fekri *et al*., 2016). Transferrin-bubble liposomes were also used by Demachi *et al*. (2015) to decorate Colon-26 cells with microbubbles to actively carry therapeutic cells for cellular therapy. They reported that they could control these transferrin-bubble liposome decorated cells under ultrasound exposure, measuring their displacement as proportional to the ultrasound pressure, which they did not observe for control cells.

More work has been carried out using ultrasound and transferrin-targeted liposomes. For example, AlSawaftah et al. (2021) used transferrin-modified calcein-loaded liposomes to treat HeLa cells. They investigated drug release from pegylated calcein-loaded liposomes modified with transferrin and triggered

with low-frequency ultrasound. They showed an increase in calcein uptake for these targeted liposomes, which was further enhanced using low-frequency ultrasound (35 kHz). Previous work from this group investigated the release kinetics of calcein from target liposomes upon low-frequency ultrasound exposure (20 kHz), with human serum albumin (HSA), transferrin and arginylglycylaspartic acid (Awad *et al*., 2019) as targeting ligands. They showed increased calcein release for both the human serum albumin- and transferrin-loaded liposomes following ultrasound exposure.

The extensive use of the transferrin receptor as a cancer therapy target in a wide variety of cancers attests to the applicability of this receptor as a therapeutic target. In this *Chapter*, targeting His-transferrin-loaded microbubbles was investigated qualitatively using confocal microscopy and quantitatively using flow cytometry. These His-transferrin-functionalised microbubbles were compared to His-human serum albumin microbubbles, which function as control microbubbles. Furthermore, the transferrin receptor was blocked on A549 cells using free transferrin to assess the specific binding of microbubbles to the transferrin receptor rather than a non-specific binding of the proteins to the cell membrane. Lastly, the effect of ultrasound exposure (0.5 MHz, 150 and 100 kPa PNP, 10% DC, 60-second total exposure) on the targeting ability of both His-transferrin and His-human serum albumin microbubbles was investigated.

5.2 Methods

5.2.1 Microbubbles

As before, a batch sonication protocol was employed to prepare functionalised microbubbles comprising of DSPC (18:0 PC, Avanti Polar Lipids, USA), polyoxyethylene (40) stearate (PEG40S, Sigma Aldrich, UK), and 18:1 nickel-nitrilotriacetic acid (Ni-NTA)-functionalised lipids (*Chapter 2*, *Section 2.2.1*). For this *Chapter*, following centrifugation, microbubbles were loaded with AF680-His_6-transferrin or CF660C-His_6-transferrin (100 μg/mL, SinoBiological, UK, 76.6 kDa) or CF660C-His_6-human serum albumin (100 μg/mL, Abcam, UK, 67 kDa) through an 8-minute incubation and subsequent washing, as described in *Chapter 2* for His-GFP and His-AF488.

Whether His_6-transferrin or His_6-human serum albumin, these proteins were fluorescently labelled to allow observation through confocal microscopy and flow cytometry. To this end, Alexa Fluor™ 680 antibody labelling kit (Invitrogen™, ThermoFisher Scientific, UK) and CF660C Protein Labeling Kit (Biotum, UK) were used to label the proteins and, subsequently, the degree of labelling was assessed using a fluorescent plate reader (FLUOstar Omega, BMG Labtech, UK), as per the manufacturer's guidelines. For the AF680-labelled His-transferrin, protein recovery was ~100%, and the degree of labelling was ~2 dye molecules/protein. For the CF660C-labelled His-transferrin and His-human serum albumin, protein recovery was ~70 and ~100%, respectively, and the degree of labelling was ~2 dye molecules/protein.

5.2.2 Cell culture

In this *Chapter*, immortalised human alveolar adenocarcinoma cells (A549s), as described in *Chapters 3* and *4*, were used. Cells were grown in T-75 flasks in a temperature- and CO_2-controlled incubator at 37°C and 5% CO_2, according to the protocol as outlined in *Chapter 3*, *Section 3.2.2*. Cell concentration and viability were measured using trypan blue and a Countess® Automated Cell Counter (Invitrogen).

For the confocal microscopy experiments, ~0.2 x 10^6 cells were seeded in 35 mm diameter tissue culture-treated Ibidi μDishes (Ibidi, Germany) in 2 mL of growth medium, 48 hours prior to exposure, to obtain near 80% confluence. For flow cytometry experiments, A549 cells were made up to a concentration of 2 x 10^6 per mL in T-25 cells culture flasks to achieve 4 x 10^5 cells per SAT3 transwell during experiments. The cells were kept on ice and periodically gently shaken to avoid adherence to the culture flask. The protocol for the cell preparation for flow cytometry experiments is described in further detail in *Chapter 4*. Unless stated otherwise, all cell culture materials were purchased from ThermoFisher Scientific (UK).

To assess the specificity of the binding of His-transferrin microbubbles to transferrin receptors present on the cell membrane of A549 cells, experiments were carried out with A549 cells which had had their transferrin receptor blocked by free transferrin. To this end, ~ 1.0 x 10^6 cells in μDishes (~80% confluence) were incubated with 10 mg of human transferrin (Sigma Aldrich, UK) for 1 hour at 37 ˚C with 5% CO_2, as per the protocol specified by Muralidharan *et al*. (2017). For the suspension experiment, the same free transferrin : cell ratio was maintained, with 10 mg of human transferrin being incubated with 1.0 x 10^6

cells in suspension for 1 hour at 37 ˚C, while gently shaking every 10 minutes to promote the mixing of cells and free transferrin and avoid the adherence of the cells to the culture flask.

5.2.3 Ultrasound set-up

For all flow cytometry experiments, the SAT3 set-up was used as described in *Chapter 3*, Section *3.2.3.3*. A range of peak negative pressures - 0, 100 and 150 kPa - was investigated with different microbubble formulations at a constant microbubble concentration of 1 x 10^8 MBs per mL to assess the targeting ability of His-transferrin microbubbles compared to His-human serum albumin microbubbles. After exposure, the cell samples were split for either flow cytometry analysis immediately or 35 minutes post exposure (two times 70 µL in 430 µL of DPBS each). The experimental protocol, data collection and analysis were performed as described in *Chapter 3*, *Sections 3.2.3.4* and *3.2.3.5*.

5.2.4 Targeting protocol

The targeting protocol for assessing microbubble targeting to adherent cells in Ibidi μDishes was as follows. Cells were incubated for 8 minutes with 1 μg/mL of the plasma membrane stain CellMask Green (ThermoFisher Scientific, UK). Simultaneously, 12 mL of either His-transferrin or His-human serum albumin microbubbles was prepared at a final concentration of 2 x 10^7 MBs/mL in DPBS. Cells were washed twice with warm DPBS. As for the SAT2 experiments described in *Chapter 3*, *Section 3.2.3.1*, a PDMS lid was press-fitted to the μDish, and the headspace was subsequently filled with the microbubble suspension. The μDish was then turned over so that the cells were situated at the top of the dish and placed on a shaker (IKA KS 130 basic, UK). The dish was shaken gently for 5 minutes at 80 rpm to facilitate contact between the microbubbles and the cell layer. The microbubble suspension in the μDish was then replaced with warmed DPBS, and the dish was placed on the shaker the right way up and shaken more violently at 480 rpm for 1 minute. This was done so that any non-attached microbubbles would come off the cell layer. The microbubble suspension in the μDish was then replaced with 1 mL of warmed DPBS, and the μDish was imaged on the confocal microscope, as outlined in *Section 5.2.5*.

The targeting protocol for the suspension experiments using flow cytometry closely resembles the protocol for the SAT3 experiments described in *Chapters 3* and *4*. In short, 200 μL of 2 x 10^6 A549 cells/mL was incubated with four different concentrations - 2 x 10^6, 1 x 10^7, 5 x 10^7, 1 x 10^8 - of either His-transferrin or His-human serum albumin microbubbles as specified for each experiment in the *Results* section, corresponding to 1, 5, 25 and 50 microbubbles per cell. Then, the flow cytometry protocol detailed below was followed.

5.2.5 Targeting assessment - confocal microscopy

For the adherent A549 cells in Ibidi μDishes, qualitative analysis of the targeting ability of His-transferrin microbubbles was performed using confocal fluorescence microscopy (LSM 780 and LSM 710, Carl Zeiss AG, Germany), with magnifications including 10x (EC Plan-NeoFluar 10x/0.3 M27), 20x (Plan-Apochromat 20x/0.8 M27), 40x (EC Plan-NeoFluar 40x/1.3 Oil DIC M27) and 63x (Plan-Apochromat 63x / 1.40 Oil DIC M27).

Cells were stained with a plasma membrane stain, 1 μg/mL CellMask Green, which has its excitation maximum at 522 nm and its emission maximum at 535 nm and can be analysed using standard FITC settings on the microscope. On the LSM 780 and LSM 710, it was excited by the 488 nm laser, and the emitted signal is picked up between 493 and 628 nm. His-transferrin and His-human serum albumin, labelled with either Alexa Fluor 680 or CF660C, microbubbles were excited by the 633 nm laser. The emitted signal was picked up between 661 and 759 nm. Photomultiplier tube (PMT) reflections were simultaneously obtained to resemble brightfield images.

Qualitatively, using confocal microscopy, the coating of the cells (green fluorescent) with microbubbles (black shadows on the PMT reflections) can be observed, as shown in *Figures 5.2* and *5.5*. Furthermore, the protein-lipid transfer from both His-transferrin and His-human serum albumin microbubbles to the cell membranes was investigated at 40x magnification, as shown in *Figures 5.3* and *5.6*.

5.2.6 Targeting assessment - flow cytometry

To obtain quantitative data as well as the qualitative results using confocal microscopy, flow cytometry (Beckman Coulter CytoFLEX, USA) was employed to assess the number of cells to which the various microbubble formulations were attached, as well as the viability of the cells after treatment. Each particle was analysed for visible light scatter and multiple fluorescence parameters. In this *Chapter*, the fluorescence parameters studied included CF660C (ex/em: 667/685 nm) and 4',6-diamidino-2-phenylindole, dihydrochloride (DAPI) (ex/em: 358/461 nm). DAPI (Invitrogen™ , ThermoFisher Scientific, UK) was used as a live/dead stain and indicator of permeabilisation, similar to how PI was used in *Chapter 4*. DAPI is normally cell-impermeant and can thus be used as a live/dead stain and model drug, as its uptake indicates membrane permeabilisation, whether due to sonoporation or death.

As in *Chapter 4*, two populations could readily be gated in the FSC vs SSC plots: i) a population overlapping with the live control cells, named population 1, and ii) a population that appears to comprise a larger proportion of the total after exposure to both microbubbles alone and microbubbles with ultrasound treatment, named population 2, as can be seen in the flow cytometry data presented in *Appendix A.4*. In *Chapter 4*, this second population was morphologically different from the majority of the control cells and showed a generally higher percentage of PI uptake, possibly indicating permeabilisation or cell death. In the interest of the aim of this *Chapter* - investigating the feasibility of targeting microbubbles to the cell membrane to promote microbubble material transfer rather than internalisation - cells in this second population were excluded from the analysis.

All samples (70 μL of cell suspension in 430 μL of DPBS) were measured at time equals 5 minutes after ultrasound exposure and time equals 35 minutes after ultrasound exposure - allowing for 5 minutes incubation with 5 μL of 10 μg/mL DAPI stock solution for each time point (Miltenyi Biotec, DAPI Staining Protocol for FACS). The range of time points was chosen to observe any direct effects of the ultrasound treatment and any effects occurring on the order of minutes, e.g., the potential resealing of membrane pores due to sonoporation (Helfield *et al*., 2016). Samples were kept on ice immediately after treatment to slow down degradation and enzymatic activity. It is important to note, however, that keeping the samples on ice also leads to inhibition of transferrin receptor recycling via the endocytotic pathways (Sheff *et al*., 1999). For

each sample, 10,000 events (microbubbles or cells) were analysed, and appropriate controls (live cells, heated and thus dead/dying cells, and microbubbles) were carried out prior to commencing the experiment.

The APC-A700, corresponding to CF660C and thus microbubbles, and PB450, corresponding to DAPI, channel gatings, as shown in the *Appendix*, *Section A.4*, were chosen based on the live cell control sample, which is negative for both CF660C and DAPI. To assess targeting efficiency, the percentage of cells positive for CF660C and negative for DAPI was investigated for both His-transferrin and His-human serum albumin microbubbles on regular A549 cells and His-transferrin microbubbles on A549 cells which had their transferrin receptor blocked. The figures show the individual repeats ($N = 2$ or 3) and the mean (black line).

5.3 Results and Discussion

The work in this *Chapter* examined the ability of His-transferrin loaded microbubbles to target A549 cells and, subsequently, promote 'membrane tagging'. This was assessed both qualitatively using confocal microscopy and quantitatively using flow cytometry. The His-transferrin loaded microbubbles were compared to His-human serum albumin microbubbles on non-TfR blocked A549 cells. Furthermore, experiments were conducted in which the transferrin receptor on A549 cells was blocked using free transferrin to assess the specificity of the binding of His-transferrin microbubbles. Lastly, the effect of ultrasound exposure (0.5 MHz, 100 and 150 kPa peak negative pressure, 10% duty cycle, and a 60-second total exposure duration) on the microbubble targeting and lipid transfer from both His-transferrin and His-human serum albumin microbubbles to cells was investigated.

The results below are summarised by i) qualitative assessment of targeting efficiency and microbubble material transfer using confocal microscopy and ii) quantitative assessment of targeting efficiency and lipid transfer using flow cytometry. The figures correspond to:

1. His-transferrin microbubbles versus control microbubbles, assessed by confocal microscopy (*Figures 5.1-5.3*),

2. His-transferrin versus His-human serum albumin microbubbles with non-blocked and blocked Tf-receptor A549 cells, assessed by confocal microscopy (*Figures 5.4-5.6*),
3. His-transferrin versus His-human serum albumin microbubbles without ultrasound, assessed by flow cytometry (*Figures 5.7* and *5.8*),
4. His-transferrin versus His-human serum albumin microbubbles at 0, 100 and 150 kPa peak negative pressure, assessed by flow cytometry (*Figures 5.9-5.13*),
5. His-transferrin versus His-human serum albumin microbubbles with non-blocked and blocked transferrin receptor A549 cells, assessed by flow cytometry (*Figures 5.14-5.17*).

5.3.1 Qualitative observation of His-Tf microbubbles targeting to A549s using confocal microscopy

5.3.1.1 His-Tf targeted microbubbles versus control microbubbles

Firstly, the targeting ability of His-transferrin functionalised microbubbles to A549 cells was assessed using confocal microscopy and compared to microbubbles that were not loaded with His-transferrin.

Figure 5.1 shows that both His-transferrin and control microbubbles, which are the same DSPC : PEG40S : DGS-NTA(Ni) microbubbles but without the fluorescent AF488, have comparable microbubble size distributions, eliminating differences in microbubble size and concentration as possible causes for the difference in results. *Figure 5.2*, and especially the enlarged fields-of-view (*E*) and (*F*), shows an increased targeting ability of His-transferrin loaded microbubbles (*A*, *C*, *E*) compared to microbubbles that lack His-transferrin (*B*, *D*, *F*), with the latter showing attachment of a negligible quantity of microbubbles.

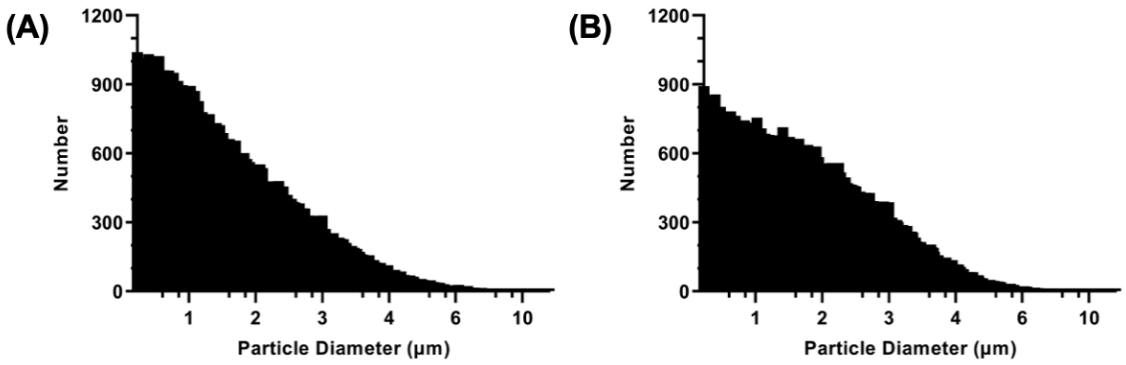


Figure 5.3. Microbubble size distribution histograms for His-transferrin microbubbles (A) and control microbubbles (B). *(A) has a mean diameter of 2.09 µm and a concentration of 5.1 x 10^9 MBs/mL (number of events = 51212), and (B) has a mean diameter of 2.16 µm and a concentration of 5.2 x 10^9 MBs/mL (number of events = 51694), respectively.*

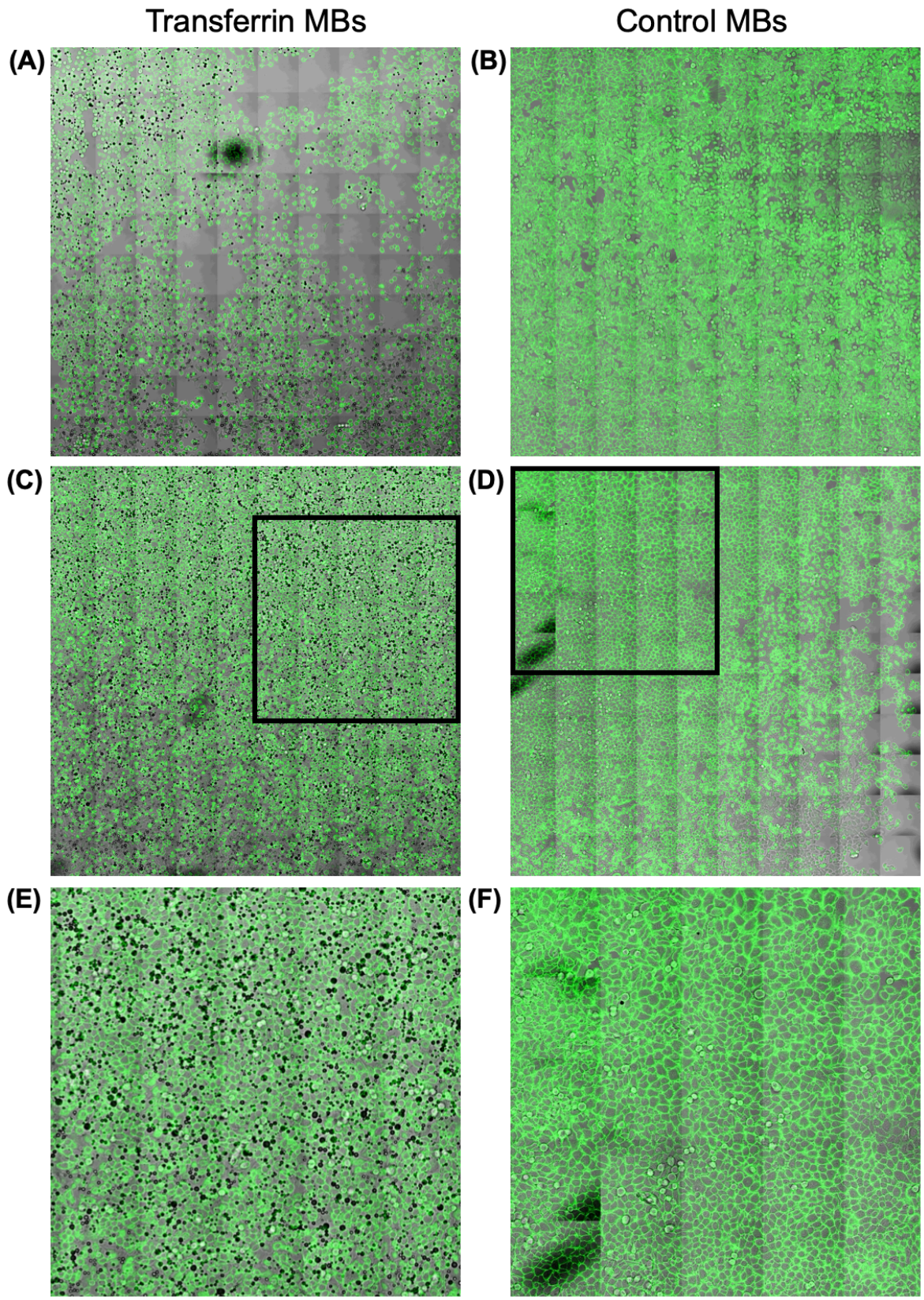


Figure 5.2. Qualitative assessment of His-transferrin microbubbles versus control microbubbles. *10x tilescan confocal microscopy images of A549 cells (green) and microbubble PMT overlays (brightfield-like) for two repeats of His-transferrin functionalised microbubbles (A, C) and control microbubbles (B, D). Zoomed in fields of view of His-transferrin microbubbles (E) and control microbubbles (F) as indicated by the black squares on (C) and (D), showing a clear difference in targeting ability of both microbubble types (N = 2 for all). Image size in (A - D) is 1934.39 x 1934.39 µm.*

To ensure the His-transferrin microbubbles were specifically attached to the cells/cell membranes, a higher magnification was used (40x objective). Four example fields of view are shown in *Figure 5.3*. It is clear that the His-transferrin microbubbles and microbubble lipid fragments, leftover after the dissolution of the microbubbles, were deposited on the cell membrane.

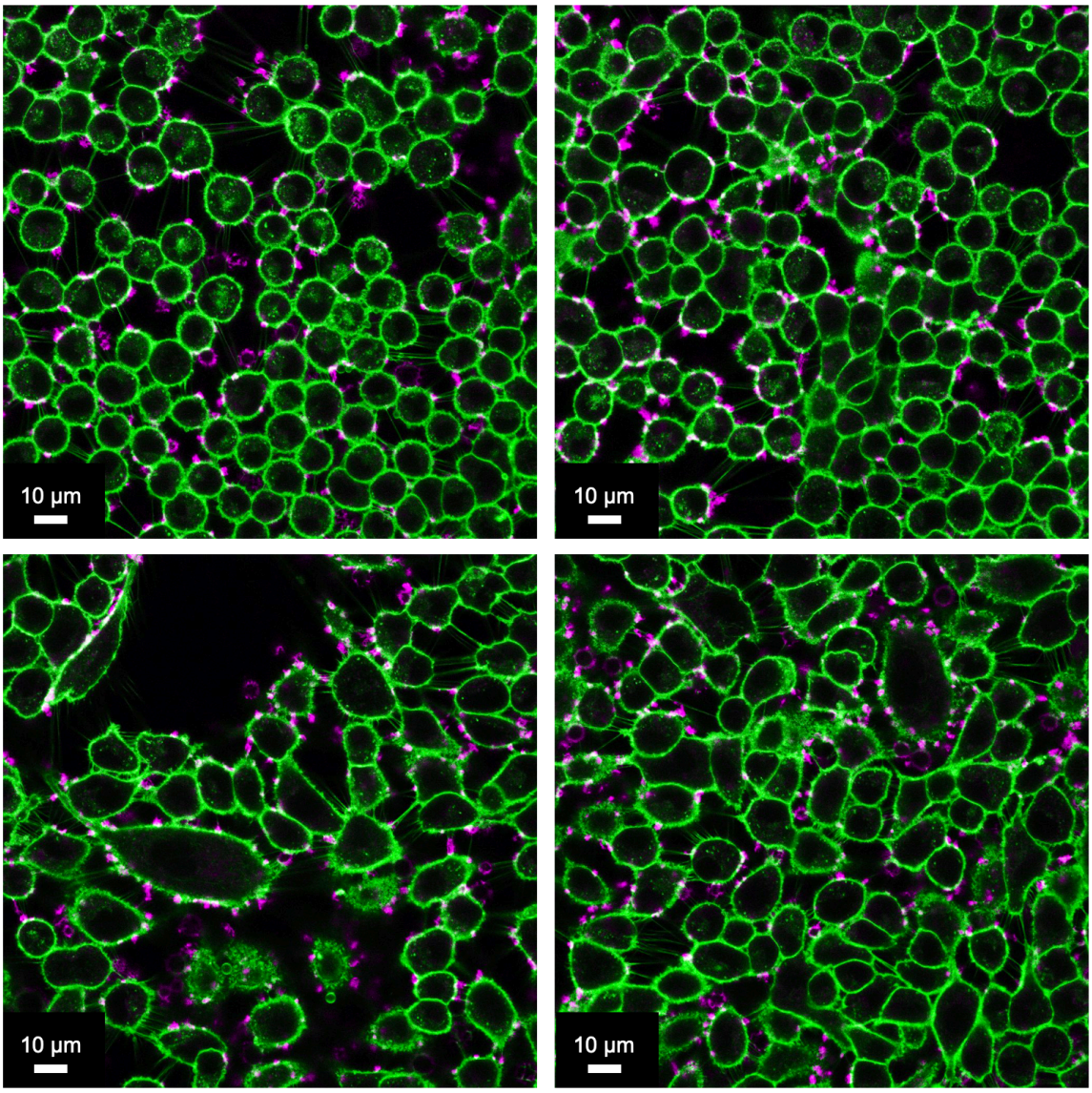


Figure 5.3. Example confocal microscopy images (40x) of A549 cells (green) and Alexa Fluor 680 labelled His-transferrin functionalised lipids and microbubbles (magenta). *It shows both microbubbles and microbubble fragment deposits on the cell membrane (N=3).*

5.3.1.2 His-Tf versus His-HSA microbubbles with regular and Tf-receptor blocked A549 cells

Secondly, to assess the specificity of the His-transferrin loaded microbubble binding to A549 cells, two alternatives were investigated: i) the binding of His-human serum albumin microbubbles to A549 cells, and

ii) the binding of His-transferrin microbubbles to A549 cells where the transferrin receptor was blocked by free human transferrin.

His-human serum albumin microbubbles function as control protein-loaded microbubbles, as A549 cells exhibit human serum albumin receptors, albeit not upregulated (Peng *et al*., 2015; Chaiwaree *et al*., 2020). Human transferrin and human serum albumin are both negatively charged at the physiological pH at which these experiments were conducted, as their isoelectric points are 5.7 (Vesterberg & Breig, 1981) and 4.7 (Vlasova & Saletsky, 2009), respectively. Therefore, the charge of these proteins is unlikely to contribute to their targeting to negatively charged plasma membranes.

Another way to test the specificity of the microbubble targeting is by blocking the receptor to which the His-transferrin microbubbles bind. This was achieved by blocking the transferrin receptors by saturating these receptors with free transferrin, as per the protocol described by Muralidharan *et al*. (2017).

First, *Figure 5.4* shows that both His-transferrin and His-human serum albumin microbubbles have comparable microbubble size distributions. In *Figure 5.5*, a comparison between these three conditions can be observed, which shows His-transferrin microbubbles present on non-TfR blocked A549 cells in larger quantities than both His-human serum albumin microbubbles on non-TfR blocked A549 cells and His-transferrin microbubbles on TfR blocked A549 cells. No distinct difference can be observed between the latter two conditions from these confocal images.

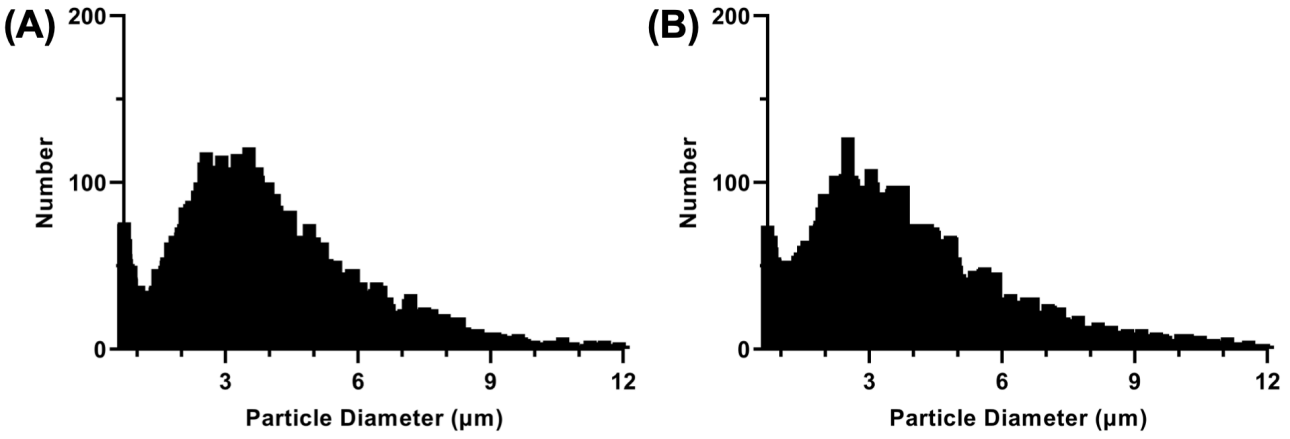


Figure 5.4. Microbubble size distribution histograms for His-transferrin microbubbles (A) and His-human serum albumin microbubbles (B). *It shows His-transferrin microbubbles (A), with a mean diameter of 2.59 µm and a concentration of 1.9 x 10^9 MBs/mL (number of events = 19244), and His-human serum albumin microbubbles (B), with a mean diameter of 2.37 µm and a concentration of 2.0 x 10^9 MBs/mL (number of events = 19776).*

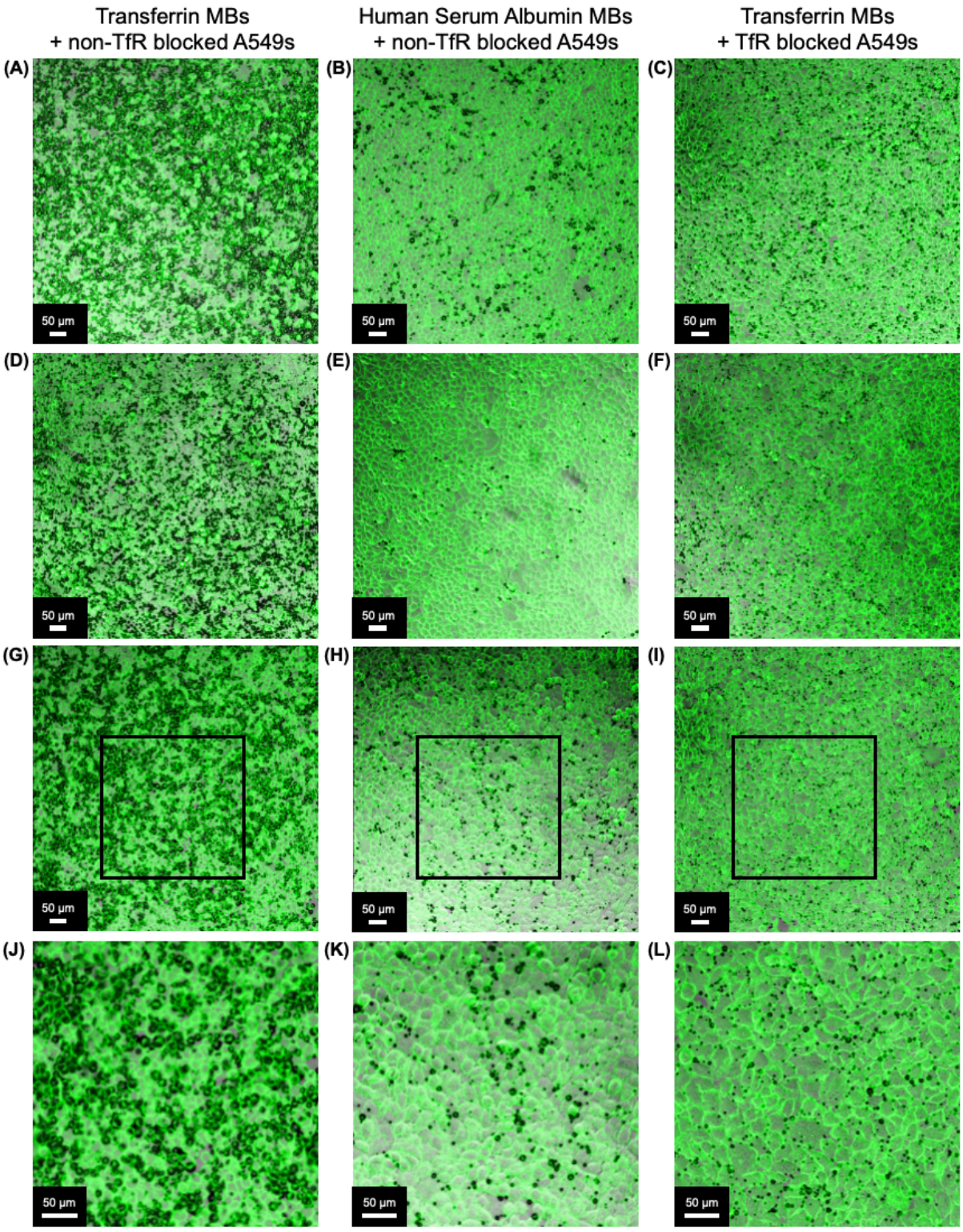


Figure 5.5. Qualitative assessment of His-transferrin and His-human serum albumin microbubbles on non-TfR blocked A549s and His-transferrin microbubbles on TfR blocked A549s. *10x confocal microscopy images of A549s (green) and microbubble PMT overlays (brightfield-like) of His-transferrin functionalised microbubbles (A, D, G) and His-human serum albumin microbubbles (B, E, H) with non-TfR blocked A549s, with zoomed-in fields of view of His-transferrin microbubbles (J) and His-human serum albumin (K) as indicated by the black squares. His-transferrin functionalised microbubbles with transferrin receptor blocked cells (C, F, I), with the zoomed-in field of view (L) as indicated by the black square (N = 3 for all). It shows a clear difference in targeting ability of both microbubbles.*

As in the previous section, *Figure 5.6* shows a higher magnification, with microbubbles and microbubble deposits present on cell membranes, with two example fields of view for each microbubble/cell condition. The blebbing of the plasma membrane stands out in all three cases, which is likely caused by the shear stress the fluid puts on the cells upon shaking (Thone & Kwon, 2020) rather than the microbubbles, as DPBS controls showed a similar cellular response. There appears to be a difference in microbubble/microbubble fragment attachment between the three conditions examined. However, as can be seen in the flow cytometry analysis in the *Appendix*, *Section A.4*, *Figure A.4.1*, the His-transferrin functionalised microbubbles are less bright than the His-human serum albumin functionalised microbubbles. Therefore, their observed fluorescence was close to the noise threshold, resulting in dim and hard to see microbubbles and microbubble fragments in *Figure 5.6*. To further assess this, flow cytometry was used, as shown in *Section 5.3.2*.

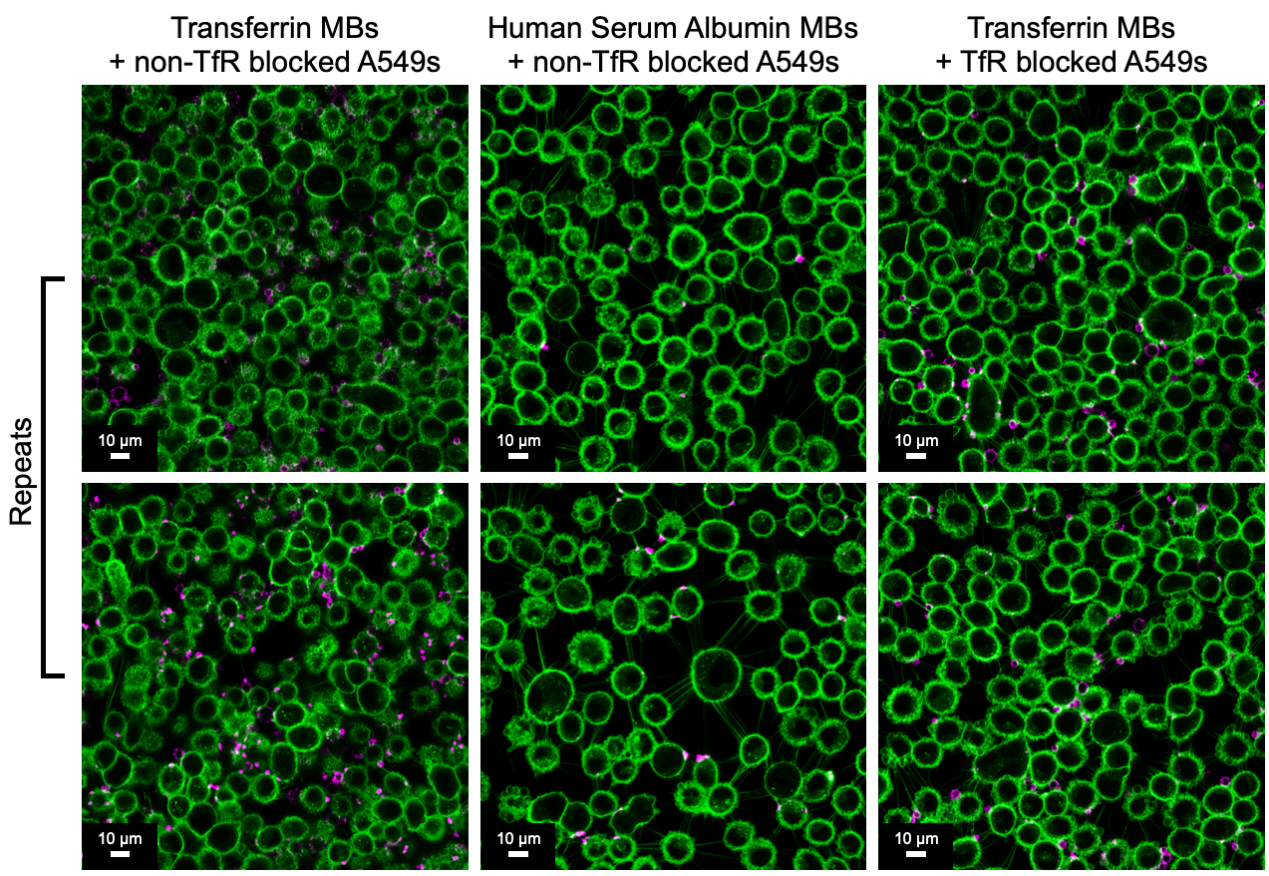


Figure 5.6. Example confocal microscopy images (40x) of A549 cells (green) and CF660C-labelled His-transferrin and His-human serum albumin functionalised microbubbles (magenta) on non-TfR blocked A549s, as well as CF660C-labelled His-transferrin microbubbles (magenta) on transferrin receptor blocked A549 cells. *It shows both microbubbles and microbubble fragment deposits on the cell membrane.*

5.3.2 Quantitative observation of His-Tf microbubbles targeting to A549s using flow cytometry

5.3.2.1 His-Tf versus His-HSA microbubbles without ultrasound

To assess the targeting effect of His-transferrin targetting of the microbubbles quantitatively, microbubbles and cells were mixed in the SAT3 and subsequently analysed using flow cytometry. A comparison was made with His-human serum albumin-loaded microbubbles, at two different microbubble concentrations: 1 x 10^8 MBs/mL (50 MBs/cell, *Figure 5.7*) and 2 x 10^6 MBs/mL (1 MB/cell, *Figure 5.8*). As in *Chapter 4*, two populations were identified. As shown in *Figure 5.7*, at a concentration of 50 microbubbles per cell, nearly every cell in population 1 was positive for CF660C-tagged His-transferrin, ~97%, compared to ~28% of cells being positive for CF660C-tagged His-human serum albumin, resulting in a substantial difference between these two microbubble types, at t = 5 and at t = 35 minutes.

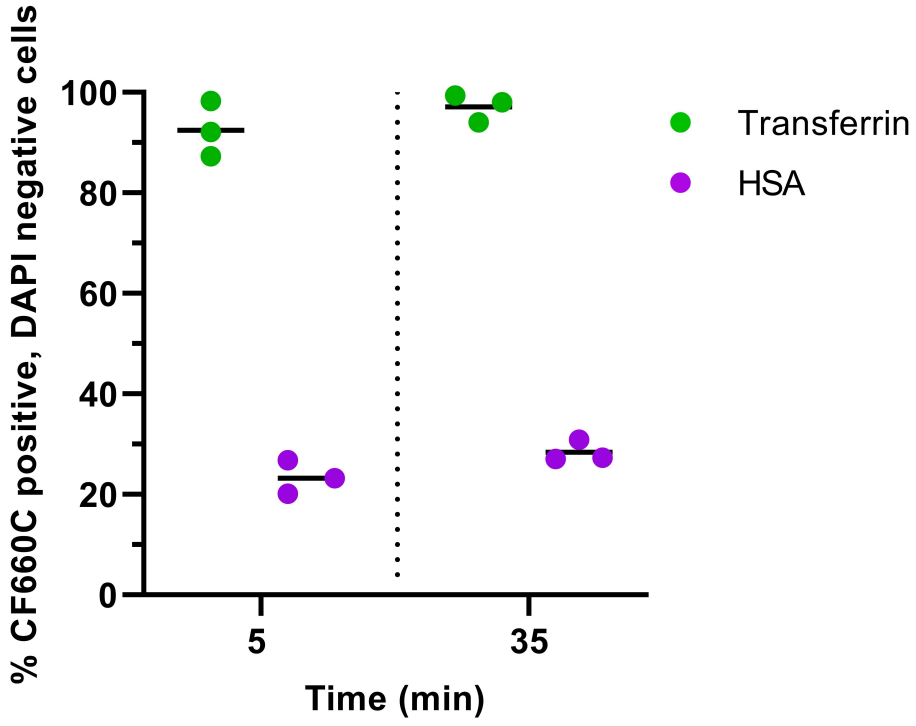


Figure 5.7. 'Membrane tagging' with and potential internalisation of His-transferrin for A549 cells at 1 x 10^8 MBs/mL (50 MBs/cell). *The % of A549 cells in population 1, of which examples are seen in Figures A.4.2 and A.4.3 in Appendix A.4, that were positive for CF660C due to microbubble material transfer and negative for DAPI, showing a difference between His-transferrin (green) and His-human serum albumin (magenta) functionalised microbubbles at t = 5 and t = 35 minutes, N = 3 for all conditions.*

As shown in *Figure 5.8*, at a concentration of 1 microbubble per cell, the fraction of cells positive for CF660C-tagged His-transferrin dropped to ~19%, compared to ~4% of cells being positive for CF660C-tagged His-human serum albumin, resulting in a substantial difference between these two microbubble types, at t = 5 and t = 35 minutes.

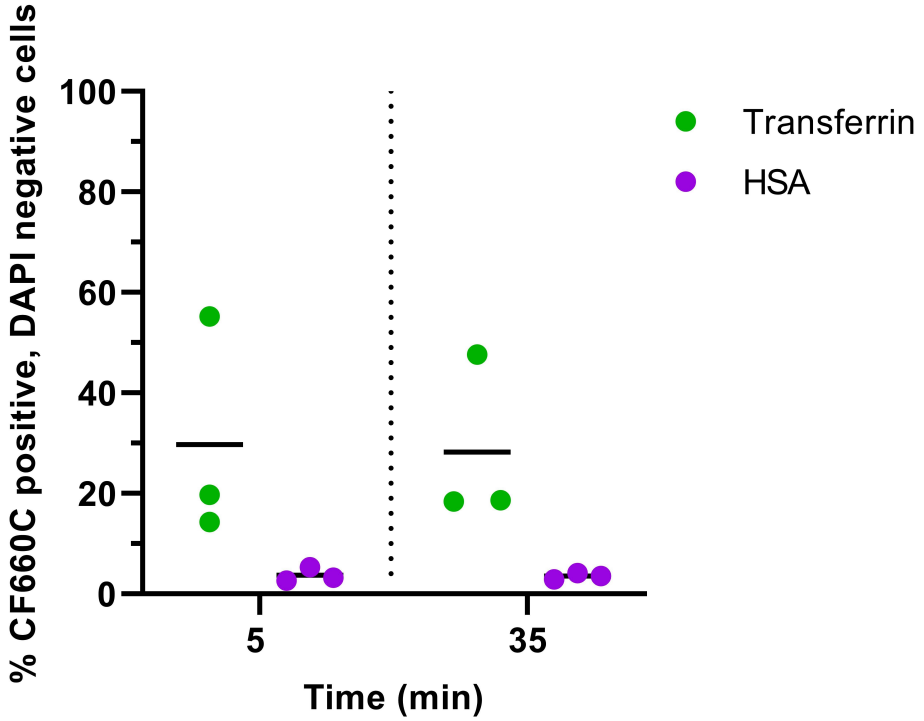


Figure 5.8. 'Membrane tagging' with and potential internalisation of His-transferrin for A549 cells at 2 x 10^6 MBs/mL (1 MB/cell). *The % of A549 cells in population 1, of which examples are seen in Figures A.4.2 and A.4.3 in Appendix A.4, that were positive for CF660C due to microbubble material transfer and negative for DAPI, showing a difference between both His-transferrin (green) and His-human serum albumin (magenta) functionalised microbubbles, at t = 5 and t = 35 minutes. N = 3 for transferrin microbubbles, and N = 3 for HSA microbubbles.*

Interestingly, the achieved degree of labelling of both His-transferrin and His-human serum albumin was the same, with two molecules of fluorophore per protein. Still, the flow cytometry plots in *Figure A.4.1* in the *Appendix*, *Section A.4* show the average His-transferrin microbubble to be less bright than the average His-human serum albumin microbubble. This might indicate a lower degree of protein-loading on the His-transferrin microbubbles compared to the His-human serum albumin microbubbles. As flow cytometry gives an arbitrary unit of fluorescence, this observation, combined with the above comparison between the two microbubble conditions at 0 kPa in *Figures A.4.2* and *A.4.3* in the *Appendix*, *Section A.4*, might indicate that

the number of microbubbles/microbubble fragments stuck to cells is even larger for His-transferrin microbubbles than for His-human serum albumin microbubbles.

5.3.2.2 His-Tf versus His-HSA microbubbles at 0, 100 and 150 kPa PNP

To investigate whether the use of ultrasound affects the observed targeting, both microbubble conditions were compared at a microbubble concentration of 1 x 10^8 MBs/mL and ultrasound driving conditions of 0.5 MHz centre frequency, 10% DC, 0, 100 and 150 kPa PNP, and a total exposure duration of 60 seconds.

As in *Chapter 4*, two populations could be readily identified in the FSC vs SSC plots: i) a population overlapping with the live control cells, named population 1, and ii) a population that appears to comprise a larger proportion of the total after exposure to both microbubbles alone and microbubbles with ultrasound treatment, named population 2.

Figure 5.9 shows that both His-transferrin and His-human transferrin albumin microbubbles have comparable microbubble size distributions, eliminating major differences in the microbubble populations as a cause for the results portrayed in *Figures 5.10* to *5.12*.

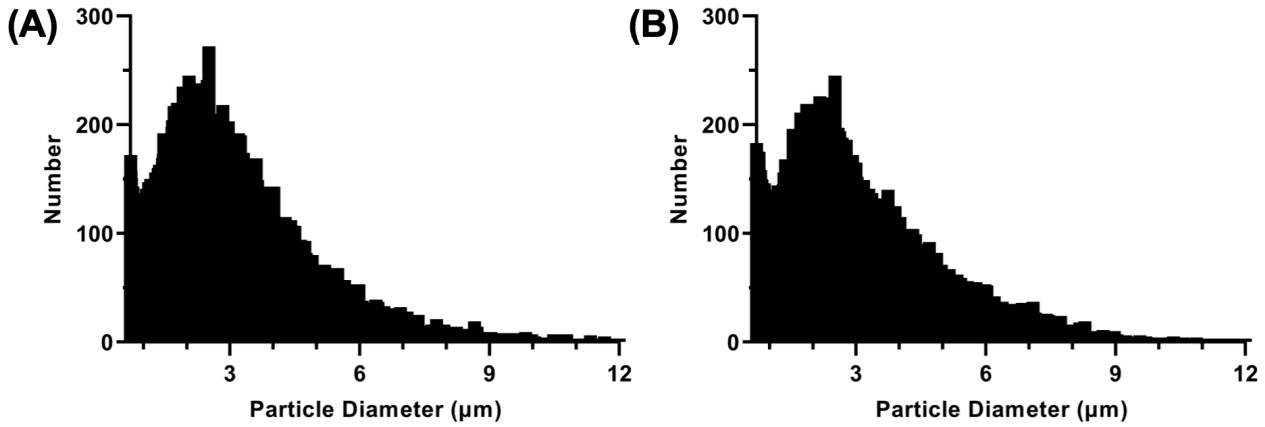


Figure 5.9. Microbubble size distribution histograms for His-transferrin microbubbles (A) and His-human serum albumin microbubbles (B). *His-transferrin MBs (A), with a mean diameter of 2.04 µm and a concentration of 4.5 x 10^9 MBs/mL (number of events = 45151), and His-human serum albumin MBs (B), with a mean diameter of 1.96 µm and a concentration of 4.2 x 10^9 MBs/mL (number of events = 42270).*

At a concentration of 50 MBs/cell, *Figure 5.10* shows the fraction of cells present in population 1 for both His-transferrin microbubbles (green) and His-human serum albumin microbubbles (magenta) at the three

different ultrasound parameters. Again, regardless of microbubble type, the 0 kPa no ultrasound control group allows for the largest fraction of cells to remain in population 1, ~75%, which decreases to ~62% at 100 kPa and ~60% at 150 kPa.

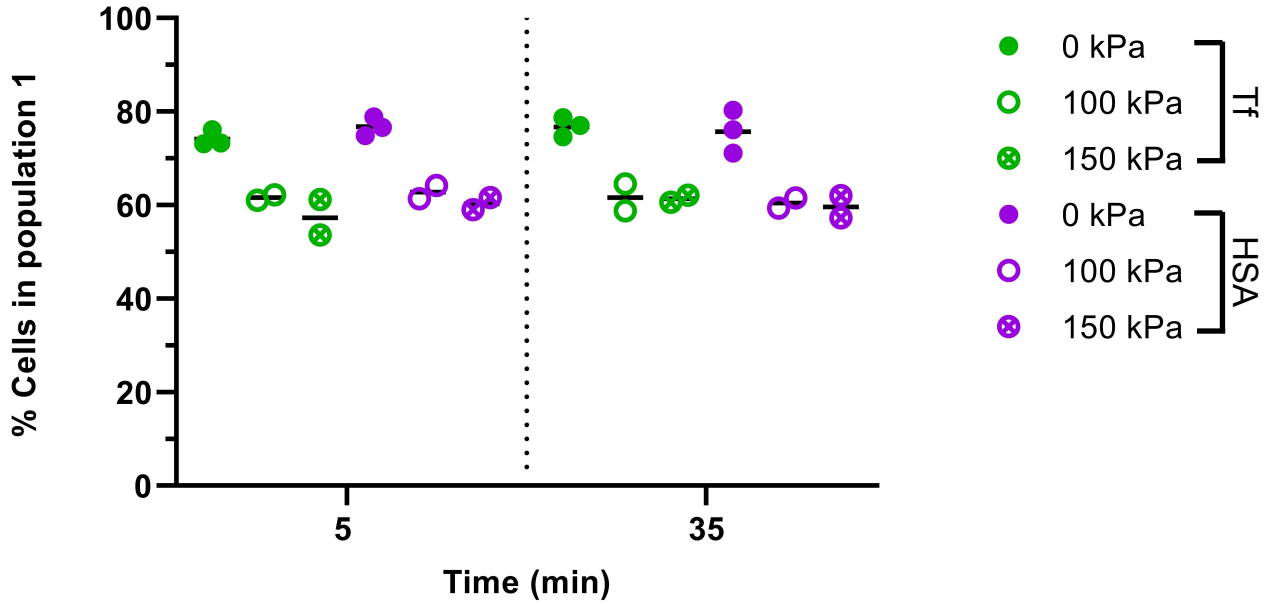


Figure 5.10. Population statistics for A549 cells in response to varying peak negative pressures at 1 x 10^8 MBs/mL. *The % of A549 cells in population 1, of which examples are seen in Figures A.4.2 and A.4.3 in Appendix A.4, for both His-transferrin (green) and His-human serum albumin (magenta) functionalised microbubbles, at t = 5 and t = 35 minutes. Ultrasound conditions were 0.5 MHz centre frequency, 10% DC, total exposure duration of 60 seconds, and 0 (solid) (N = 3), 100 (open) (N = 2) and 150 (cross) (N = 2) kPa PNP.*

In comparison, *Figure 5.11* shows the fraction of cells present in population 1 at a lower microbubble concentration of 1 microbubble/cell (2 x 10^6 MBs/mL) without ultrasound. This fraction is ~64% for both microbubble types.

As can be seen in *Figure 5.12*, for the higher microbubble concentration of 50 microbubbles per cell, the fraction of cells in population 1 that are positive for CF660C-tagged His-transferrin is ~98%, compared to ~29% of cells being positive for CF660C-tagged His-human serum albumin at t = 35 minutes, resulting in a substantial difference between these two microbubble types, at both t = 5 and t = 35 minutes at each investigated pressure.

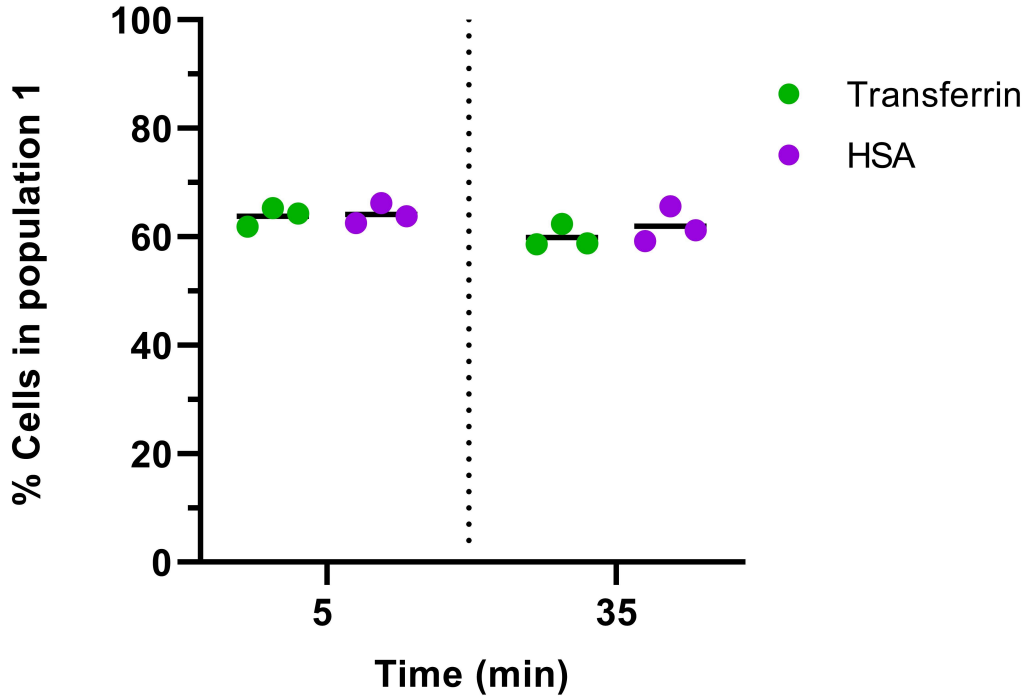


Figure 5.11. Population statistics for A549 cells at 2 x 10⁶ MBs/mL of His-transferrin and His-human serum albumin microbubbles. *The % of A549 cells in population 1, of which examples are seen in Figures A.4.2 and A.4.3 in Appendix A.4, for both His-transferrin (green) and His-human serum albumin (magenta) functionalised microbubbles, at t = 5 and t = 35 minutes, N = 3 for all conditions.*

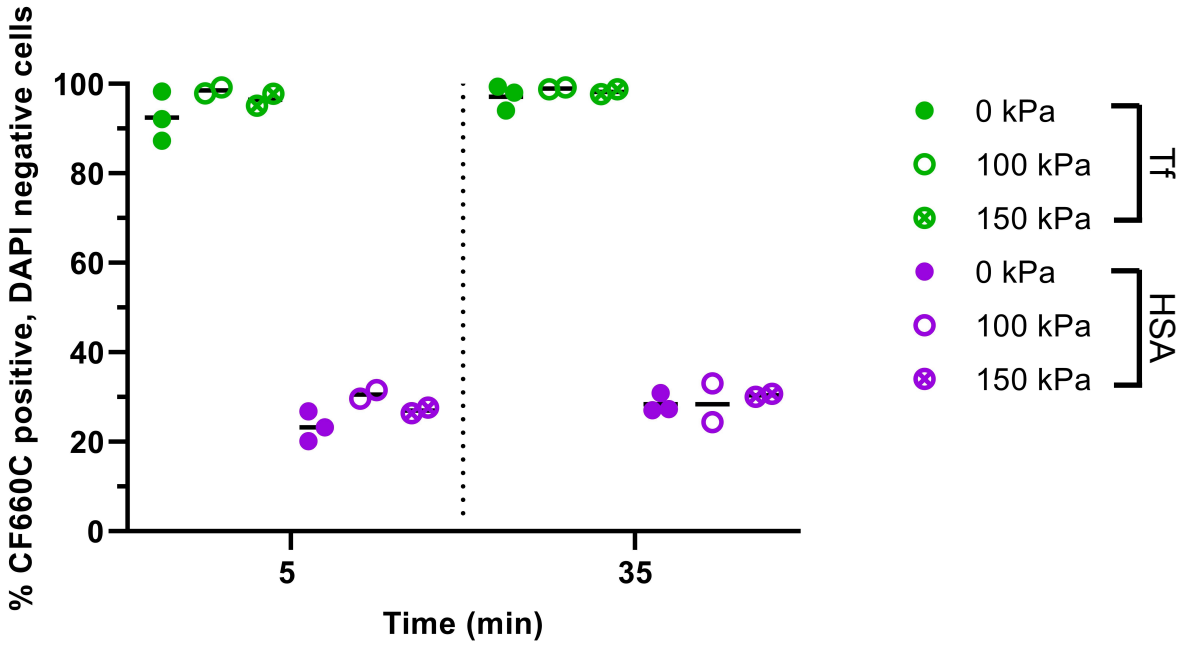


Figure 5.12. 'Membrane tagging' with and potential internalisation of His-transferrin and His-human serum albumin for A549 cells at 1 x 10⁸ MBs/mL (50 MBs/cell). *The % of A549 cells in population 1, of which examples are seen in Figures A.4.2 and A.4.3 in Appendix A.4, that are positive for CF660C, either due to membrane lipid transfer or internalisation, and negative for DAPI, for both His-transferrin (green) and His-human serum albumin (magenta) functionalised microbubbles, at t = 5 and 35 minutes. Ultrasound conditions were 0.5 MHz centre frequency, 10% DC, total exposure duration of 60 seconds, and 0 (solid) (N = 3), 100 (open) (N = 2) and 150 (cross) (N = 2) kPa PNP.*

Another interesting observation is the acoustic behaviour of the microbubbles, particularly prevalent at 100 kPa, as shown in *Figure 5.13*. There is an initial spike in both the broadband and ultraharmonic signal powers for both the His-transferrin and His-human serum albumin microbubbles. However, this subsequently subsides, only to grow again after 20 seconds. This behaviour was not observed at these ultrasound parameters with His-GFP or His-AF488 functionalised microbubbles in *Chapters 3* and *4*, despite similar ultrasound parameters used in the same SAT set-up.

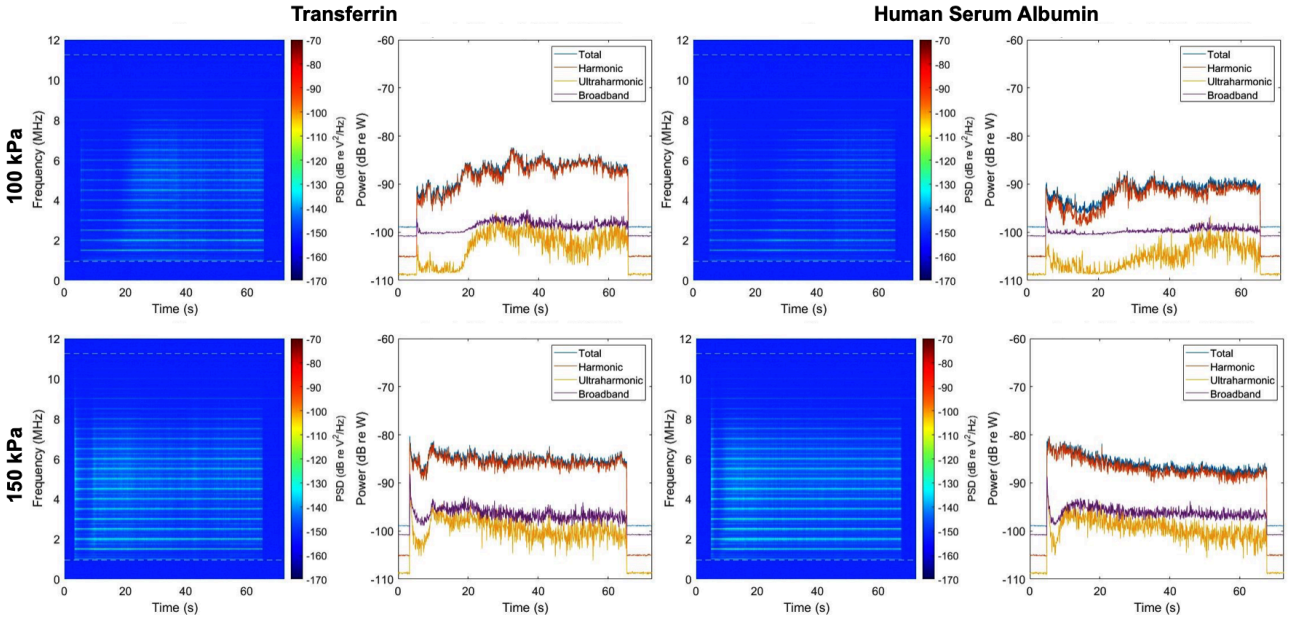


Figure 5.13. Example spectrum histories over a 60-second exposure of a suspension of His-transferrin and His-human serum albumin MBs at 1 x 10⁸ MBs/mL*. Full spectra and total, harmonic, ultraharmonic and broadband signal powers are shown as a function of time. Drive conditions were 0.5 MHz, 100 and 150 kPa PNP, 10% DC, 60 seconds total exposure duration.*

5.3.2.3 His-Tf versus His-HSA microbubbles with regular and Tf-receptor blocked A549 cells

Lastly, the ability of His-transferrin microbubbles to target A549 cells, which had their transferrin receptors blocked, was investigated and compared to the two conditions discussed above: non-TfR blocked A549 cells with either His-transferrin or His-human serum albumin functionalised microbubbles.

Figure 5.14 shows again that both His-transferrin and His-human transferrin albumin microbubbles have comparable microbubble size distributions, to eliminate major differences in microbubble populations as a cause for the results portrayed in *Figures 5.15* to *15.7*. The results are shown in *Figures 5.15*, *5.16* and *5.17* for microbubble concentrations of 50, 25 and 5 microbubbles per cell, respectively. Examples of the associated flow cytometry data are shown in the *Appendix*, *Section A.4*, *Figure A.4.4*.

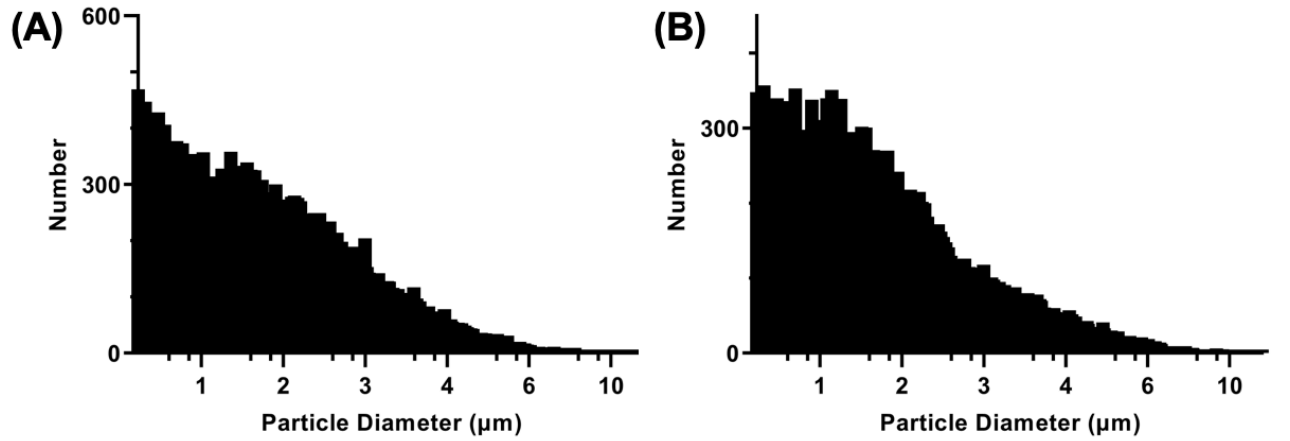


Figure 5.14. Microbubble size distribution histograms for His-transferrin microbubbles (A) and His-human serum albumin microbubbles (B). *His-transferrin MBs (A), with a mean diameter of 1.87 µm and a concentration of 2.55 x 10^9 MBs/mL (N = 25500), and His-human serum albumin MBs (B), with a mean diameter of 1.89 µm and a concentration of 2.08 x 10^9 MBs/mL (N = 20793).*

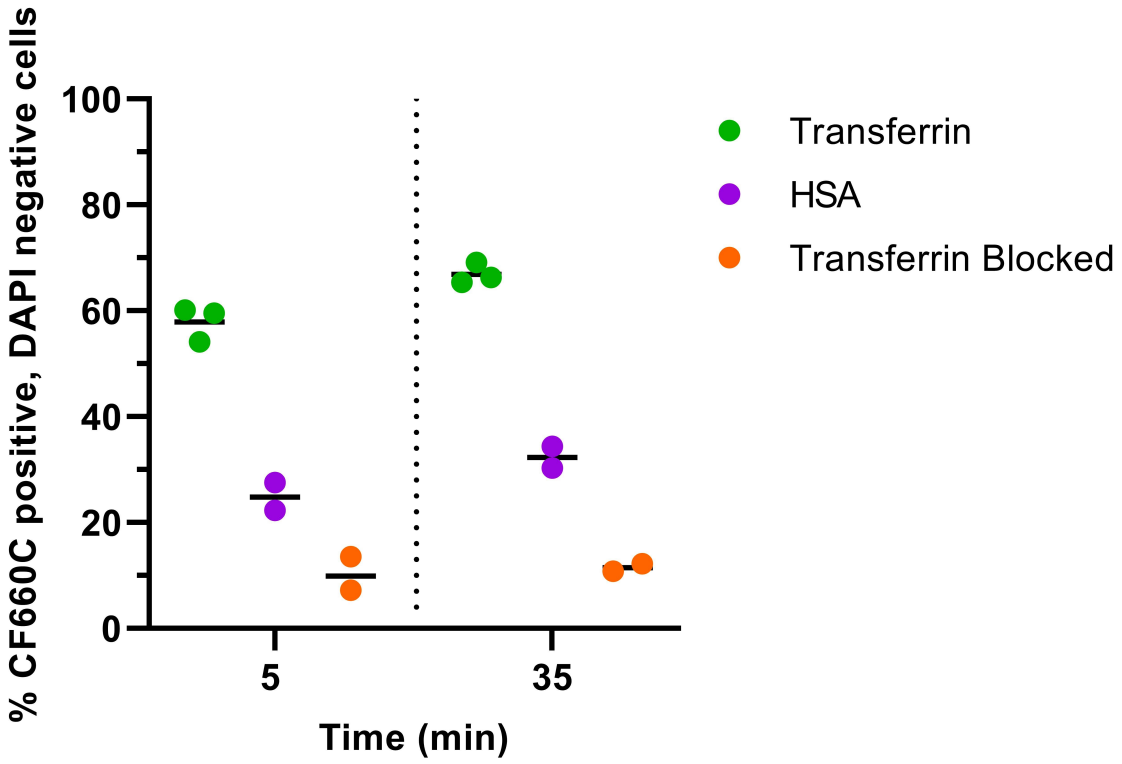


Figure 5.15. 'Membrane tagging' with and potential internalisation of His-transferrin and His-human serum albumin for non-TfR and TfR blocked A549 cells at 1 x 10^8 MBs/mL (50 MBs/cell). *The % of A549 cells in population 1 that are positive for CF660C, either due to membrane lipid transfer or internalisation, and negative for DAPI, showing a difference between both His-transferrin (green, N = 3) and His-human serum albumin (magenta, N = 2) functionalised microbubbles with non-TfR blocked A549 cells, and His-transferrin microbubbles with blocked transferrin receptor A549 cells (orange, N = 2).*

For 50 microbubbles per cell, as shown in *Figure 5.15*, the fraction of cells in population 1 that are positive for CF660C-tagged His-transferrin is ~67%, compared to ~32% of cells being positive for CF660C-tagged His-human serum albumin and ~12% of blocked cells being positive for CF660C-tagged His-transferrin, at t = 35 minutes, resulting in observable differences between these three conditions at both time points. Time also has appears to have an effect, as these numbers increased from 58%, 25% and 10% respectively from t = 5 minutes. A possible reason for the higher level of 'targeted' cells with His-human serum albumin compared to the control condition of His-transferrin microbubbles with blocked cells might be that A549 cells do express human serum albumin receptors (Peng *et al*., 2015; Chaiwaree *et al*., 2020).

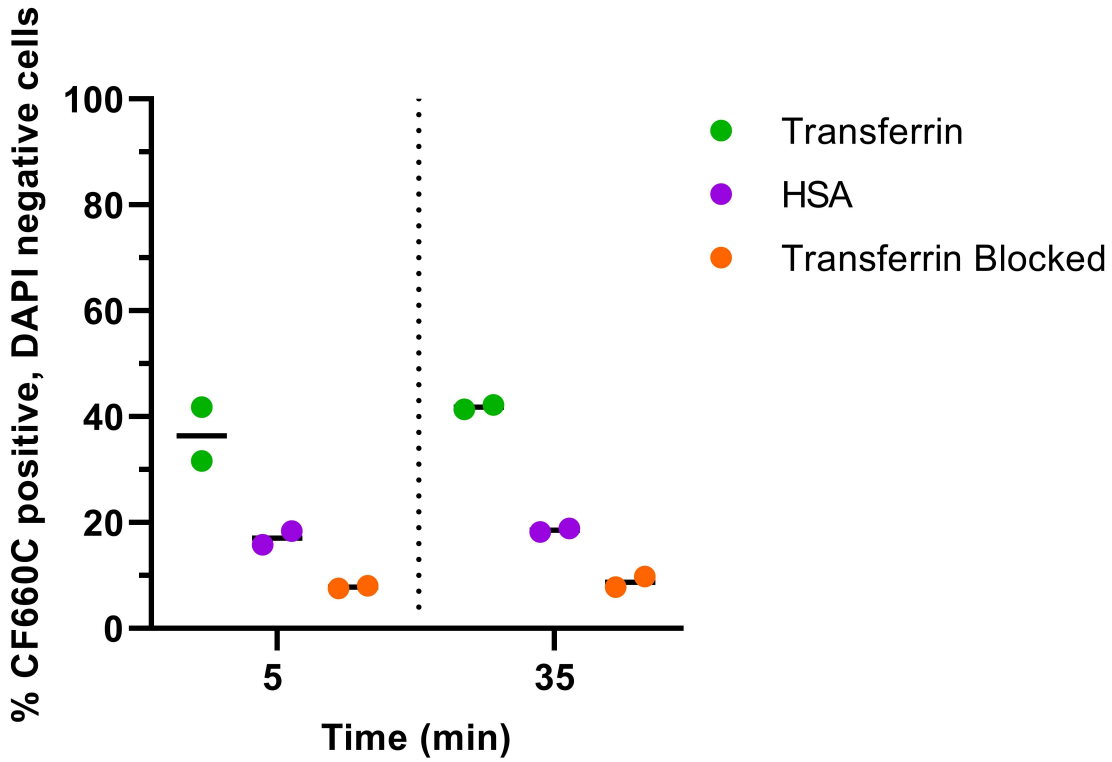


Figure 5.16. 'Membrane tagging' with and potential internalisation of His-transferrin and His-human serum albumin for non-TfR and TfR blocked A549 cells at 5 x 10⁷ MBs/mL (25 MBs/cell). *The % of A549 cells in population 1 that are positive for CF660C, either due to membrane lipid transfer or internalisation, and negative for DAPI, showing a difference between both His-transferrin (green, N = 2) and His-human serum albumin (magenta, N = 2) functionalised microbubbles with non-TfR blocked A549 cells, and His-transferrin microbubbles with blocked transferrin receptor A549 cells (orange, N = 2)*

For 25 microbubbles per cell, as shown in *Figure 5.16*, the fraction of cells in population 1 that are positive for CF660C-tagged His-transferrin is ~42%, compared to ~19% of cells being positive for CF660C-tagged His-human serum albumin and ~9% of blocked cells being positive for CF660C-tagged His-transferrin, at t =

35 minutes, resulting in an observable effect of the microbubble/cell condition on the 'membrane tagging'. A decrease in CF660C positive cells, regardless of microbubble type, was observed with this decrease in microbubble concentration.

For 5 microbubbles per cell, as shown in *Figure 5.17*, the first thing that is observed is the large variance in the samples treated with both His-transferrin and His-human serum albumin microbubbles, possibly simply due to more room for error in pipetting very small volumes of microbubbles (< 1 μL). The fraction of cells in population 1 that are positive for CF660C-tagged His-transferrin is ~8%, compared to ~8% of cells being positive for CF660C-tagged His-human serum albumin and ~3% of blocked cells being positive for CF660C-tagged His-transferrin, at t = 35 minutes.

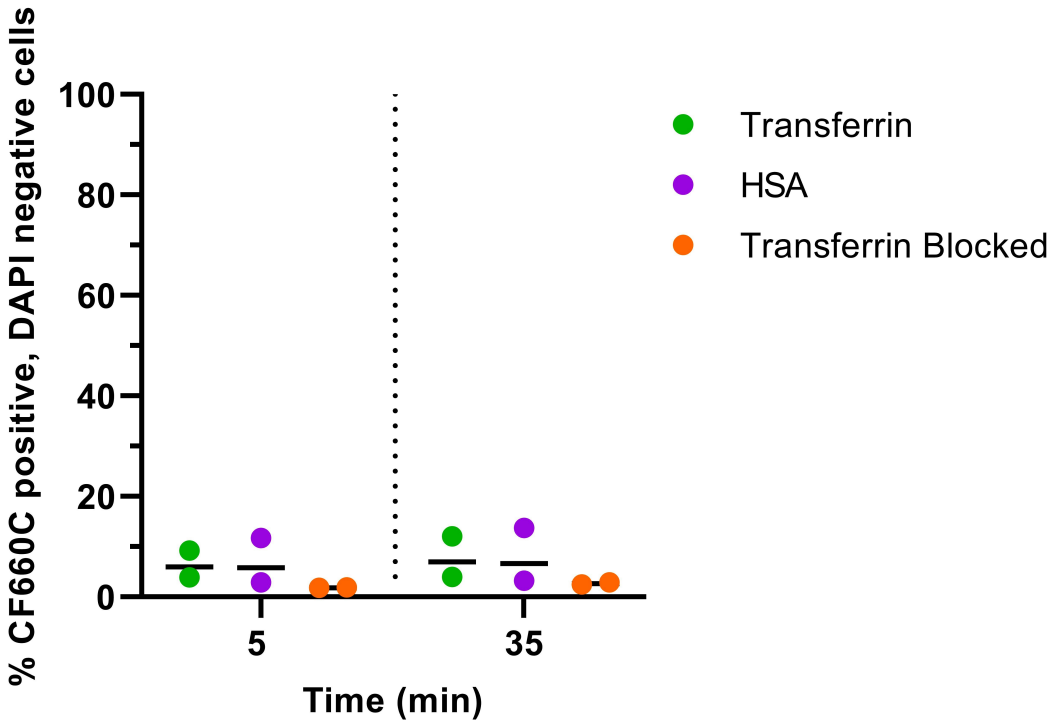


Figure 5.17. Membrane tagging' with and potential internalisation of His-transferrin and His-human serum albumin for non-TfR and TfR blocked A549 cells at 1 x 10^7 MBs/mL (5 MBs/cell). *The % of A549 cells in population 1 that are positive for CF660C, either due to membrane lipid transfer or internalisation, and negative for DAPI, showing no substantial difference between both His-transferrin (green, N = 2) and His-human serum albumin (magenta, N = 2) functionalised microbubbles with non-TfR blocked A549 cells, and His-transferrin microbubbles with blocked transferrin receptor A549 cells (orange, N = 2).*

5.4 Conclusion

This *Chapter* aimed to explore the feasibility of targeting microbubbles to cells prior to ultrasound exposure, potentially enhancing lipid transfer to and/or microbubble fusion with the cell membrane. This would improve the specificity of this mechanism, and thus of any potential future therapies, and limit off-target interactions by selectively directing microbubbles to structures of interest. It could also improve the 'membrane tagging', as observed in *Chapters 3* and *4*. His-transferrin functionalised microbubbles were used, as the A549 cells used in the experiments in this *Thesis* exhibit overexpressed transferrin receptors on their outer membranes.

The results show a significant increase in microbubble-cell attachment and microbubble material transfer for His-transferrin functionalised microbubbles compared to His-human serum albumin microbubbles on non-TfR blocked A549 cells. There was also only limited binding of His-transferrin functionalised microbubbles to A549 cells with blocked transferrin receptors, confirming targeting specificity. However, it should be noted that not only cancer cells exhibit high levels of the transferrin receptor on their cell membrane, but also healthy cells, such as liver cells (Trinder & Baker, 2003; Robb & Wessling-Resnick, 2004). Thus, this model system might not be suitable for clinical translation due to the risk of off-target toxicity, and alternative targeting proteins may be required.

Interestingly, the use of ultrasound did not significantly affect the fraction of cells being positive for CF660C, whether coupled to His-transferrin or His-human serum albumin. However, flow cytometry does not provide any insight into how the fluorescent components are incorporated in the cells, i.e. whether the microbubbles or microbubble fragments are present on or in the cell membrane or internalised in the cells - DAPI serves as a good indication, but it ultimately depends on the timescale over which the potential membrane resealing occurs. Therefore, future work should include the use of confocal microscopy to corroborate the results as shown in *Figures 5.10* and *5.12* and give insight into the effect of ultrasound on how the fluorescent functionalised lipids are incorporated in the cell.

One way to advance the work presented in this *Chapter* is to assess the targeting efficiency and lipid transfer in a co-culture experiment, with two cell lines of which one expresses the receptor of interest, e.g., the transferrin receptor, and the other one does not, as elaborated upon in *Chapter 6*. This platform would be

more representative of *in vivo* conditions, give a better indication of the selective targeting ability of the microbubbles and would allow for a direct, simultaneous comparison of the targeting ability at the same conditions and parameters for both cell types. This would further provide a comparison with the results in *Figure 5.16*, where the targeting efficiency of His-transferrin microbubbles to the transferrin receptor was compared for separate samples of non-TfR and TfR blocked A549 cells.

Chapter 6 - Conclusions and Future Work

6.1 Objectives and Conclusions

The main aim of this *DPhil Project* was to assess the feasibility of developing microbubbles functionalised with a protein of choice to tag target cell membranes to make diseased cells, such as cancer cells, more visible to the immune system or immune cells more potent in detecting diseased cells. To this end, a novel microbubble was designed, as described in *Chapter 2*, to study the interactions of microbubbles with the cell membrane, employing confocal microscopy. Subsequently, the use of these microbubbles to 'tag' cell membranes with these proteins was assessed qualitatively with adherent cells in *Chapter 3*. The role of both microbubble and ultrasound properties in the successful tagging of the cell membrane was explored. In *Chapter 4*, this 'membrane tagging' was investigated quantitatively using flow cytometry. Lastly, in *Chapter 5*, the targeting ability and effect on 'membrane tagging' of protein-functionalised microbubbles was investigated by functionalising microbubbles with His-transferrin to specifically target A549 cells expressing the equivalent receptor. The specific contributions of the thesis are summarised in the following *Section*.

6.1.1 Contributions

6.1.1.1 Chapter 2: The Design, Fabrication and Characterisation of Protein-Loaded Microbubbles

This *Chapter* demonstrates the successful fabrication and characterisation of protein/dye-functionalised microbubbles using a metallochelating complex through an NTA(Ni) and histidine residues interaction, with a fluorescent model protein/dye, and discusses potential avenues for their optimisation. It explored the microbubble population characteristics, such as concentration and size distribution. Secondly, it showed the specificity of the NTA(Ni) and histidine residue binding and the diffusion of this complex in the microbubble shell compared to GUVs. It, furthermore, showed the serendipitous discovery of membrane domains. Lastly, it estimated the loading capacity of DGS-NTA(Ni) microbubbles with His-AF488 and showed the potential loss of His-AF488 from the microbubble shell under physiological conditions (temperature and serum).

6.1.1.2 Chapter 3: Qualitative Assessment of His-Functionalised Microbubble-Cell Membrane Interactions

After the successful fabrication and characterisation of the protein/dye-functionalised microbubbles in *Chapter 2*, *Chapter 3* investigated the potential of utilising these bubbles to tag cell membranes. Pilot experiments were conducted with His-GFP functionalised microbubbles and adherent A549 cells.

This *Chapter* showed the transfer of material from the microbubble to the cell membrane, defined as 'membrane tagging'. There was a clear indication of lipid transfer to and/or microbubble fusion of His-GFP NTA(Ni) functionalised microbubbles to A549 cell membranes in three systems for acoustic transfection. This 'membrane tagging' is distinctly different from the internalisation of microbubble material as observed with lyso-microbubbles.

6.1.1.3 Chapter 4: Quantitative Assessment of His-Functionalised Microbubble-Cell Membrane Interactions

Following on from the pilot experiments in *Chapter 3*, where His-GFP functionalised lipid transfer and/or microbubble fusion with A549 cell membranes was observed qualitatively using confocal microscopy, this *Chapter* aimed to investigate this process quantitatively for cells in suspension using flow cytometry. Both A549 cells, naturally adherent cells, and Jurkat T cells, suspension cells, were investigated. A549 cells represent solid tumour cells, while Jurkat cells represent either suspension tumour or suspension immune cells.

It was observed for both A549 cells and Jurkat T cells that an increasing fraction of cells aligned with cell population 2 rather than cell population 1, which overlaps with live control cells. This shift, corresponding to morphological changes, was increasingly observed for higher pressures and duty cycles, i.e. more strenuous ultrasound conditions, albeit to a lesser extent for the former. This change may indicate damage and functional alteration of the cells due to microbubble-mediated ultrasound exposure. Whether this change is reversible and, if so, on what time scales, currently falls outside the scope of this *Thesis*. For A549 cells at high duty cycle conditions, the fraction of cells in population 1 decreased, and the fraction of cells in the second, morphologically different population increased proportionately. For Jurkat cells at high duty cycle conditions, while the fraction of cells in population 1 decreased, the fraction of cells in the

morphologically different population increased disproportionally compared to the A549 cells. This might be due to Jurkat cells being more susceptible to the effects of ultrasound, leading to the destruction of cells rather than morphological changes. For both cell lines, this shift was largely maintained over the course of 30 minutes.

For the primary biological effect of interest - membrane tagging - it was observed for both cell lines that the no or gentle ultrasound conditions contributed to the largest fraction of cells being AF488-positive and PI-negative - indicative of membrane tagging - in population 1. This might be due to the microbubbles only partially being destroyed or not at all, and, therefore, being able to either transfer material to, fuse with or attach to the cell membrane. Interestingly, for the Jurkat cells, in contrast to the A549 cells, an increase over time was observed in this AF488 positive and PI-negative fraction of cells in the second, morphologically different population. This suggests that, while the cells remain morphologically different, a recovery mechanism occurs with a decreasing number of cells permeable to PI at t = 30 minutes. This is corroborated by the PI data, which showed a decrease in PI uptake for Jurkat cells over the course of 30 minutes. For A549 cells, especially the first experiment in *Section 4.3.2.1* showed a pronounced decrease in PI uptake - a decrease much less pronounced in the two subsequent experiments in *Sections 4.3.2.2* and *4.3.2.3*. This is possibly due to the use of a different set-up and, hence, different experimental conditions.

For Jurkat cells, the no to low ultrasound conditions resulted in the most AF488 transfer to PI-negative cells for the cells in population 1, but the more intense ultrasound conditions – either higher pressure or duty cycle - resulted in the most AF488 transfer to PI-negative cells for cells in the second, morphologically different cell population, at t = 30 minutes. Combined with the decrease in PI-positive Jurkat cells over time as observed using flow cytometry, this could potentially indicate sonoporation takes place, and cells exhibit a recovery mechanism, resealing their membrane pores. For A549 cells, minimal AF488 positive and PI-negative cells are found in this second, morphologically different population.

Low pressures and low duty cycles are generally favourable for His-AF488 tagging in PI-negative cells in population 1 for both A549 cells and Jurkat cells. It is important to note, however, that flow cytometry as employed in this *Chapter* only gives a simple yes/no answer as to whether His-AF488 is present, but it does not elucidate in which way His-AF488 is present, i.e. through membrane tagging,

internalisation or microbubble attachment. The PI results and the confocal microscopy results indicated internalisation occured after ultrasound treatment, as well as the desired 'membrane tagging'.

6.1.1.4 Chapter 5: Specific Targeting of His-Functionalised Microbubbles to Cell Membranes

The observations in *Chapter 4* raised the question of why the *Results* in *Chapter 3* showed greatly enhanced 'membrane tagging' using ultrasound in adherent A549 cells, while the *Results* in *Chapter 4* for A549 cells in suspension do not. A possible explanation could be the fact that microbubble behaviour and subsequent 'membrane tagging' affect cells differently in suspension conditions, in which free mixing occurs due to the ultrasound field and secondary microbubble effects such as microstreaming, compared to adherent conditions, in which the cells are stationary and cannot 'escape' oscillating microbubbles.

A potential avenue to address this would be the specific targeting of microbubbles to the cells prior to ultrasound exposure. This would improve the specificity of this mechanism, and thus of any potential therapies, and limit off-target interactions by selectively directing microbubbles to structures of interest.

To this end, *Chapter 5* explored the feasibility of targeting microbubbles to cells prior to ultrasound exposure to potentially enhance lipid transfer to and/or microbubble fusion with the cell membrane. His-transferrin functionalised microbubbles were used, as the A549 cells used in these experiments exhibit overexpressed transferrin receptors on their outer membranes.

The *Results* show a significant increase in microbubble-cell attachment between His-transferrin functionalised microbubbles and His-human serum albumin microbubbles on non-TfR blocked A549 cells. There was also only limited binding of His-transferrin functionalised microbubbles to A549 cells with blocked transferrin receptors, confirming the targeting specificity of these functionalised microbubbles. However, it should be noted that not only cancer cells exhibit high levels of the transferrin receptor on their cell membrane, but also healthy cells, such as liver cells (Trinder & Baker, 2003; Robb & Wessling-Resnick, 2004). Thus, this model system might not be relevant for clinical translation due to the risk of off-target toxicity, and alternative targeting proteins may be required.

Interestingly, ultrasound did not significantly affect the fraction of cells showing 'membrane tagging', as described in *Chapter 4*, with either His-transferrin or His-human serum albumin microbubbles. However, flow cytometry does not provide any insight into how the fluorescent components are incorporated

in the cells, i.e. whether the microbubbles or microbubble fragments are present on or in the cell membrane or internalised in the cells. Therefore, future work should include both flow cytometry and confocal microscopy to give insight into the effect of ultrasound on how the fluorescent functionalised lipids are incorporated in the cell. One approach to this is the ImageStream Technology from Amnis (Luminex, Austin, Texas), as elaborated upon in *Section 6.3.1.4* below.

6.2 Limitations

Limitations of the microbubbles presented in this *Thesis* could be identified, such as their *in vivo* stability - in terms of microbubble stability, circulation time, and protein-loading capacity. *Chapter 2* provided evidence for a potential loss of the His-tagged protein in *in vivo* conditions due to the presence of native amino acids with electron-donating groups, e.g., glutamine, competing for the same Ni binding places, as observed by Rüger *et al*. (2006). Furthermore, the equilibrium of bound His-tags to Ni is affected by the pH, with a decrease in pH leading to a weaker equilibrium and thus less bound His-tags. This could potentially become a problem in more acidic environments, such as lysosomes.

Another concern regarding the use of the proposed NTA(Ni)-functionalised microbubbles *in vivo* is the presence of Ni, a toxic compound. Possible effects of Ni include immunosuppression, as shown by Harkin *et al*. (2003) in rats, at a plasma concentration of 0.2 - 0.6 μg/mL. Studies into the effect of Ni nanoparticles have also shown a variety of toxic effects on cells, animals and humans and on multiple systems, such as the respiratory system, cardiovascular system and reproductive system (Wu & Kong, 2020).

C*hapters 3* and *4* illustrated the potential effect of a boundary on the microbubble behaviour and subsequent 'membrane tagging', as successful membrane tagging was achieved in adherent cells in *Chapter 3* - grown on a glass or polymer boundary - but not, to the same degree, in suspension cells in *Chapter 4*. The phase difference between the reradiated sound field and the sound field reflected of the boundary, and thus the net direction of the microbubble movement, is determined by the elasticity of said boundary (Stride & Coussios, 2019). For this reason, observations made in conventional *in vitro* set-ups, like those presented in *Chapter 3*, may not represent the additional complexities of *in vivo* situations, such as the heterogeneous nature of tissues or suspension target cells, e.g., immune cells. Since the SATs were designed for real-time

monitoring of acoustic emissions, with biological assays being performed outside of the acoustic experiment, another limitation is the fact it is impossible to directly relate local microbubble behaviour to local biological effects.

Additionally, *Chapter 3* provided qualitative information and *Chapter 4* and *5* provided quantitative information regarding the 'membrane tagging' bioeffect. Ideally, however, both the qualitative and quantitative measurements take place simultaneously, so not only the efficiency of microbubble material transfer, e.g., the fraction of cells positive for microbubble material, but also the way in which this material transfers, e.g., onto the cell membrane or intracellularly, can be investigated.

Lastly, the microbubbles proposed in this *Thesis* are designed to deliver protein to the cell membrane. With an envisioned application in immunotherapy and as a potential alternative to CAR T cell therapy, one major drawback that could readily be identified is the lack of delivery of the intracellular portion of the CAR with the protein-functionalised microbubbles, potentially leading to an absent or ineffective immune response. One way to combat this issue might be the delivery of a transgene construct, as is the case for the later generations of CAR T cell therapy, e.g. the 'armoured' fourth-generation CAR, in which the transfer of two transgenic cassettes takes place - one for the CAR and one for an inducible cytokine (Zhang, Liu, Zhong,& Zhang, 2017). This would require intracellular ultrasound-mediated delivery of the microbubble cargo, for which the protein-functionalised microbubbles in this *Thesis* were not optimised. However, *Chapter 4* provides preliminary evidence for reversible membrane sonoporation, which could be further investigated for this purpose. To address some of these challenges, future work is proposed as outlined in *Section 6.3*.

6.3 Future work

Building on the work in *Chapters 2*, *3*, *4* and *5*, there are many additional *in vitro* and, eventually, *in vivo* studies that could potentially be undertaken to make strides towards the ultimate goal of this *DPhil Project*: tagging target cell membranes to make diseased target cells, such as cancer cells, more visible to the immune system or immune cells more potent in detecting diseased cells. These steps are outlined below.

6.3.1 In Vitro

6.3.1.1 Improving microbubble stability in *in vivo* conditions

As the *Results* in *Chapter 2* showed, the His-AF488 functionalised microbubbles show promising stability under experimental *in vitro* conditions, i.e. capped and on ice (~ 4 ˚C). However, exposing them for prolonged times (10 mins) to mammalian cell culture medium, supplemented with bovine serum at 37 ˚C, causes the His-tagged entity to desorb from the microbubble membrane. Potential avenues to be explored to improve these NTA(Ni)-functionalised microbubbles are:

1. The use of different chelating metal ions in addition to nickel (II), such as cobalt (II) and zinc (II),
2. The physicochemical character of the metallochelating lipid used, such as the chain length, saturation, potential PEG linker, use of NTA_3, and use of an anti-His_6 antibody head group,
3. The ligand loading efficiency and optimal surface density through ligand incubation protocols, such as variations in the concentration of both the His-tagged protein/dye and the chelating lipid,
4. The strengthening of the histidine-tag by moving to ten or twelve histidine residues, rather than the six histidine residues present in all His-tagged entities used in this *Thesis*.

A potential future experiment to test the microbubble stability in *in vivo* conditions would be to conduct stability experiments in human blood. This would give insight into the ability of the microbubbles to retain their His-tagged cargo for a variety of microbubble compositions. When performing fluorescence-based analysis, however, it should be kept in mind that blood is autofluorescent due to various fluorophores present in, e.g., blood cells and serum proteins (Shrirao *et al*., 2021). Therefore, the fluorescent labelling or innate fluorescence of the His-tagged cargo should be considered carefully.

6.3.1.2 Exploration of the ultrasound regime for suspension cells

In *Chapter 3*, the ultrasound parameters - 0.5 MHz, 0.2 MPa peak negative pressure, 60-second continuous wave - were inspired by previous work from Carugo *et al*. (2017), which demonstrated microbubble material transfer on adherent A549 cells under ultrasound exposure. The *Results* in *Chapter 3* showed His-GFP

NTA(Ni) functionalised microbubble material transfer to A549 cell membranes under ultrasound exposure in three systems for acoustic transfection. Subsequently, the effect of ultrasound at varying parameters on the 'membrane tagging' of suspension cells was investigated in *Chapter 4*. Two ultrasound parameters were varied: duty cycle - 0 to 100% - and pressure - 0 to 200 kPa. Interestingly, the same dependence on ultrasound exposure on the 'membrane tagging' is not observed for the A549 and Jurkat cells in suspension. However, the PI results in this *Chapter* indicate sonoporation and subsequent resealing of the membrane may occur at the ultrasound parameters used, promoting internalisation of microbubble content rather than 'membrane tagging'. Therefore, future work could include exploring the ultrasound parameter space away from this sonoporation regime, e.g., even lower pressures, shorter duty cycles, and shorter exposure times.

6.3.1.3 High-speed camera experiment to visualise microbubble behaviour

To the best of the author's knowledge, all studies demonstrating sonoprinting and microbubble material transfer, similar to the proposed 'membrane tagging', have been performed on adherent cells (e.g., De Cock *et al*., 2016; Carugo *et al*., 2017; Roovers *et al*., 2019a; Roovers *et al*., 2019b). Interestingly, while the *Results* in *Chapter 3* show greatly enhanced 'membrane tagging' using His-GFP microbubbles and ultrasound in adherent A549 cells, the *Results* in *Chapter 4* for A549 cells and Jurkat cells in suspension do not. A possible explanation could be the fact that microbubble behaviour and subsequent 'membrane tagging' affect cells differently in suspension conditions, in which free mixing occurs due to the ultrasound field and secondary microbubble effects such as microstreaming, compared to adherent conditions, in which the cells are stationary and cannot 'escape' oscillating microbubbles.

To better understand how cell-bubble interactions are affected by the surrounding medium, Kudo used high-speed imaging to visualise translational movements of microbubbles beside a scaffold. They observed that a bubble on a soft scaffold surface moves translationally in a direction away from the surface. In contrast, a bubble on a hard scaffold surface, such as a glass coverslip, remains on the surface (Kudo, 2016). Work has been carried out to visualise the interaction of microbubbles with cells in suspension from a sonoporation perspective (Kudo, 2016; Nejad *et al*., 2016). However, it would be interesting to visualise the interaction of His-protein/dye functionalised microbubbles with cells in suspension, using ultra-high-speed imaging, focusing on achieving 'membrane tagging'. The potential for ultra-high-speed imaging to be

combined with fluorescence (Beekers *et al*., 2019) would provide insight into the mechanism of material transfer, as seen in *Chapter 3* and, to a lesser degree, in *Chapter 4*.

6.3.1.4 ImageStream: Combining Confocal Microscopy and Flow Cytometry

Chapter 3 focussed on the qualitative assessment of His-functionalised microbubble-cell membrane interactions, whereas *Chapter 4* focussed on the quantitative assessment of these interactions. Ideally, both the qualitative and quantitative measurements take place simultaneously, so not only the efficiency of microbubble material transfer, e.g., the fraction of cells positive for microbubble material but also the way in which this material transfers, e.g., onto the cell membrane or intracellularly, can be investigated. Amnis developed such a system, called the ImageStream, which combines the quantitative power of flow cytometry with high content image analysis. It can image cells directly in suspension with the resolution of a 60x microscope objective. It provides information regarding the morphology, fluorescence localisation and population statistics. Results of a pilot study to confirm the feasibility of this technique can be found in the *Appendix*, *Section A.5*.

6.3.1.5 Co-Culture Targeting Experiment

Chapter 5 shows a significant increase in microbubble-cell attachment for His-transferrin functionalised microbubbles compared to His-human serum albumin microbubbles on non-TfR blocked A549 cells. There was also only limited binding of His-transferrin functionalised microbubbles to A549 cells with blocked transferrin receptors, confirming targeting specificity. However, this *in vitro* experimental design is not a good reflection of *in vivo* situations in which various cell types, each expressing their own receptors, coexist in the same environment.

Therefore, one way to advance this work is to assess the targeting efficiency and lipid transfer in a co-culture experiment with two cell lines: one expresses the receptor of interest, e.g., the transferrin receptor, and the other does not. This platform would be more representative of *in vivo* conditions, give a better indication of the selective targeting ability of the microbubbles and would allow for a direct, simultaneous comparison at the same conditions and parameters for both cell types investigated. This would further allow a comparison with the *Results* in *Chapter 5, Figure 5.15*, where the targeting efficiency of His-transferrin

microbubbles to the transferrin receptor was compared for separate samples of regular and blocked A549 cells. The choice of targeting molecule is flexible, which is one of the assets of this microbubble design. Therefore, more clinically relevant proteins could be considered, especially with an eye on *in vivo* experiments.

6.3.1.6 His-tagged protein localisation on or within the cell membrane

As eluded to in other *Chapters*, neither the confocal microscopy nor the flow cytometry data give insight into the localisation of the transferred protein-lipid complex in or on the cell membrane and the subsequent accessibility of the protein, which is vital in future *in vitro* and *in vivo* applications.

Fortunately, recent developments in microscopy allow imaging of nanoscopic structures using superresolution microscopy, such as Structured Illumination Microscopy (SIM), STimulated Emission Depletion (STED) microscopy, or Single Molecule Localisation Microscopy (SMLM) (Wegel *et al*., 2016). For example, Honigmann *et al*. (2014) and Sezgin *et al*. (2019) have employed STED microscopy to study the spatial and temporal heterogeneity of lipid interactions in the cell membrane using fluorescent probes.
To investigate the accessibility of the protein, one approach would be to employ flow cytometry to assess the attachment of a fluorescent antibody, which would attach to the 'membrane tagged' cells if the transferred proteins are accessible on the cell membrane, with the appropriate controls to account for, e.g., non-specific antibody binding.

6.3.2 In Vivo

Heavily dependent on the successful completion of future *in vitro* work, as outlined above, the next step is to explore the effectiveness of the proposed protein-functionalised microbubbles to tag target cell membranes *in vivo*. Below, three potential experiments are outlined to explore and assess the applicability of protein-functionalised microbubbles *in vivo*.

6.3.2.1 T cell 'Membrane Tagging'

Firstly, a straightforward assessment of the intravenous delivery of the protein-functionalised microbubbles is proposed, as compared to control microbubbles, in a suitable *in vivo* mouse model. The aim of this experiment would be three-fold: i) to assess whether the functionalised microbubbles have the inherent ability to target and tag native immune cells, such as T cells, in systemic circulation, ii) to investigate the effect ultrasound has on this process, and iii) to assess the timescale over which this effect takes place, i.e. how long immune cells remain tagged with the protein of interest. This is particularly of interest, as cells must remain tagged long enough to be attracted to diseased cells. As compared to, for example, CAR T cell therapy, the proposed membrane tagging does not involve genetic alteration of the cells.

To this end, microbubbles could be loaded with various antibodies that specifically target receptors present at high levels and (almost) exclusively on T cell membranes. Examples of these receptors that have been used in a variety of T-cell targeting nanoparticle studies include CD3 (Smith *et al*., 2017), CD4 (Ramishetti *et al*., 2015), CD7 (Lee *et al*., 2012; Kumar *et al*., 2008) and CD8 (Schmid *et al*., 2017; Yang *et al*., 2019). To direct these microbubble-targeted cells to diseased cells, a second protein or antibody can be loaded on the microbubble shell that targets cancer cells, similar to the multiple His-tagged entities on GUVs used by Jenkins *et al*. (2018). Relevant examples for this *Thesis* include CD19 for B-cell and follicular lymphoma or B-cell Maturation Antigen (BCMA) for multiple myeloma, which are two targets used in currently approved FDA CAR T cell therapies. At present, there are no approved CAR T cell therapies for solid tumours. Using antibodies as a targeting agent, the potential for the induction of receptor signalling and thus potentially triggering a cellular response should be noted. CD3 binding, for example, is known not solely to be responsible for T cell activation but equally for immunosuppression and T cell anergy (Wolf *et al*., 1994).

For this proposed *in vivo* experiment, only the first step in this process - targeting the microbubbles to the T cells - is required. Five potential treatment groups can be envisioned: i) an ultrasound only control group, ii) a relevant protein/antibody-functionalised microbubble group, as elaborated upon in the paragraph above, iii) a control protein/antibody-functionalised microbubble group, such as GFP, iv) a relevant protein/antibody-functionalised microbubble plus ultrasound group, and, lastly v) a control protein/antibody-functionalised microbubble plus ultrasound group.

The experiment's outcome could be determined by blood analysis, for example, by assessing the presence of the relevant protein/antibody with which the microbubbles were functionalised on T cells. These assays might include Western Blotting, an Enzyme-Linked ImmunoSorbent Assay (ELISA) or fluorescence analysis using a fluorescence plate reader or confocal microscope. The timescale over which the desired 'membrane tagging' of T cells takes place can be assessed by taking bleeds over time. It should be noted that, while T cells in the blood are the easiest target for microbubble targeting, only an estimated 2 to 3% of all T cells are found in the blood, with the majority of T cells being present in lymphoid tissues, such as the bone marrow, spleen, tonsils and lymph nodes (Kumar, Connors & Faber, 2018). To this end, the lymph nodes and spleen would be removed for further examination post cull at a pre-determined endpoint.

6.3.2.2 Solid Tumour Challenge Study

Following on from *Section 6.3.2.1*, if indeed 'membrane tagging' can be established in immune cells *in vivo*, the next step could explore whether tagging immune cells with antibodies against antigens expressed on tumour cells could prevent the development of tumours. Microbubbles would be loaded with both an immune cell targeting protein, as outlined above, and a second His-tagged entity that specifically recognises cancer cells, such as an antibody, against i) tumour specific antigens, such as oncoviral and neoantigens, e.g., alphafetoprotein (AFP) expression in germ cell tumours and hepatocellular carcinoma (Abelev, 1971), or ii) tumour associated antigens, such as overexpressed proteins, e.g., human epidermal growth factor receptor 2 (HER2) in breast cancer patients (Meric-Bernstam *et al.,* 2019) or melanoma-associated antigen (MAGE) in malignant melanoma (Tio *et al*., 2019).

To examine the feasibility of this, an experiment could be designed where mice are challenged with relevant tumour implantation, and treatment occurs within three days of the implant. Tumour growth rate is subsequently assessed through calliper measurement. If the treatment successfully heightens the immune response by functionalising immune cells through 'membrane tagging', the tumour growth would be affected. It is important to use a control group to establish a baseline for tumour growth, where mice are merely implanted with tumour cells, and no further treatment is given. Other groups envisioned are the same as in *Section 6.3.2.1*, unless demonstrated to be non-effective.

6.3.2.3 The Effect of Ultrasound-Mediated Targeted Microbubbles on Established Tumours

Lastly, the main aim of this *DPhil Project* was to design and develop microbubbles functionalised with a protein of choice to tag target cell membranes to make diseased target cells, such as cancer cells, more visible to the immune system or immune cells more potent in detecting diseased cells. The previous two *Sections* have focussed primarily on the latter half of this objective, targeting immune cells in suspension. This last *Section* focuses on the first half of the objective instead: making diseased target cells more visible to the immune system. To do this, it is envisioned that diseased cells are tagged with proteins that will attract immune cells, for example, peptide/major histocompatibility complex (pMHC) and antibodies against cluster of differentiation (CD) 58, ICAM-1 or CD45 (Jenkins *et al*., 2018). Microbubbles will be similarly targeted to these diseased cells by loading the microbubble with a second His-tagged molecule, such as an antibody against tumour-specific antigens or tumour-associated antigens, as explained in the previous *Section*.

While the previous *Section* investigated the feasibility of using functionalised microbubbles to prime the immune system through 'membrane tagging' to prevent tumour growth, a more realistic *in vivo* application targets already developed tumours. To this end, a study is proposed here, where relevant tumours are allowed to develop before being subsequently treated with ultrasound and protein-functionalised microbubbles. The benefit of the use of ultrasound and cavitation agents, such as microbubbles, has been demonstrated both in the BUBBL group and in the literature (Chen & Hwang, 2013; Kwan *et al*., 2015), for example, through increasing extravasation of particles from the vasculature into the tumour environment (Yemane *et al*., 2019). The use of ultrasound could promote functionalised microbubble or tagged immune cell uptake in the tumour environment.

Therefore, an initial study is proposed in which five groups are assessed and compared to a non-treatment control group: i) an ultrasound only control group, ii) a relevant protein/antibody-functionalised microbubble group, as elaborated upon in the paragraph above, iii) a control protein/antibody-functionalised microbubble group, such as GFP, iv) a relevant protein/antibody-functionalised microbubble plus ultrasound group, and, lastly, v) a control protein/antibody-functionalised microbubble plus ultrasound group, with the possibility of excluding some groups based on the results of the studies proposed in *Sections 6.3.2.1 and 6.3.2.2*. If successful, this could potentially grow into a 90-day study with additional treatment time points, based on information learnt from *Section 6.3.2.1* regarding the timescale of the desired 'membrane tagging'

bioeffect. This would provide an insight into the effectiveness of the proposed protein/antibody-functionalised microbubbles to tag the membrane of diseased cells and, subsequently, alert the immune system. Its effect on tumour growth would measure the success of this treatment. If successful, this proposed therapy could be an inexpensive, low-risk alternative to CAR T cell therapy.

Appendix

A.1 The effect of the microbubble fabrication method on microbubble material transfer

The effect of optimising the microbubble fabrication method on the 'membrane tagging' bio effect is investigated in this *Section*. Apart from the microbubble fabrication method, the experiments followed the ultrasound exposure and subsequent analysis methods as detailed in the main body of *Chapter 3*. Experiments were carried out in the SAT3.

A.1.1 Microbubble fabrication

For the experiments investigating the effect of optimising the microbubble fabrication protocol on the qualitative observation of lipid transfer/fusion in the SAT3, NTA(Ni)-His-GFP functionalised microbubbles were manufactured in two ways.

For the first fabrication method, lipid films were dried overnight on a hotplate, subsequently resuspended and sonicated using the Qsonica Q125 (probe diameter is 3.18 mm, 125 W, 20 kHz, Newtown, Ct, USA). The sonicator probe was moved to the liquid-gas interface in an upward fashion. The vial headspace was not filled with sulphur hexafluoride (SF_6) prior to bubble sonication, and the needle to regulate SF_6 gas flow was positioned outside the glass vial during sonication. In contrast, for the second, optimised fabrication method, lipid films were dried under a vacuum at 60 ˚C for 45 minutes (Eppendorf, Concentrator plus, V-AQ), subsequently resuspended and sonicated using the Microson XL 2000 (probe diameter 3 mm, 20 W, 22.5 kHz, Misonix Incorporated, NY, USA). The sonicator probe was moved to the liquid-gas interface in a downward fashion, so attachment of the liquid meniscus to the probe could be observed. The headspace of the vial was filled with SF_6 for 15 seconds prior to bubble sonication, and a low flow rate of SF_6 was employed with the needle being positioned inside the glass vial during sonication.

Furthermore, the batches of microbubbles made according to the first fabrication protocol were washed via the centrifugal method using a filtered needle (BD™ 18 G Blunt Filter (5 μm) Needle, UK). In contrast, the batches of microbubbles made according to the second fabrication protocol were washed via the centrifugal method using a regular needle (BD™ 18 G Blunt Fill Needle, UK). All microbubbles were characterised with the Beckman Coulter Multisizer as described in *Section 2.2.2.2* in *Chapter 2*.

A.1.2 Microbubble behaviour - ultrasound exposure parameter study

To get a better idea of the behaviour of the His-AF488 functionalised microbubbles in response to ultrasound exposure, His-AF488 microbubbles made via two manufacturing methods were compared across an extensive parameter space, as summarised in *Table A.1.1*.

MB type	US centre frequency (MHz)	Peak negative pressure (kPa)	Duty cycle (%)	Duration of exposure (s)
His-AF488 Fabrication method 1	0.5	200	100	60
	0.5	200	10	60
	0.5	200	1	60
His-AF488 Fabrication method 2	0.5	200	100	60
	0.5	200	10	60
	0.5	200	1	60

Table A.1.1. Ultrasound driving conditions for the comparison between microbubbles made with manufacturing methods 1 and 2, as specified in the Appendix, Section A.1.

A.1.3 Results and Discussion

An interesting thing to note is the apparent dependence of the 'membrane tagging' bioeffect on the microbubble fabrication method. To this end, microbubbles were made according to the two fabrication methods as described in *Section A.1.1* above. The lipid transfer/microbubble fusion results for each microbubble fabrication method are shown in the confocal images in *Figure A.1.1*. The corresponding microbubble behaviour upon ultrasound exposure (0.5 MHz centre frequency, 200 kPa peak negative pressure, continuous wave, and a 60-second total exposure duration) is shown in *Figures A.1.2* and *A.1.3* for both fabrication methods, respectively.

Even though the concentration-matched microbubbles' response to ultrasound, e.g. the signal powers and spectrum histories, are comparable, the biological effect, as shown in *Figure A.1.1*, varies greatly between the two microbubble populations. The desired 'membrane tagging' bioeffect is observed for microbubbles made according to the first fabrication method and not for microbubbles made according to the

second, improved fabrication method. The fact that the acoustic response was similar suggests that the difference in size had a negligible effect.

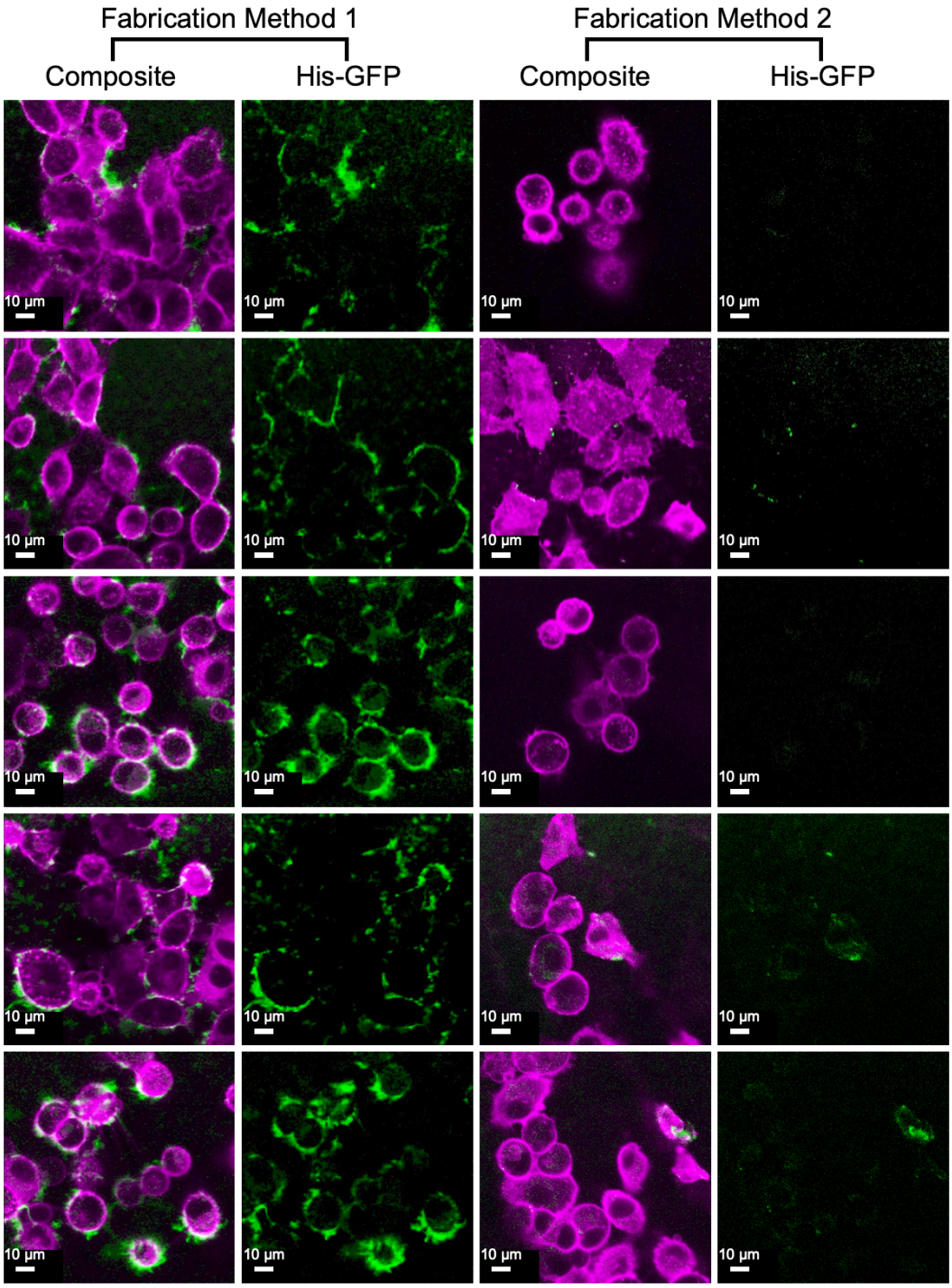


Figure A.1.1. 'Membrane tagging' observed in the SAT3 for two microbubble fabrication methods. *Confocal microscopy images of A549 cells stained with Cell Mask Deep Red (magenta) and His-GFP NTA(Ni) lipids and microbubbles (green) after 60s of ultrasound exposure (0.5 MHz, 200 kPa PNP, CW) in the SAT3, with on the left microbubbles made according to fabrication method 1 (N = 3) and on the right microbubbles with a mean diameter of made according to fabrication method 2 (N = 3). A distinct qualitative difference in the transfer/fusion of His-GFP NTA(Ni) lipid to the cellular membranes can be observed.*

Apart from their size distribution, one other distinct difference between the two microbubble populations is the concentration at which they are produced: 7 x 10^8 MBs/mL for the batch of microbubbles made by the first fabrication method and 4.2 x 10^9 MBs/mL for the batch of microbubbles made by the second fabrication method, as can be seen in *Figures A.1.2* and *A.1.3*, constituting not only a small increase in size but also a ~6 fold increase in the concentration, and thus larger total surface area.

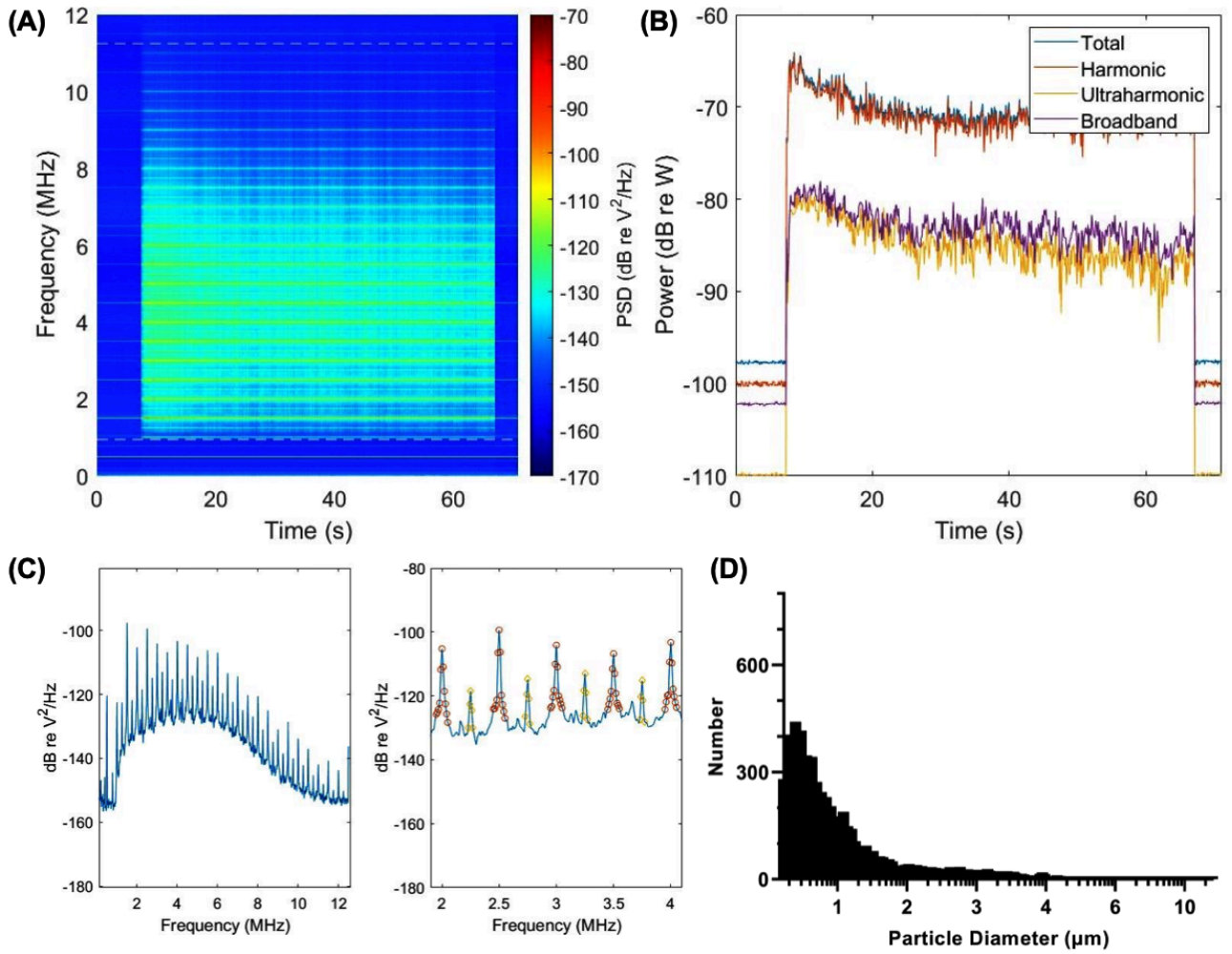


Figure A.1.2. Example spectrum histories over a 60-second exposure of a suspension of His-GFP microbubbles made according to fabrication method 1 at 1*10⁸ MBs/mL in the SAT3. *(A) Full spectra and (B) total, harmonic, ultraharmonic and broadband signal powers, all as a function of time. (C) Frequency domain PCD trace corresponding to the onset of the ultrasound signal (left), zoomed in (right), showing harmonics (orange) and ultraharmonics (yellow). Drive conditions were 0.5 MHz, 0.2 MPa peak negative pressure, continuous wave, 60 seconds of total exposure. (D) Microbubble size distribution histogram (number of events = 7073), with a mean diameter of 1.6 µm and a concentration of 7.0 x 10^8 MBs/mL.*

Given that both microbubble batches were incubated with 20 μg of His-GFP, the density of His-GFP on the 'second fabrication method' microbubbles might be insufficient to be adequately visualised on the confocal microscope. This explanation would fit with the observed lipid transfer/microbubble fusion in *Figure 3.9* in *Chapter 3*, with microbubbles made with fabrication method 1 and the same ultrasound parameters, but with a microbubble mean diameter of 3.7 μm. This issue was resolved using the cheaper and brighter His-AF488, of which a larger molar quantity was incubated with the microbubbles made according to the second, improved fabrication method, ensuring stable and bright microbubbles.

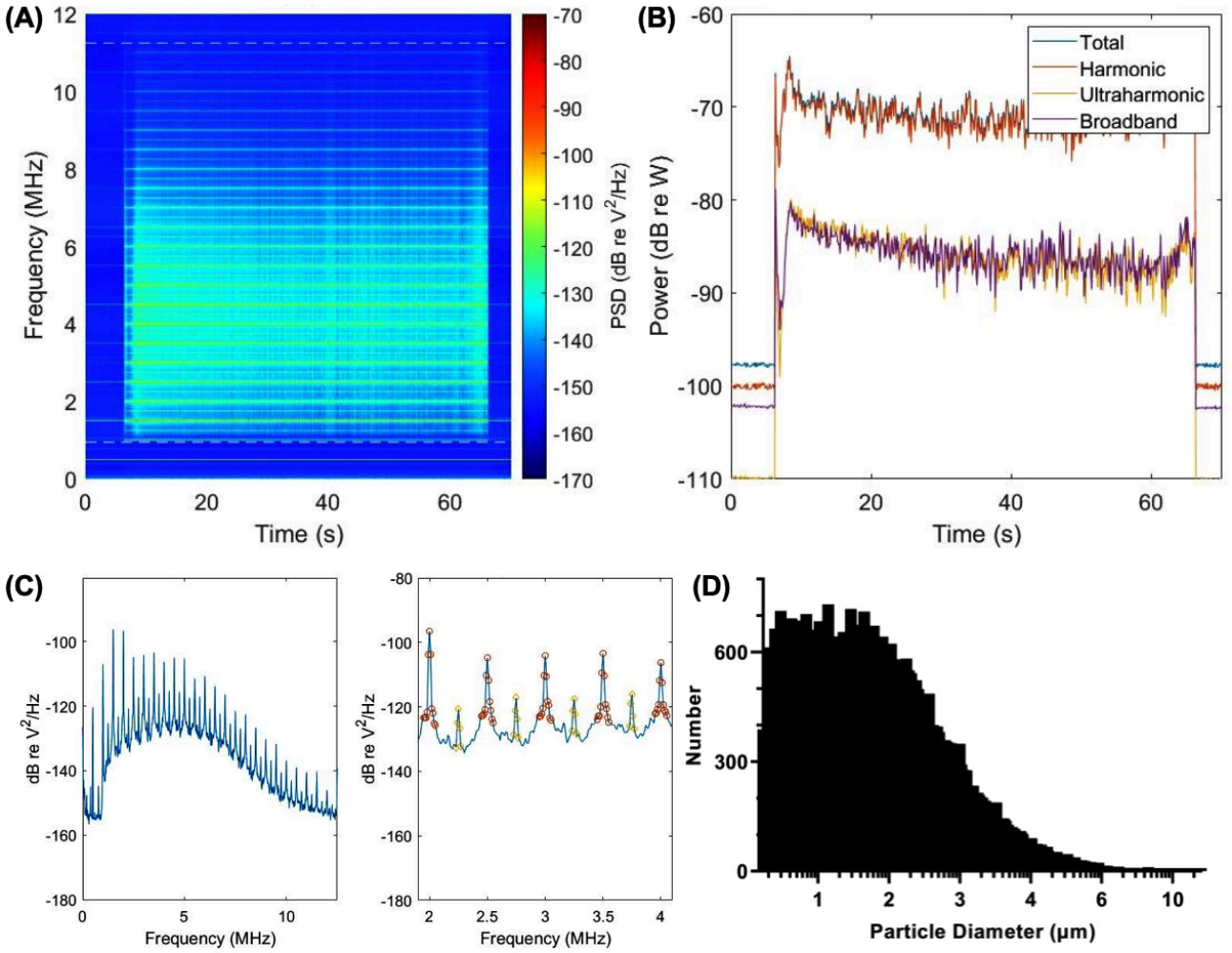


Figure A.1.3. Example spectrum histories over a 60-second exposure of a suspension of His-GFP microbubbles made according to fabrication method 2 at 1*10⁸ MBs/mL in the SAT3.*(A) Full spectra and (B) total, harmonic, ultraharmonic and broadband signal powers, all as a function of time. (C) Frequency domain PCD trace corresponding to the onset of the ultrasound signal (left), zoomed in (right), showing harmonics (orange) and ultraharmonics (yellow). Drive conditions were 0.5 MHz, 0.2 MPa peak negative pressure, continuous wave, 60 seconds of total exposure. (D) Microbubble size distribution histogram (number of events = 46901), with a mean diameter of 2.1 µm and a concentration of 4.2 x 10⁹ MBs/mL.*

In light of the *Results* above, showing a potential dependence of the microbubble manufacturing method on the 'membrane tagging' observed, the acoustic behaviour of microbubbles made with both fabrication methods was compared. The ultrasound driving conditions were at 0.5 MHz centre frequency, 200 kPa peak negative pressure, with duty cycles of 1, 10 and 100%, and a total exposure duration of 60 seconds, of which the continuous wave condition is comparable to the experimental conditions in *Chapter 3* and the *Appendix, Sections A.1* and *A.2*.

The microbubbles made according to method 1 appear to show lower signal powers across all spectrum components than those made according to method 2. The effect gets more pronounced as the duty cycle decreases, as seen in *Figure A.1.4*.

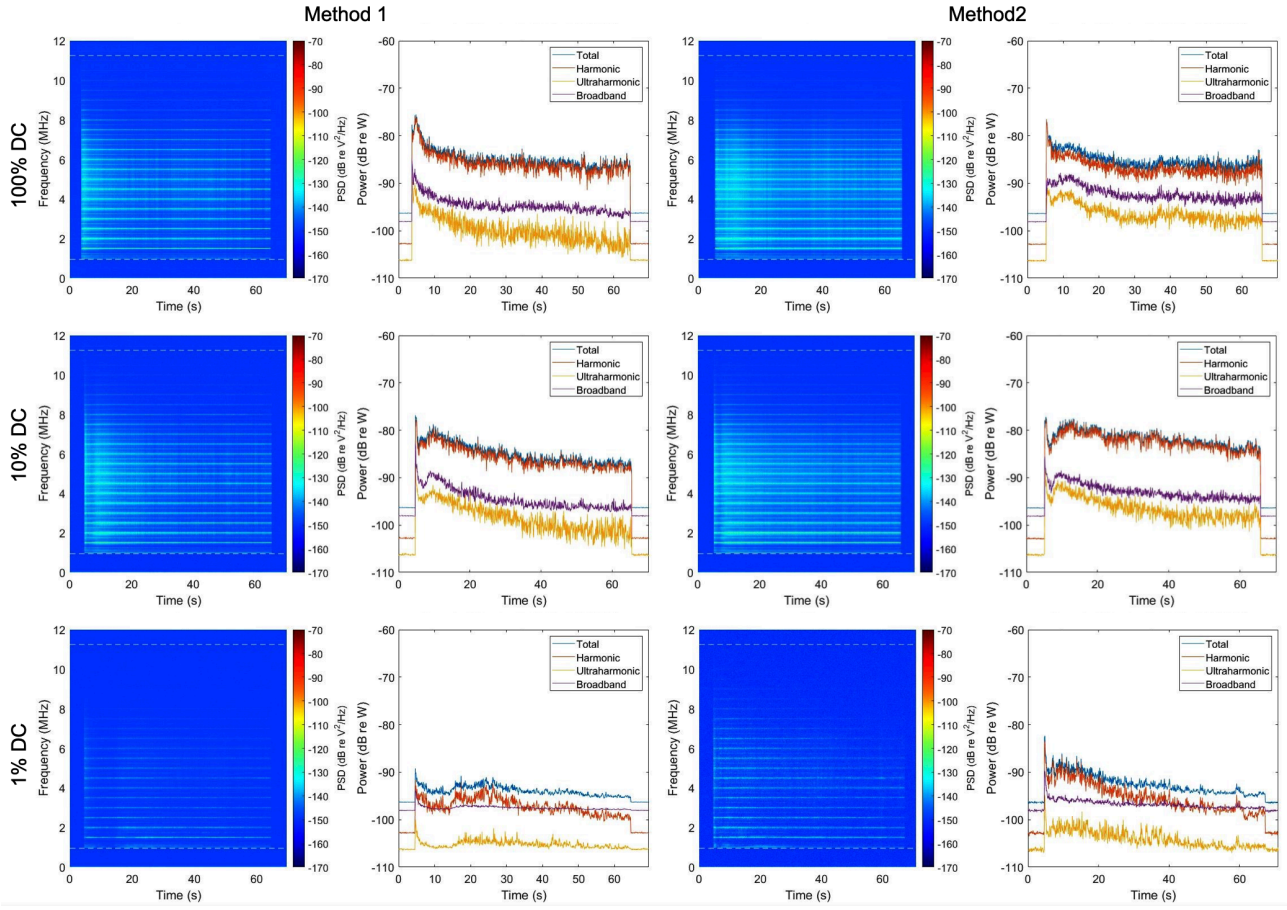


Figure A.1.4. Example spectrum histories over a 60-second exposure of a suspension of His-GFP microbubbles, made with both fabrication methods, at 2 x 10⁷ MBs/mL. *Full spectra and total, harmonic, ultraharmonic and broadband signal powers, all as a function of time, are shown. Drive conditions were 0.5 MHz, 200 kPa peak negative pressure, for three DC: 100, 10 and 1%, 60 seconds total exposure duration.*

Figure A.1.5 shows representative microbubble size distributions histograms of SonoVue microbubbles and His-GFP microbubbles manufactured with both fabrication methods as outlined in the *Appendix*, *Section A.1*.

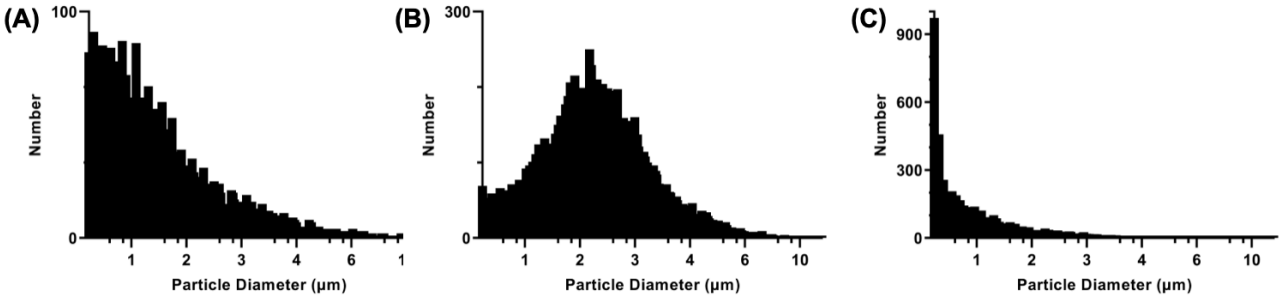


Figure A.1.5. Microbubble size distribution histograms for microbubbles as used in the experiments in Section 3.3.4, after centrifugation. *(A) SonoVue microbubbles, with a mean diameter of 1.92 µm and a concentration of 3.3 x 10^8 MBs/mL (number of events = 3302), (B) His-AF488 microbubbles, with a mean diameter of 2.46 µm and a concentration of 1.6 x 10^9 MBs/mL (number of events = 14775), and (C) filtered His-AF488 microbubbles, with a mean diameter of 1.55 µm and a concentration of 6.0 x 10^8 MBs/mL (number of events = 6045).*

A.2 'Membrane tagging' versus 'internalisation', using lyso-microbubbles

Previous work, both in the BUBBL group and the wider community, has focussed on optimising microbubbles for intracellular drug delivery (Aron *et al*., 2019; Horsley *et al*., 2019; Stride, 2019). For example, Aron *et al*. *(*2019) showed a ~5 fold increase in sonoporation compared to control microbubbles for microbubbles containing 16:0 lyso-PC. However, to modulate the immune response, there is a need for a microbubble that does not deliver lipids or other cargo intracellularly but 'tags' the cellular membrane with a relevant protein, as immune signalling starts at the cellular membrane rather than intracellularly. In this *Section* of the *Appendix*, 18:1 NBD Lyso PE-functionalised microbubbles are subjected to the same microbubble-mediated ultrasound exposure conditions as the His-GFP DGS-NTA(Ni)-functionalised microbubbles in *Chapter 3*. Apart from the microbubble fabrication method, the experiments followed the ultrasound exposure and subsequent analysis methods, as detailed in *Chapter 3*. Experiments were carried out in the SAT3.

A.2.1 Microbubble fabrication

For the comparison between the 'membrane tagging' with the His-GFP functionalised microbubbles in *Chapter 3*, e.g. as visualised in *Figure 3.9*, and the 'internalisation' with lyso-microbubbles, lyso-microbubbles were manufactured following the unoptimised fabrication method 1 as detailed above, but with 1,2-dibehenoyl-sn-glycero-3-phosphocholine (22:0 PC) : PEG40S : 18:1 NBD Lyso PE with molar ratio 9 : 1 : 0.1 (Avanti Polar Lipids, USA).

Lyso PE is a phospholipid with its second hydrocarbon chain removed. Incorporating the latter into a microbubble consisting of phosphatidylcholine and PEG40S leads to an increase in the curvature of the cell membrane upon interaction with the bubble (Aron *et al*., 2019). This increase in curvature may be balanced by increased membrane surface tension (Aron, 2018). As preserving membrane surface tension is favoured over preserving cell volume, the increase in membrane surface tension may be accompanied by an influx of water. The result of this influx of water is hypothesised by Aron *et al*. to be the formation of water defects in the cell membrane, thereby lowering the energy barrier for pore formation and thus internalising the microbubble's

components (Aron, 2018). All microbubbles were characterised with the Beckman Coulter Multisizer as described in *Section 2.2.2.2* in *Chapter 2*.

A.2.2 Results and Discussion

Under identical conditions, e.g. same cells and same ultrasound exposure conditions, the His-GFP functionalised microbubbles were compared to lyso-microbubbles. The results of the experiments with the fabricated lyso-microbubbles are shown in *Figures A.2.4* and *A.2.5*.

A fluorescent, unsaturated lysolipid (18:1 NBD Lyso PE), known for promoting pore formation in lipid bilayers, was used to investigate lyso-microbubbles' lipid transfer to / microbubble fusion with cell membranes and compare these results to the results obtained in *Section 3.3.3* and *A.1.2*. To this end, lyso-microbubbles were exposed in the SAT3 to the same ultrasound conditions (0.5 MHz centre frequency, 200 kPa PNP, continuous wave, 60 seconds) as the His-GFP NTA(Ni) microbubbles in *Chapter 3*, *Figure 3.9* and *Appendix A.1*, *Figure A.1.1*. Striking is the different incorporation/uptake of the fluorescent lipids between these two microbubble types, with distinct 'internalisation' into the cytosol being observed for lyso-microbubbles in *Figure A.2.4* below, compared to 'membrane tagging' as observed for the His-GFP NTA(Ni) microbubbles in *Chapter 3*, *Figure 3.9*, and *Appendix A.1*, *Figure A.1.1*.

Interesting in both cases is the non-uniformity of the effect, with neighbouring cells showing vastly different degrees of 'tagging' and 'internalisation'. This may be due to spatial heterogeneity in the microbubble cavitation effects, which could be visualised in future work by combining confocal microscopy to capture the cellular response, and ultra-high-speed imaging to capture the microbubble behaviour, as shown in work by Beekers *et al*. (2019).

Furthermore, it should be noted that even though samples were exposed to the same ultrasound driving conditions and microbubble concentrations, there is a difference in both the percentage of cells positive for 18:1 NBD Lyso PE as well as the corresponding brightness of 18:1 NBD Lyso PE for the NBD positive cells. As all microscopy parameters are equal, this may be due to the fact that samples were given more time - 30 minutes rather than 15 minutes - after ultrasound treatment before imaging.

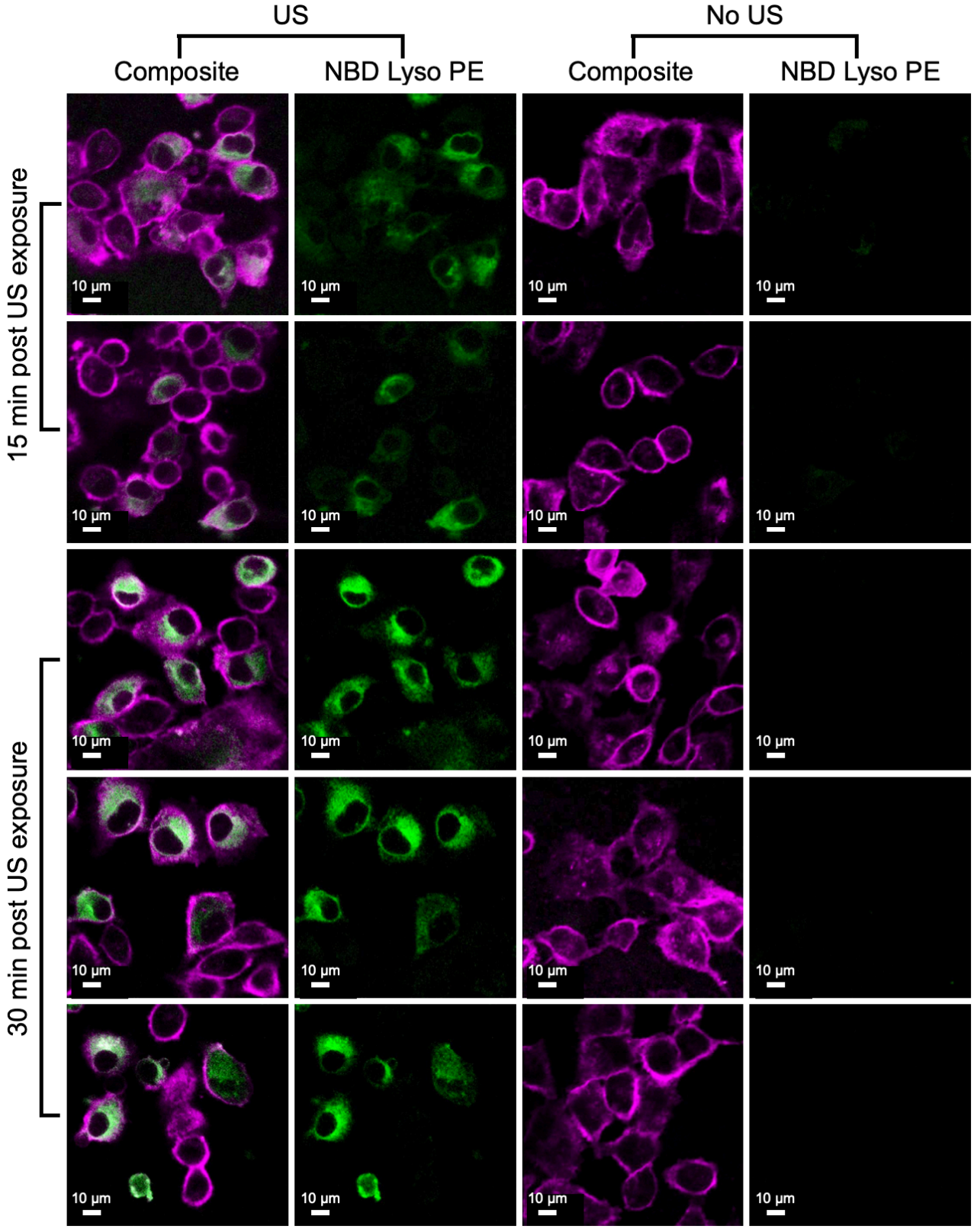


Figure A.2.1. 'Internalisation' observed in the SAT3 for lyso-microbubbles. *Confocal microscopy images of A549 cells stained with Cell Mask Deep Red (magenta) and 18:1 NBD Lyso PE lipids (green) for cells images 15 minutes (N = 2) and 30 minutes (N=1) after 60 seconds of ultrasound exposure (0.5 MHz, 200 kPa PNP, CW) in the SAT3, and corresponding no ultrasound controls on the right. A distinct qualitative difference in the amount, as well as how the 18:1 NBD Lyso PE is incorporated, can be observed.*

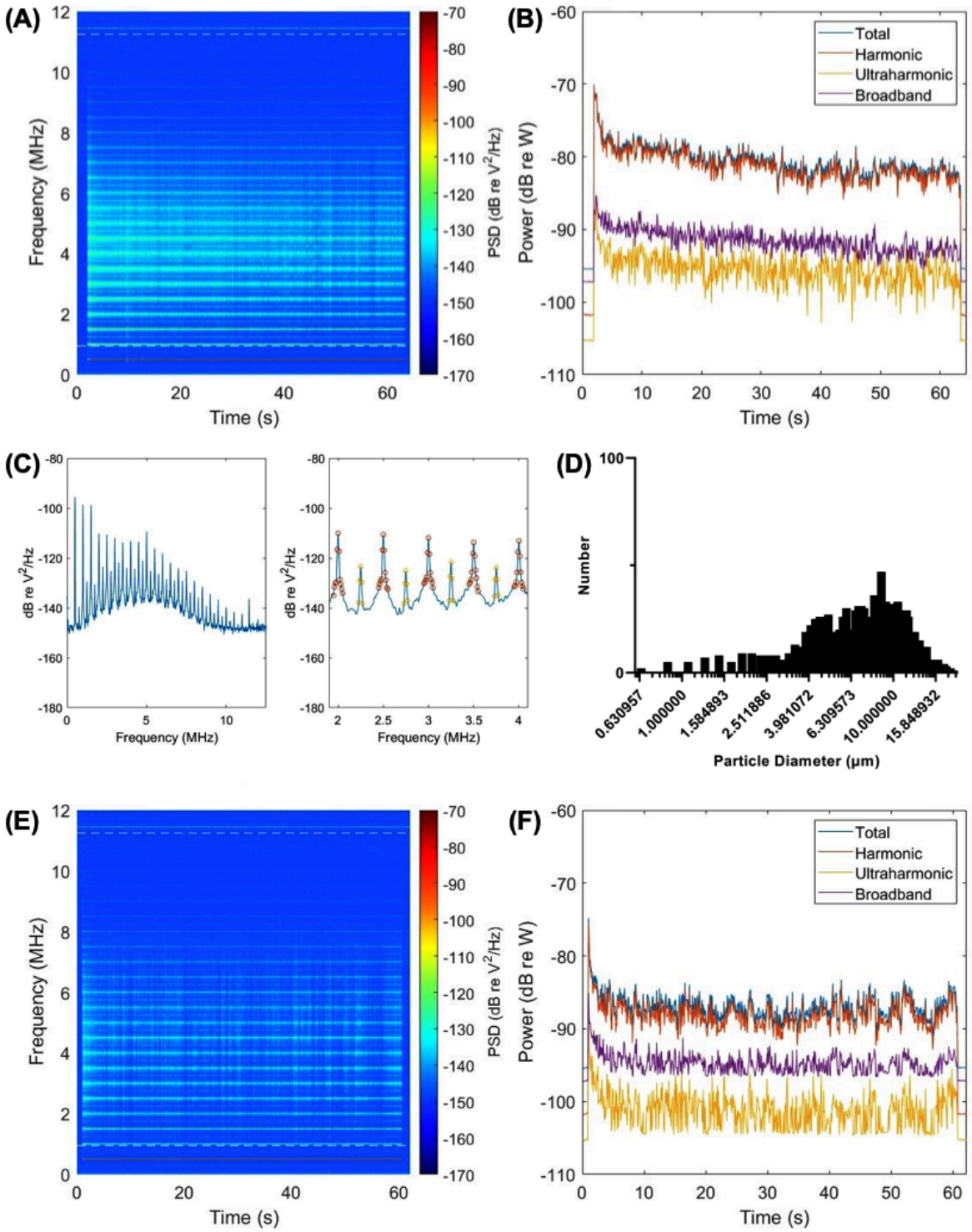


Figure A.2.2. Example spectrum histories over a 60-second exposure of a suspension of 18:1 NBD Lyso PE microbubbles at 1*10⁸ MBs/mL in the SAT3. *(A) Full spectra and (B) total, harmonic, ultraharmonic and broadband signal powers, all as a function of time, are representative of the 30 min samples in Figure A.2.4. (C) Frequency domain PCD trace corresponding to the onset of the ultrasound signal (left), zoomed in (right) showing harmonics (orange) and ultraharmonics (yellow). Drive conditions were 0.5 MHz, 0.2 MPa peak negative pressure, continuous wave, 60 seconds of total exposure. (D) Microbubble size distribution histogram (number of events = 1348), with a mean diameter of 8.5 µm and a concentration of 1.6 x 10⁷ MBs/mL. (E) Full spectra and (F) total, harmonic, ultraharmonic and broadband signal powers, all as a function of time, are representative of a 15 min sample in Figure A.2.4, showing lower total powers for all signal components.*

However, a more likely explanation is the difference in microbubble activity, of which an example can be seen in figure 15 (F) (15 min) versus (B) (30 min), with lower signal powers observed for the samples measured 15 minutes post treatment compared to the samples measured 30 minutes later. This may be due to the degradation of the microbubbles, as figure 15 (D) shows the lyso microbubbles were abnormally large (~8.5 μm) and, therefore, potentially less stable over time. This potential degradation may have primarily affected the samples assessed on the confocal microscope 15 minutes post treatment, as they were conducted second to the 30-minute samples. Though preliminarily very interesting, repeats of this experiment, with good, stable microbubbles, are required to have confidence in these conclusions.

A.3 Chapter 4 - supplementary figures

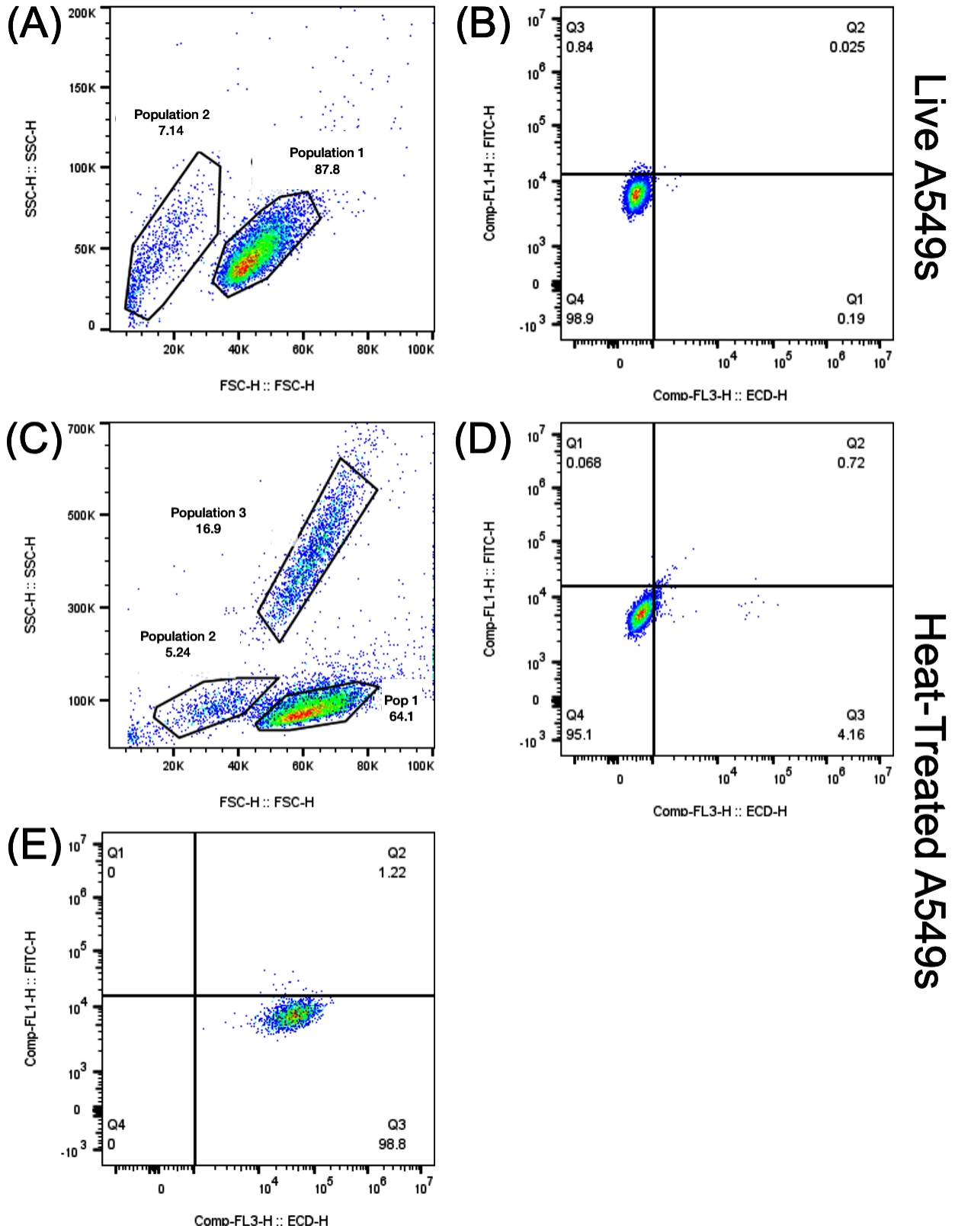


Figure A.3.1. Flow cytometry analysis of live A549 cells (A - B) and heat-treated A549 cells (C - E) as a negative control for His-AF488 and both negative (live) and positive (heat-treated) controls for PI. *Forward vs side scatter plots (A, C), showing three populations, corresponding FITC (~AF488) vs ECD (PI) plots for the live, healthy cells in the gate 'population 1' (B, D) and heat-affected cells in the gate 'population 3' (E), compensated for spectral mixing of His-AF488 into the PI channel.*

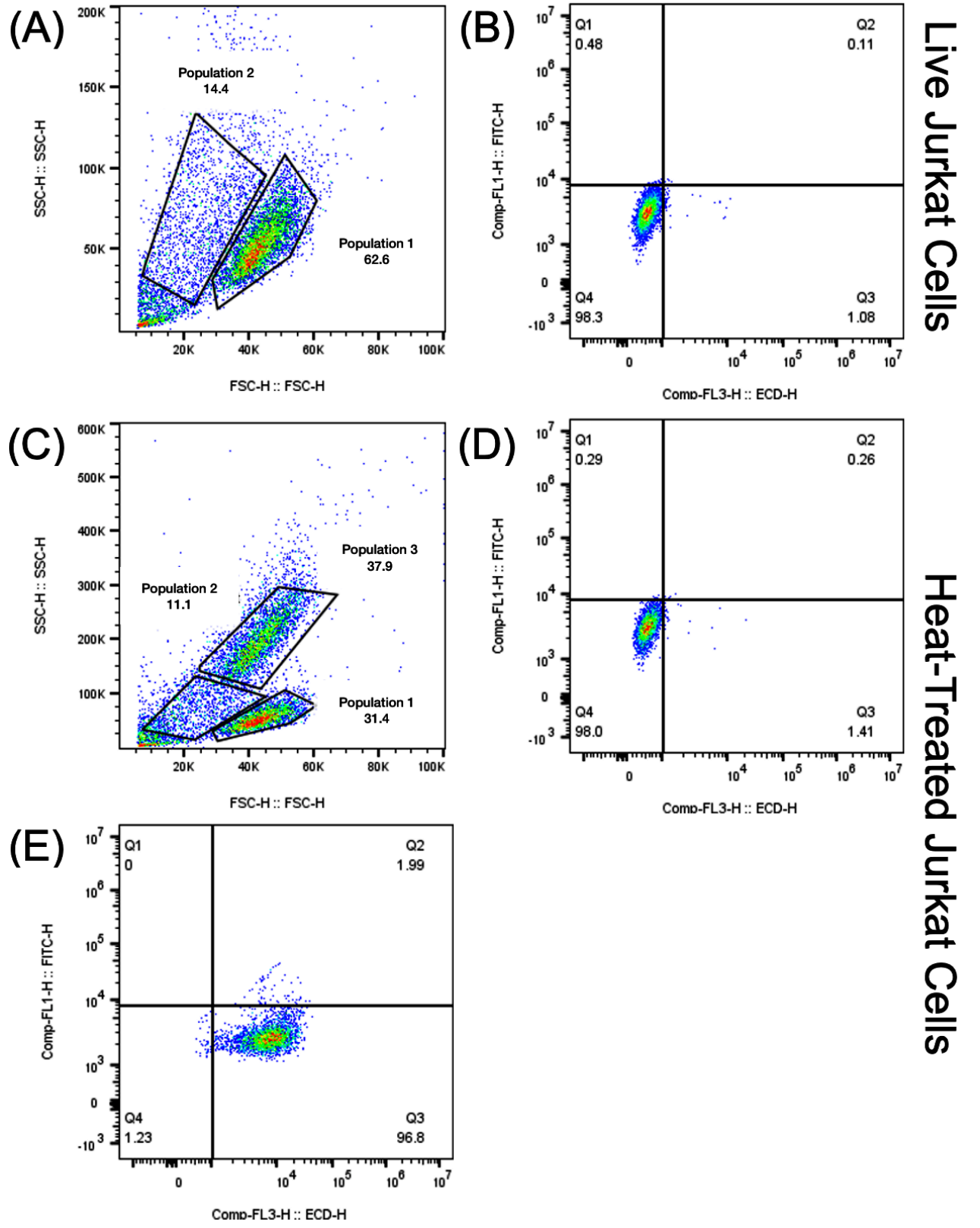


Figure A.3.2. Flow cytometry analysis of live Jurkat cells (A - B) and heat-treated Jurkat cells (C - E) as a negative control for His-AF488 and both negative (live) and positive (heat-treated) controls for PI. *Forward vs side scatter plots (A, C), showing three populations, corresponding FITC (~AF488) vs ECD (PI) plots for the live, healthy cells in the gate 'population 1' (B, D) and heat-affected cells in the gate 'population 3' (E), compensated for spectral mixing of His-AF488 into the PI channel.*

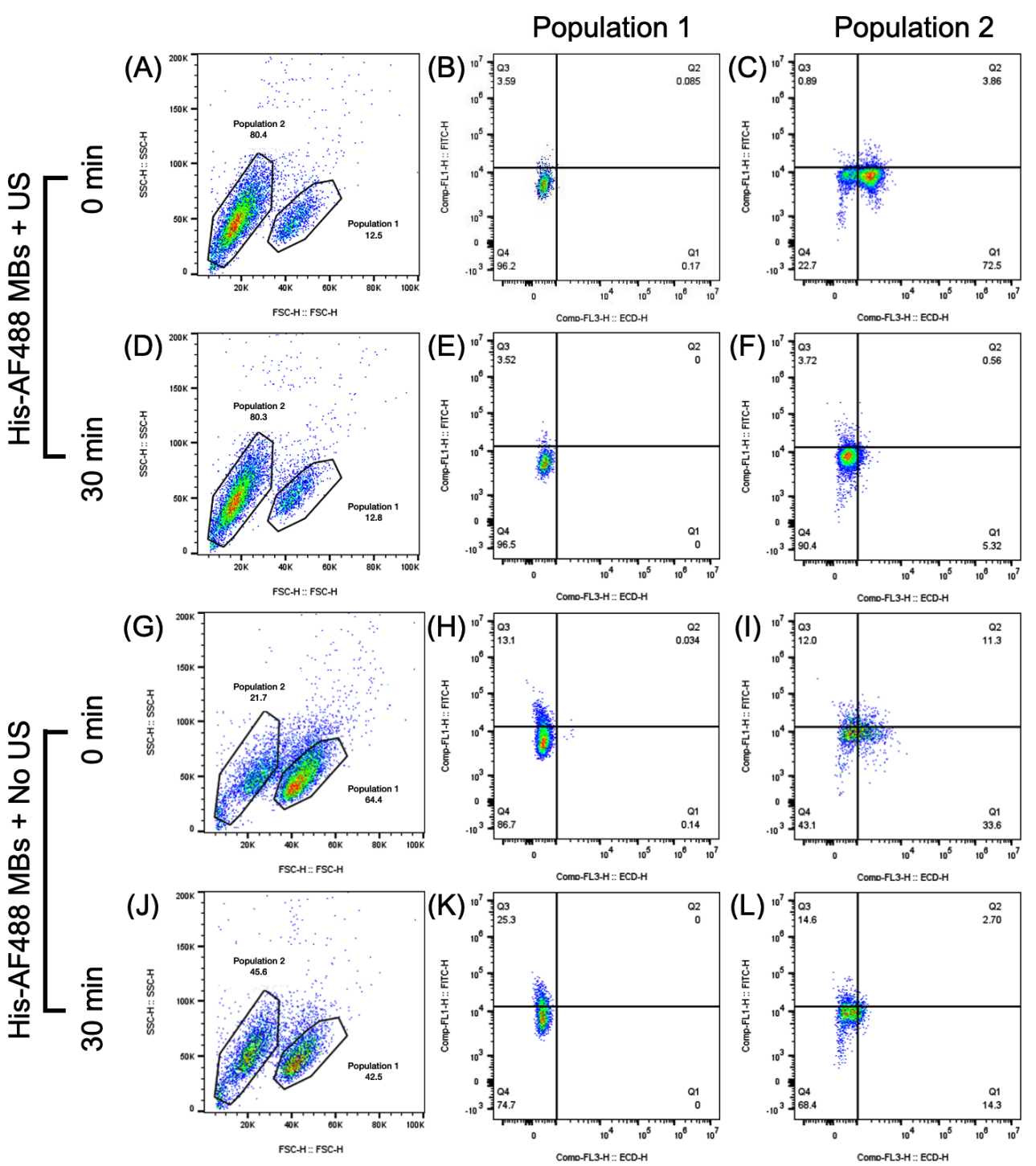


Figure A.3.3. Example of flow cytometry analysis of A549 cells in the experiment in Chapter 4, Section 4.3.2.1, with (A - F) corresponding to A549 cells treated with His-AF488 microbubbles and ultrasound, and (G - L) corresponding to A549 cells only treated with His-AF488 microbubbles (no ultrasound control), at both t = 0 and t = 30 min. *Forward vs side scatter plots (A, D, G, H) and corresponding FITC (~AF488) vs ECD (PI) plots for the live, healthy cells in the gate 'population 1' (B, E, H, K) and cells in the ultrasound-affected gate 'population 2' (C, F, I, L), which proportion increases with exposure to both microbubbles and ultrasound. All data is compensated for spectral mixing of His-AF488 into the PI channel. Ultrasound driving conditions were: 0.5 MHz, 200 kPa PNP, continuous wave, 60 seconds total exposure duration.*

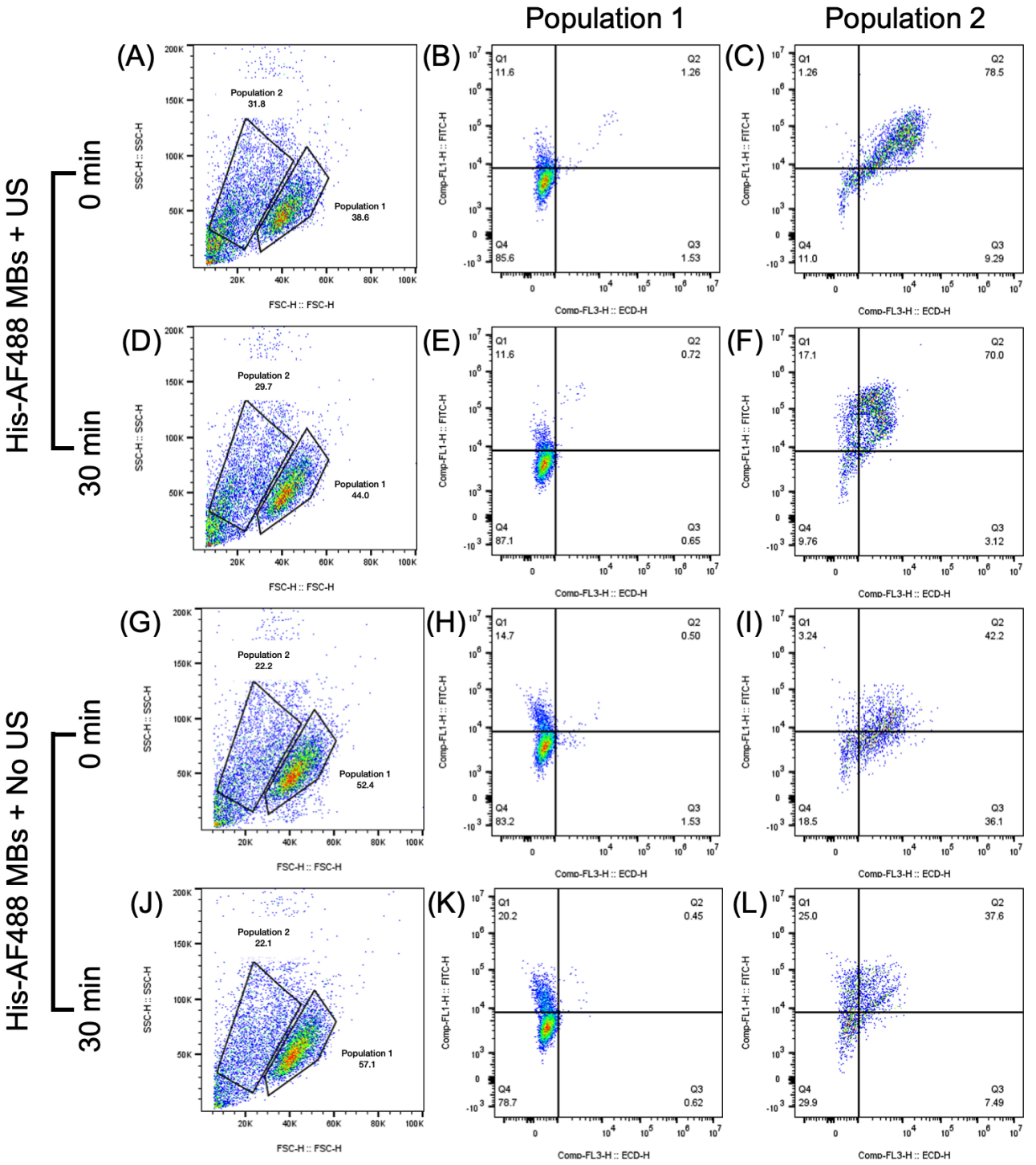


Figure *A.3.4. Example of flow cytometry analysis of Jurkat cells in the experiment in Chapter 4, Section 4.3.3.1, with (A - F) corresponding to Jurkat cells treated with His-AF488 microbubbles and ultrasound, and (G - L) corresponding to Jurkat cells only treated with His-AF488 microbubbles (no ultrasound control), at both t = 0 and t = 30 min.* *Forward vs side scatter plots (A, D, G, H) and corresponding FITC (~AF488) vs ECD (PI) plots for the live, healthy cells in the gate 'population 1' (B, E, H, K) and cells in the ultrasound-affected gate 'population 2' (C, F, I, L), which proportion increases with exposure to both microbubbles and ultrasound. All data is compensated for spectral mixing of His-AF488 into the PI channel. Ultrasound driving conditions were: 0.5 MHz, 200 kPa PNP, continuous wave, 60 seconds total exposure duration.*

A.4 Chapter 5 - supplementary figures

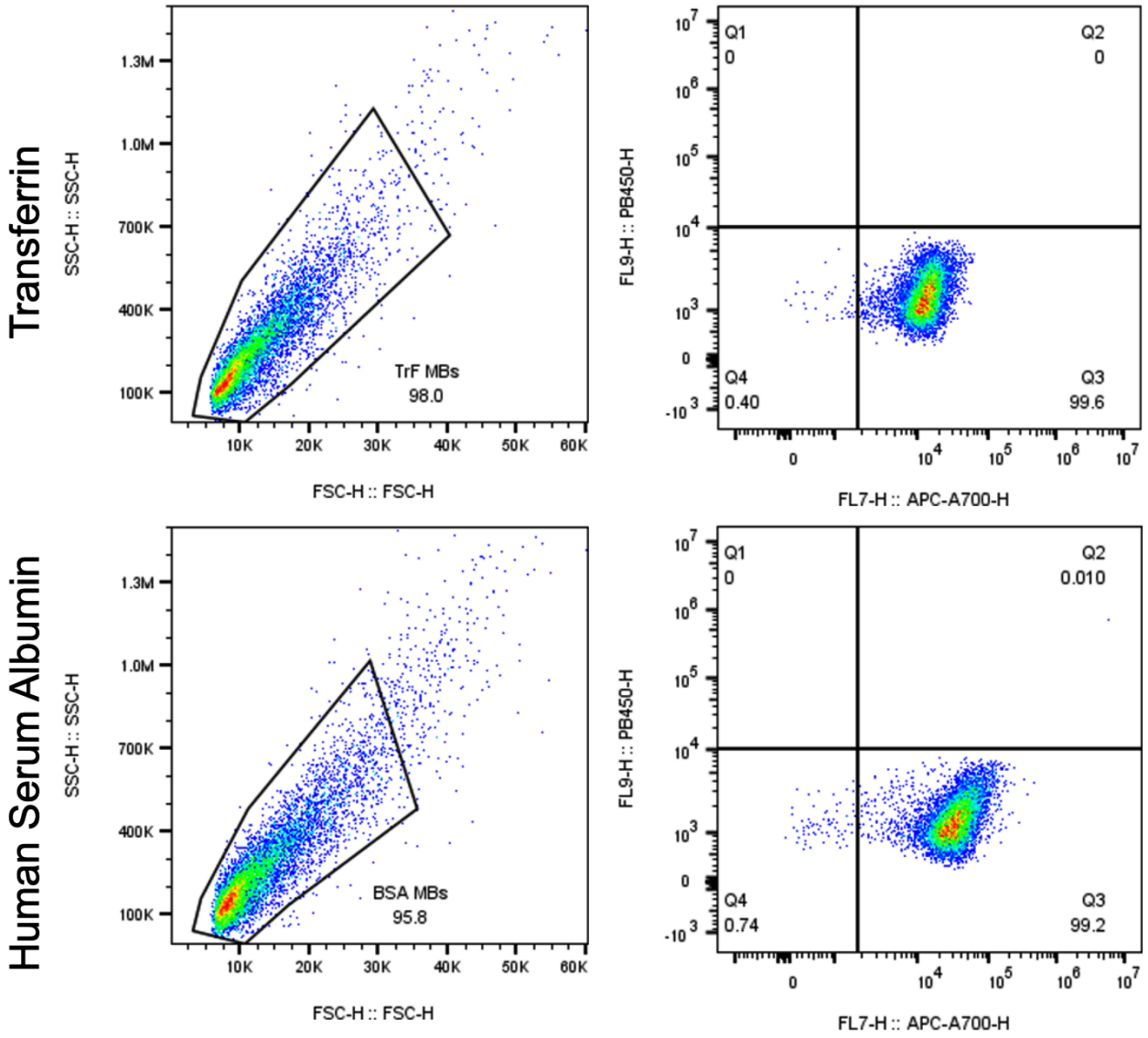


Figure A.4.1. Flow cytometry analysis of His-transferrin and His-human serum albumin functionalised microbubbles used in the experiments in Chapter 5, Section 5.3.2.2. *It shows the forward vs side scatter plots and corresponding APC-A700 (~AF680/ CF660C) vs PB450 (DAPI) plots. Given the same degree of labelling for both the His-transferrin and His-humans serum albumin, the difference in fluorescence intensity in the APC-A700 channel might be due to a difference in protein loading of the microbubbles.*

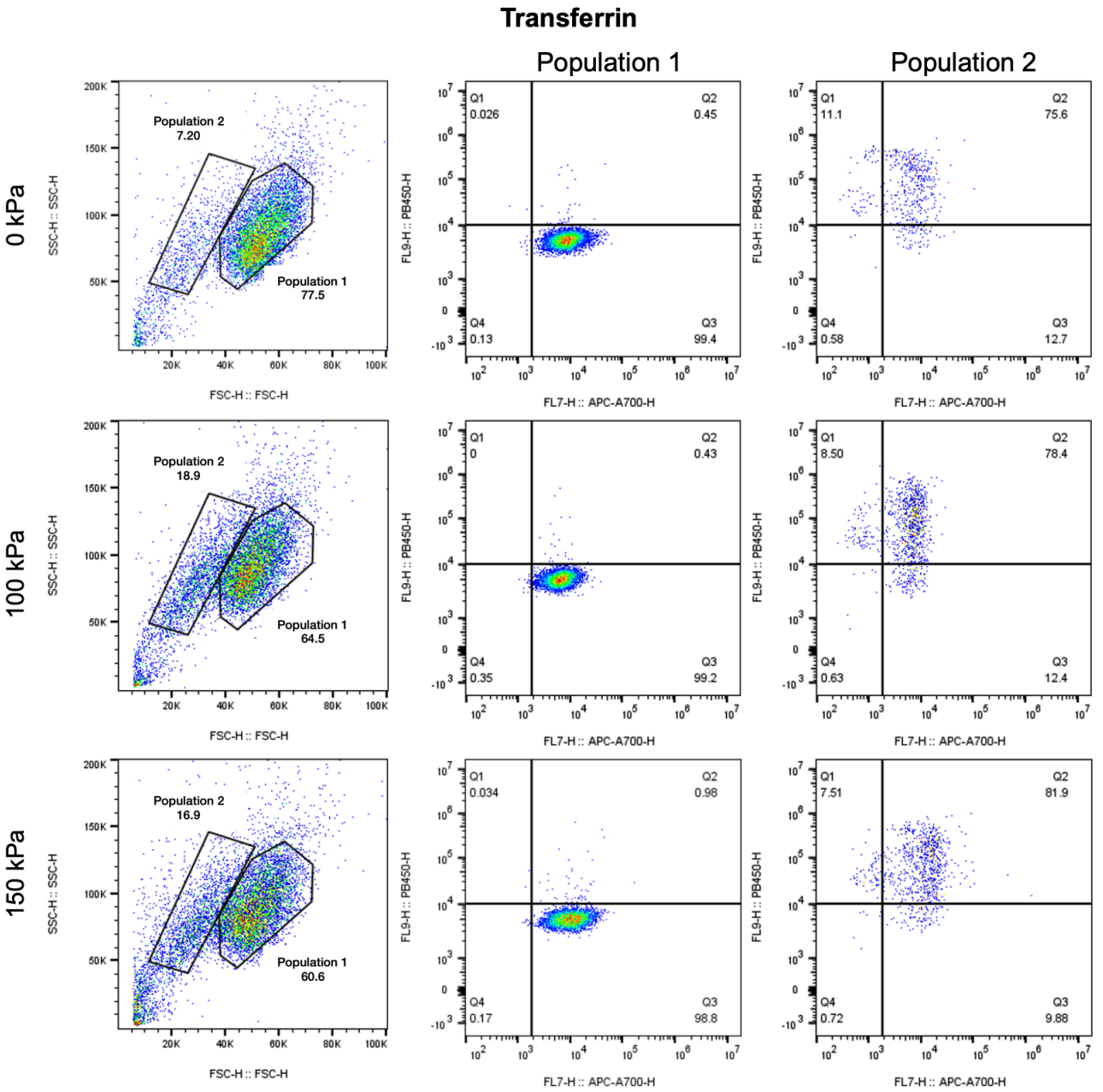


Figure A.4.2. Examples of flow cytometry analysis of A549 cells in the experiment in Section 5.3.2.2, with A549 cells treated with His-transferrin functionalised microbubbles and ultrasound, at t = 30 minutes. *The forward vs side scatter plots and corresponding APC-A700 (~AF680/CF660C) vs PB450 (DAPI) plots for the live cells in population 1 and cells in population 2, gated as described in Chapter 4. Ultrasound driving conditions were: 0.5 MHz, 100 and 150 kPa PNP, continuous wave, and a 60-second total exposure duration.*

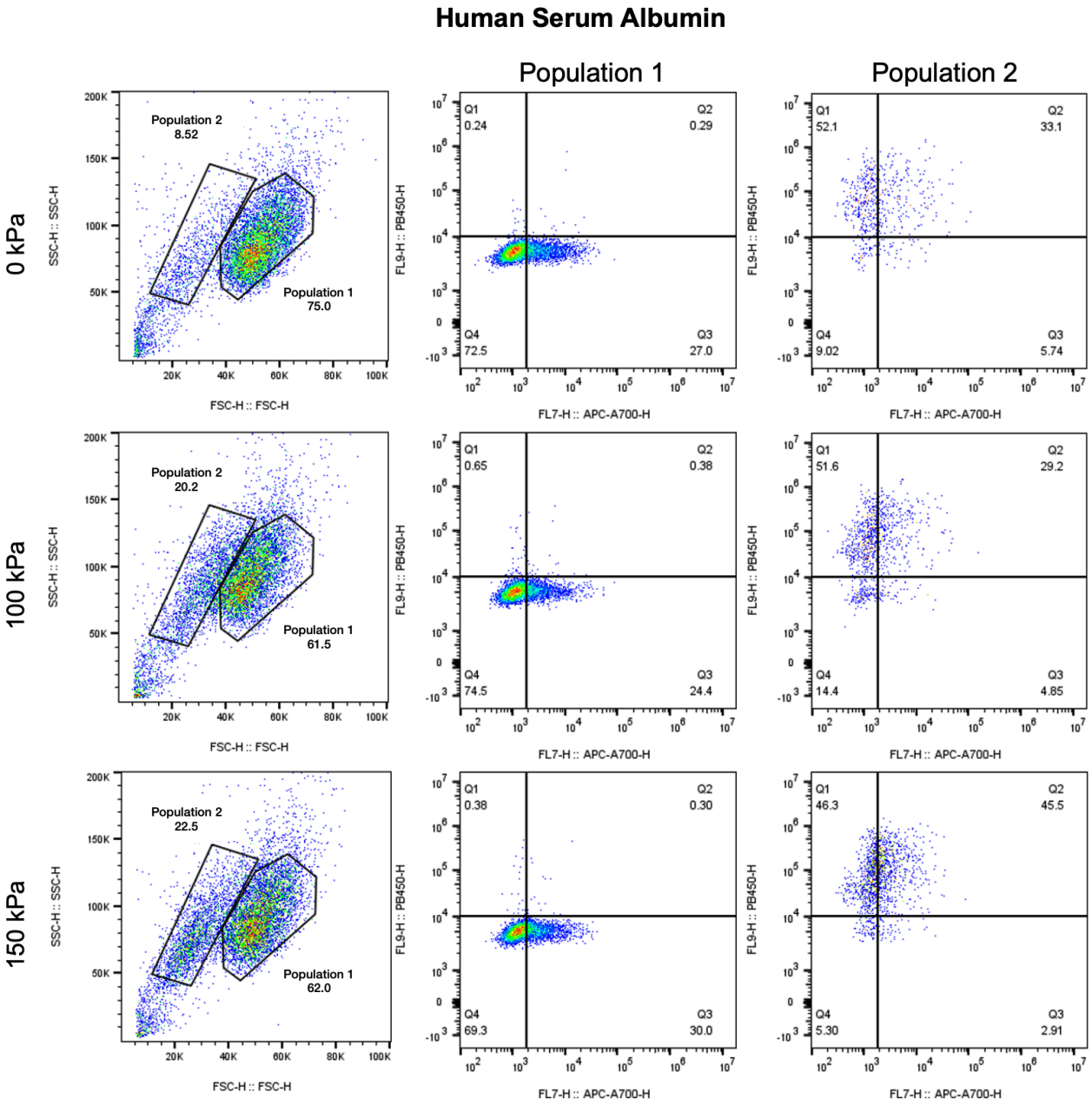


Figure A.4.3. Examples of flow cytometry analysis of A549 cells in the experiment in Section 5.3.2.2., with A549 cells treated with His-human serum albumin functionalised microbubbles and ultrasound, at t = 30 minutes*. The forward vs side scatter plots and corresponding APC-A700 (~AF680/CF660C) vs PB450 (DAPI) plots for the live cells in population 1 and cells in population 2, gated as described in Chapter 4. Ultrasound driving conditions were: 0.5 MHz, 100 and 150 kPa PNP, continuous wave, 6 and a 60-second total exposure duration.*

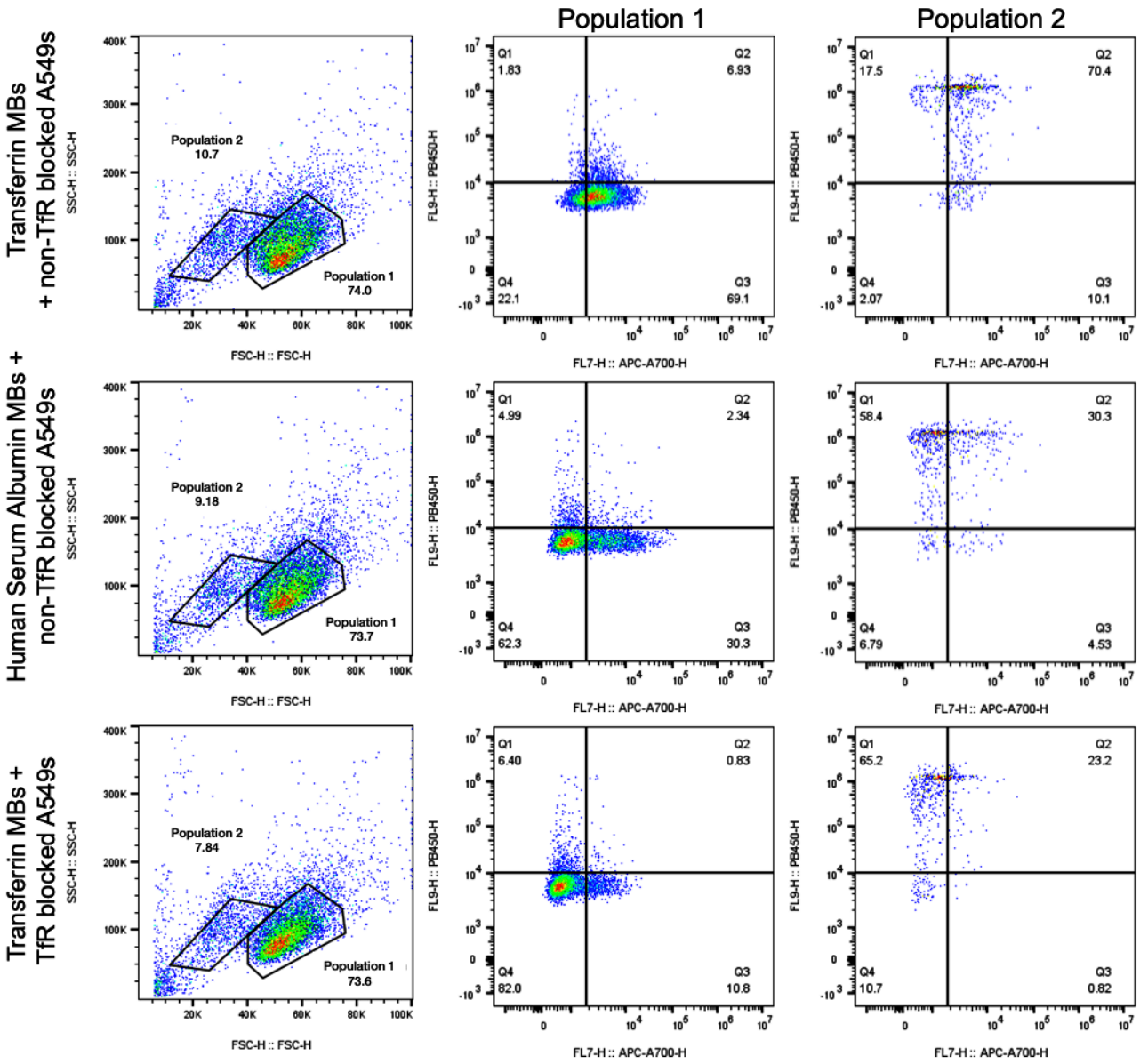


Figure A.4.4. Examples of flow cytometry analysis of A549 cells in the experiment in section 5.3.2.3., with A549 cells treated with His-transferrin and His-human serum albumin functionalised microbubbles, at t = 30 minutes. *Shown are the forward vs side scatter plots, and corresponding APC-A700 (~AF680/CF660C) vs PB450 (DAPI) plots for the live cells in population 1 and cells in population 2, gated as described in Chapter 4, for non-TfR blocked A549 cells plus both His-transferrin and His-human serum albumin functionalised microbubbles, and blocked transferrin receptor A549 cells with His-transferrin functionalised microbubbles.*

A.5 ImageStream: combining confocal microscopy and flow cytometry

With help from Dr Robert Hedley, a pilot experiment was conducted with A549 cells in suspension and His-AF488 functionalised microbubbles. Three sample conditions were assessed: i) A549 cells with His-AF488 microbubbles, ii) A549 cells with His-AF488 microbubbles and 10% duty cycle ultrasound, and, lastly, iii) A549 cells with His-AF488 microbubbles and continuous wave ultrasound. The experiment was conducted in the SAT3, with a 0.5 MHz centre frequency ultrasound parameters, 200 kPa peak negative pressure, and a 60-second total exposure duration. The corresponding results are shown in *Figure A.5.1*.

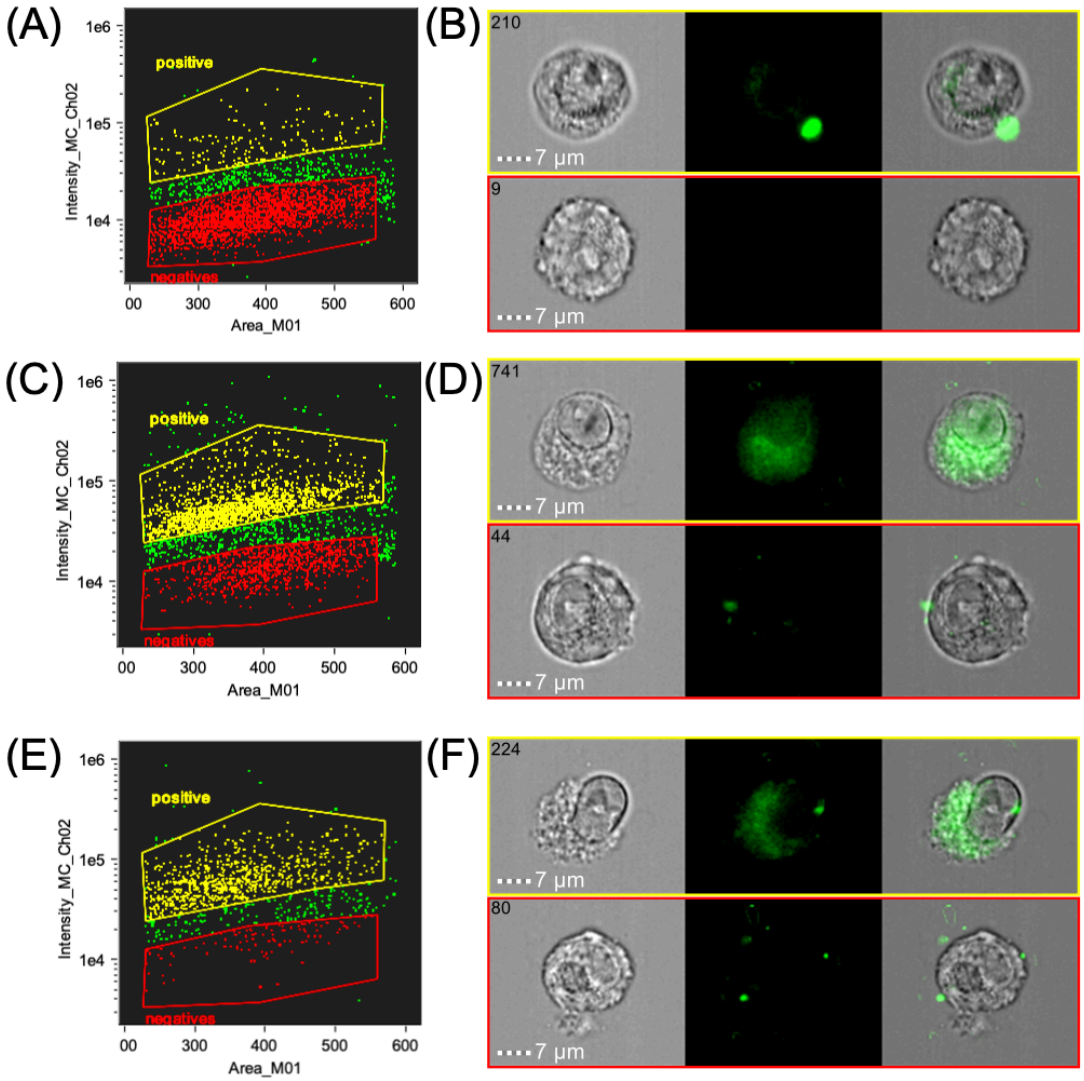


Figure A.5.1. ImageStream analysis of A549 cells and His-AF488 microbubbles under ultrasound exposure. *The area versus intensity of the His-AF488 channel (A, C, E) and corresponding brightfield, fluorescent and the respective composite images (B, D, F) are shown for A549 cells with His-AF488 microbubbles (A, B), A549 cells with His-AF488 microbubbles and ultrasound with 10% duty cycle (C, D), and, lastly, A549 cells with His-AF488 microbubbles and continuous wave ultrasound (E, F). Analysis with IDEAS software was conducted with Dr Robert Hedley.*

Without ultrasound, only ~7% of the cells (N = 2519) were positive for His-AF488. Under ultrasound exposure, this increased to ~54% for the 10% duty cycle condition (N = 2925) and ~73% for the continuous wave condition (N = 1080) (A.5.*1.A*, A.5.*1.C*, A.5.*1.E*, respectively). It should be noted that the conditions for these experiments were different from those in *Chapter 4*, with the number of microbubbles per cell being considerably lower due to the need for a large number of cells (~20 x 10^6 cells per mL) for the ImageStream system and the microbubble concentration kept at 1 x 10^8 per mL to ensure no shielding would occur. *Figure* A.5.*1.B*, A.5.*1.D* and A.5.*1.F* show representative microscopy images for the three conditions, with mostly internalisation occurring, possibly due to sonoporation, in both ultrasound samples (A.5.*1.D* and A.5.*1.F*). Though this system provides both qualitative and quantitative data, the main downside is the acquisition time, which is significantly longer than for flow cytometry or confocal microscopy alone. This limits the use of this system for high-throughput experiments, e.g., experiments in which the parameter space is explored.

References

Abelev, G. I. (1971). Alpha-fetoprotein in ontogenesis and its association with malignant tumors. *Advances in cancer research*, *14*, 295-358.

Abelev, G. I. (1971). Alpha-fetoprotein in ontogenesis and its association with malignant tumors. *Advances in cancer research*, *14*, 295-358.

Acconcia, C. N., Leung, B. Y., Winch, G., Wang, J., Hynynen, K., & Goertz, D. E. (2019). Acoustic radiation force induced accumulation and dynamics of microbubbles on compliant surfaces. *Physics in Medicine & Biology*, *64*(13), 135003.

Alberts, B., Bray, D., Hopkin, K., Johnson, A. D., Lewis, J., Raff, M., Roberts, K. & Walter, P. (2014). *Essential cell biology*. Garland Science.

Algarra, I., Cabrera, T., & Garrido, F. (2000). The HLA crossroad in tumor immunology. *Human immunology*, *61*(1), 65-73.

Ali, N. M., Dzaharudin, F., & Alias, E. A. (2020). Nonlinear dynamics of a shell encapsulated microbubble near solid boundary in an ultrasonic field. *Journal of Mechanical Engineering and Sciences*, *14*(3), 7235-7243.

Alkins, R., Burgess, A., Ganguly, M., Francia, G., Kerbel, R., Wels, W. S., & Hynynen, K. (2013). Focused ultrasound delivers targeted immune cells to metastatic brain tumors. *Cancer research*, *73*(6), 1892-1899.

Allen, T. M., Williamson, P., & Schlegel, R. A. (1988). Phosphatidylserine as a determinant of reticuloendothelial recognition of liposome models of the erythrocyte surface. *Proceedings of the National Academy of Sciences*, *85*(21), 8067-8071.

Alonso, A., Della Martina, A., Stroick, M., Fatar, M., Griebe, M., Pochon, S., ... & Meairs, S. (2007). Molecular imaging of human thrombus with novel abciximab immunobubbles and ultrasound. *Stroke*, *38*(5), 1508-1514.

AlSawaftah, N. M., Awad, N. S., Paul, V., Kawak, P. S., Al-Sayah, M. H., & Husseini, G. A. (2021). Transferrin-modified liposomes triggered with ultrasound to treat HeLa cells. *Scientific reports*, *11*(1), 1-15.

Anwer, K., Kao, G., Proctor, B., Anscombe, I., Florack, V., Earls, R., ... & Sullivan, S. M. (2000). Ultrasound enhancement of cationic lipid-mediated gene transfer to primary tumors following systemic administration. *Gene therapy*, *7*(21), 1833.

Arbyn, M., Xu, L., Simoens, C., & Martin-Hirsch, P. P. (2018). Prophylactic vaccination against human papillomaviruses to prevent cervical cancer and its precursors. *Cochrane database of systematic reviews*, (5).

Aron, M. (2018). Investigating the Role of Microbubble Composition in Ultrasound Mediated Drug Delivery (unpublished doctoral dissertation). University of Oxford, Oxford, United Kingdom.

Aron, M., Vince, O., Gray, M., Mannaris, C., & Stride, E. (2019). Investigating the Role of Lipid Transfer in Microbubble-Mediated Drug Delivery. *Langmuir*, *35*(40), 13205-13215.

Arruebo, M., Vilaboa, N., Sáez-Gutierrez, B., Lambea, J., Tres, A., Valladares, M., & González-Fernández, Á. (2011). Assessment of the evolution of cancer treatment therapies. *Cancers*, *3*(3), 3279-3330.

Awad, N. S., Paul, V., Mahmoud, M. S., Al Sawaftah, N. M., Kawak, P. S., Al Sayah, M. H., & Husseini, G. A. (2019). Effect of pegylation and targeting moieties on the ultrasound-mediated drug release from liposomes. *ACS Biomaterials Science & Engineering*, *6*(1), 48-57.

Ayee, M. A., & Levitan, I. (2016). Paradoxical impact of cholesterol on lipid packing and cell stiffness. *Front Biosci (Landmark Ed)*, *21*, 1245-1259.

Banchereau, J., & Palucka, K. (2018). Immunotherapy: Cancer vaccines on the move. *Nature reviews Clinical oncology*, *15*(1), 9.

Basuli, D., Tesfay, L., Deng, Z., Paul, B., Yamamoto, Y., Ning, G., ... & Torti, S. V. (2017). Iron addiction: a novel therapeutic target in ovarian cancer. *Oncogene*, *36*(29), 4089-4099.

Bayer, E. A., Wilchek, M., & Skutelsky, E. (1976). Affinity cytochemistry: The localization of lectin and antibody receptors on erythrocytes via the avidin-biotin complex. *FEBS letters*, *68*(2), 240-244.

Beekers, I., Lattwein, K. R., Kouijzer, J. J., Langeveld, S. A., Vegter, M., Beurskens, R., ... & Kooiman, K. (2019). Combined confocal microscope and Brandaris 128 ultra-high-speed camera. *Ultrasound in Medicine & Biology*, *45*(9), 2575-2582.

Beguin, E., Shrivastava, S., Dezhkunov, N. V., McHale, A. P., Callan, J. F., & Stride, E. (2019). Direct Evidence of Multibubble Sonoluminescence Using Therapeutic Ultrasound and Microbubbles. *ACS applied materials & interfaces*, *11*(22), 19913-19919.

Bioley, G., Bussat, P., Lassus, A., Schneider, M., Terrettaz, J., & Corthésy, B. (2012a). The phagocytosis of gas-filled microbubbles by human and murine antigen-presenting cells. *Biomaterials*, *33*(1), 333-342.

Bioley, G., Lassus, A., Bussat, P., Terrettaz, J., Tranquart, F., & Corthésy, B. (2012b). Gas-filled microbubble-mediated delivery of antigen and the induction of immune responses. *Biomaterials*, *33*(25), 5935-5946.

Blake, F. G. *Technical Memo. 12* (Acoustics Research Laboratory, Harvard University, 1949).

Boon, T., Cerottini, J. C., Van den Eynde, B., van der Bruggen, P., & Van Pel, A. (1994). Tumor antigens recognized by T lymphocytes. *Annual review of immunology*, *12*(1), 337-365.

Borden, M. A., Martinez, G. V., Ricker, J., Tsvetkova, N., Longo, M., Gillies, R. J., ... & Ferrara, K. W. (2006). Lateral phase separation in lipid-coated microbubbles. *Langmuir*, *22*(9), 4291-4297.

Bracco Diagnostics, Inc. (August, 2014 - January, 2016). *A Pilot Clinical Trial Using BR55 Ultrasound Contrast Agent in the Assessment of Prostate Cancer by Molecular Imaging of VEGFR2*. Identifier NCT02142608. https://clinicaltrials.gov/ct2/show/NCT02142608

Bunnell, S. C., Kapoor, V., Trible, R. P., Zhang, W., & Samelson, L. E. (2001). Dynamic actin polymerization drives T cell receptor–induced spreading: a role for the signal transduction adaptor LAT. *Immunity*, *14*(3), 315-329.

Burgdorf, S., Kautz, A., Böhnert, V., Knolle, P. A., & Kurts, C. (2007). Distinct pathways of antigen uptake and

intracellular routing in CD4 and CD8 T cell activation. *science*, *316*(5824), 612-616.

Butterfield, L. H. (2015). Cancer vaccines. *Bmj*, *350*, h988.

Callens, C., Moura, I. C., Lepelletier, Y., Coulon, S., Renand, A., Dussiot, M., ... & Hermine, O. (2008). Recent advances in adult T-cell leukemia therapy: focus on a new anti-transferrin receptor monoclonal antibody. *Leukemia*, *22*(1), 42-48.

Canavese, G., Ancona, A., Racca, L., Canta, M., Dumontel, B., Barbaresco, F., ... & Cauda, V. (2018). Nanoparticle-assisted ultrasound: A special focus on sonodynamic therapy against cancer. *Chemical Engineering Journal*, *340*, 155-172.

Cancer Research UK, Cancer Statistics for the UK, https://www.cancerresearchuk.org/health-professional/cancer-statistics-for-the-uk#heading-Three. Accessed April 2019.

Candelaria, P. V., Leoh, L. S., Penichet, M. L., & Daniels-Wells, T. R. (2021). Antibodies targeting the transferrin receptor 1 (TfR1) as direct anti-cancer agents. *Frontiers in immunology*, *12*, 583.

Cao, Y., Chen, Y., Yu, T., Guo, Y., Liu, F., Yao, Y., ... & Ran, H. (2018). Drug release from phase-changeable nanodroplets triggered by low-intensity focused ultrasound. *Theranostics*, *8*(5), 1327.

Carugo, D., Aron, M., Sezgin, E., de la Serna, J. B., Kuimova, M. K., Eggeling, C., & Stride, E. (2017). Modulation of the molecular arrangement in artificial and biological membranes by phospholipid-shelled microbubbles. *Biomaterials*, *113*, 105-117.

Carugo, D., Owen, J., Crake, C., Lee, J. Y., & Stride, E. (2015). Biologically and acoustically compatible chamber for studying ultrasound-mediated delivery of therapeutic compounds. *Ultrasound in medicine & biology*, *41*(7), 1927-1937.

Casey, G., Cashman, J. P., Morrissey, D., Whelan, M. C., Larkin, J. O., Soden, D. M., ... & O'Sullivan, G. C. (2010). Sonoporation mediated immunogene therapy of solid tumors. *Ultrasound in medicine & biology*, *36*(3), 430-440.

Cercek, A., Lumish, M., Sinopoli, J., Weiss, J., Shia, J., Lamendola-Essel, M., ... & Diaz Jr, L. A. (2022). PD-1 Blockade in Mismatch Repair–Deficient, Locally Advanced Rectal Cancer. *New England Journal of Medicine*.

Chaiwaree, S., Prapan, A., Suwannasom, N., Laporte, T., Neumann, T., Pruß, A., ... & Bäumler, H. (2020). Doxorubicin–Loaded Human Serum Albumin Submicron Particles: Preparation, Characterization and In Vitro Cellular Uptake. *Pharmaceutics*, *12*(3), 224.

Chapman, D. (1975). Phase transitions and fluidity characteristics of lipids and cell membranes. *Quarterly reviews of biophysics*, *8*(2), 185-235.

Cheever, M. A., & Higano, C. S. (2011). PROVENGE (Sipuleucel-T) in Prostate Cancer: The First FDA-Approved Therapeutic Cancer VaccineTherapeutic Prostate Cancer Vaccine. *Clinical Cancer Research*, *17*(11), 3520-3526.

Chen MM, Whitlow CT. Chapter 1. Scope of Diagnostic Imaging. In: Chen MM, Pope TL, Ott DJ. eds. *Basic Radiology, 2e*. McGraw Hill; 2011. Accessed March 31, 2022. https://accessmedicine.mhmedical.com/content.aspx?bookid=360&sectionid=39669007

Chen, H. K., Zhang, S. M., Chang, J. L., Chen, H. C., Lin, Y. C., Shih, C. P., ... & Wang, C. H. (2018). Insonation of systemically delivered cisplatin-loaded microbubbles significantly attenuates nephrotoxicity of chemotherapy in experimental models of head and neck cancer. *Cancers*, *10*(9), 311.

Chen, H., & Hwang, J. H. (2013). Ultrasound-targeted microbubble destruction for chemotherapeutic drug delivery to solid tumors. *Journal of therapeutic ultrasound*, *1*(1), 1-8.

Chignola, R., Foroni, R., Franceschi, A., Pasti, M., Candiani, C., Anselmi, C., ... & Colombatti, M. (1995). Heterogeneous response of individual multicellular tumour spheroids to immunotoxins and ricin toxin. *British journal of cancer*, *72*(3), 607-614.

Chikh, G. G., Li, W. M., Schutze-Redelmeier, M. P., Meunier, J. C., & Bally, M. B. (2002). Attaching histidine-tagged peptides and proteins to lipid-based carriers through use of metal-ion-chelating lipids. *Biochimica Et Biophysica Acta (BBA)-Biomembranes*, *1567*, 204-212.

Chiou, B., & Connor, J. R. (2018). Emerging and dynamic biomedical uses of ferritin. *Pharmaceuticals*, *11*(4), 124.

Colangeli, S., Parchi, P., Andreani, L., Beltrami, G., Scoccianti, G., Sacchetti, F., ... & Capanna, R. (2018). Cryotherapy efficacy and safety as local therapy in surgical treatment of musculoskeletal tumours. A retrospective case series of 143 patients. *Journal of biological regulators and homeostatic agents*, *32*(6 Suppl. 1), 65-70.

Collis, J., Manasseh, R., Liovic, P., Tho, P., Ooi, A., Petkovic-Duran, K., & Zhu, Y. (2010). Cavitation microstreaming and stress fields created by microbubbles. *Ultrasonics*, *50*(2), 273-279.

Cordeiro, E. R., Cathelineau, X., Thueroff, S., Marberger, M., Crouzet, S., & de la Rosette, J. J. (2012). High-intensity focused ultrasound (HIFU) for definitive treatment of prostate cancer. *BJU international*, *110*(9), 1228-1242.

Costley, D., Mc Ewan, C., Fowley, C., McHale, A. P., Atchison, J., Nomikou, N., & Callan, J. F. (2015). Treating cancer with sonodynamic therapy: a review. *International Journal of Hyperthermia*, *31*(2), 107-117.

Coviello, C., Kozick, R., Choi, J., Gyöngy, M., Jensen, C., Smith, P. P., & Coussios, C. C. (2015). Passive acoustic mapping utilizing optimal beamforming in ultrasound therapy monitoring. *The Journal of the Acoustical Society of America*, *137*(5), 2573-2585.

Crake, C., de Saint Victor, M., Owen, J., Coviello, C., Collin, J., Coussios, C. C., & Stride, E. (2015). Passive acoustic mapping of magnetic microbubbles for cavitation enhancement and localization. *Physics in Medicine & Biology*, *60*(2), 785.

Crowder, K. C., Hughes, M. S., Marsh, J. N., Barbieri, A. M., Fuhrhop, R. W., Lanza, G. M., & Wickline, S. A. (2005). Sonic activation of molecularly-targeted nanoparticles accelerates transmembrane lipid delivery to cancer cells through contact-mediated mechanisms: implications for enhanced local drug delivery. *Ultrasound in medicine & biology*, *31*(12), 1693-1700.

Dayton, P. A., Allen, J. S., & Ferrara, K. W. (2002). The magnitude of radiation force on ultrasound contrast

agents. *The Journal of the Acoustical Society of America*, *112*(5), 2183-2192.

Dayton, P., Klibanov, A., Brandenburger, G., & Ferrara, K. (1999). Acoustic radiation force in vivo: a mechanism to assist targeting of microbubbles. *Ultrasound in medicine & biology*, *25*(8), 1195-1201.

De Cock, I., Lajoinie, G., Versluis, M., De Smedt, S. C., & Lentacker, I. (2016). Sonoprinting and the importance of microbubble loading for the ultrasound mediated cellular delivery of nanoparticles. *Biomaterials*, *83*, 294-307.

De Cock, I., Zagato, E., Braeckmans, K., Luan, Y., de Jong, N., De Smedt, S. C., & Lentacker, I. (2015). Ultrasound and microbubble mediated drug delivery: acoustic pressure as determinant for uptake via membrane pores or endocytosis. *Journal of controlled release*, *197*, 20-28.

de Jong, R. N., Beurskens, F. J., Verploegen, S., Strumane, K., van Kampen, M. D., Voorhorst, M., ... & Parren, P. W. (2016). A novel platform for the potentiation of therapeutic antibodies based on antigen-dependent formation of IgG hexamers at the cell surface. *PLoS biology*, *14*(1), e1002344.

Della Martina, A., Allemann, E., Bettinger, T., Bussat, P., Lassus, A., Pochon, S., & Schneider, M. (2008). Grafting of abciximab to a microbubble-based ultrasound contrast agent for targeting to platelets expressing GP IIb/IIIa–characterization and in vitro testing. *European journal of pharmaceutics and biopharmaceutics*, *68*(3), 555-564.

Delogu, L. G., Vidili, G., Venturelli, E., Ménard-Moyon, C., Zoroddu, M. A., Pilo, G., ... & Bianco, A. (2012). Functionalized multiwalled carbon nanotubes as ultrasound contrast agents. *Proceedings of the National Academy of Sciences*, *109*(41), 16612-16617.

Demachi, F., Murayama, Y., Hosaka, N., Mochizuki, T., Masuda, K., Enosawa, S., ... & Maruyama, K. (2015). Preliminary study on forming microbubble-surrounded cells as carriers for cellular therapy and evaluation of ultrasound controllability by fluorescence imaging. *Japanese Journal of Applied Physics*, *54*(7S1), 07HF19.

Den Brok, M. H. M. G. M., Sutmuller, R. P., Nierkens, S., Bennink, E. J., Frielink, C., Toonen, L. W., ... & Adema, G. J. (2006). Efficient loading of dendritic cells following cryo and radiofrequency ablation in combination with immune modulation induces anti-tumour immunity. *British journal of cancer*, *95*(7), 896.

Dewitte, H., Roovers, S., De Smedt, S. C., & Lentacker, I. (2019). Enhancing nucleic acid delivery with ultrasound and microbubbles. In *Nanotechnology for Nucleic Acid Delivery* (pp. 241-251). Humana Press, New York, NY.

Dhatchinamoorthy, K., Colbert, J. D., & Rock, K. L. (2021). Cancer immune evasion through loss of MHC class I antigen presentation. *Frontiers in immunology*, *12*, 636568.

Dijkmans, P. A., Juffermans, L. J. M., Musters, R. J. P., van Wamel, A., Ten Cate, F. J., van Gilst, W., ... & Kamp, O. (2004). Microbubbles and ultrasound: from diagnosis to therapy. *European Journal of Echocardiography*, *5*(4), 245-246.

Dimcevski, G., Kotopoulis, S., Bjånes, T., Hoem, D., Schjøtt, J., Gjertsen, B. T., ... & Postema, M. (2016). A human clinical trial using ultrasound and microbubbles to enhance gemcitabine treatment of inoperable pancreatic cancer. *Journal of Controlled Release*, *243*, 172-181.

Doinikov, A. A., & Bouakaz, A. (2010). Acoustic microstreaming around a gas bubble. *The Journal of the Acoustical Society of America*, *127*(2), 703-709.

Doinikov, A. A., & Bouakaz, A. (2010). Theoretical investigation of shear stress generated by a contrast microbubble on the cell membrane as a mechanism for sonoporation. *The Journal of the Acoustical Society of America*, *128*(1), 11-19.

Dong, Y., Xu, Y., Li, P., Wang, C., Cao, Y., & Yu, J. (2017). Antibiofilm effect of ultrasound combined with microbubbles against Staphylococcus epidermidis biofilm. *International Journal of Medical Microbiology*, *307*(6), 321-328.

Duan, X., Alfred, C. H., & Wan, J. M. (2019). Cellular bioeffect investigations on low-intensity pulsed ultrasound and sonoporation: Platform design and flow cytometry protocol. *IEEE Transactions on Ultrasonics, Ferroelectrics, and Frequency Control*, *66*(9), 1422-1434.

Dunn, G. P., Old, L. J., & Schreiber, R. D. (2004). The three Es of cancer immunoediting. *Annu. Rev. Immunol.*, *22*, 329-360.

Dussik, K. T. (1942). Über die Möglichkeit, hochfrequente mechanische Schwingungen als diagnostisches Hilfsmittel zu verwerten. *Zeitschrift für die gesamte Neurologie und Psychiatrie*, *174*(1), 153-168.

Dustin, M. L., & Baldari, C. T. (2017). The immune synapse: Past, present, and future. In *The Immune Synapse* (pp. 1-5). Humana Press, New York, NY.

Dzaharudin, F., Ooi, A., & Manasseh, R. (2017). Effects of boundary proximity on monodispersed microbubbles in ultrasonic fields. *Journal of Sound and Vibration*, *410*, 330-343.

Elliott, R. L., Stjernholm, R., & Elliott, M. C. (1988). Preliminary evaluation of platinum transferrin (MPTC-63) as a potential nontoxic treatment for breast cancer. *Cancer detection and prevention*, *12*(1-6), 469-480.

Escoffre, J. M., Deckers, R., Bos, C., & Moonen, C. (2016). Bubble-assisted ultrasound: application in immunotherapy and vaccination. In *Therapeutic Ultrasound* (pp. 243-261). Springer, Cham.

Essaghir, A., & Demoulin, J. B. (2012). A minimal connected network of transcription factors regulated in human tumors and its application to the quest for universal cancer biomarkers. *PloS one*, *7*(6), e39666.

Facciorusso, A., Di Maso, M., & Muscatiello, N. (2016). Microwave ablation versus radiofrequency ablation for the treatment of hepatocellular carcinoma: A systematic review and meta-analysis. *International Journal of Hyperthermia*, *32*(3), 339-344.

Fan, Z., Kumon, R. E., & Deng, C. X. (2014). Mechanisms of microbubble-facilitated sonoporation for drug and gene delivery. *Therapeutic delivery*, *5*(4), 467-486.

Fan, Z., Liu, H., Mayer, M., & Deng, C. X. (2012). Spatiotemporally controlled single cell sonoporation. *Proceedings of the National Academy of Sciences*, *109*(41), 16486-16491.

Fechheimer, M., Boylan, J. F., Parker, S., Sisken, J. E., Patel, G. L., & Zimmer, S. G. (1987). Transfection of mammalian cells with plasmid DNA by scrape

loading and sonication loading. *Proceedings of the National Academy of Sciences*, *84*(23), 8463-8467.

Fekri, F., Delos Santos, R. C., Karshafian, R., & Antonescu, C. N. (2016). Ultrasound microbubble treatment enhances clathrin-mediated endocytosis and fluid-phase uptake through distinct mechanisms. *PloS one*, *11*(6), e0156754.

Fellinger, K., & Schmidt, J. (1954). Klinik and Therapies des Chromischen Gelenkreumatismus, 549–552. *Vienna, Austria: Maudrich*.

Ferrara, K., Pollard, R., & Borden, M. (2007). Ultrasound microbubble contrast agents: fundamentals and application to gene and drug delivery. *Annu. Rev. Biomed. Eng.*, *9*, 415-447.

Ferrone, C., & Dranoff, G. (2010). Dual roles for immunity in gastrointestinal cancers. *Journal of Clinical Oncology*, *28*(26), 4045.

Feshitan, J. A., Chen, C. C., Kwan, J. J., & Borden, M. A. (2009). Microbubble size isolation by differential centrifugation. *Journal of colloid and interface science*, *329*(2), 316-324.

Filippa, L., Trento, A., & Álvarez, A. M. (2012). Sauter mean diameter determination for the fine fraction of suspended sediments using a LISST-25X diffractometer. *Measurement*, *45*(3), 364-368.

Flynn, H. G. (1975). Cavitation dynamics: II. Free pulsations and models for cavitation bubbles. *The Journal of the Acoustical Society of America*, *58*(6), 1160-1170.

Garbin, V., Cojoc, D., Ferrari, E., Di Fabrizio, E., Overvelde, M. L. J., Van Der Meer, S. M., ... & Versluis, M. (2007). Changes in microbubble dynamics near a boundary revealed by combined optical micromanipulation and high-speed imaging. *Applied physics letters*, *90*(11), 114103.

Garg, S., Thomas, A. A., & Borden, M. A. (2013). The effect of lipid monolayer in-plane rigidity on in vivo microbubble circulation persistence. *Biomaterials*, *34*(28), 6862-6870.

Geers, B., De Wever, O., Demeester, J., Bracke, M., De Smedt, S. C., & Lentacker, I. (2013). Targeted liposome-loaded microbubbles for cell-specific ultrasound-triggered drug delivery. *Small*, *9*(23), 4027-4035.

Geers, B., Lentacker, I., Sanders, N. N., Demeester, J., Meairs, S., & De Smedt, S. C. (2011). Self-assembled liposome-loaded microbubbles: The missing link for safe and efficient ultrasound triggered drug-delivery. *Journal of controlled release*, *152*(2), 249-256.

Gelderblom, E., Wolbers, F., De Jong, N., Van den Berg, A., & Versluis, M. (2013, June). Time-resolved high-speed fluorescence imaging of bubble-induced sonoporation. In *Proceedings of Meetings on Acoustics ICA2013* (Vol. 19, No. 1, p. 075070). Acoustical Society of America.

Gooden, M. J., de Bock, G. H., Leffers, N., Daemen, T., & Nijman, H. W. (2011). The prognostic influence of tumour-infiltrating lymphocytes in cancer: a systematic review with meta-analysis. *British journal of cancer*, *105*(1), 93-103.

Gramiak, R., & Shah, P. M. (1968). Echocardiography of the aortic root. *Investigative radiology*, *3*(5), 356-366.

Gray, M. D., Lyon, P. C., Mannaris, C., Folkes, L. K., Stratford, M., Campo, L., ... & Carlisle, R. (2019). Focused ultrasound hyperthermia for targeted drug release from thermosensitive liposomes: results from a phase I trial. *Radiology*, *291*(1), 232-238.

Gray, M., Vasilyeva, A. V., Brans, V., & Stride, E. (2021). Studying Cavitation Enhanced Therapy. *JoVE (Journal of Visualized Experiments)*, (170), e61989.

Grüll, H., & Langereis, S. (2012). Hyperthermia-triggered drug delivery from temperature-sensitive liposomes using MRI-guided high intensity focused ultrasound. *Journal of Controlled Release*, *161*(2), 317-327.

Guiot, C., Pastore, G., Napoleone, M., Gabriele, P., Trotta, M., & Cavalli, R. (2006). Thermal response of contrast agent microbubbles: Preliminary results from physico-chemical and US-imaging characterization. *Ultrasonics*, *44*, e127-e130.

Habashy, H. O., Powe, D. G., Staka, C. M., Rakha, E. A., Ball, G., Green, A. R., ... & Gee, J. M. (2010). Transferrin receptor (CD71) is a marker of poor prognosis in breast cancer and can predict response to tamoxifen. *Breast cancer research and treatment*, *119*(2), 283-293.

Haen, S. P., Pereira, P. L., Salih, H. R., Rammensee, H. G., & Gouttefangeas, C. (2011). More than just tumor destruction: immunomodulation by thermal ablation of cancer. *Clinical and Developmental Immunology*, *2011*.

Hanahan, D., & Weinberg, R. A. (2000). The hallmarks of cancer. *cell*, *100*(1), 57-70.

Hanahan, D., & Weinberg, R. A. (2011). Hallmarks of cancer: the next generation. *cell*, *144*(5), 646-674.

Harkin, A., Hynes, M. J., Masterson, E., Kelly, J. P., O'Donnell, J. M., & Connor, T. J. (2003). A toxicokinetic study of nickel-induced immunosuppression in rats. *Immunopharmacology and immunotoxicology*, *25*(4), 655-670.

Hayashi, S., Mizuno, M., Yoshida, J., & Nakao, A. (2009). Effect of sonoporation on cationic liposome-mediated IFNβ gene therapy for metastatic hepatic tumors of murine colon cancer. *Cancer gene therapy*, *16*(8), 638.

Helfield, B. L., Chen, X., Qin, B., Watkins, S. C., & Villanueva, F. S. (2017). Mechanistic insight into sonoporation with ultrasound-stimulated polymer microbubbles. *Ultrasound in medicine & biology*, *43*(11), 2678-2689.

Helfield, B. L., Leung, B. Y., & Goertz, D. E. (2014). The effect of boundary proximity on the response of individual ultrasound contrast agent microbubbles. *Physics in Medicine & Biology*, *59*(7), 1721.

Helfield, B., Chen, X., Watkins, S. C., & Villanueva, F. S. (2016). Biophysical insight into mechanisms of sonoporation. *Proceedings of the National Academy of Sciences*, *113*(36), 9983-9988.

Hernot, S., & Klibanov, A. L. (2008). Microbubbles in ultrasound-triggered drug and gene delivery. *Advanced drug delivery reviews*, *60*(10), 1153-1166.

Hilgenfeldt, S., Lohse, D., & Zomack, M. (2000). Sound scattering and localized heat deposition of pulse-driven microbubbles. *The Journal of the Acoustical Society of America*, *107*(6), 3530-3539.

Hill, C. R., Bamber, J. C., & ter Haar, G. R. (Eds.). (2004). Physical principles of medical ultrasonics.

Holt, R. G., & Roy, R. A. (2001). Measurements of bubble-enhanced heating from focused, MHz-frequency ultrasound in a tissue-mimicking material. *Ultrasound in medicine & biology*, *27*(10), 1399-1412.

Honigmann, A., Mueller, V., Ta, H., Schoenle, A., Sezgin, E., Hell, S. W., & Eggeling, C. (2014). Scanning STED-FCS reveals spatiotemporal heterogeneity of lipid

interaction in the plasma membrane of living cells. *Nature communications*, *5*(1), 1-12.

Horsley, H., Owen, J., Browning, R., Carugo, D., Malone-Lee, J., Stride, E., & Rohn, J. L. (2019). Ultrasound-activated microbubbles as a novel intracellular drug delivery system for urinary tract infection. *Journal of Controlled Release*, *301*, 166-175.

Hu, Y., Wan, J. M., & Alfred, C. H. (2013). Membrane perforation and recovery dynamics in microbubble-mediated sonoporation. *Ultrasound in medicine & biology*, *39*(12), 2393-2405.

Hu, Z., Yang, X. Y., Liu, Y., Sankin, G. N., Pua, E. C., Morse, M. A., ... & Zhong, P. (2007). Investigation of HIFU-induced anti-tumor immunity in a murine tumor model. *Journal of translational medicine*, *5*(1), 34.

Huang, X., Yuan, F., Liang, M., Lo, H. W., Shinohara, M. L., Robertson, C., & Zhong, P. (2012). M-HIFU inhibits tumor growth, suppresses STAT3 activity and enhances tumor specific immunity in a transplant tumor model of prostate cancer. *PloS one*, *7*(7), e41632.

Huber, P. E., & Pfisterer, P. (2000). In vitro and in vivo transfection of plasmid DNA in the Dunning prostate tumor R3327-AT1 is enhanced by focused ultrasound. *Gene therapy*, *7*(17), 1516.

Huber, P. E., Mann, M. J., Melo, L. G., Ehsan, A., Kong, D., Zhang, L., ... & Hynynen, K. (2003). Focused ultrasound (HIFU) induces localized enhancement of reporter gene expression in rabbit carotid artery. *Gene Therapy*, *10*(18), 1600.

Hughes, J., Vudattu, N., Sznol, M., Gettinger, S., Kluger, H., Lupsa, B., & Herold, K. C. (2015). Precipitation of autoimmune diabetes with anti-PD-1 immunotherapy. *Diabetes Care*, *38*(4), 55-57.

Hynynen, K., McDannold, N., Vykhodtseva, N., & Jolesz, F. A. (2003). Non-invasive opening of BBB by focused ultrasound. In *Brain Edema Xii* (pp. 555-558). Springer, Vienna.

Ita, K. (2016). Transdermal delivery of vaccines–Recent progress and critical issues. *Biomedicine & Pharmacotherapy*, *83*, 1080-1088.

Jain, A., Barve, A., Zhao, Z., Jin, W., & Cheng, K. (2017). Comparison of avidin, neutravidin, and streptavidin as nanocarriers for efficient siRNA delivery. *Molecular pharmaceutics*, *14*(5), 1517-1527.

Jenkins, E., Santos, A. M., O'Brien-Ball, C., Felce, J. H., Wilcock, M. J., Hatherley, D., ... & Sezgin, E. (2018). Reconstitution of immune cell interactions in free-standing membranes. *J Cell Sci*, *132*(4), jcs219709.

Jiang, T., Shi, T., Zhang, H., Hu, J., Song, Y., Wei, J., ... & Zhou, C. (2019). Tumor neoantigens: from basic research to clinical applications. *Journal of hematology & oncology*, *12*(1), 1-13.

Juffermans, L. J., van Dijk, A., Jongenelen, C. A., Drukarch, B., Reijerkerk, A., de Vries, H. E., ... & Musters, R. J. (2009). Ultrasound and microbubble-induced intra- and intercellular bioeffects in primary endothelial cells. *Ultrasound in medicine & biology*, *35*(11), 1917-1927.

Jung, S. E., Cho, S. H., Jang, J. H., & Han, J. Y. (2011). High-intensity focused ultrasound ablation in hepatic and pancreatic cancer: complications. *Abdominal imaging*, *36*(2), 185-195.

Kates, M., Pugh, E. L., & Ferrante, G. (1984). Regulation of membrane fluidity by lipid desaturases. In *Membrane fluidity* (pp. 379-395). Springer, Boston, MA.

Keir, M. E., Butte, M. J., Freeman, G. J., & Sharpe, A. H. (2008). PD-1 and its ligands in tolerance and immunity. *Annu. Rev. Immunol.*, *26*, 677-704.

Kennedy, J. E. (2005). High-intensity focused ultrasound in the treatment of solid tumours. *Nature reviews cancer*, *5*(4), 321.

Khajah, M. A., & Luqmani, Y. A. (2016). Involvement of membrane blebbing in immunological disorders and cancer. *Medical Principles and Practice*, *25*(Suppl. 2), 18-27.

Kheirolomoom, A., Dayton, P. A., Lum, A. F., Little, E., Paoli, E. E., Zheng, H., & Ferrara, K. W. (2007). Acoustically-active microbubbles conjugated to liposomes: characterization of a proposed drug delivery vehicle. *Journal of Controlled Release*, *118*(3), 275-284.

Kheyfets, B., Galimzyanov, T., & Mukhin, S. (2018). Microscopic Description of the Thermodynamics of a Lipid Membrane at a Liquid–Gel Phase Transition. *JETP Letters*, *107*(11), 718-724.

Kircheis, R., Schüller, S., Brunner, S., Ogris, M., Heider, K. H., Zauner, W., & Wagner, E. (1999). Polycation-based DNA complexes for tumor-targeted gene delivery in vivo. *The journal of gene medicine*, *1*(2), 111-120.

Kirkwood, J. M., Butterfield, L. H., Tarhini, A. A., Zarour, H., Kalinski, P., & Ferrone, S. (2012). Immunotherapy of cancer in 2012. *CA: a cancer journal for clinicians*, *62*(5), 309-335.

Klibanov, A. L. (2005). Ligand-carrying gas-filled microbubbles: ultrasound contrast agents for targeted molecular imaging. *Bioconjugate chemistry*, *16*(1), 9-17.

Köksoy, C., Kuzu, A., Kutlay, J., Erden, I., Özcan, H., & Ergin, K. (1995). The diagnostic value of colour Doppler ultrasound in central venous catheter related thrombosis. *Clinical Radiology*, *50*(10), 687-689.

Kondo, K., Noguchi, M., Mukai, K., Matsuno, Y., Sato, Y., Shimosato, Y., & Monden, Y. (1990). Transferrin receptor expression in adenocarcinoma of the lung as a histopathologic indicator of prognosis. *Chest*, *97*(6), 1367-1371.

Kooiman, K., Vos, H. J., Versluis, M., & de Jong, N. (2014). Acoustic behavior of microbubbles and implications for drug delivery. *Advanced drug delivery reviews*, *72*, 28-48.

Korpanty, G., Carbon, J. G., Grayburn, P. A., Fleming, J. B., & Brekken, R. A. (2007). Monitoring response to anticancer therapy by targeting microbubbles to tumor vasculature. *Clinical Cancer Research*, *13*(1), 323-330.

Korpanty, G., Grayburn, P. A., Shohet, R. V., & Brekken, R. A. (2005). Targeting vascular endothelium with avidin microbubbles. *Ultrasound in medicine & biology*, *31*(9), 1279-1283.

Krasovitski, B., & Kimmel, E. (2004). Shear stress induced by a gas bubble pulsating in an ultrasonic field near a wall. *IEEE transactions on ultrasonics, ferroelectrics, and frequency control*, *51*(8), 973-979.

Kratz, F., Beyer, U., Roth, T., Tarasova, N., Collery, P., Lechenault, F., ... & Falken, U. (1998). Transferrin conjugates of doxorubicin: synthesis, characterization, cellular uptake, and in vitro efficacy. *Journal of pharmaceutical sciences*, *87*(3), 338-346.

Krieger J, Tódt K, Langowski J. "Biophysics of Macromolecules (B040): Practical Course Biophysics: Fluorescence Correlation Spectroscopy"

http://www.dkfz.de/Macromol/ teaching/files/ fcs_practical.pdf

Kudo, N. (2016). High-speed observation for a better understanding of bubble dynamics in an in vivo-like situation of sonoporation. *The Journal of the Acoustical Society of America*, *140*(4), 2984-2985.

Kumar, Brahma V., Thomas J. Connors, and Donna L. Farber. "Human T cell development, localization, and function throughout life." *Immunity* 48.2 (2018): 202-213.

Kumar, P., Ban, H. S., Kim, S. S., Wu, H., Pearson, T., Greiner, D. L., ... & Shankar, P. (2008). T cell-specific siRNA delivery suppresses HIV-1 infection in humanized mice. *Cell*, *134*(4), 577-586.

Kumon, R. E., Aehle, M., Sabens, D., Parikh, P., Han, Y. W., Kourennyi, D., & Deng, C. X. (2009). Spatiotemporal effects of sonoporation measured by real-time calcium imaging. *Ultrasound in medicine & biology*, *35*(3), 494-506.

Kwan, J. J., & Borden, M. A. (2012). Lipid monolayer collapse and microbubble stability. *Advances in colloid and interface science*, *183*, 82-99.

Kwan, J. J., Graham, S., Myers, R., Carlisle, R., Stride, E., & Coussios, C. C. (2015a). Ultrasound-induced inertial cavitation from gas-stabilizing nanoparticles. *Physical Review E*, *92*(2), 023019.

Kwan, J. J., Myers, R., Coviello, C. M., Graham, S. M., Shah, A. R., Stride, E., ... & Coussios, C. C. (2015b). Ultrasound-propelled nanocups for drug delivery. *small*, *11*(39), 5305-5314.

Lajoinie, G., De Cock, I., Coussios, C. C., Lentacker, I., Le Gac, S., Stride, E., & Versluis, M. (2016). In vitro methods to study bubble-cell interactions: Fundamentals and therapeutic applications. *Biomicrofluidics*, *10*(1), 011501.

Langeveld, S. A., Beekers, I., Collado-Lara, G., van der Steen, A. F., de Jong, N., & Kooiman, K. (2021). The impact of lipid handling and phase distribution on the acoustic behavior of microbubbles. *Pharmaceutics*, *13*(1), 119.

Lata, S., Reichel, A., Brock, R., Tampé, R., & Piehler, J. (2005). High-affinity adaptors for switchable recognition of histidine-tagged proteins. *Journal of the American Chemical Society*, *127*(29), 10205-10215.

Lawrie, A., Brisken, A. F., Francis, S. E., Cumberland, D. C., Crossman, D. C., & Newman, C. M. (2000). Microbubble-enhanced ultrasound for vascular gene delivery. *Gene therapy*, *7*(23), 2023-2027.

Le, D. T., Durham, J. N., Smith, K. N., Wang, H., Bartlett, B. R., Aulakh, L. K., ... & Diaz Jr, L. A. (2017). Mismatch repair deficiency predicts response of solid tumors to PD-1 blockade. *Science*, *357*(6349), 409-413.

Lee, I. S., Lee, N., Park, J., Kim, B. H., Yi, Y. W., Kim, T., ... & Hyeon, T. (2006). Ni/NiO core/shell nanoparticles for selective binding and magnetic separation of histidine-tagged proteins. *Journal of the American Chemical Society*, *128*(33), 10658-10659.

Lee, J., Yun, K. S., Choi, C. S., Shin, S. H., Ban, H. S., Rhim, T., ... & Lee, K. Y. (2012). T cell-specific siRNA delivery using antibody-conjugated chitosan nanoparticles. *Bioconjugate chemistry*, *23*(6), 1174-1180.

Lentacker, I., De Cock, I., Deckers, R., De Smedt, S. C., & Moonen, C. T. W. (2014). Understanding ultrasound induced sonoporation: definitions and underlying mechanisms. *Advanced drug delivery reviews*, *72*, 49-64.

Lentacker, I., De Smedt, S. C., & Sanders, N. N. (2009). Drug loaded microbubble design for ultrasound triggered delivery. *Soft Matter*, *5*(11), 2161-2170.

Lentacker, I., De Smedt, S. C., Demeester, J., Van Marck, V., Bracke, M., & Sanders, N. N. (2007). Lipoplex-loaded microbubbles for gene delivery: a trojan horse controlled by ultrasound. *Advanced Functional Materials*, *17*(12), 1910-1916.

Lentacker, I., Geers, B., Demeester, J., De Smedt, S. C., & Sanders, N. N. (2010). Design and evaluation of doxorubicin-containing microbubbles for ultrasound-triggered doxorubicin delivery: cytotoxicity and mechanisms involved. *Molecular Therapy*, *18*(1), 101-108.

Leow, R. S., Wan, J. M., & Yu, A. C. (2015). Membrane blebbing as a recovery manoeuvre in site-specific sonoporation mediated by targeted microbubbles. *Journal of the Royal Society Interface*, *12*(105), 20150029.

Li, D., Pellegrino, A., Hallack, A., Petrinic, N., Jérusalem, A., & Cleveland, R. O. (2018). Response of single cells to shock waves and numerically optimized waveforms for cancer therapy. *Biophysical journal*, *114*(6), 1433-1439.

Li, M., Dzaharudin, F., Ooi, A., & Manasseh, R. (2010). The effect of a solid boundary on the dynamics of a small group of ultrasound driven microbubbles. In *Proceedings of the 20th International Congress on Acoustics* (pp. 639-646).

Li, Z. G., Liu, A. Q., Klaseboer, E., Zhang, J. B., & Ohl, C. D. (2013). Single cell membrane poration by bubble-induced microjets in a microfluidic chip. *Lab on a Chip*, *13*(6), 1144-1150.

Liang, H. D., Tang, J., & Halliwell, M. (2010). Sonoporation, drug delivery, and gene therapy. *Proceedings of the Institution of Mechanical Engineers, Part H: Journal of Engineering in Medicine*, *224*(2), 343-361.

Lindau, D., Gielen, P., Kroesen, M., Wesseling, P., & Adema, G. J. (2013). The immunosuppressive tumour network: myeloid-derived suppressor cells, regulatory T cells and natural killer T cells. *Immunology*, *138*(2), 105-115.

Lindner, J. R. (2004). Microbubbles in medical imaging: current applications and future directions. *Nature reviews Drug discovery*, *3*(6), 527-533.

Lindner, J. R., Coggins, M. P., Kaul, S., Klibanov, A. L., Brandenburger, G. H., & Ley, K. (2000a). Microbubble persistence in the microcirculation during ischemia/reperfusion and inflammation is caused by integrin-and complement-mediated adherence to activated leukocytes. *Circulation*, *101*(6), 668-675.

Lindner, J. R., Song, J., Xu, F., Klibanov, A. L., Singbartl, K., Ley, K., & Kaul, S. (2000b). Noninvasive ultrasound imaging of inflammation using microbubbles targeted to activated leukocytes. *Circulation*, *102*(22), 2745-2750.

Liu, H. L., Hsieh, H. Y., Lu, L. A., Kang, C. W., Wu, M. F., & Lin, C. Y. (2012). Low-pressure pulsed focused ultrasound with microbubbles promotes an anticancer immunological response. *Journal of translational medicine*, *10*(1), 221.

Liu, X., Gong, P., Song, P., Xie, F., Miller II, A. L., Chen, S., & Lu, L. (2019). Rapid conjugation of nanoparticles,

proteins and siRNAs to microbubbles by strain-promoted click chemistry for ultrasound imaging and drug delivery. *Polymer Chemistry*, *10*(6), 705-717.

Lu, P., Zhu, X. Q., Xu, Z. L., Zhou, Q., Zhang, J., & Wu, F. (2009). Increased infiltration of activated tumor-infiltrating lymphocytes after high intensity focused ultrasound ablation of human breast cancer. *Surgery*, *145*(3), 286-293.

Lukáč, R., Kauerová, Z., Mašek, J., Bartheldyová, E., Kulich, P., Koudelka, S., ... & Turánek, J. (2011). Preparation of metallochelating microbubbles and study on their site-specific interaction with rGFP-HisTag as a model protein. Langmuir, 27(8), 4829-4837.

Lum, A. F., Borden, M. A., Dayton, P. A., Kruse, D. E., Simon, S. I., & Ferrara, K. W. (2006). Ultrasound radiation force enables targeted deposition of model drug carriers loaded on microbubbles. *Journal of Controlled Release*, *111*(1-2), 128-134.

Lux, J., Vezeridis, A. M., Hoyt, K., Adams, S. R., Armstrong, A. M., Sirsi, S. R., & Mattrey, R. F. (2017). Thrombin-activatable microbubbles as potential ultrasound contrast agents for the detection of acute thrombosis. *ACS applied materials & interfaces*, *9*(43), 37587-37596.

Lyon, P. C., Griffiths, L. F., Lee, J., Chung, D., Carlisle, R., Wu, F., ... & Coussios, C. C. (2017). Clinical trial protocol for TARDOX: a phase I study to investigate the feasibility of targeted release of lyso-thermosensitive liposomal doxorubicin (ThermoDox®) using focused ultrasound in patients with liver tumours. *Journal of therapeutic ultrasound*, *5*(1), 1-8.

Maeda, H., Wu, J., Sawa, T., Matsumura, Y., & Hori, K. (2000). Tumor vascular permeability and the EPR effect in macromolecular therapeutics: a review. *Journal of controlled release*, *65*(1-2), 271-284.

Magde, D., Elson, E., & Webb, W. W. (1972). Thermodynamic fluctuations in a reacting system—measurement by fluorescence correlation spectroscopy. *Physical Review Letters*, *29*(11), 705.

Makkouk A., Weiner GJ. (2015) Cancer immunotherapy and breaking immune tolerance: new approaches to an old challenge. Cancer Res 75:5–10. doi:10.1158/0008-5472. CAN-14-2538

Malliaros, J., Quinn, C., Arnold, F. H., Pearse, M. J., Drane, D. P., Stewart, T. J., & Macfarlan, R. I. (2004). Association of antigens to ISCOMATRIX™ adjuvant using metal chelation leads to improved CTL responses. *Vaccine*, *22*(29-30), 3968-3975.

Mannaris, C., Bau, L., Grundy, M., Gray, M., Lea-Banks, H., Seth, A., ... & Coussios, C. C. (2019). Microbubbles, nanodroplets and gas-stabilizing solid particles for ultrasound-mediated extravasation of unencapsulated drugs: an exposure parameter optimization study. *Ultrasound in medicine & biology*, *45*(4), 954-967.

Mannaris, C., Teo, B. M., Seth, A., Bau, L., Coussios, C., & Stride, E. (2018). Gas-stabilizing gold nanocones for acoustically mediated drug delivery. *Advanced healthcare materials*, *7*(12), 1800184.

Marmor, J. B., & Hahn, G. M. (1980). Combined radiation and hyperthermia in superficial human tumors. *Cancer*, *46*(9), 1986-1991.

Marmottant, P., Biben, T., & Hilgenfeldt, S. (2008). Deformation and rupture of lipid vesicles in the strong shear flow generated by ultrasound-driven microbubbles. *Proceedings of the Royal Society A: Mathematical, Physical and Engineering Sciences*, *464*(2095), 1781-1800.

Mašek, J., Bartheldyová, E., Korvasová, Z., Škrabalová, M., Koudelka, Š., Kulich, P., ... & Turánek, J. (2011). Immobilization of histidine-tagged proteins on monodisperse metallochelation liposomes: Preparation and study of their structure. *Analytical biochemistry*, *408*(1), 95-104.

Matin, S. F., Sharma, P., Gill, I. S., Tannenbaum, C., Hobart, M. G., Novick, A. C., & Finke, J. H. (2010). Immunological response to renal cryoablation in an in vivo orthotopic renal cell carcinoma murine model. *The Journal of urology*, *183*(1), 333-338.

McDannold, N., Arvanitis, C. D., Vykhodtseva, N., & Livingstone, M. S. (2012). Temporary disruption of the blood–brain barrier by use of ultrasound and microbubbles: safety and efficacy evaluation in rhesus macaques. *Cancer research*, *72*(14), 3652-3663.

McDannold, N., Vykhodtseva, N., & Hynynen, K. (2006). Targeted disruption of the blood–brain barrier with focused ultrasound: association with cavitation activity. *Physics in Medicine & Biology*, *51*(4), 793.

McDannold, N., Vykhodtseva, N., Raymond, S., Jolesz, F. A., & Hynynen, K. (2005). MRI-guided targeted blood-brain barrier disruption with focused ultrasound: histological findings in rabbits. *Ultrasound in medicine & biology*, *31*(11), 1527-1537.

McEwan, C., Owen, J., Stride, E., Fowley, C., Nesbitt, H., Cochrane, D., ... & Callan, J. F. (2015). Oxygen carrying microbubbles for enhanced sonodynamic therapy of hypoxic tumours. *Journal of Controlled Release*, *203*, 51-56.

McIntosh, T. J., & Simon, S. A. (2006). Roles of bilayer material properties in function and distribution of membrane proteins. *Annu. Rev. Biophys. Biomol. Struct.*, *35*, 177-198.

McKinnon, K. M. (2018). Flow cytometry: an overview. *Current protocols in immunology*, *120*(1), 5-1.

Mead, B. P., Mastorakos, P., Suk, J. S., Klibanov, A. L., Hanes, J., & Price, R. J. (2016). Targeted gene transfer to the brain via the delivery of brain-penetrating DNA nanoparticles with focused ultrasound. *Journal of Controlled Release*, *223*, 109-117.

Meijering, B. D., Juffermans, L. J., van Wamel, A., Henning, R. H., Zuhorn, I. S., Emmer, M., ... & de Jong, N. (2009). Ultrasound and microbubble-targeted delivery of macromolecules is regulated by induction of endocytosis and pore formation. *Circulation research*, *104*(5), 679-687.

Melenhorst, J. J., Chen, G. M., Wang, M., Porter, D. L., Chen, C., Collins, M. A., ... & June, C. H. (2022). Decade-long leukaemia remissions with persistence of CD4+ CAR T cells. *Nature*, 1-7.

Meng, Y., Reilly, R. M., Pezo, R. C., Trudeau, M., Sahgal, A., Singnurkar, A., ... & Lipsman, N. (2021). MR-guided focused ultrasound enhances delivery of trastuzumab to Her2-positive brain metastases. *Science translational medicine*, *13*(615), eabj4011.

Merckel, L. G., Knuttel, F. M., Deckers, R., van Dalen, T., Schubert, G., Peters, N. H., ... & van Gorp, J. M. (2016). First clinical experience with a dedicated MRI-guided high-intensity focused ultrasound system for breast cancer ablation. *European radiology*, *26*(11), 4037-4046.

Meric-Bernstam, F., Johnson, A. M., Dumbrava, E. E. I., Raghav, K., Balaji, K., Bhatt, M., ... & Piha-Paul, S. A. (2019). Advances in HER2-targeted therapy: novel agents and opportunities beyond breast and gastric cancer. *Clinical Cancer Research*, *25*(7), 2033-2041.

Mesiwala, A. H., Farrell, L., Wenzel, H. J., Silbergeld, D. L., Crum, L. A., Winn, H. R., & Mourad, P. D. (2002). High-intensity focused ultrasound selectively disrupts the blood-brain barrier in vivo. *Ultrasound in medicine & biology*, *28*(3), 389-400.

Miliotou, A. N., & Papadopoulou, L. C. (2018). CAR T-cell therapy: a new era in cancer immunotherapy. *Current pharmaceutical biotechnology*, *19*(1), 5-18.

Mitragotri, S. (2005). Healing sound: the use of ultrasound in drug delivery and other therapeutic applications. *Nature reviews Drug discovery*, *4*(3), 255.

Mitragotri, S. (2017). Sonophoresis: ultrasound-mediated transdermal drug delivery. In *Percutaneous Penetration Enhancers Physical Methods in Penetration Enhancement* (pp. 3-14). Springer, Berlin, Heidelberg.

Mittal, D., Gubin, M. M., Schreiber, R. D., & Smyth, M. J. (2014). New insights into cancer immunoediting and its three component phases—elimination, equilibrium and escape. *Current opinion in immunology*, *27*, 16-25.

Molnar, C., & Gair, J. (2015). *Concepts of Biology*. Accessed via https://opentextbc.ca/biology/chapter/23-2-adaptive-immune-response/.

Mooney, R., Schena, E., Saccomandi, P., Zhumkhawala, A., Aboody, K., & Berlin, J. M. (2017). Gold nanorod-mediated near-infrared laser ablation: in vivo experiments on mice and theoretical analysis at different settings. *International Journal of Hyperthermia*, *33*(2), 150-159.

Morrow, M. R., Whitehead, J. P., & Lu, D. (1992). Chain-length dependence of lipid bilayer properties near the liquid crystal to gel phase transition. *Biophysical journal*, *63*(1), 18-27.

Mulvana, H., Browning, R. J., Luan, Y., de Jong, N., Tang, M. X., Eckersley, R. J., & Stride, E. (2017). Characterization of contrast agent microbubbles for ultrasound imaging and therapy research. *IEEE transactions on ultrasonics, ferroelectrics, and frequency control*, *64*(1), 232-251.

Mulvana, H., Stride, E., Hajnal, J. V., & Eckersley, R. J. (2010). Temperature dependent behavior of ultrasound contrast agents. *Ultrasound in medicine & biology*, *36*(6), 925-934.

Muralidharan, R., Amreddy, N., Babu, A., Srivastava, A., Panneerselvam, J., Chen, A., ... & Ramesh, R. (2016). 489. Tumor-Targeted Hursirna-Nanoparticle Delivery Inhibits Lung Tumor Growth In Vitro and In Vivo. *Molecular Therapy*, *24*, S194.

Muralidharan, R., Babu, A., Amreddy, N., Srivastava, A., Chen, A., Zhao, Y. D., ... & Ramesh, R. (2017). Tumor-targeted nanoparticle delivery of HuR siRNA inhibits lung tumor growth in vitro and in vivo by disrupting the oncogenic activity of the RNA-binding protein HuR. *Molecular cancer therapeutics*, *16*(8), 1470-1486.

Myrset, A. H., Fjerdingstad, H. B., Bendiksen, R., Arbo, B. E., Bjerke, R. M., Johansen, J. H., ... & Skurtveit, R. (2011). Design and characterization of targeted ultrasound microbubbles for diagnostic use. *Ultrasound in medicine & biology*, *37*(1), 136-150.

Nakano, H., Ishida, Y., Hatakeyama, T., Sakuraba, K., Hayashi, M., Sakurai, O., & Hataya, K. (2008). Contrast-enhanced intraoperative ultrasonography equipped with late Kupffer-phase image obtained by sonazoid in patients with colorectal liver metastases. *World Journal of Gastroenterology: WJG*, *14*(20), 3207.

Nakatsuka, M. A., Mattrey, R. F., Esener, S. C., Cha, J. N., & Goodwin, A. P. (2012). Aptamer-crosslinked microbubbles: smart contrast agents for thrombin-activated ultrasound imaging. *Advanced Materials*, *24*(45), 6010-6016.

Nejad, S. M., Hosseini, H., Akiyama, H., & Tachibana, K. (2016). Reparable cell sonoporation in suspension: theranostic potential of microbubble. *Theranostics*, *6*(4), 446.

Nelson, J. L., Roeder, B. L., Carmen, J. C., Roloff, F., & Pitt, W.G. (2002). Ultrasonically activated chemotherapeutic drug delivery in a rat model. *Cancer research*, *62*(24), 7280-7283.

Nesbitt, H., Sheng, Y., Kamila, S., Logan, K., Thomas, K., Callan, B., ... & Callan, J. F. (2018). Gemcitabine loaded microbubbles for targeted chemo-sonodynamic therapy of pancreatic cancer. *Journal of controlled release*, *279*, 8-16.

Nesbitt, H., Sheng, Y., Kamila, S., Logan, K., Thomas, K., Callan, B., ... & Callan, J. F. (2018). Gemcitabine loaded microbubbles for targeted chemo-sonodynamic therapy of pancreatic cancer. *Journal of controlled release*, *279*, 8-16.

Ng, P. P., Cruz, J. S. D., Sorour, D. N., Stinebaugh, J. M., Shin, S. U., Shin, D. S., ... & Penichet, M. L. (2002). An anti-transferrin receptor-avidin fusion protein exhibits both strong proapoptotic activity and the ability to deliver various molecules into cancer cells. *Proceedings of the National Academy of Sciences*, *99*(16), 10706-10711.

Nye, J. A., & Groves, J. T. (2008). Kinetic control of histidine-tagged protein surface density on supported lipid bilayers. *Langmuir*, *24*(8), 4145-4149.

O'Reilly, M. A., & Hynynen, K. (2018). Ultrasound and Microbubble-Mediated Blood-Brain Barrier Disruption for Targeted Delivery of Therapeutics to the Brain. In *Targeted Drug Delivery* (pp. 111-119). Humana Press, New York, NY.

Oda, Y., Suzuki, R., Otake, S., Nishiie, N., Hirata, K., Koshima, R., ... & Maruyama, K. (2012). Prophylactic immunization with Bubble liposomes and ultrasound-treated dendritic cells provided a four-fold decrease in the frequency of melanoma lung metastasis. *Journal of controlled release*, *160*(2), 362-366.

Olsman, M., Sereti, V., Mühlenpfordt, M., Johnsen, K. B., Andresen, T. L., Urquhart, A. J., & de Lange Davies, C. (2021). Focused ultrasound and microbubble treatment increases delivery of transferrin receptor-targeting liposomes to the brain. *Ultrasound in Medicine & Biology*, *47*(5), 1343-1355.

Omata, D., Unga, J., Suzuki, R., & Maruyama, K. (2020). Lipid-based microbubbles and ultrasound for therapeutic application. *Advanced Drug Delivery Reviews*.

Oostindie, S. C., van der Horst, H. J., Lindorfer, M. A., Cook, E. M., Tupitza, J. C., Zent, C. S., Burack, R., VanDerMeid, K. R., Strumane, K., Chamuleau, M., Mutis, T., de Jong, R. N., Schuurman, J., Breij, E.,

Beurskens, F. J., Parren, P., & Taylor, R. P. (2019). CD20 and CD37 antibodies synergize to activate complement by Fc-mediated clustering. *Haematologica*, *104*(9), 1841–1852.

Ottoboni, S., Short, R. E., Kerby, M. B., Tickner, E. G., Steadman, E., & Ottoboni, T. B. (2006). Characterization of the in vitro adherence behavior of ultrasound responsive double-shelled microspheres targeted to cellular adhesion molecules. *Contrast media & molecular imaging*, *1*(6), 279-290.

Owen, D. M., Rentero, C., Magenau, A., Abu-Siniyeh, A., & Gaus, K. (2012). Quantitative imaging of membrane lipid order in cells and organisms. *Nature protocols*, *7*(1), 24-35.

Owen, J., Kamila, S., Shrivastava, S., Carugo, D., Bernardino de la Serna, J., Mannaris, C., ... & Stride, E. (2018). The Role of PEG-40-stearate in the Production, Morphology, and Stability of Microbubbles. *Langmuir*, *35*(31), 10014-10024.

Paganelli, G., Belloni, C., Magnani, P., Zito, F., Pasini, A., Sassi, I., ... & Fazio, F. (1992). Two-step tumour targetting in ovarian cancer patients using biotinylated monoclonal antibodies and radioactive streptavidin. *European journal of nuclear medicine*, *19*(5), 322-329.

Panidis, I. P., Ross, J., & Mintz, G. S. (1986). Normal and abnormal prosthetic valve function as assessed by Doppler echocardiography. *Journal of the American College of Cardiology*, *8*(2), 317-326.

Paris, J. L., Mannaris, C., Cabañas, M. V., Carlisle, R., Manzano, M., Vallet-Regí, M., & Coussios, C. C. (2018). Ultrasound-mediated cavitation-enhanced extravasation of mesoporous silica nanoparticles for controlled-release drug delivery. *Chemical Engineering Journal*, *340*, 2-8.

Park, J., Lee, H., Lim, G. S., Kim, N., Kim, D., & Kim, Y. C. (2019). Enhanced transdermal drug delivery by sonophoresis and simultaneous application of sonophoresis and iontophoresis. *AAPS PharmSciTech*, *20*(3), 1-7.

Partlow, K. C., Lanza, G. M., & Wickline, S. A. (2008). Exploiting lipid raft transport with membrane targeted nanoparticles: a strategy for cytosolic drug delivery. *Biomaterials*, *29*(23), 3367-3375.

Pasparakis, M., Alexopoulou, L., Episkopou, V., & Kollias, G. (1996). Immune and inflammatory responses in TNF alpha-deficient mice: a critical requirement for TNF alpha in the formation of primary B cell follicles, follicular dendritic cell networks and germinal centers, and in the maturation of the humoral immune response. *Journal of Experimental Medicine*, *184*(4), 1397-1411.

Patil, J., & Shah, V. I. (1996). Transferrin receptor expression by blast cells in acute lymphoblastic leukemia correlates with white cell count & immunophenotype. *The Indian journal of medical research*, *104*, 226-233.

Peng, S. W., Ko, W. H., Yeh, M. K., Chiang, C. H., & Chen, J. L. (2015). The mechanism of high transfection efficiency of human serum albumin conjugated polyethylenimine in A549 cells. *Journal of Medical Sciences*, *35*(2), 57.

Penn, I. (2000). Post-transplant malignancy: the role of immunosuppression. *Drug safety*, *23*, 101-113.

Pereno, V., Aron, M., Vince, O., Mannaris, C., Seth, A., de Saint Victor, M., ... & Stride, E. (2018). Layered acoustofluidic resonators for the simultaneous optical and acoustic characterisation of cavitation dynamics, microstreaming, and biological effects. *Biomicrofluidics*, *12*(3), 034109.

Pereno, V., Lei, J., Carugo, D., & Stride, E. (2020). Microstreaming inside model cells induced by ultrasound and microbubbles. *Langmuir*, *36*(23), 6388-6398.

Postema, M., Van Wamel, A., Lancée, C. T., & De Jong, N. (2004). Ultrasound-induced encapsulated microbubble phenomena. *Ultrasound in medicine & biology*, *30*(6), 827-840.

Prentice, P., Cuschieri, A., Dholakia, K., Prausnitz, M., & Campbell, P. (2005). Membrane disruption by optically controlled microbubble cavitation. *Nature physics*, *1*(2), 107-110.

Price, R. J., Skyba, D. M., Kaul, S., & Skalak, T. C. (1998). Delivery of colloidal particles and red blood cells to tissue through microvessel ruptures created by targeted microbubble destruction with ultrasound. *Circulation*, *98*(13), 1264-1267.

Prise, K. M., & O'sullivan, J. M. (2009). Radiation-induced bystander signalling in cancer therapy. *Nature Reviews Cancer*, *9*(5), 351.

Punjabi, M., Xu, L., Ochoa-Espinosa, A., Kosareva, A., Wolff, T., Murtaja, A., ... & Kaufmann, B. A. (2019). Ultrasound molecular imaging of atherosclerosis with nanobodies: translatable microbubble targeting murine and human VCAM (vascular cell adhesion molecule) 1. *Arteriosclerosis, thrombosis, and vascular biology*, *39*(12), 2520-2530.

Ramishetti, S., Kedmi, R., Goldsmith, M., Leonard, F., Sprague, A. G., Godin, B., ... & Peer, D. (2015). Systemic gene silencing in primary T lymphocytes using targeted lipid nanoparticles. *ACS nano*, *9*(7), 6706-6716.

Rapoport, N. Y., Christensen, D. A., Fain, H. D., Barrows, L., & Gao, Z. (2004). Ultrasound-triggered drug targeting of tumors in vitro and in vivo. *Ultrasonics*, *42*(1-9), 943-950.

Rapoport, N., Gao, Z., & Kennedy, A. (2007). Multifunctional nanoparticles for combining ultrasonic tumor imaging and targeted chemotherapy. *Journal of the National Cancer Institute*, *99*(14), 1095-1106.

Raso, V., & Basala, M. (1984). A highly cytotoxic human transferrin-ricin A chain conjugate used to select receptor-modified cells. *Journal of Biological Chemistry*, *259*(2), 1143-1149.

Rawicz, W., Olbrich, K. C., McIntosh, T., Needham, D., & Evans, E. (2000). Effect of chain length and unsaturation on elasticity of lipid bilayers. *Biophysical journal*, *79*(1), 328-339.

Reuschenbach, M., von Knebel Doeberitz, M., & Wentzensen, N. (2009). A systematic review of humoral immune responses against tumor antigens. *Cancer immunology, immunotherapy*, *58*(10), 1535.

Riccardi, C., & Nicoletti, I. (2006). Analysis of apoptosis by propidium iodide staining and flow cytometry. *Nature protocols*, *1*(3), 1458-1461.

Rifai, B., Arvanitis, C. D., Bazan-Peregrino, M., & Coussios, C. C. (2010). Cavitation-enhanced delivery of macromolecules into an obstructed vessel. *The Journal of the Acoustical Society of America*, *128*(5), EL310-EL315.

Robb, A., & Wessling-Resnick, M. (2004). Regulation of transferrin receptor 2 protein levels by transferrin. *Blood*, *104*(13), 4294-4299.

Rong, N., Zhou, H., Liu, R., Wang, Y., & Fan, Z. (2018). Ultrasound and microbubble mediated plasmid DNA uptake: A fast, global and multi-mechanisms involved process. *Journal of controlled release*, *273*, 40-50.

Roovers, S., Deprez, J., Priwitaningrum, D., Lajoinie, G., Rivron, N., Declercq, H., ... & Lentacker, I. (2019a). Sonoprinting liposomes on tumor spheroids by microbubbles and ultrasound. *Journal of controlled release*, *316*, 79-92.

Roovers, S., Lajoinie, G., De Cock, I., Brans, T., Dewitte, H., Braeckmans, K., ... & Lentacker, I. (2019b). Sonoprinting of nanoparticle-loaded microbubbles: Unraveling the multi-timescale mechanism. *Biomaterials*, *217*, 119250.

Roovers, S., Segers, T., Lajoinie, G., Deprez, J., Versluis, M., De Smedt, S. C., & Lentacker, I. (2019c). The role of ultrasound-driven microbubble dynamics in drug delivery: from microbubble fundamentals to clinical translation. *Langmuir*.

Rosberger, D. F., Coleman, D. J., Silverman, R., Woods, S., Rondeau, M., & Cunningham-Rundles, S. (1994). Immunomodulation in choroidal melanoma: reversal of inverted CD4/CD8 ratios following treatment with ultrasonic hyperthermia. *Biotechnology therapeutics*, *5*(1-2), 59-68.

Rosenthal, I., Sostaric, J. Z., & Riesz, P. (2004). Sonodynamic therapy—a review of the synergistic effects of drugs and ultrasound. *Ultrasonics sonochemistry*, *11*(6), 349-363.

Ross, J. S., Slodkowska, E. A., Symmans, W. F., Pusztai, L., Ravdin, P. M., & Hortobagyi, G. N. (2009). The HER-2 receptor and breast cancer: ten years of targeted anti–HER-2 therapy and personalized medicine. *The oncologist*, *14*(4), 320-368.

Rüger, R., Müller, D., Fahr, A., & Kontermann, R. E. (2006). In vitro characterization of binding and stability of single-chain Fv Ni-NTA-liposomes. *Journal of drug targeting*, *14*(8), 576-582.

Rychak, J. J., Klibanov, A. L., & Hossack, J. A. (2005). Acoustic radiation force enhances targeted delivery of ultrasound contrast microbubbles: in vitro verification. *IEEE transactions on ultrasonics, ferroelectrics, and frequency control*, *52*(3), 421-433.

Sakaguchi, S., Sakaguchi, N., Shimizu, J., Yamazaki, S., Sakihama, T., Itoh, M., ... & Takahashi, T. (2001). Immunologic tolerance maintained by CD25+ CD4+ regulatory T cells: their common role in controlling autoimmunity, tumor immunity, and transplantation tolerance. *Immunological reviews*, *182*(1), 18-32.

Sakakima, Y., Hayashi, S., Yagi, Y., Hayakawa, A., Tachibana, K., & Nakao, A. (2005). Gene therapy for hepatocellular carcinoma using sonoporation enhanced by contrast agents. *Cancer gene therapy*, *12*(11), 884.

Schena, E., Saccomandi, P., & Fong, Y. (2017). Laser ablation for cancer: past, present and future. *Journal of functional biomaterials*, *8*(2), 19.

Schindelin, J., Arganda-Carreras, I., Frise, E., Kaynig, V., Longair, M., Pietzsch, T., ... & Cardona, A. (2012). Fiji: an open-source platform for biological-image analysis. *Nature methods*, *9*(7), 676-682.

Schmid, D., Park, C. G., Hartl, C. A., Subedi, N., Cartwright, A. N., Puerto, R. B., ... & Goldberg, M. S. (2017). T cell-targeting nanoparticles focus delivery of immunotherapy to improve antitumor immunity. *Nature communications*, *8*(1), 1-12.

Schneider, M. (1999). Characteristics of sonovue™. *Echocardiography*, *16*, 743-746.

Schreiber, R. D., Old, L. J., & Smyth, M. J. (2011). Cancer immunoediting: integrating immunity's roles in cancer suppression and promotion. *Science*, *331*(6024), 1565-1570.

Schreiber, R. D., Old, L. J., & Smyth, M. J. (2011). Cancer immunoediting: integrating immunity's roles in cancer suppression and promotion. *Science*, *331*(6024), 1565-1570.

Schroeder, A., Kost, J., & Barenholz, Y. (2009). Ultrasound, liposomes, and drug delivery: principles for using ultrasound to control the release of drugs from liposomes. *Chemistry and physics of lipids*, *162*(1-2), 1-16.

Scott, A. M., Wolchok, J. D., & Old, L. J. (2012). Antibody therapy of cancer. *Nature reviews cancer*, *12*(4), 278.

Sennoga, C. A., Mahue, V., Loughran, J., Casey, J., Seddon, J. M., Tang, M., & Eckersley, R. J. (2010). On sizing and counting of microbubbles using optical microscopy. *Ultrasound in medicine & biology*, *36*(12), 2093-2096.

Sezgin, E., & Schwille, P. (2011). Fluorescence techniques to study lipid dynamics. *Cold Spring Harbor perspectives in biology*, *3*(11), a009803.

Sezgin, E., Levental, I., Mayor, S., & Eggeling, C. (2017). The mystery of membrane organization: composition, regulation and roles of lipid rafts. *Nature reviews Molecular cell biology*, *18*(6), 361-374.

Sezgin, E., Schneider, F., Galiani, S., Urbančič, I., Waithe, D., Lagerholm, B. C., & Eggeling, C. (2019). Measuring nanoscale diffusion dynamics in cellular membranes with super-resolution STED–FCS. *Nature protocols*, *14*(4), 1054-1083.

Shah, V. I. (1990). Correlation of transferrin receptor expression with histologic grade and immunophenotype in chronic lymphocytic leukemia and non-Hodgkin's lymphoma. *Hematologic pathology*, *4*(1), 37-41.

Shapiro, G., Wong, A. W., Bez, M., Yang, F., Tam, S., Even, L., ... & Ferrara, K. W. (2016). Multiparameter evaluation of in vivo gene delivery using ultrasound-guided, microbubble-enhanced sonoporation. *Journal of Controlled Release*, *223*, 157-164.

Sheen, A. J., Poston, G. J., & Sherlock, D. J. (2002). Cryotherapeutic ablation of liver tumours. *British Journal of Surgery*, *89*(11), 1396-1401.

Sheff, D. R., Daro, E. A., Hull, M., & Mellman, I. (1999). The receptor recycling pathway contains two distinct populations of early endosomes with different sorting functions. *The Journal of cell biology*, *145*(1), 123-139.

Shekhar, H., Smith, N. J., Raymond, J. L., & Holland, C. K. (2018). Effect of temperature on the size distribution, shell properties, and stability of Definity®. *Ultrasound in medicine & biology*, *44*(2), 434-446.

Shrirao, A. B., Schloss, R. S., Fritz, Z., Shrirao, M. V., Rosen, R., & Yarmush, M. L. (2021). Autofluorescence of blood and its application in biomedical and clinical research. *Biotechnology and Bioengineering*, *118*(12), 4550-4576.

Shrivastava, S., Cleveland, R. O., & Schneider, M. F. (2018). On measuring the acoustic state changes in lipid membranes using fluorescent probes. *Soft Matter*, *14*(47), 9702-9712.

Sindhwani, S., Syed, A. M., Ngai, J., Kingston, B. R., Maiorino, L., Rothschild, J., ... & Chan, W. C. (2020). The entry of nanoparticles into solid tumours. *Nature materials*, *19*(5), 566-575.

Singer, S. J., & Nicolson, G. L. (1972). The Fluid Mosaic Model of the Structure of Cell Membranes: Cell membranes are viewed as two-dimensional solutions of oriented globular proteins and lipids. *Science*, *175*(4023), 720-731.

Singh, M., Atwal, H., & Micetich, R. (1998). Transferrin directed delivery of adriamycin to human cells. *Anticancer research*, *18*(3A), 1423-1427.

Sirsi, S. R., Hernandez, S. L., Zielinski, L., Blomback, H., Koubaa, A., Synder, M., ... & Borden, M. A. (2012). Polyplex-microbubble hybrids for ultrasound-guided plasmid DNA delivery to solid tumors. *Journal of Controlled Release*, *157*(2), 224-234.

Skyba, D. M., Price, R. J., Linka, A. Z., Skalak, T. C., & Kaul, S. (1998). Direct in vivo visualization of intravascular destruction of microbubbles by ultrasound and its local effects on tissue. *Circulation*, *98*(4), 290-293.

Slagle, C. J., Thamm, D. H., Randall, E. K., & Borden, M. A. (2018). Click conjugation of cloaked peptide ligands to microbubbles. *Bioconjugate Chemistry*, *29*(5), 1534-1543.

Smith, C. A., & Coussios, C. C. (2020). Spatiotemporal assessment of the cellular safety of cavitation-based therapies by passive acoustic mapping. *Ultrasound in Medicine & Biology*, *46*(5), 1235-1243.

Smith, S. L., & Jennings, P. E. (2015). Lung radiofrequency and microwave ablation: a review of indications, techniques and post-procedural imaging appearances. *The British Journal of Radiology*, *88*(1046), 20140598.

Smith, T. T., Stephan, S. B., Moffett, H. F., McKnight, L. E., Ji, W., Reiman, D., ... & Stephan, M. T. (2017). In situ programming of leukaemia-specific T cells using synthetic DNA nanocarriers. *Nature nanotechnology*, *12*(8), 813-820.

Smyth, M. J., Godfrey, D. I., & Trapani, J. A. (2001). A fresh look at tumor immunosurveillance and immunotherapy. *Nature immunology*, *2*(4), 293.

Song, K. H., Harvey, B. K., & Borden, M. A. (2018). State-of-the-art of microbubble-assisted blood-brain barrier disruption. *Theranostics*, *8*(16), 4393.

Stride, E. (2009). Physical principles of microbubbles for ultrasound imaging and therapy. *Cerebrovascular Diseases*, *27*(Suppl. 2), 1-13.

Stride, E. (2019). Magnetic nanodroplets for targeted drug delivery. *Ultrasound in Medicine & Biology*, *45*, S49.

Stride, E. P., & Coussios, C. C. (2010). Cavitation and contrast: the use of bubbles in ultrasound imaging and therapy. *Proceedings of the Institution of Mechanical Engineers, Part H: Journal of Engineering in Medicine*, *224*(2), 171-191.

Stride, E., & Coussios, C. (2019). Nucleation, mapping and control of cavitation for drug delivery. *Nature Reviews Physics*, *1*(8), 495-509.

Stride, E., Segers, T., Lajoinie, G., Cherkaoui, S., Bettinger, T., Versluis, M., & Borden, M. (2020). Microbubble agents: New directions. *Ultrasound in medicine & biology*, *46*(6), 1326-1343.

Suetens, P. (2016). *Fundamentals of medical imaging*. Cambridge: Cambridge University Press, p. 128-158.

Sundaram, J., Mellein, B. R., & Mitragotri, S. (2003). An experimental and theoretical analysis of ultrasound-induced permeabilization of cell membranes. *Biophysical journal*, *84*(5), 3087-3101.

Suslick, K. S. (1988). *Ultrasound: its chemical, physical, and biological effects*. United States of America: VCH Publishers, Inc.

Suzuki, R., Namai, E., Oda, Y., Nishiie, N., Otake, S., Koshima, R., ... & Maruyama, K. (2010). Cancer gene therapy by IL-12 gene delivery using liposomal bubbles and tumoral ultrasound exposure. *Journal of Controlled Release*, *142*(2), 245-250.

Suzuki, R., Oda, Y., Utoguchi, N., Namai, E., Taira, Y., Okada, N., ... & Maruyama, K. (2009). A novel strategy utilizing ultrasound for antigen delivery in dendritic cell-based cancer immunotherapy. *Journal of Controlled Release*, *133*(3), 198-205.

Suzuki, R., Takizawa, T., Negishi, Y., Hagisawa, K., Tanaka, K., Sawamura, K., ... & Maruyama, K. (2007). Gene delivery by combination of novel liposomal bubbles with perfluoropropane and ultrasound. *Journal of Controlled Release*, *117*(1), 130-136.

Tachibana, K., Feril Jr, L. B., & Ikeda-Dantsuji, Y. (2008). Sonodynamic therapy. *Ultrasonics*, *48*(4), 253-259.

Tachibana, K., Uchida, T., Hisano, S., & Morioka, E. (1997). Eliminating adult T-cell leukaemia cells with ultrasound. *The Lancet*, *349*(9048), 325.

Tachibana, K., Uchida, T., Ogawa, K., Yamashita, N., & Tamura, K. (1999). Induction of cell-membrane porosity by ultrasound. *The Lancet*, *353*(9162), 1409.

Tachibana, K., Uchida, T., Tamura, K., Eguchi, H., Yamashita, N., & Ogawa, K. (2000). Enhanced cytotoxic effect of Ara-C by low intensity ultrasound to HL60 cells. *Cancer letters*, *149*(1-2), 189-194.

Tan, J., Li, P., Xue, H., & Li, Q. (2020). Cyanidin-3-glucoside prevents hydrogen peroxide (H2O2)-induced oxidative damage in HepG2 cells. *Biotechnology Letters*, *42*(11), 2453-2466.

ter Haar, G., & Coussios, C. (2007). High intensity focused ultrasound: physical principles and devices. *International journal of hyperthermia*, *23*(2), 89-104.

The QIAexpressionist ™. A handbook for high-level expression and purification of 6xHis-tagged proteins. Fifth Edition. June 2003. To be accessed: https://kirschner.med.harvard.edu/files/protocols/QIAGEN_QIAexpressionist_EN.pdf

Thomas, J. D. (1997). How leaky is that mitral valve? Simplified Doppler methods to measure regurgitant orifice area. *Circulation*, *95*(3), 548-550.

Thompson, N. L. (2002). Fluorescence correlation spectroscopy. In Lakowicz, J. R. (Ed.), *Topics in fluorescence spectroscopy* (pp. 337-378). New York: Kluwer Academic Publishers.

Thone, M. N., & Kwon, Y. J. (2020). Extracellular blebs: Artificially-induced extracellular vesicles for facile production and clinical translation. *Methods*, *177*, 135-145.

Tian, Y., Martinez, M. M., & Pappas, D. (2011). Fluorescence correlation spectroscopy: A review of biochemical and microfluidic applications. *Applied Spectroscopy*, *65*(4), 115-124.

Tio, D., Kasiem, F. R., Willemsen, M., van Doorn, R., van der Werf, N., Hoekzema, R., ... & Bekkenk, M. W. (2019). Expression of cancer/testis antigens in cutaneous melanoma: a systematic review. *Melanoma Research*, *29*(4), 349-357.

Topalian, S. L., Hodi, F. S., Brahmer, J. R., Gettinger, S. N., Smith, D. C., McDermott, D. F., ... & Leming, P. D.

(2012). Safety, activity, and immune correlates of anti–PD-1 antibody in cancer. *New England Journal of Medicine*, *366*(26), 2443-2454.

Topalian, S. L., Weiner, G. J., & Pardoll, D. M. (2011). Cancer immunotherapy comes of age. *Journal of Clinical Oncology*, *29*(36), 4828.

Trinder, D., & Baker, E. (2003). Transferrin receptor 2: a new molecule in iron metabolism. *The international journal of biochemistry & cell biology*, *35*(3), 292-296.

Tu, J., Zhang, H., Yu, J., Liufu, C., & Chen, Z. (2018). Ultrasound-mediated microbubble destruction: a new method in cancer immunotherapy. *OncoTargets and therapy*, *11*, 5763.

Turk, M. J., Wolchok, J. D., Guevara-Patino, J. A., Goldberg, S. M., & Houghton, A. N. (2002). Multiple pathways to tumor immunity and concomitant autoimmunity. *Immunological reviews*, *188*(1), 122-135.

Uchinomiya, S. H., Nonaka, H., Fujishima, S. H., Tsukiji, S., Ojida, A., & Hamachi, I. (2009). Site-specific covalent labeling of His-tag fused proteins with a reactive Ni (II)–NTA probe. *Chemical communications*, (39), 5880-5882.

Unga, J., & Hashida, M. (2014). Ultrasound induced cancer immunotherapy. *Advanced drug delivery reviews*, *72*, 144-153.

Unnikrishnan, S., & Klibanov, A. L. (2012). Microbubbles as ultrasound contrast agents for molecular imaging: preparation and application. *American journal of roentgenology*, *199*(2), 292-299.

Upadhyay, A., Dalvi, S. V., Gupta, G., & Khanna, N. (2017). Effect of PEGylation on performance of protein microbubbles and its comparison with lipid microbubbles. *Materials Science and Engineering: C*, *71*, 425-430.

Vajdic, C. M., & Van Leeuwen, M. T. (2009). Cancer incidence and risk factors after solid organ transplantation. *International journal of cancer*, *125*(8), 1747-1754.

van Broekhoven, C. L., & Altin, J. G. (2005). The novel chelator lipid 3 (nitrilotriacetic acid)-ditetradecylamine (NTA3-DTDA) promotes stable binding of His-tagged proteins to liposomal membranes: Potent anti-tumor responses induced by simultaneously targeting antigen, cytokine and costimulatory signals to T cells. *Biochimica Et Biophysica Acta (BBA)-Biomembranes*, *1716*(2), 104-116.

van Broekhoven, C. L., Parish, C. R., Demangel, C., Britton, W. J., & Altin, J. G. (2004). Targeting dendritic cells with antigen-containing liposomes: a highly effective procedure for induction of antitumor immunity and for tumor immunotherapy. *Cancer research*, *64*(12), 4357-4365.

van den Bijgaart, R. J., Eikelenboom, D. C., Hoogenboom, M., Fütterer, J. J., den Brok, M. H., & Adema, G. J. (2017). Thermal and mechanical high-intensity focused ultrasound: perspectives on tumor ablation, immune effects and combination strategies. *Cancer Immunology, Immunotherapy*, *66*(2), 247-258.

van Rooij, T., Beekers, I., Lattwein, K. R., Van Der Steen, A. F., De Jong, N., & Kooiman, K. (2017). Vibrational responses of bound and nonbound targeted lipid-coated single microbubbles. *IEEE Transactions on Ultrasonics, Ferroelectrics, and Frequency Control*, *64*(5), 785-797.

Van Wamel, A., Bouakaz, A., Versluis, M., & de Jong, N. (2004). Micromanipulation of endothelial cells: ultrasound-microbubble-cell interaction. *Ultrasound in medicine & biology*, *30*(9), 1255-1258.

Van Wamel, A., Kooiman, K., Harteveld, M., Emmer, M., Folkert, J., Versluis, M., & De Jong, N. (2006). Vibrating microbubbles poking individual cells: drug transfer into cells via sonoporation. *Journal of controlled release*, *112*(2), 149-155.

Vesterberg, O., & Breig, U. (1981). Quantitative analysis of multiple molecular forms of transferrin using isoelectric focusing and zone immunoelectrophoresis assay (ZIA). *Journal of Immunological Methods*, *46*(1), 53-62.

Vlasova, I. M., & Saletsky, A. M. (2009). Study of the denaturation of human serum albumin by sodium dodecyl sulfate using the intrinsic fluorescence of albumin. *Journal of Applied Spectroscopy*, *76*(4), 536-541.

Vos, H. J., Emmer, M., & De Jong, N. (2008, November). Oscillation of single microbubbles at room versus body temperature. In *2008 IEEE Ultrasonics Symposium* (pp. 982-984). IEEE.

Wagner, E., Zenke, M., Cotten, M., Beug, H., & Birnstiel, M. L. (1990). Transferrin-polycation conjugates as carriers for DNA uptake into cells. *Proceedings of the National Academy of Sciences*, *87*(9), 3410-3414.

Waithe, D., Clausen, M. P., Sezgin, E., & Eggeling, C. (2016). FoCuS-point: software for STED fluorescence correlation and time-gated single photon counting. *Bioinformatics*, *32*(6), 958-960.

Wang, L., Tu, J., Guo, X. S., Xu, D., & Zhang, D. (2014). Microstreaming velocity field and shear stress created by an oscillating encapsulated microbubble near a cell membrane. *Chinese Physics B*, *23*(12), 124302.

Wang, S., Wang, C. Y., Unnikrishnan, S., Klibanov, A. L., Hossack, J. A., & Mauldin Jr, F. W. (2015). Optical verification of microbubble response to acoustic radiation force in large vessels with in vivo results. *Investigative radiology*, *50*(11), 772.

Wang, W., Liu, G. J., Xie, X. Y., Xu, Z. F., Chen, L. D., Huang, G. L., ... & Lu, M. D. (2012). Development and evaluation of lipid microbubbles targeted to alpha (v) beta (3)-integrin via biotin–avidin bridge. *Journal of microencapsulation*, *29*(2), 177-184.

Warmuth, M., Johansson, T., & Mad, P. (2010). Systematic review of the efficacy and safety of high-intensity focussed ultrasound for the primary and salvage treatment of prostate cancer. *European urology*, *58*(6), 803-815.

Wawryka, P., Kiełbik, A., & Iwanek, G. (2019). Microbubble based sonoporation—from the basics into clinical implications. *Medical Research Journal*, *4*(3), 178-183.

Wegel, E., Göhler, A., Lagerholm, B. C., Wainman, A., Uphoff, S., Kaufmann, R., & Dobbie, I. M. (2016). Imaging cellular structures in super-resolution with SIM, STED and Localisation Microscopy: A practical comparison. *Scientific reports*, *6*(1), 1-13.

Wei, K., Skyba, D. M., Firschke, C., Jayaweera, A. R., Lindner, J. R., & Kaul, S. (1997). Interactions between microbubbles and ultrasound: in vitro and in vivo observations. *Journal of the American College of Cardiology*, *29*(5), 1081-1088.

Weiner, L. M., Murray, J. C., & Shuptrine, C. W. (2012). Antibody-based immunotherapy of cancer. *Cell*, *148*(6), 1081-1084.

Weiner, L. M., Surana, R., & Wang, S. (2010). Monoclonal antibodies: versatile platforms for cancer immunotherapy. *Nature Reviews Immunology*, *10*(5), 317.

Wheatley, M. A., & Singhal, S. (1995). Structural studies on stabilized microbubbles: development of a novel contrast agent for diagnostic ultrasound. *Reactive Polymers*, *25*(2-3), 157-166.

Wheatley, M. A., Lathia, J. D., & Oum, K. L. (2007). Polymeric ultrasound contrast agents targeted to integrins: importance of process methods and surface density of ligands. *Biomacromolecules*, *8*(2), 516-522.

Wheatley, M. A., Schrope, B., & Shen, P. (1990). Contrast agents for diagnostic ultrasound: development and evaluation of polymer-coated microbubbles. *Biomaterials*, *11*(9), 713-717.

White, S., Taetle, R., Seligman, P. A., Rutherford, M., & Trowbridge, I. S. (1990). Combinations of anti-transferrin receptor monoclonal antibodies inhibit human tumor cell growth in vitro and in vivo: evidence for synergistic antiproliferative effects. *Cancer research*, *50*(19), 6295-6301.

Widengren, J., Mets, U., & Rigler, R. (1995). Fluorescence correlation spectroscopy of triplet states in solution: a theoretical and experimental study. *The Journal of Physical Chemistry*, *99*(36), 13368-13379.

Wightman, L., Patzelt, E., Wagner, E., & Kircheis, R. (1999). Development of transferrin-polycation/DNA based vectors for gene delivery to melanoma cells. *Journal of drug targeting*, *7*(4), 293-303.

Willmann, J. K., Paulmurugan, R., Chen, K., Gheysens, O., Rodriguez-Porcel, M., Lutz, A. M., ... & Gambhir, S. S. (2008). US imaging of tumor angiogenesis with microbubbles targeted to vascular endothelial growth factor receptor type 2 in mice. *Radiology*, *246*(2), 508-518.

Wilschut, J., & Hoekstra, D. (1984). Membrane fusion: from liposomes to biological membranes. *Trends in Biochemical Sciences*, *9*(11), 479-483.

Wolf, H., Müller, Y., Salmen, S., Wilmanns, W., & Jung, G. (1994). Induction of anergy in resting human T lymphocytes by immobilized anti-CD3 antibodies. *European journal of immunology*, *24*(6), 1410-1417.

Wu, F., Wang, Z. B., Lu, P., Xu, Z. L., Chen, W. Z., Zhu, H., & Jin, C. B. (2004). Activated anti-tumor immunity in cancer patients after high intensity focused ultrasound ablation. *Ultrasound in medicine & biology*, *30*(9), 1217-1222.

Wu, J. (2002). Theoretical study on shear stress generated by microstreaming surrounding contrast agents attached to living cells. *Ultrasound in medicine & biology*, *28*(1), 125-129.

Wu, J., Leong-Poi, H., Bin, J., Yang, L., Liao, Y., Liu, Y., ... & Liu, Y. (2011). Efficacy of contrast-enhanced US and magnetic microbubbles targeted to vascular cell adhesion molecule–1 for molecular imaging of atherosclerosis. *Radiology*, *260*(2), 463-471.

Wu, J., Ross, J. P., & Chiu, J. F. (2002). Reparable sonoporation generated by microstreaming. *The Journal of the Acoustical Society of America*, *111*(3), 1460-1464.

Wu, W., Shi, X., & Xu, C. (2016). Regulation of T cell signalling by membrane lipids. *Nature reviews. Immunology*, *16*(11), 690–701.

Wu, Y., & Kong, L. (2020). Advance on toxicity of metal nickel nanoparticles. *Environmental Geochemistry and Health*, *42*(7), 2277-2286.

Xia, W. J., & Onyuksel, H. (2000). Mechanistic studies on surfactant-induced membrane permeability enhancement. *Pharmaceutical research*, *17*(5), 612-618.

Xu, X., & London, E. (2000). The effect of sterol structure on membrane lipid domains reveals how cholesterol can induce lipid domain formation. *Biochemistry*, *39*(5), 843-849.

Yagel, S., Valsky, D. V., & Messing, B. (2005). Detailed assessment of fetal ventricular septal defect with 4D color Doppler ultrasound using spatio-temporal image correlation technology. *Ultrasound in Obstetrics and Gynecology*, *25*(1), 97-98.

Yamamoto, T., Ogasawara, Y., Kimura, A., Tanaka, H., Hiramatsu, O., Tsujioka, K., ... & Kajiya, F. (1996). Blood velocity profiles in the human renal artery by Doppler ultrasound and their relationship to atherosclerosis. *Arteriosclerosis, thrombosis, and vascular biology*, *16*(1), 172-177.

Yan, F., Sun, Y., Mao, Y., Wu, M., Deng, Z., Li, S., ... & Zheng, H. (2018). Ultrasound molecular imaging of atherosclerosis for early diagnosis and therapeutic evaluation through leucocyte-like multiple targeted microbubbles. *Theranostics*, *8*(7), 1879.

Yanagisawa, K., Moriyasu, F., Miyahara, T., Yuki, M., & Iijima, H. (2007). Phagocytosis of ultrasound contrast agent microbubbles by Kupffer cells. *Ultrasound in medicine & biology*, *33*(2), 318-325.

Yang, C., Li, Y., Du, M., & Chen, Z. (2019). Recent advances in ultrasound-triggered therapy. *Journal of drug targeting*, *27*(1), 33-50.

Yang, Q., Jones, S. W., Parker, C. L., Zamboni, W. C., Bear, J. E., & Lai, S. K. (2014). Evading immune cell uptake and clearance requires PEG grafting at densities substantially exceeding the minimum for brush conformation. *Molecular pharmaceutics*, *11*(4), 1250-1258.

Yang, R., Reilly, C. R., Rescorla, F. J., Sanghvi, N. T., Fry, F. J., Franklin Jr, T. D., & Grosfeld, J. L. (1992). Effects of high-intensity focused ultrasound in the treatment of experimental neuroblastoma. *Journal of pediatric surgery*, *27*(2), 246-251

Yang, Y. S. S., Moynihan, K. D., Bekdemir, A., Dichwalkar, T. M., Noh, M. M., Watson, N., ... & Irvine, D. J. (2019). Targeting small molecule drugs to T cells with antibody-directed cell-penetrating gold nanoparticles. *Biomaterials science*, *7*(1), 113-124.

Yeh, J. S. M., Sennoga, C. A., McConnell, E., Eckersley, R., Tang, M. X., Nourshargh, S., ... & Nihoyannopoulos, P. (2015). A targeting microbubble for ultrasound molecular imaging. *PloS one*, *10*(7), e0129681.

Yemane, P. T., Åslund, A. K., Snipstad, S., Bjørkøy, A., Grendstad, K., Berg, S., ... & de Lange Davies, C. (2019). Effect of ultrasound on the vasculature and extravasation of nanoscale particles imaged in real time. *Ultrasound in Medicine & Biology*, *45*(11), 3028-3041.

You, D. G., Deepagan, V. G., Um, W., Jeon, S., Son, S., Chang, H., ... & Pomper, M. G. (2016). ROS-generating TiO

2 nanoparticles for non-invasive sonodynamic therapy of cancer. *Scientific reports*, *6*, 23200.

Yu, J., Fischman, D. A., & Steck, T. L. (1973). Selective solubilization of proteins and phospholipids from red blood cell membranes by nonionic detergents. *Journal of supramolecular structure*, *1*(3), 233-248.

Yumura, K., Ui, M., Doi, H., Hamakubo, T., Kodama, T., Tsumoto, K., & Sugiyama, A. (2013). Mutations for Wdecreasing the immunogenicity and maintaining the function of core streptavidin. *Protein Science*, *22*(2), 213-221.

Zarnitsyn, V. G., & Prausnitz, M. R. (2004). Physical parameters influencing optimization of ultrasound-mediated DNA transfection. *Ultrasound in medicine & biology*, *30*(4), 527-538.

Zatloukal, K., Wagner, E., Cotten, M., Phillips, S., Plank, C., Steinlein, P., ... & Birnstiel, M. L. (1992). Transferrinfection. A Highly Efficient Way to Express Gene Constructs in Eukaryotic Cells. *Annals of the New York Academy of Sciences*, (1), 136-153.

Zhang, C., Liu, J., Zhong, J. F., & Zhang, X. (2017). Engineering car-t cells. *Biomarker research*, *5*(1), 1-6.

Zhang, L., Yi, H., Song, J., Huang, J., Yang, K., Tan, B., ... & Li, X. (2019). Mitochondria-targeted and ultrasound-activated nanodroplets for enhanced deep-penetration sonodynamic cancer therapy. *ACS applied materials & interfaces*, *11*(9), 9355-9366.

Zhao, Y. Z., Liang, H. D., Mei, X. G., & Halliwell, M. (2005). Preparation, characterization and in vivo observation of phospholipid-based gas-filled microbubbles containing hirudin. *Ultrasound in medicine & biology*, *31*(9), 1237-1243.

Zhou, Q., Zhu, X. Q., Zhang, J., Xu, Z. L., Lu, P., & Wu, F. (2008). Changes in circulating immunosuppressive cytokine levels of cancer patients after high intensity focused ultrasound treatment. *Ultrasound in medicine & biology*, *34*(1), 81-87.

Zhou, Y., Shi, J., Cui, J., & Deng, C. X. (2008). Effects of extracellular calcium on cell membrane resealing in sonoporation. *Journal of Controlled Release*, *126*(1), 34-43.

Zhou, Y., Yang, K., Cui, J., Ye, J. Y., & Deng, C. X. (2012). Controlled permeation of cell membrane by single bubble acoustic cavitation. *Journal of controlled release*, *157*(1), 103-111.

Zhu, X., Guo, J., He, C., Geng, H., Yu, G., Li, J., ... & Yan, F. (2016). Ultrasound triggered image-guided drug delivery to inhibit vascular reconstruction via paclitaxel-loaded microbubbles. *Scientific reports*, *6*, 21683.

Zhu, Y., Yao, S., & Chen, L. (2011). Cell surface signaling molecules in the control of immune responses: a tide model. *Immunity*, *34*(4), 466–478.

Zolochevska, O., Xia, X., Williams, B. J., Ramsay, A., Li, S., & Figueiredo, M. L. (2011). Sonoporation delivery of interleukin-27 gene therapy efficiently reduces prostate tumor cell growth in vivo. *Human gene therapy*, *22*(12), 1537-1550.